THE STRUCTURAL CHARACTERIZATION OF TWO PROKARYOTIC MEMBRANE PROTEINS: CfrA and ELIC

Casey L. Carswell

Thesis submitted to the

Faculty of Graduate and Postdoctoral Studies

in partial fulfillment of the requirements

for the Doctorate in Philosophy in Biochemistry

Department of Biochemistry, Microbiology and Immunology

Faculty of Medicine

University of Ottawa

© Casey L. Carswell, Ottawa, Canada, 2014

To my mother, Nancy Carswell. Wish you were here!

Abstract

This thesis focuses on the structural and functional characterization of two integral membrane proteins; CfrA, an outer membrane TonB-dependent ferric-enterobactin transporter from *Campylobacter jejuni*, and ELIC, a pentameric ligand-gated ion channel (pLGIC) from *Erwinia Chrysanthemi*. CfrA was cloned, expressed, solubilized, purified and reconstituted into model membranes for biophysical characterization by Fourier transform infrared spectroscopy. The structural characterization revealed a predominantly β -sheet secondary structure, a high peptide backbone solvent exposure, and a high thermal stability, all consistent with the structural and biophysical properties observed for other TonB dependent transporters. Both a homology model of CfrA and sequence alignments of CfrA with other ferric enterobactin transporters suggested a unique mode of ligand binding, thus raising the possibility that CfrA-containing *C. jejuni* can be specifically inhibited, while sparing the gram negative bacteria in the endogenous microflora. To investigate the molecular determinates of binding to CfrA, I set out to crystallize CfrA in the presence and absence of ligand. Hundreds of crystal trials eventually led to crystals diffracting to 3.6Å resolution, with a complete data set acquired at 5Å resolution. The resulting crystal structure led to a structural model of the CfrA β-barrel. Additional optimization of crystal conditions resulted in promising crystals that diffracted relatively well on a home source. However, testing of new crystals at a synchrotron was hindered by logistic and inconsistent access to beam time. The isolated plug domain was also cloned, expressed, and purified to gain insight into the plug domains conformational dynamics and its involvement in mechanism of transport. The purified plug domain exhibited the expected mixed α-helix/β-sheet secondary structure, and underwent denaturation at a temperature of 50 ^{o}C. Surprisingly, exposure to

$^{2}H_2O$ buffer led to the complete exchange of all peptide hydrogens for deuterium within minutes, suggesting a highly dynamic structure. Conditions for producing the ^{15}N-labeled plug in defined media were optimized. Preliminary ^{1}H-^{15}N HSQC NMR spectra suggested a folded structure that is amenable to structural and dynamic studies, although a dynamic equilibrium between monomeric and possibly dimeric forms prevented a more detailed analysis.

In the second part of this thesis, I developed a protocol for the expression, purification, and reconstitution of ELIC into model membranes in order to test the role of intramembrane aromatic interactions in ELIC gating and lipid sensing. ELIC was reconstituted into both asolectin (aso-ELIC) and 1-palmitoyl-2-oleoyl phosphatidylcholine (PC-ELIC), membranes that stabilize the homologous nicotinic acetylcholine receptor (nAChR) in functional coupled versus non-functional uncoupled conformations, respectively. In both membrane environments, ELIC exhibits a mixed α-helical (~30%) and β-sheet (~35%) secondary structure, with a thermal denaturation temperatures of approximately 60°C, values intermediate between those of the nAChR and the close prokaryotic homolog, GLIC, in similar membranes. Unlike the uncoupled PC-nAChR, PC-ELIC does not undergo enhanced peptide $^{1}H/^{2}H$ exchange, suggesting that ELIC does not adopt a similar uncoupled conformation in PC bilayers. Injections in *Xenopus laevis* oocytes led to the fusion of of aso-ELIC with the plasma membrane and the appearance of currents that respond in a dose-dependent manner to cysteamine. In contrast, injection of PC-ELIC into oocytes does not lead to the appearance of cysteamine-induced currents. Together, the data suggest that although ELIC has a decreased propensity to adopt an uncoupled conformation relative to the nAChR, its ability to undergo cysteamine-induced channel gating is sensitive to its lipid

environment. The decreased propensity to uncouple may reflect an increased level of aromatics at the interface between the transmembrane α-helices, M1, M3, and M4. To test this hypothesis further, the level or aromatic residues at the M1, M3, and M4 interface in both GLIC and ELIC were varied, and in both cases the levels of intramembrane aromatic interactions correlated with the efficiency of coupling of binding and gating. The data provide further evidence for a role of intramembrane aromatics in channel gating and in dictating the propensity of pentameric ligand-gated ion channels to adopt an uncoupled conformation.

Acknowledgments

At this point I would like to express my sincere gratitude to some of the many people who made this work possible.

- First and foremost I would like to thank my supervisor Dr. Baenziger for allowing me the opportunity to experience the many ups and downs of life in science.

- To Dr. Stephanie Ravaud and Dr. Goto for their help in the acquisition of diffraction data and NMR data respectively.

- To my mother. I know you would be ecstatic about the completion of this degree. She taught me that life isn't always perfect but if you work hard it will all work itself out. She taught me to take care of mine and not to worry about what others think/do. I have to admit that I'm still working on that one.

- To my father. Your constant presence and support has provided me with the opportunity to complete this degree and your support means a lot. I guess the back up career as a painter will not be needed.

- To my sisters. Your constant unwavering support meant more to me than you can possibly understand. The late night phone calls, the days where I didn't move from your couch, and the days that would go by without contact all without resentment or guilt. Thank you for listening. Thank you for the best present ever - the title of aunt. My 2 beautiful nephews and the rapidly approaching birth of the twins are a constant reminder that life is constantly evolving. Their obvious enjoyment and pleasure in everything new is a reminder to enjoy the process and to take the time to enjoy the little pleasures.

- To my family, thank you for listening and supporting me throughout this process especially since you guys never really knew what I was talking about. Without the constant unwavering support – the completion of this degree would not be possible.

- To my girls. Thank you for listening to my relentless science lectures on anything from the absolute requirement for vaccines to the use of antibiotics on viral infections. You ladies

were there when I needed a science break and never begrudged my prolonged absences that were often required to complete my degree.

- To my science buddies. I could not have completed this degree without you guys. You guys have mastered the ability to calm me down when I would have done something drastic and for that alone I will be forever in your debt!

Preface

This thesis is presented as a collection of three manuscripts with two additional experimental chapters. The data is presented as described below:

Chapter 3

Casey L. Carswell, Marc D. Rigden and John E. Baenziger. (2008) Expression, purification, and structural characterization of CfrA, a putative iron transporter from *Campylobacter jejuni*. *J. Bacteriol.* **190(16)**, 5650-5662.

Chapter 4

The Crystallization of CfrA

Chapter 5

The Expression, Purification, and Structural Characterization of the Isolated Plug Domain

Chapter 7

Casey L. Carswell and John E. Baenziger (2014) The ligand-gated ion channels ELIC and GLC exhibit distinct structural and functional sensitivities to lipids. Submitted to the Journal of Biological Chemistry.

Chapter 8

Casey L. Carswell, J.P. Daniel Therien, Peter D. Juranka, Julian A. Surujballi, and John E. Baenziger (2014) Intramembrane aromatics facilitate the gating of pentameric ligand-gated ion channels and govern susceptibility to potentiation. Submitted to the Journal of Neuroscience.

Table of Contents

ABSTRACT ..... **III**

ACKNOWLEDGMENTS ..... **VI**

PREFACE ..... **VIII**

LIST OF FIGURES ..... **XII**

LIST OF TABLES ..... **XV**

LIST OF ABBREVIATION ..... **XVII**

1 - GENERAL INTRODUCTION **1**

1.1 MEMBRANE PROTEINS ARE ESSENTIAL FOR LIFE 2

1.2 COMMON OBSTACLES HINDERING STRUCTURAL CHARACTERIZATION OF MEMBRANE PROTEINS 2

1.3 STRUCTURAL CHARACTERIZATION OF MEMBRANE PROTEINS 4

1.4 MEMBRANE PROTEINS FOLDS 6

1.5 THESIS OUTLINE 10

PART I

2 THE BATTLE FOR IRON (HUMAN VS BACTERIA) **11**

2.1 THE BIOLOGICAL ROLE OF IRON 12

2.2 DIETARY INTAKE OF IRON 12

2.3 IRON HOMEOSTASIS 15

2.4 IRON AND INFECTION 17

2.5 IRON ACQUISITION BY BACTERIA 17

2.6 TONB DEPENDENT TRANSPORT 19

2.7 FOOD BORNE PATHOGENS AND *CAMPYLOBACTER JEJUNI* 27

2.8 TONB DEPENDENT TRANSPORT IN *CAMPYLOBACTER JEJUNI* 28

3 CfrA EXPRESSION, PURIFICATION **30**

3.1 PREFACE 31

3.2 ABSTRACT 32

3.3 INTRODUCTION 33

3.4 EXPERIMENTAL PROCEDURES 36

3.4.1 Construction of the cfrA plasmid. *36*

3.4.2 Protein Expression. *36*

3.4.3 Protein Purification. *36*

3.4.4 Sucrose Gradients. *39*

3.4.5 FTIR Spectroscopy. *39*

3.4.6 Homology Model. *40*

3.5 RESULTS 41

3.5.1 Expression, purification, and membrane reconstitution of CfrA. *41*

3.5.2 Structural and Biophysical Characterization of CfrA. *47*

3.5.3 A Structural Model of CfrA. *55*

3.6 DISCUSSION 62

3.6.1 Expression, Purification, Reconstitution, and Structural Characterization of CfrA. *62*

3.6.2 Homology Model of CfrA. *64*

3.6.3 Selectivity of Siderophore Binding. *64*

4 CFRA CRYSTALLIZATION 69
4.1 INTRODUCTION 70
4.2 EXPERIMENTAL PROCEDURES 72
4.2.1 Materials 72
4.2.2 Constructs, Expression and Purification of CfrA. 72
4.2.3 Fourier Transform Infrared Spectroscopy (FTIR). 73
4.2.4 Crystallization. 73
4.2.5 Ferric-Enterobactin. 73
4.3 RESULTS 74
4.3.1 Crystallization trials in DDM. 74
4.3.2 Purification in LDAO. 74
4.3.3 Crystallization trials in LDAO. 76
4.3.4 Optimization of crystallization. 80
4.3.5 Crystallization with ligand. 80
4.3.6 Synchrotron results. 82
4.3.7 LPS experiments. 82
4.4 DISCUSSION 88

5 THE EXRESSION, PURIFCATION, AND STRUCTURAL CHARACTERIZATION OF THE ISOLATED PLUG DOMAIN 91
5.1 INTRODUCTION 92
5.2 EXPERIMENTAL PROCEDURES 94
5.2.1 Constructs. 94
5.2.2 Plug expression in LB. 94
5.2.3 Plug expression with ^{15}N-labelled NH_4Cl in M9 Minimal Media. 94
5.2.4 Plug purification. 96
5.2.5 Fourier Transform Infrared Spectroscopy (FTIR). 96
5.3 RESULTS 98
5.3.1 Expression of the plug domain. 98
5.3.2 Purification of plug. 100
5.3.3 Structural and Biophysical characterization of the plug domain. 102
5.3.4 Preliminary 2D Heteronuclear Single Quantum Coherence (HSQC) NMR Spectrum. 104
5.4 DISCUSSION 106

PART II

6 THE ROLE OF INTRAMEMBRANE AROMATICS IN PENTAMERIC LIGAND GATED ION CHANNEL LIPID SENSING 110
6.1 ELECTRICAL EXCITABILITY 111
6.2 TRANSMISSION OF ELECTRICAL SIGNALS 113
6.3 SYNAPTIC COMMUNICATION 114
6.4 PENTAMERIC LIGAND GATED ION CHANNELS 116
6.5 THE PROTOTYPIC MEMBER OF THE PLGICS 117
6.6 PLGIC AGONIST BINDING 119
6.7 COUPLING BINDING TO GATING 121
6.8 THE UNCOUPLED NACHR 123
6.9 A POTENTIAL ROLE FOR INTRAMEMBRANE AROMATICS IN UNCOUPLING 128
6.10 PROKARYOTIC PLGICS 128

7 EXPRESSION AND PURIFICATION OF ELIC: 134
7.1 PREFACE 135
7.2 ABSTRACT 136

7.3 INTRODUCTION 137
7.4 EXPERIMENTAL PROCEDURES 140
7.4.1 Materials *140*
7.4.2 Preparation of ELIC Proteoliposomes. *140*
7.4.3 Fourier transform infrared spectroscopy (FTIR). *141*
7.4.4 Electrophysiology. *141*
7.5 RESULTS 143
7.5.1 Membrane reconstitution of ELIC. *143*
7.5.2 Structure of membrane-reconstituted ELIC *148*
7.5.3 Thermal stability of membrane reconstituted ELIC. *151*
7.5.4 Gating of membrane-reconstituted ELIC. *154*
7.5.5 Effects of an uncoupling lipid environment on ELIC structure. *154*
7.5.6 Effects of an uncoupling lipid environment on ELIC function. *156*
7.6 DISCUSSION 158

8 ROLE OF INTRAMEMBRANE AROMATICS IN LGIC 163
8.1 PREFACE 164
8.2 ABSTRACT 165
8.3 INTRODUCTION 166
8.4 EXPERIMENTAL PROCEDURES 169
8.4.1 RNA constructs for oocyte expression *169*
8.4.2 Electrophysiology. *169*
8.4.3 Data Analysis. *170*
8.4.4 Homology Model. *170*
8.5 RESULTS 171
8.5.1 Aromatic deletions in GLIC *171*
8.5.2 Aromatic additions to ELIC. *174*
8.6 DISCUSSION 177

9 DISCUSSION/CONCLUSIONS 180
9.1 STRUCTURAL CHARACTERIZATION OF CFRA 181
9.2 STRUCTURAL AND FUNCTIONAL CHARACTERIZATION OF ELIC 183
9.3 ELIC AND THE UNCOUPLED STATE 185
9.4 INTRAMEMBRANE AROMATICS INTERACTIONS INFLUENCE THE PROPENSITY TO FORM AN UNCOUPLED RECEPTOR 187
9.5 INCREASED AROMATIC AND LIPID SENSITIVITIES *IN VIVO*? 188
9.6 INCREASED AROMATIC CONTENT AND POTENTIATION/INHIBITION *IN VIVO*? 188

10 REFERENCES 195

List of Figures

PART I

Figure 1.1: Membrane Protein Folds 8

Figure 1.2: Common functions of Membrane Proteins 9

Figure 1.3: Iron Distribution and Hemostatsis 14

Figure 2.1: Bacterial Iron Acquisition Systems 18

Figure 2.2: Common Siderophore Structures 20

Figure 2.3: Structures of Siderophore Transporter from *E.coli* 21

Figure 2.4: Binding of Ligand to (A) FhuA and FecA (B) 23

Figure 2.5: TonB Dependent Transport 25

Figure 3.1: Expression of CfrA in *E. coli* Strain C41 42

Figure 3.2: Solubilization of the N-terminal 6His CfrA 44

Figure 3.3: Purification of N-terminal 10His CfrA 46

Figure 3.4: FTIR spectra of CfrA 48

Figure 3.5: Resolution-Enhanced and Curve Fit of CfrA 50

Figure 3.6: Comparison of the Extent of Peptide Hydrogen-Deuterium Exchange 53

Figure 3.7: Thermal denaturation of CfrA. 56

Figure 3.8: Topology of iron-siderophore transporters 58

Figure 3.9: Alignments of CfrA model with other iron-siderophore transporter 59

Figure 4.1: Production and Structural Characterization of CfrA 77

Figure 4.2: Optimization of CfrA Crystallization 78

Figure 4.3: Crystal Morphologies 81

Figure 4.4: Production and characterization of ferric-enterobactin 83

Figure 4.5: The Structural Characterization of CfrA by X-ray Crystallography 84

Figure 4.6: The Presence of LPS in Detergent-Solubilised CN10 86

Figure 5.1: Purification and structural characterization of the plug domain 99

Figure 5.2: The Re-Distribution of the Plug 101

Figure 5.3: Structural Characterization of the Plug Domain by FTIR..... 103

Figure 5.4: Preliminary NMR spectra (^{1}H-^{15}N HSQC)……105

Figure 5.5: Surface Representation of the Plug Domains……108

PART II

Figure 6.1: Neuron Structure..... 112

Figure 6.2: Synaptic Communication 115

Figure 6.3: nAChR Structure 118

Figure 6.4: Binding to AChBP..... 120

Figure 6.5: Coupling Interface between Agonist binding and Transmembrane domains 122

Figure 6.6: Reaction scheme for pLGICs 124

Figure 6.7: Proposed mechanism of Agonist binding leading to channel gating 125

Figure 6.8: Lipid Uncoupling Model..... 127

Figure 6.9: Prokaryotic Pentameric Ligand-Gated Ion Channels..... 129

Figure 6.10: Comparison of Intramembrane Aromatic Content of pLGICs. 132

Figure 7.1: Intramembrane Aromatic Content of pLGICS……138

Figure 7.2: Structure of ELIC during Sample Preparation 144

Figure 7.3: Surface Electrostatic Potential of ELIC, GLIC and the nAChR……147

Figure 7.4: Structural Comparisons of ELIC, GLIC and the nAChR……149

Figure 7.5: Representative Curve Fits of the Amide I Bands..... 150

Figure 7.6: Thermal Denaturation Spectra of (A) aso-ELIC and (B) PC-ELIC..... 152

Figure 7.7: Representative Thermal Denaturation Curves..... 153

Figure 7.8: Cysteamine-Induced Response of Membrane Reconstituted ELIC..... 155

Figure 8.1: The structural basis for pLGIC lipid sensing..... 167

Figure 8.2: Gating is Inhibited by Aromatic Deletions to GLIC……172

Figure 8.3: Gating is Potentiated by Aromatic Additions to ELIC..... 175

Figure 9.1: Sequence Alignment of Neuronal Subunits of the nAChR..... 189

Figure 9.2: Homology Models of Neuronal Subunits of the nAChR..... 190
Figure 9.3: Crystal Structure of Propofol Bound to GLIC..... 192

List of Tables

Table 3.1: Primer sequences for CfrA constructs 37

Table 3.2: Secondary Structure of CfrA 51

Table 5.1: Primer Sequences for the Isolated Plug Domain 95

Table 7.1: Thermal Stability of ELIC 146

Table 7.2: Secondary Structure in reconstituted membranes 150

Table 8.1: Effects of Aromatic Deletions and Additions on pLGIC Gating 183

List of Abbreviation

^{1}H	Hydrogen
^{2}H	Deuterium
$^{2}H_2O$	Deuterium oxide
ABD	Agonist binding domain
Amp_{100}	100 μg/ml ampicillin
Aso-ELIC	ELIC reconstituted into asolectin lipids
Aso-GLIC	GLIC reconstituted into asolectin lipids
Aso-nAChR	nAChR reconstituted into asolectin lipids
BfrA	*Bordetella bronchiseptica* ferric receptor
C.jejuni	*Campylobacter jejuni*
CC6	CfrA C-terminal 6-His tagged CfrA
CC8	CfrA C-terminal 8-His tagged CfrA
CfrA	Campylobacter ferric receptor
CMC	Critical micelle concentration
CN10	CfrA N-terminal 10-His tagged CfrA
CN6	CfrA N-terminal 6-His tagged CfrA
CV	Column volume
DDM	N-dodecyl-β-D-maltoside
DMT1	Divalent metal transporter 1
E.coli	*Escherichia coli*
EC_{50}	Concentration at half maximal activity
ELIC	*Erwinia chrysathemi* pLGIC
ESRF	European Synchrotron and Radiation Facility
FecA	Ferric citrate transporter from E.coli
FepA	Ferric enterobactin transporter from E.coli
FhuA	Ferric ferrichrome transporter from E.coli
FPN	Ferroportin
FTIR	Fourier transform infrared spectroscopy
Fur	Ferric uptake regulator
GBS	Guillian Barré syndome
GLIC	*Gleobacter violaceus* pLGIC
HRV	Herpes simplex virus
HSQC	Heteronuclear Single Quantum Coherence
IC_{50}	Concentration at half maximal inhibition
IPTG	Isopropyl-β-D-thiogalatopyranoside
LB	Luria bertani
LDAO	N-dodecyl-N-N-dimethylamine-N-oxide
LPS	Lipopolysaccharide
M1	Transmembrane helix 1
M2	Transmembrane helix 2
M3	Transmembrane helix 3
M4	Transmembrane helix 4

MF	Membrane fraction
MPD	2 – methyl-2,4-pentandiol
nAChR	Nicotinic acetylcholine receptor
NMR	Nuclear magnetic resonance
OD_{600}	Optical density at 600nm
PC	Phosphatidylcholine
PC-ELIC	ELIC reconstituted into phosphatidylcholine membranes
PC-GLIC	GLIC reconstituted into phosphatidylcholine membranes
PC-nAChR	nAChR reconstituted into phosphatidylcholine membranes
pCN10	Plasmid containing CfrA N-terminal 10 His tag
PCR	Polymerase chain reaction
PEG	Polyethylene glycol
pLGIC	Pentameric ligand gated ion channel
PMSF	Phenylmethansulphonylfluoride
Post M4	C-terminal of Transmembrane Helix M4
pPLUG	Plasmid containing plug N-terminal 10 His tagged plug
SB-1	Substrate binding loop 1
SB-2	Substrate binding loop 2
Sb-3	Substrate binding loop 3
SDS	Sodium dodecyl sulfate
SF	Soluble fraction
STI	Soybean trypsin inhibitor
TBDT	TonB dependent transporter
TCEP	Tris (carboxyethyl) phosphine
Td	Thermal denaturation temperature
TM	Transmembrane
TMD	Transmembrane domain
TROSY	Transverse relaxation-optimized spectroscopy

1 INTRODUCTION

1.1 Membrane proteins are essential for life

The survival of multicellular organisms is highly dependent on the ability of individual cells to acquire essential nutrients and to communicate with other cells. The ability of cells to perform these essential tasks is aided by the presence of a membrane, which surrounds and encapsulates the cell. Cell membranes are composed of a variety of both lipids and proteins. Lipids spontaneously aggregate to form bilayers that present a hydrophobic barrier between the inside and outside of the cell. This barrier both protects the cell from the external environment and compartmentalizes cellular functions. In contrast, the embedded membrane proteins are typically responsible for complex processes, such as cell-to-cell communication and the acquisition of cellular metabolites.

Membrane proteins account for 20-30% of the proteins encoded in the proteome of most organisms (1). With over half of known therapeutics targeting membrane proteins, the elucidation of membrane protein structure and thus function should lead to important advancements in the treatment of disease states (2,3). Due to the amphipathic nature of membrane proteins, their structural characterization remains inherently difficult (see below) (4). Although there has been a substantial increase in membrane protein structures deposited in the protein data bank in recent years, membrane protein structures still account for only 2% of known structures (5). In order to exploit the vast potential of membrane proteins for possible therapeutic interventions, extensive structural characterization is required.

1.2 Common obstacles hindering structural characterization of membrane proteins

A common stumbling block during the structural characterization of membrane proteins is the production of pure homogenous protein samples, which are essential for successful structural characterization. There are several limiting factors hindering the generation of

pure membrane proteins (6). The first obstacle involves expression. Many membrane proteins are not produced in sufficient quantities by natural sources for structural studies; therefore, a heterologous expression system must be used. There are three common problems regarding membrane protein expression in heterologous expression systems (a) the membrane protein may be toxic to the host, (b) the membrane protein may be expressed at low levels, and (c) the membrane protein may be un/misfolded (7). Different heterologous expression systems, such as bacterial, yeast, insect and mammalian cells, are typically used to express different membrane proteins; however, the choice of expression system remains largely empirical (7-11). Optimization beyond the choice of expression system is also often needed. For example, fusions of the protein of interest with a "carrier" protein (e.g. Mystic) have been shown to increase expression and membrane insertion in some systems (12-14). Expression into inclusion bodies followed by refolding has also been successful in certain cases (15).

Once expression is optimized, a detergent must be identified that will (a) solubilize the protein from the lipid bilayer, (b) maintain the structure and function of the protein during the purification and (c) facilitate the crystallization or NMR analysis of the protein (see below) (16). Numerous detergents have been used with success for solubilization and crystallization of membrane proteins; however, extensive screening and optimization is critical (17-19). In particular, the size of the detergent belt surrounding the protein can hinder both solution state NMR and crystallization experiments. The size of the detergent belt can increase the dimensions of the detergent-protein complex over the size limit of solution state NMR experiments (~100kDa) (20). The detergent belt size can also hinder the formation of protein-protein contacts that are necessary for the formation of a protein crystal

(21,22) (see below). Detergent exchange is often needed, as the detergent optimized for solubilization is not best suited for crystallization or NMR experiments (23).

1.3 Structural Characterization of Membrane Proteins

The main techniques used for the determination of high-resolution structures of membrane proteins are solution state nuclear magnetic resonance (NMR) and X-ray crystallography, both of which require the solubilization of the membrane protein from the bilayer (24).

Briefly, solution state NMR of a membrane protein uses a nucleus of an atom with a nuclear spin of 1/2 (^{1}H,^{13}C and ^{15}N) that when placed in a magnetic field will either align with (lower energy) or against (higher energy) the magnetic field. When external energy is supplied, the nuclei in the lower energy state absorb energy and adopt the higher energy state. The adsorption of radiofrequency is used to determine the structure. The application of solution state NMR, which was traditionally used for soluble proteins, to membrane proteins is complicated by the slow tumbling rates of large detergent-protein complexes. This typically results in peak broadening, poor sensitivity and reduced spectral resolution. However, with the advent of higher magnetic fields and the transverse relaxation-optimized spectroscopy (TROSY) method, the opportunity to study larger molecules by solution state NMR is possible (20,25,26). Two main challenges still remain with respect to solution state NMR: (a) generating the amount of pure protein in an appropriate membrane mimic (see below) and (b) signal overlap caused by redundancy of the amino acids and secondary structure within the membrane environment (27). In spite of these limitations, a number of membrane protein structures have been solved to high resolution (26,28,29). Solution state NMR is an active and rapidly developing field with respect to membrane proteins and will aid in structural determination in the coming years (30).

X-ray crystallography is the prominent method for acquiring atomic level information of membrane proteins (15). The starting point for crystallography is the production of a protein crystal. Protein crystals are built up from protein monomers packed together in a regular repeating fashion. Protein crystallization is a process by which a pure homogenous protein sample is encouraged, by different means, to supersaturate causing formation of a highly ordered crystal. Supersaturation is a non-equilibrium state where the protein is present in solution in excess of its solubility limit, forcing protein molecules to move closer in space and thus the formation of protein-protein contacts. Equilibrium will begin to be reestablished in the environment when the proteins interact in an ordered, repeating fashion, a process referred to as nucleation. Nucleation is followed by growth of the protein crystal until equilibrium of the environment is reached (16). Discovering ideal conditions that encourage the protein of interest to supersaturate, nucleate and grow in a highly ordered fashion is a major stumbling block in the production of atomic resolution structures solved by X-ray crystallography. One needs to identify the chemical, biochemical and physical conditions that yield some form of crystalline material.

Once conditions that favor crystallization are found, the optimization process begins. One needs to determine conditions that yield a highly ordered crystal that diffract X rays to high resolution. The use of additives and substrates during crystallization have been helpful in the acquisition of high-resolution structural information. Another variable to consider is the presence of lipids, although the protein has been removed from the bilayer there is the potential that lipids are still bound to the protein. Some proteins have been shown to require either the removal of certain lipids (FhuA) or the presence of lipids in order to form a highly ordered crystal (ELIC) and/or maintain functionality (31-33). Note that membrane protein

crystals are typically smaller and more delicate then their soluble counterparts. As a result the atomic resolution of a membrane protein structure is often lower then that of soluble proteins (4). The testing to discover conditions that produce high quality crystals capable of diffracting to high resolution is complex and takes considerable time, patience and persistence.

1.4 Membrane Proteins Folds

There are two main classes of membrane proteins, intrinsic or integral and extrinsic or peripheral. Intrinsic membrane proteins have one or more segments that transverse the hydrophobic lipid bilayer, and typically extend into the aqueous medium on either side of the bilayer. Within the integral membrane protein class there is a subcategory of integral monotopic proteins. These membrane proteins are embedded in one leaflet of the membrane and thus are exposed to the aqueous medium on one side of the bilayer. In contrast, extrinsic membrane proteins associate peripherally with the bilayer either indirectly though interactions with an intrinsic membrane protein or directly through the interaction with lipid headgroups. The focus of this thesis is on two intrinsic membrane proteins, which will simply be referred to as membrane proteins.

Membrane proteins typically experience three distinct environments: a hydrophilic water environment, a polar environment located at the level of the lipid headgroups, and a hydrophobic lipid environment located at the center of the bilayer adjacent to the lipid acyl chains. To accommodate the three separate environments, membrane proteins strive to limit the energetic penalty associated with membrane protein insertion by maximizing hydrogen bonds with the polar environment and matching the length of the hydrophobic core of the membrane protein with the length of the hydrophobic lipid acyl chains (34).

To date, two main types of protein tertiary structures that fulfill the above physical and chemical requirements have been identified in a cellular membranes: α-helical and β-barrel membrane proteins (Figure 1.1). α-helical membrane proteins are predicted to represent 27 % of all proteins in the human genome (35). They can possess a single α-helix passing though the bilayer, such as in guanylate cyclase, or can pass through the bilayer many times, as documented for the nicotinic acetylcholine receptor (36,37). α-helical proteins typically arrange themselves within the bilayer, sometimes permitting the formation of a water filled channel through the membrane and other times packing densely thus hindering solvent penetration into the bilayer environment (38,39).

β-barrel proteins are typically formed from multiple β-strands arranged in a circular fashion forming a central pore. In gram negative bacteria, genes encoding β-barrel proteins, referred to as porins, are predicted to account for 2-3% of the protein coding region in the genome (40)) They can range from 8 β-strands, in the human retinol binding protein, to 22 β-strands, as seen in TonB dependent transporters (TBDT) (41,42). Typically, the centre of the pore is solvent exposed with loops controlling the size of metabolite able to pass through the protein. However, not all β-barrel proteins allow free flow of metabolites from the extracellular solution to the intracellular solution. TonB dependent transporters have a domain situated in the pore of the barrel occluding free transport from the extracellular solution to the periplasmic space (Figure 1.1C).

There are many types of membrane proteins (Figure 1.2). For example, transporters regulate the transport of molecules/metabolites/nutrients into the cell. Receptors receive and translate extracellular signals into intracellular action. Enzymes convert one molecule into another form to produce essential cell components or to generate energy during metabolic processes,

Figure 1.1

Membrane protein global folds. **(A)** The nAChR (2BG9) showing transmembrane α-helices.**(B)** OmpF (3K19), a porin, showing a transmembrane β-barrel. **(C)** FepA (1FEP) showing a different of transmembane β-barrel. The barrel is occluded preventing free passage of metabolites from the extracellular solution into the periplasm.

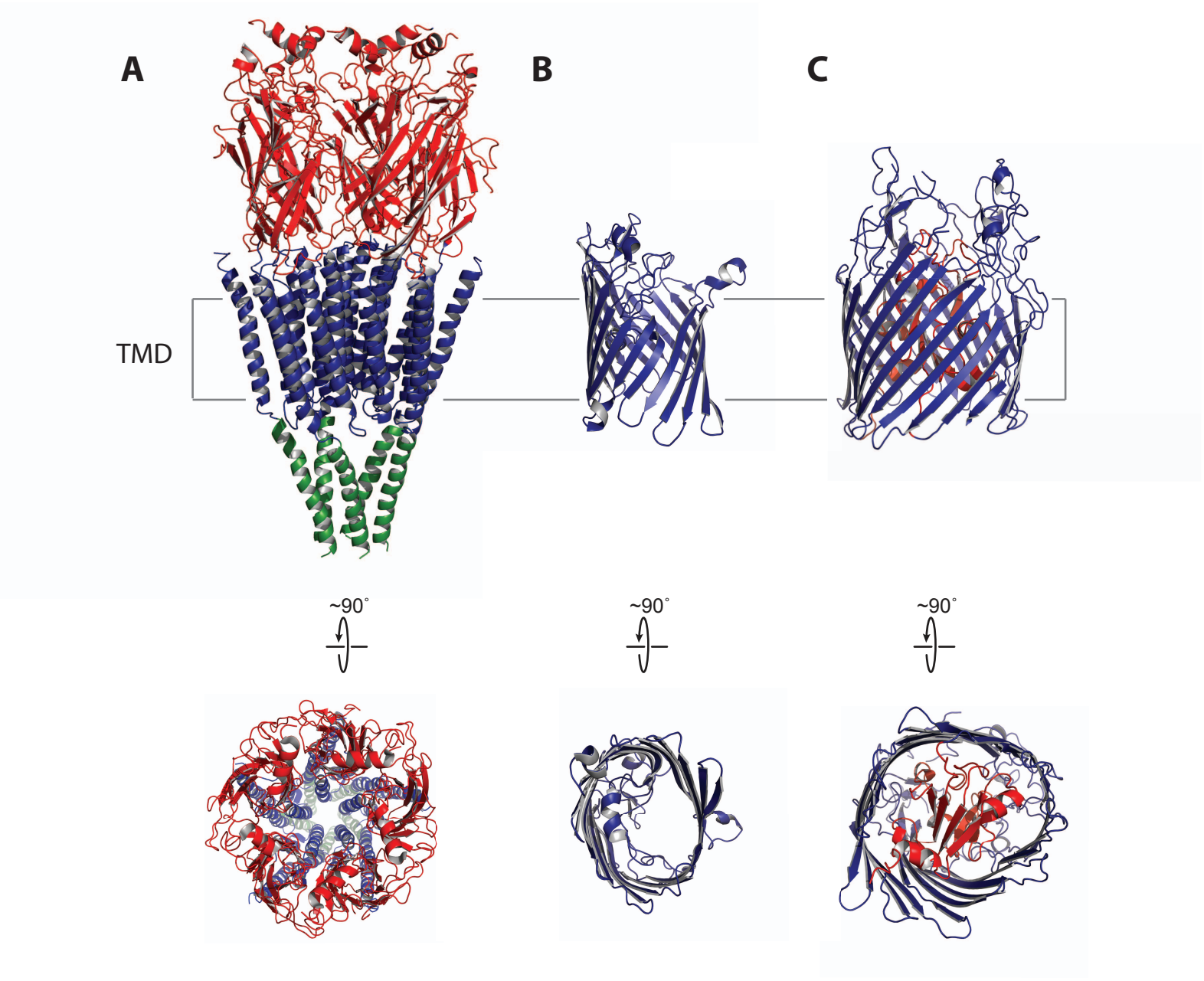
A
B
C
TMD
~90˚
~90˚
~90˚
nAChR (2BG9)
(OmpF (3K19)
FepA (1FEP)

Figure 1.2

Common functions of membrane proteins. Transporters regulate the transport of molecules/metabolites/nutrients into the cell. Receptors receive and translate extracellular signals into intracellular action. Enzymes convert one molecule into another form to produce essential cell components or to generate energy during metabolic processes.

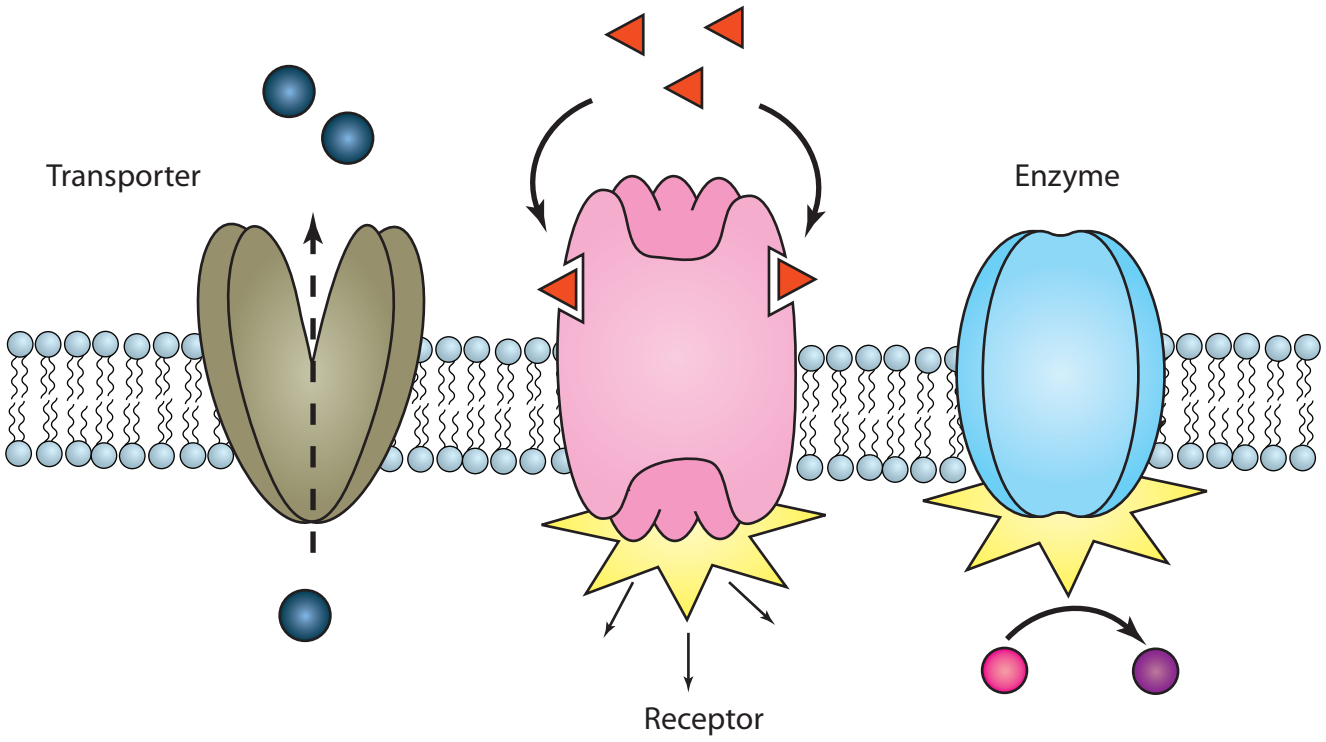
Transporter
Enzyme
Receptor

etc. The work in this thesis is focused on two distinct types of membrane proteins, a membrane protein transporter and a membrane protein receptor.

1.5 Thesis Outline

This thesis will focus on two distinct projects involving the structural characterization of two membrane proteins. The first project is centered on a TonB dependent transporter (TBDT) from *Campylobacter jejuni* implicated in the acquisition of iron. The goal of the first project (Chapters 3 though 5) was to express, purify, and structurally characterize CfrA, and to explore molecular determinates of enterobactin binding. Chapter 3 describes the successful expression, purification, reconstitution and biophysical characterization of CfrA in model membranes. The progress made towards high-resolution structural data of CfrA is described in Chapter 4. The successful crystallization of CfrA resulted in a model at 5Å resolution. Chapter 5 describes the structural characterization of the isolated plug domain of CfrA. The second project (Chapters 7 and 8) involves the structural and functional characterization of a prokaryotic homolog of a pentameric ligand gated ion-channel (pLGIC) from *Erwinia Chrysanthemi* (ELIC). Chapter 7 compares the structures, thermal stability and lipid sensitivities of ELIC to another pLGIC, GLIC, and proposes a role for intramembrane aromatic interactions in determining lipid sensitivity. The role of aromatics in pLGIC function was explored further in Chapter 8. As the work presented here is focused into two distinct projects the remaining introduction has also been divided into two parts: The Battle for Iron (Human vs. Bacteria) and The Role of Intramembrane Aromatics in Pentameric Ligand Gated Ion Channel Lipid Sensing.

PART I

2 The Battle for Iron (Human vs Bacteria)

2.1 The Biological Role of Iron

Because of both the abundance of iron on the earth's surface and its unique capacity to act as both an electron acceptor and donor, iron has become the chosen metal for redox reactions in almost all biological processes ranging from respiration, to the TCA cycle, to DNA synthesis (43,44). Iron is essential for the growth, survival, and well-being of almost all living organisms.

Unfortunately, the evolution from an anaerobic to an aerobic environment on the earth's surface, over the past 2 billion years, has resulted in the conversion of the previously available ferrous ion (Fe^{2+}) iron to the oxidized ferric form (Fe^{3+}), which is highly insoluble in aqueous solution (10^{-18} M at pH 7.0) and thus unavailable to most organisms (43-45). On the other hand, free iron within the cell can catalyze the conversion of hydrogen peroxide to free radicals, which can cause cellular damage leading to cell death and ultimately organ failure (43,46,47). Surplus iron has been associated with various human disease states such as cardiovascular and neurodegenerative diseases (48). As a result of both problems, all organisms ranging from simple microbes to multicellular mammals have developed complex mechanisms for acquiring, storing, and regulating the levels of iron *in vivo*.

2.2 Dietary Intake of Iron

Adults possess roughly 4-5g of total iron (49). Approximately 60-70% of the iron pool is incorporated into hemoglobin, as part of the heme prosthetic group, in circulating erythrocytes. The heme prosthetic group reversibly binds oxygen allowing transport of oxygen from the respiratory organs to peripheral tissues. Other metalloproteins such as myoglobin and the enzyme aconitase account for an additional 10-15% of total iron stores

(50-52). The majority of the remaining iron is stored in the form of ferritin, with less then 1% in the form of transferrin/lactoferrin (Figure 2.1A) (50,53). Ferritin is an iron storage protein found in all cell types. It is formed from 24 identical or similar subunits forming a hollow sphere capable of storing 4,500 iron molecules as the mineral ferrihydrites (Fe_2O_3 * H_2O) within the hollow center (54,55). Transferrin is a blood plasma glycoprotein involved in the transport of iron throughout the body. The the pH dependence of iron binding to transferrin is of importance. At pH 7.4, transferrin has a high affinity for iron, however as pH decreases the binding affinity for iron decreases. The significance of the pH dependence of iron binding will be explained below. Lactoferrin is similar to transferrin but present in lymph and mucosal secretions (56).

The limited iron removed through slothing of intestinal and mucosal cells is replenished through dietary absorption. Dietary ferric iron is reduced by ferric reductase and transported into the proximal duodenum by the divalent metal transporter-1 (DMT1) where the ferrous iron will either be incorporated into metalloproteins for cellular processes, stored as ferritin, or transported out of the cell into the blood stream by ferroportin (FPN), oxidized by a ferrioxidase (hephasetin), and subsequently bound by transferrin for transport to peripheral cells via the blood stream. Dietary heme is transported into the duodenum by heme carrier protein-1 (HCP1), where heme oxygenase catalyzes the degradation to ferrous iron, carbon dioxide and biliverdin. Once reduced within the cell, the fate of ferrous iron derived from dietary heme follows the same pathway as described for dietary ferric iron. Peripheral cells satisfy their iron requirements via circulating transferrin. Upon binding, holo-transferrin uptake involves binding to the transferrin receptor. The complex (transferrin/transferrin receptor) is internalized by the process of receptor-mediated endocytosis. Once within the

Figure 2.1

Iron Distribution and Hemostatsis. **(A)** The normal distribution within the body is shown. Adults possess approximately 4-5g of total iron. Approximately 60-70% of the iron pool is incorporated into hemoglobin, as part of the heme prosthetic group, in circulating erythrocytes. Other metalloproteins such as myoglobin and the enzyme aconitase account for an additional 10-15% of total iron store. The majority of the remaining iron is stored in the form of ferritin, with less then 1% in the form of transferrin/lactoferrin. **(B)** Dietary ferric iron is reduced by ferric reductase and transported into the proximal duodenum by the DMT1 where the ferrous iron will either be incorporated into metalloproteins for cellular processes, stored as ferritin, or transported out of the cell into the blood stream by FPN, oxidized by a ferrioxidase (hephasetin), and subsequently bound by transferrin for transport to peripheral cells via the blood stream in need of iron. **(C)** In the target cells, holo-transferrin uptake involves binding to the transferrin receptor where the complex (transferrin/transferrin receptor) is internalized by the process of receptor-mediated endocytosis. Once within the endosome, the decrease in pH facilitates iron removal from transferrin and the iron is transported into the cytoplasm by DMT1. Apo-transferrin and the transferrin receptor are recycled to the cell surface where apo-transferrin is released. **(D)** Circulating macrophages engulf senescent red blood cells. Once within the phagosome, heme oxygenase catalyzes the degradation of heme to iron, carbon monoxide and biliverdin. The iron is transported into the cytoplasm by DMT1. Again, once within the cell, the iron can be stored as ferritin, used for cellular processes, or exported by FPN. Within the blood stream, the ferrous iron is oxidized by ceruloplasmin, bound to transferrin and transported to peripheral cells.

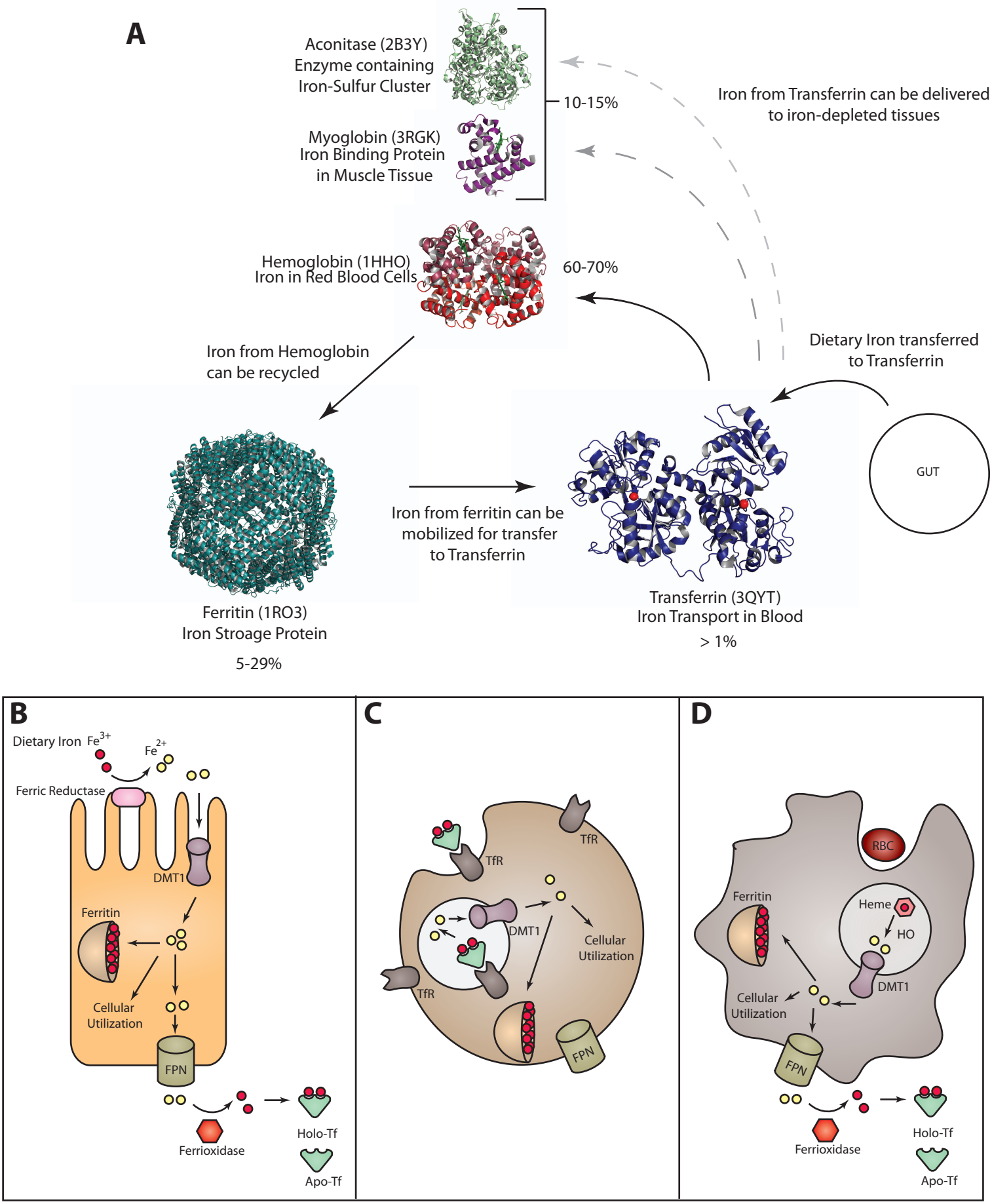
A
Aconitase (2B3Y)
Enzyme containing
Iron-Sulfur Cluster
Myoglobin (3RGK)
Iron Binding Protein
in Muscle Tissue
10-15%
Iron from Transferrin can be delivered
to iron-depleted tissues
Hemoglobin (1HHO)
Iron in Red Blood Cells
60-70%
Iron from Hemoglobin
can be recycled
Dietary Iron transferred
to Transferrin
GUT
Iron from ferritin can be
mobilized for transfer
to Transferrin
Ferritin (1RO3)
Iron Stroage Protein
5-29%
Transferrin (3QYT)
Iron Transport in Blood
> 1%
B
Dietary Iron Fe3+
Fe2+
Ferric Reductase
DMT1
Ferritin
Cellular
Utilization
FPN
Ferrioxidase
Holo-Tf
Apo-Tf
C
TfR
TfR
DMT1
Cellular
Utilization
TfR
FPN
D
RBC
Ferritin
Heme
HO
DMT1
Cellular
Utilization
FPN
Ferrioxidase
Holo-Tf
Apo-Tf

endosome, the decrease in pH facilitates iron release from transferrin, and the iron is transported into the cytoplasm by DMT1. Apo-transferrin and the transferrin receptor are recycled to the cell surface where apo-transferrin is released (49,57,58) (Figure 2.1B).

As very little iron is removed from the human body, the largest pool of iron stores is meticulously recycled through recycling of red blood cells by macrophages. Circulating macrophages engulf senescent red blood cells. Once within the phagosome, heme oxygenase catalyzes the degradation of heme to iron, carbon monoxide and biliverdin. The iron is transported into the cytoplasm by DMT1. Again, once within the cell, the iron can be stored as ferritin, used for cellular processes, or exported by FPN. Within the blood stream, the ferrous iron is oxidized by ceruloplasmin, bound to transferrin and transported to peripheral cells. (Figure 2.1C). Note, holo-transferrin binds to developing erythrocytes efficiently recycling the iron back into erythrocytes (49,57,58).

2.3 Iron Homeostasis

In humans, iron homeostasis is highly regulated (59). Intracellular iron levels are monitored by two iron regulatory proteins (IRP1 and IRP2). When iron levels are low within the cell, IRPs bind to iron regulatory element (IRE) sequences in mRNAs of iron regulated proteins such as ferritin and the transferrin receptor. IREs are present at the 5' and 3' untranslated regions (UTR) of the mRNA and determine its fate. When an IRP binds to an IRE located in the 3' UTR, the mRNA is stabilized for translation. In contrast, binding at the 5' UTR inhibits translation. For example in low iron conditions, IRPs bind to the 3' UTR of the transferrin receptor thus stabilizing the mRNA of the transferrin receptor resulting in increased iron uptake. In addition, binding of the 5'UTR of ferritin and inhibits the

expression of ferritin resulting in decreased iron storage. In contrast, at high iron levels, IRPs do not bind to their IRE resulting in decreased iron uptake and increased iron storage (57).

Iron concentrations within plasma are regulated by hepcidin. Hepcidin is considered the master regulator of systemic iron homeostasis. Hepcidin, a peptide hormone, is predominantly produced in the liver. Hepcidin expression is influenced by both increased iron stores and inflammation by as of yet unknown mechanisms (60). During periods of iron excess, hepcidin binds to FPN causing FPN to be internalized and degraded (61). The degradation of FPN halts export of iron from all cells decreasing plasma iron concentrations. The degradation of FPN in the cells of the duodenum effectively blocks the delivery of dietary iron to plasma transferrin. The short lived enterocytes are then shed into the intestine and removed from the body.

The misregulation of iron has drastic affects. Individuals suffering from iron overload acquire iron deposit in various organs specifically the liver and heart. The adverse redox chemistry of free iron leads to cellular damage resulting in liver damage and cardiomyopathy. Iron overload also enhances risk of infection (49). Mutations in both FPN and hepcidin and have been shown to cause iron overload (62,63).

Iron deficiency anemia is estimated to have caused 273,000 deaths in 2004 with 800 million people affected by the disease. Infants suffering from insufficient iron are at risk for delayed normal motor and mental functions (64-67). Pregnant mothers with hypoferremia have an increase risk of low birth weight which is associated with other risk factors (68).

2.4 Iron and Infection

As noted, most life forms, even microbes, require iron to survive. In response to infection, the limited amount of available iron in humans is thus further sequestered by biochemical possesses. As mention above, hepcidin expression is induced in response to inflammation. Hepcidin causes the degradation of FPN leading to iron sequestration with the cell. The iron loaded transferrin is rapidly depleted for erythrocyte production leaving very little iron available for bacteria. Also transferrin is typically only 30% saturated with iron; thus ideally positioned to readily capture free iron making it inaccessible to invading pathogens (58). When the binding capacity of transferrin is exceeded, iron can be chelated by other low affinity iron binding proteins in the plasma such as albumin, citrate and amino acids (49). Neutrophils and macrophages also synthesize hepcidin in response to infectious agents, allowing modulation of iron availability at the infectious foci. In addition, lipocalin-2 a protein expressed by myeloid and epithelial cells, has been shown to bind ferric-enterobactin with high affinity (69). Enterobactin is a siderophore used by bacteria to acquire iron from their host (see below). As excess iron has been shown to increase virulence of certain pathogens *in vivo* it is essential to limit free iron (53,70).

2.5 Iron Acquisition by Bacteria

Since the concentration of free iron ($\sim 10^{-24}$M) in mammals does not meet the concentration sufficient for growth ($\sim 10^{-6}$M), bacteria have evolved complex mechanisms for scavenging the necessary iron from their hosts (Figure 2.2) (44). One such mechanism involves the production of receptor proteins on the outer membrane of the bacteria. These proteins bind host iron-binding proteins (transferrin/lactoferrin) with high affinity, extract the iron, and

Figure 2.2

Bacterial Iron Acquisition Systems. (A) Bacteria synthesize and secrete a variety of siderophores. These molecules are able to chelate iron with high affinity and are subsequently bound by high affinity transporters located in the outer membrane of the bacteria and transported into the bacterium. (B) Bacteria secrete hemophores, molecules that are able to extract heme from hemoglobin and are subsequently transported into the bacterium by a hemophore transporter located in the outer membrane. (C) Finally, bacteria are able to express a variety of host receptors such as the transferrin receptor and thus are able to bind and transport transferrin into the bacterial cell.

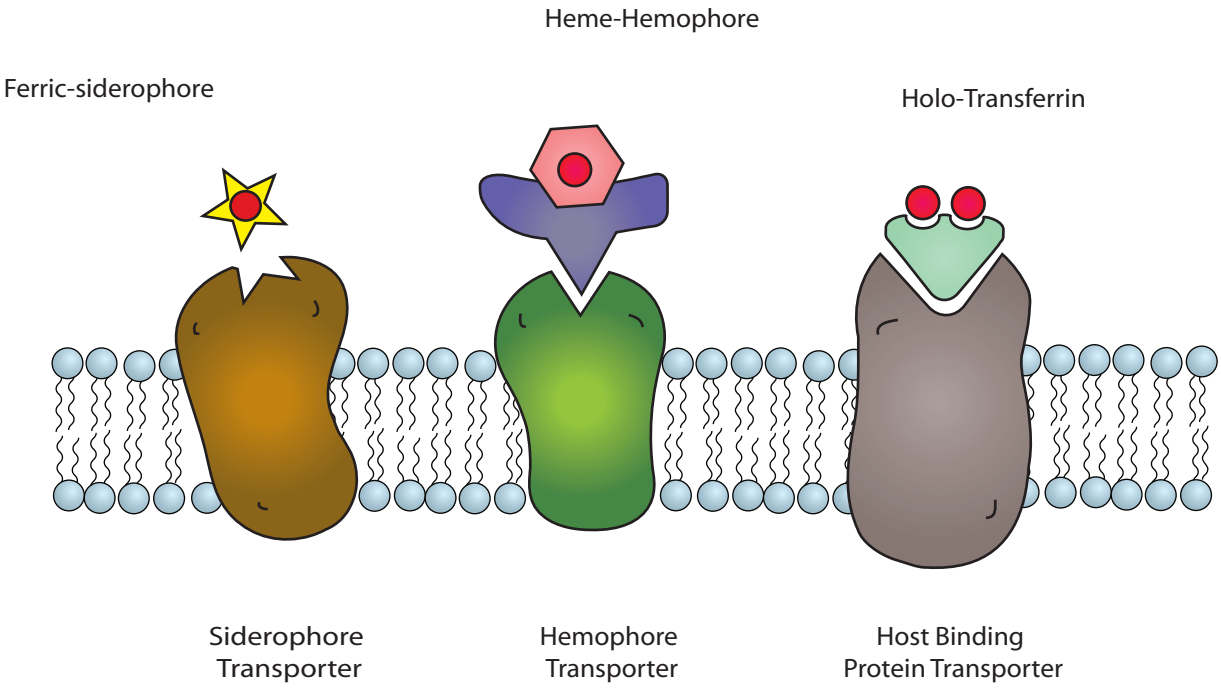
Heme-Hemophore
Ferric-siderophore
Holo-Transferrin
Siderophore Transporter
Hemophore Transporter
Host Binding Protein Transporter

transport the iron into the cell (71,72). Tbp1 and Tbp2 from *Neisseria* species are known to bind host transferrin whereas LbpA and LbpB bind lactoferrin (73,74). Another common mechanism is the secretion of a 19kDa protein, called a hemophore, that is able to extract heme from hemoglobin and transfer the heme group to an outer membrane receptor (HasR), which transports the heme into the bacterial cell (75). Finally, many bacteria synthesize and secrete a variety of low molecular weight molecules (typically 500-1000 daltons) called siderophores that chelate iron with high affinity (43,44,76). As described below, a complex energy-dependent Fe^{3+}-siderophore uptake system then concentrates the ferric-siderophore inside the cell. The importance of this method of iron acquisition is demonstrated by the decreased virulence both *in vitro* and *in vivo* of pathogens defective in siderophore transport (70,77). The chemical structures of three of bacterial siderophores are shown in Figure 2.3.

2.6 TonB Dependent Transport

The size and the low concentration of ferric-siderophores prevent efficient passage through outer membrane porins (72). To circumvent this obstacle, bacteria express protein receptors on the outer membrane to specifically bind the ferric-siderophore complex and to actively transport them into the cell. Several siderophore-mediated iron transporters from *Escherichia coli* outer membranes have been identified and studied from a structural perspective (19,32,78). Crystal structures of FhuA, FecA, Cir and FepA have been determined, the former two with ligand bound (Figure 2.4) (78). The proteins show a remarkable structural homology (65). All possess a β-barrel topology formed from 22 anti-parallel β-strands connected by short periplasmic turns and long extracellular loops (L1-L11) with a globular plug domain (42,78). The plug domain is situated in the center of the β-barrel and is comprised of five α-helices, two β-strands and a mixed four-stranded β-sheet. Above and

Figure 2.3

Common siderophore structures: **(A)** Enterobactin, **(B)** Citrate, and **(C)** Ferrichrome.

A

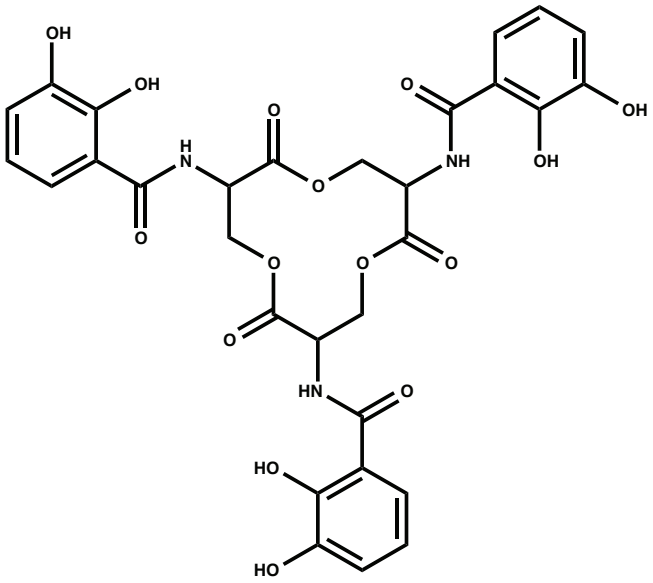

B

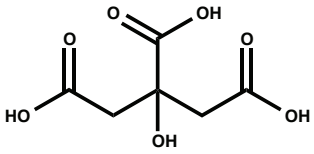

C

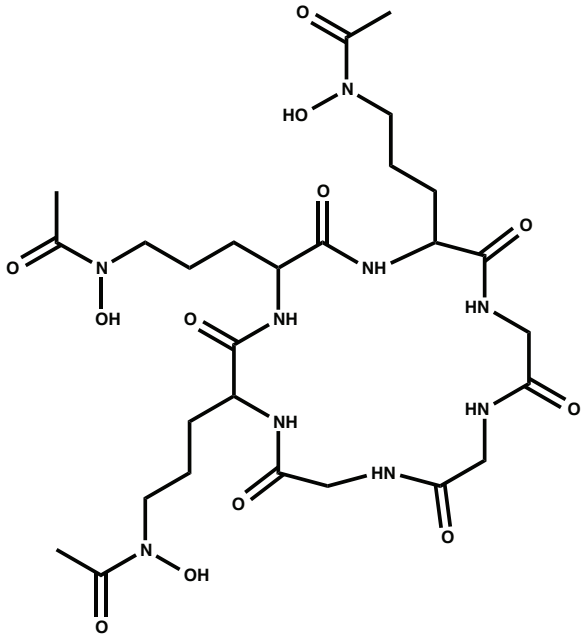

Figure 2.4

Siderophore transporter structures from *E.coli;* **(A)** FhuA (1BY5) (154) , **(B)** FecA (1KMP) (164) and **(C)** FepA (1FEP) (153). The three transporters show a considerable structural homology. The plug domain is presented separately for clarity. Note a structural alignment between the individual plug domain is presented with only the mixed β-sheet shown as loop length and placement varies. It has been suggested that the conserved motifs within the plug domain are responsible for the precise arrangement/location of the mixed β-sheet and thus the substrate binding loops contributed by the plug domain.

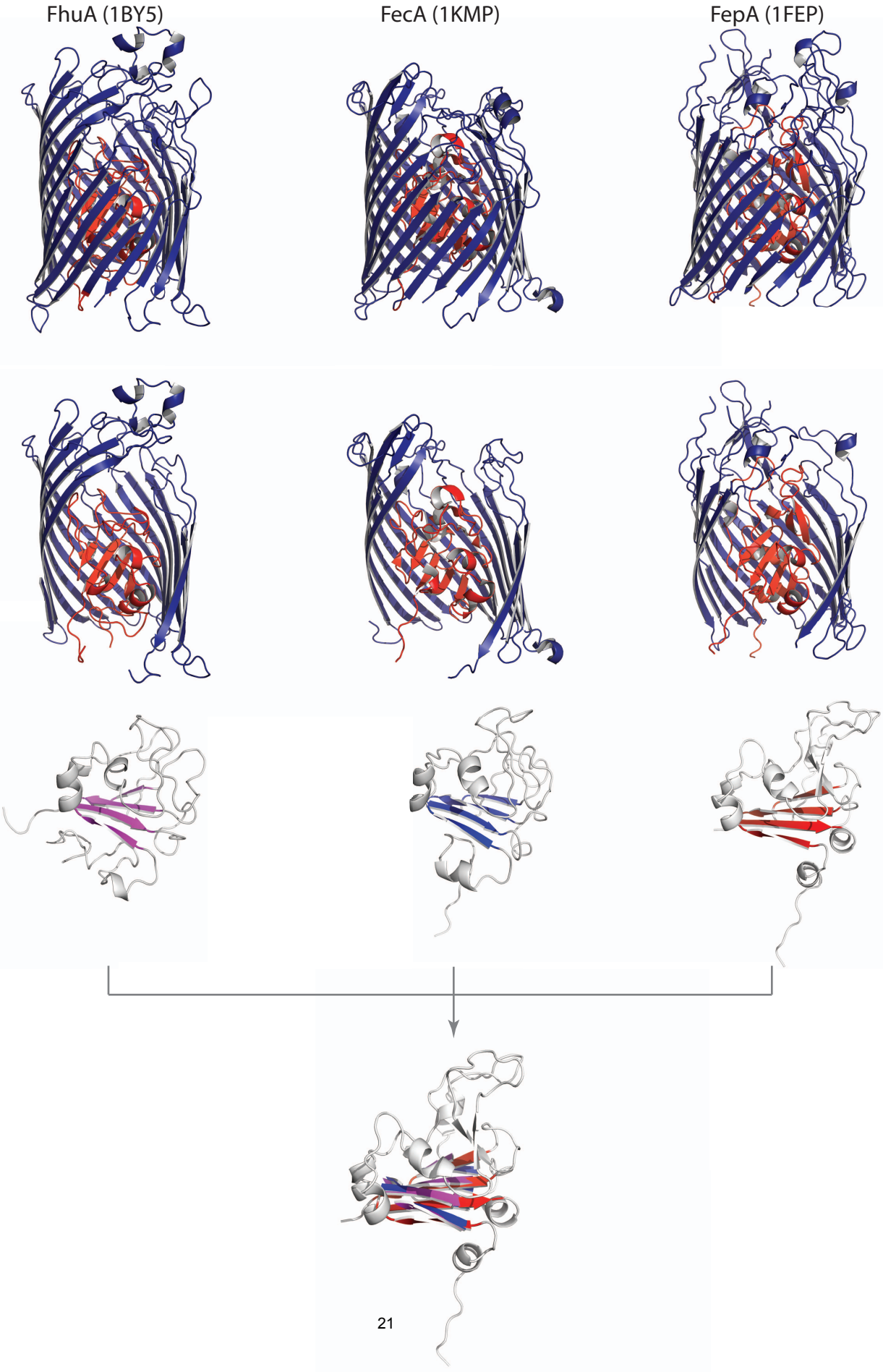
FhuA (1BY5)
FecA (1KMP)
FepA (1FEP)

below the mixed four-stranded β -sheet is the extracellular and periplasmic space respectively. Three substrate binding loops (SB1, SB2 and SB3) located within the plug domain extend from the mixed four-stranded β-sheet towards the extracellular solution. The positioning of the plug domain prevents the direct transport of ferric-siderophore from the extracellular environment into the periplasm. The N-termini of these proteins (located on the plug domain) all possess a conserved region, called a TonB box, that has been implicated in energy-dependent ferric-siderophore transport (79).

Although there is high structural homology, overall sequence identity is low (Figue 2.4). Of note, the plug domain has the highest level of sequence identity when taken as an isolated domain. The conserved motifs located in the plug-barrel interface have been suggested to be necessary for proper folding and positioning of the plug domain within the barrel (80). The position of the plug relative to the barrel is critical for ligand binding as residues involved in ligand binding have been located on the substrate binding loops of the plug and loops of the barrel (see below).

The structures of the ligand bound FhuA and FecA provide information regarding the binding pockets and thus molecular determinants of binding (Figure 2.5). Both the plug and barrel domain contribute residues to binding of the ligands. FhuA binds ferrichrome within a pocket lined by aromatic residues (Y116, Y244 and Y315). A positively charged arginine residue (R81) on substrate binding loop 2 is also involved. FecA binds the negatively charged ferric citrate using several positively charge arginine residues (R155, R365 and R380). While the ligand bound structure of FepA was unresolved, extensive biochemical analysis has identified four conserved residues (Y260, Y272, F329 add R316) that are required for the binding/transport of ferric-enterobactin to/by FepA (81). The consensus

Figure 2.5

Binding of Ligand to **(A)** FhuA (1BY5) (154) and FecA (1KMP) (164) **(B).** The binding of ferrichrome by FhuA is facilitated by the formation of an aromatic cage by surrounding aromatic residues. FecA binds the negative ferric-citrate using multiple arginine residues.

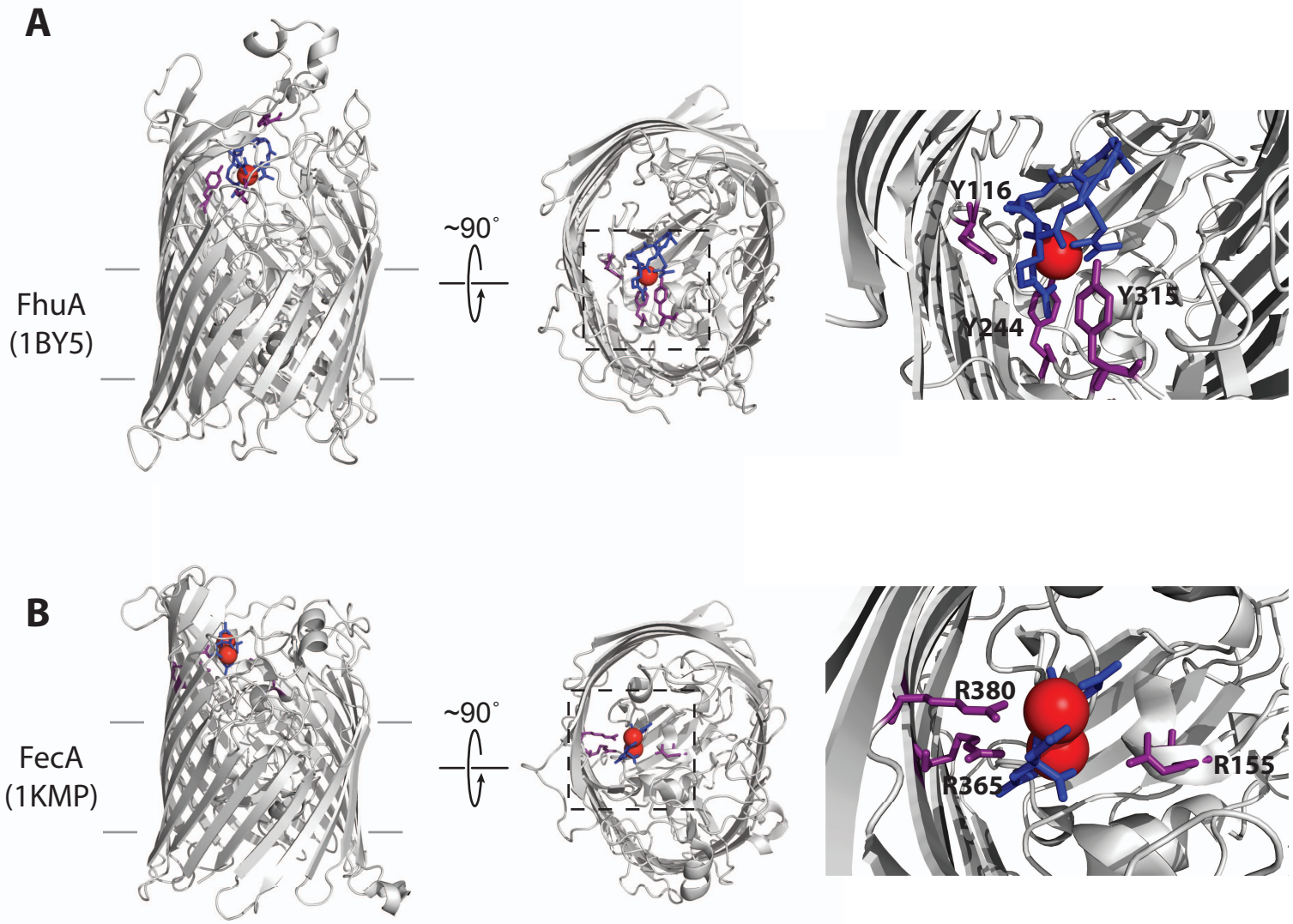
A
FhuA
(1BY5)
~90˚
Y116
Y315
Y244
B
FecA
(1KMP)
~90˚
R380
R365
R155

currently is a 2 step binding process, the first step involves "catching" of the ligand by the loop extremities which are thought to determine ligand specificity. This hypothesis is supported by experiments where chimeras of FepA and FhuA showed that the ability to discriminate between siderophores is determined by residues located within the barrel domain. The FepA barrel/FhuA plug chimera transports enterobactin and the FhuA barrel/FepA plug transports ferrichrome (82). Plug deletion mutants of both FhuA and FepA maintain a subnanomolar affinity further supporting the role of barrel residues in ligand specificity (82). In agreement, the affinity of isolated plug domain of FepA for enterobactin is reduced 100 fold compared to the full length protein (83). Once bound at the loop extremities, the ligand is "passed" to the secondary binding site closer the center of the barrel.

Binding of the ferric-siderophore is proposed to cause a conformational change in the N-terminal extension of the transporter permitting a physical interaction between the TonB box and a protein complex situated in the cytoplasmic membrane (84-87). This protein complex is thought to be composed of 3 proteins called TonB, ExbB and ExbD (84,88-95). In the bound state, the physical interaction between the TonB box and the TonB protein leads to a transduction of energy from the cytoplasmic membrane through the TonB complex to the siderophore-mediated iron transporter in the outer membrane (93,94,96-99). The energy, thought to derive from the proton motive force, triggers the conformational change in the siderophore-mediated iron transporter allowing the transport of the ferric-siderophore into the periplasm (96-98). Once within the periplasm, the ferric-siderophore is guided by a periplasmic binding protein to an inner membrane ATP binding cassette transporter and moved directly into the cell (Figure 2.6) (43).

Figure 2.6

TonB Dependent Transport. Ferric-siderophores bind to high affinity TonB dependent transporter located in the outer membrane. Upon binding, a conformation change occurs in the N-terminus of the TonB dependent transporter allowing the physical interaction with the TonB complex located in the periplasmic membrane. The physical interaction allows the transduction of energy, via the proton motive force, to the TonB dependent transport providing the energy to facilitate a conformation change in the plug domain allowing transport of the ferric-siderophore into the periplasm. The ferric siderophore is then bound by a periplasmic binding protein and transported to an ATP-Binding Cassette (ABC) and subsequently transported into the cell.

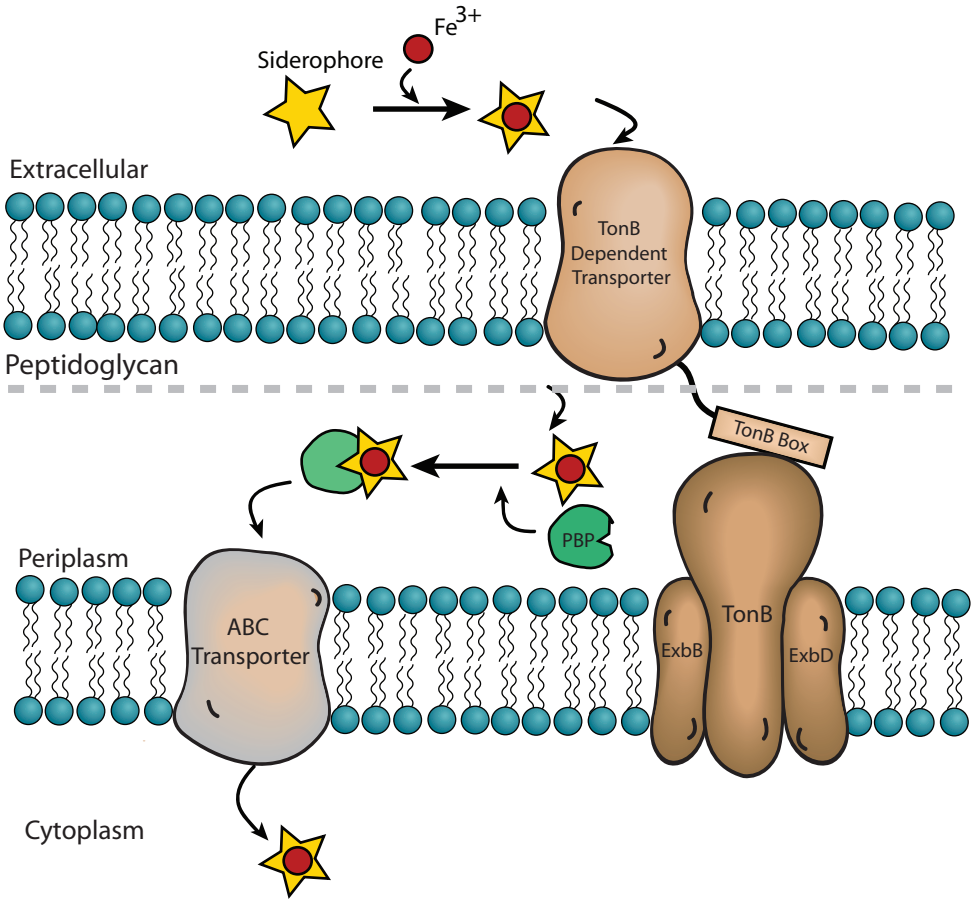
Fe3+
Siderophore
Extracellular
TonB
Dependent
Transporter
Peptidoglycan
TonB Box
PBP
Periplasm
ABC
Transporter
TonB
ExbB
ExbD
Cytoplasm

Despite the high resolution structural information and the extensive biochemical data, there are a number of fundamental questions that have yet to be answered. For example, the conformational changes required for the transport of the ferric-siderophore into the periplasm have not been elucidated. There are two common theories for the mechanism of transport though the siderophore-mediated iron transporter. One involves the complete displacement of the plug domain into the periplasmic space allowing transport of the ferric siderophore (100). The plug domain could be removed, intact, as a globular domain or it could become unfolded. The other prominent theory is that side chains are shifted creating a "channel" for the ferric-siderophore to travel though to the periplasm (100). Conflicting evidence has been reported (101-104). Cysteine mutants of FepA reacted with fluorescien maleimide or biotin maleimide upon transport suggests the partial removal of the plug domain from the barrel (102,105). However, others have found that removal of the plug is not needed for transport (106). Disulfide tethering of the cork to the barrel was not sufficient to halt ferrichrome uptake by FhuA suggesting the plug domain is not expelled from the interior of the barrel supporting the formation of a channel (104). The contradictory results may be explained by different labeling reagents, different bacterial strains or different concentrations (107). The plug domain can be expressed as a separate domain where unfolding is reversible with a reduced affinity for ligand (83,108,109). This supports the hypothesis that the plug domain unfolds as it leaves the barrel lowering the apparent affinity for the siderophore and permitting release into the periplasmic space. Also, the energy required for the conformational change is thought to originate from the proton motive force but how the energy is transferred from the cytoplasmic membrane to the outer membrane is unclear. However, recent studies suggest TonB undergoes constant motion, driven by an electrochemical force which drives enterobactin transport (110).

2.7 Food borne pathogens and *Campylobacter jejuni*

Food borne pathogens cause approximately 11 million disease episodes per year in Canada (111). In Ontario, there are approximately 1.2 episodes of acute gastrointestinal illness per person per year (112). These episodes incur an estimated cost of 3.7 billion dollars in lost productivity and other associated costs (113). *Campylobacteriosis* is one of the most prevalent causes of gastrointestinal illness in the United States (114). *Campylobacter jejuni* accounts for 90% of disease episodes caused by *Campylobacteriosis* in a case study of 3,764 patients (115). Therefore, the successful targeting of *Campylobacter* species would be extremely valuable to the medical community for the successful reduction of food borne disease episodes.

Campylobacter jejuni is a gram-negative microaerophilic rod shaped bacteria. Avian species provide a reservoir for *C.jejuni* as the bacteria are unable to elicit an immune response. As contamination of poultry meat can occur during processing, proper precaution during food preparation, must be adhered to as human infection can be established by the consumption of only a few hundred bacterial cells (116,117). *C. jejuni* infection manifests as dysentery and general malaise (118). Although, *C. jejuni* is typically self-limiting it is still a considerable strain on hospital personnel time and hospital funding. *C. jejuni* infection has also been linked to Guillain-Barré syndrome (GBS). GBS is an acute neurologic disease driven by autoimmunity and molecular mimicry in which the body elicits an immune response against peripheral nerve myelin (119). The disease manifests as muscle weakness with the potential to lead to partial/complete paralysis and death (120). The global occurrence of GBS ranges

from 0.4 to 1.7 cases per 100,000 people annually (121). Approximately, one case of GBS develops for every 1000 colonization events by *C. jejuni (122).* In a systematic review of published cases between 1982 to 2010, 31% of 2,502 GBS cases were attributable to prior *Campylobacteriosis* infection (119). The occurrence of GBS will not be eliminated with the successful avoidance of *Campylobacteriosis* infection; however, the number of cases per annum will decrease.

2.8 TonB Dependent Transport in *Campylobacter jejuni*

Although the mechanisms used by *C. jejuni* to scavenge iron appear complex, considerable evidence suggests that this microorganism uses a siderophore-mediated transport mechanism. Several strains of *C. jejuni* are able to utilize ferric-enterobactin as an iron source (123,124). A number of *C. jejuni* gene sequences have been identified, which encode proteins with significant sequence similarity to proteins in the *Campylobacter coli* siderophore transport system (125,126). Most of the corresponding gene sequences have an upstream ferric uptake regulator (Fur) box. Fur acts as a negative co-repressor during transcription of iron transport genes (126). Binding of Fur to the promoter of some of these genes in *C. jejuni* has been shown directly using mobility shift assays (127,128). Conditions of iron starvation in *C. jejuni* lead to the overexpression of a 76 kDa outer membrane protein, now called the *Campylobacter* ferric receptor (CfrA). CfrA has considerable sequence similarity with *Bordetella bronchiseptica* receptor (BfrA), a siderophore-mediated iron transporter in *Bordetella bronchiseptica* (123,129). In growth plate studies, *cfrA* deletion mutants are incapable of utilizing enterobactin as an iron source (126). Significantly, deletion mutants of *cfrA* are unable to establish a successful infection in chick colonization

assays (126). Inhibitors of CfrA function should thus be effective at treating *C.jejuni* infection.

The inability to establish a successful colonization by deletion mutants of *cfrA* identifies CfrA as an attractive potential therapeutic target. A successful therapeutic, however, would have to selectively target CfrA, while not harming the endogenous microflora. Therefore I set out to structurally characterize CfrA to investigate the molecular determinates of binding for the use as a potential therapeutic.

3 MANUSCRIPT:

1. **Casey L. Carswell,** Marc D. Rigden and John E. Baenziger. (2008) Expression, purification, and structural characterization of CfrA, a putative iron transporter from *Campylobacter jejuni*. *J. Bacteriol.* **190(16)**, 5650-5662.

3.1 Preface

This manuscript is the first of three first author publications presented in this thesis. Originally published in the Journal of Bacteriology in June 2008, this paper is my first publication. The goal of this work was to perform a preliminary biophysical characterization of CfrA with the hypothesis that CfrA was sufficiently different from other TBDT and could be specifically targeted as a therapeutic.

I initiated and performed all the experiments presented in this manuscript. The initial cloning of the CfrA constructs was done under the supervision of Marc Rigden. I wrote the manuscript in collaboration with my supervisor.

3.2 Abstract

The gene for the *Campylobacter* ferric receptor (CfrA), a siderophore-mediated iron transporter in the enteric food-borne pathogen, *C. jejuni,* was cloned and the membrane protein expressed in *E. coli*, affinity purified, and then reconstituted into model lipid membranes. FTIR spectra recorded from the membrane-reconstituted CfrA are similar to spectra that have been recorded from other siderophore-mediated iron transporters and are highly characteristic of a β-sheet protein (~44 % β-sheet and ~10 % α-helix). CfrA undergoes relatively extensive peptide hydrogen-deuterium exchange upon exposure to $^{2}H_2O$ yet is resistant to thermal denaturation at temperatures up to 95 °C. The secondary structure, relatively high aqueous solvent exposure, and high thermal stability are all consistent with a transmembrane β-barrel structure containing a plug domain. Sequence alignments indicate that CfrA contains many of the structural motifs conserved in other siderophore-mediated iron transporters, including the Ton box, PGV, IRG, RP, and LIDG motifs of the plug domain. Surprisingly, a homology model reveals that regions of CfrA that are expected to play a role in enterobactin binding exhibit sequences that differ substantially from the sequences of the corresponding regions that play an essential role in binding/transport by the *E. coli* enterobactin transporter, FepA. The sequence variations suggest that there are differences in the mechanisms used by CfrA and FepA to interact with bacterial siderophores. It may be possible to exploit these structural differences to develop CfrA-specific therapeutics.

3.3 Introduction

Campylobacter jejuni is a gram negative food-borne pathogen that commonly populates the gastrointestinal tract of birds and mammals. In humans, *C. jejuni* infection leads to severe abdominal cramping, headache, diarrhea and in extreme cases death (130,131). *C. jejuni* infects 1% of the United States population annually. Of those affected, 0.1% of the patients develop Guillian Barré syndrome - an autoimmune disorder of the peripheral nervous system that results in weakening of muscles and, in some cases, neurological problems (132-134). Both *C. jejuni* infection and Guillian Barré syndrome are a considerable burden on the public health care system (132,134).

Most bacteria, including *C. jejuni*, have an obligatory requirement for iron and have thus developed sophisticated mechanisms for scavenging iron from their hosts (129). One key mechanism involves the production of low molecular weight molecules (500-1000 Da), called siderophores, that bind ferric ions with high affinity (43,76). Secreted siderophores chelate iron from surrounding tissues and are then bound to siderophore-mediated iron receptors/transporters located in the bacterial outer-membrane. An energy dependent TonB-mediated conformational change in the ferric-siderophore transporter translocates the ferric-siderophore into the periplasm. Periplasmic binding proteins then transport the iron-bound siderophore to an inner membrane ATP binding cassette transporter that moves the iron-bound siderophore directly into the cell (43,72,78,135,136).

Although the mechanisms used by *C. jejuni* to scavenge iron appear complex, considerable evidence suggests that this microorganism uses a siderophore-mediated transport mechanism. Several strains of *C. jejuni* are able to utilize ferric-enterobactin as an iron source (123,124). A number of *C. jejuni* gene sequences have been identified, which encode

proteins with significant sequence similarity to proteins in the *Campylobacter coli* siderophore transport system (125,126). Most of the corresponding gene sequences have an upstream Fur box. Fur acts as a negative co-repressor during transcription of iron transport genes (126). Binding of Fur to the promoter of some of these genes in *C. jejuni* has been shown directly using mobility shift assays (127,128).

Conditions of iron starvation in *C. jejuni* lead to the overexpression of a 76 kDa outer membrane protein, now called the *Campylobacter* ferric receptor (CfrA). CfrA has considerable sequence similarity with BfrA, a siderophore-mediated iron transporter in *Bordetella bronchiseptica* (123,129). In growth plate studies, *cfrA* deletion mutants are incapable of utilizing enterobactin as an iron source (126). Deletion mutants of *cfrA* are also unable to establish a successful infection in chick colonization assays (126). Consequently, CfrA has been reannotated as the ferric-enterobactin transporter in *C. jejuni*.

Several siderophore-mediated iron transporters from *Escherichia coli* outer membranes have been studied from a structural perspective (19,32,78). Crystal structures of FhuA, FecA, FepA and Cir have been determined to high resolution. The proteins all possess a β-barrel topology with a plug domain that is implicated in siderophore binding and transport (42,78). The plug domain is situated in the middle of the β-barrel and prevents the direct transport of the iron loaded siderophore from the extracellular environment into the periplasm. Despite the high resolution structural information, the mechanism of transport by siderophore-mediated iron transporters across the membrane remains to be established. One limiting factor has been the lack of efficient protocols for reconstituting the siderophore-mediated transporters and their associated proteins into model membrane systems that are amenable to biochemical and biophysical studies.

Given the prevalence and potentially severe consequences of *C. jejuni* infection, the outer membrane siderophore receptor/transporter CfrA is a potential therapeutic target. As a first step towards better understanding the role played by CfrA in iron transport in *C. jejuni*, we cloned the *cfrA* gene from chromosomal DNA and present here a protocol for the expression, purification and reconstitution of CfrA into model membranes. The membrane reconstituted CfrA adopts an overall β-sheet secondary structure that is accessible to aqueous solvent, yet highly resistant to thermal denaturation. The structural/biophysical properties of CfrA are consistent with those of other siderophore-mediated iron transporters. Sequence alignments and a homology model of CfrA also show that CfrA contains many of the conserved structural motifs/sequences found in other siderophore-mediated iron transporters. Surprisingly, regions of the protein that are predicted to play a role in ferric enterobactin binding exhibit variations in sequence relative to other siderophore-mediated iron transporters including the ferric-enterobactin transporter, FepA. In fact, key aromatic residues known to play an important role in ferric-enterobactin binding/transport in FepA are absent in CfrA. The homology model and sequence comparisons suggest that FepA and CfrA use different mechanisms to interact with ferric-enterobactin. The altered sequences of the binding sites suggest that it may be possible to exploit structural differences between CfrA and FepA to develop CfrA-specific therapeutics.

3.4 Experimental Procedures

3.4.1 Construction of the cfrA plasmid. The *cfrA* gene was amplified from *Campylobacter jejuni* chromosomal DNA (NCTC 11168) using PCR with the primers listed in Table 3.1. PCR reactions were performed in an Eppendorf Mastercycler Gradient (Eppendorf) with 30 cycles of 95 ^{o}C for 30 seconds, 45 ^{o}C for 30 seconds and 72 ^{o}C for 2.5 minutes. PCR products were ligated into the pET20b vector (Novagen). The ligation mixture was transformed into chemically competent *Escherichia coli* XL1-Blue without further manipulation. Resulting transformants were screened for plasmids of appropriate size. Inserts were sequenced to ensure gene integrity. The final plasmid used in these studies was designated pCN10 (CfrA N-terminal 10-His-tagged).

3.4.2 Protein Expression. Chemically competent *E. coli* strain C41 (DE3) was transformed with pCN10 and grown on Luria Bertani (LB) plates (137). Following overnight incubation, single colonies were subcultured into 50 mL of LB medium supplemented with 100 μg/mL ampicillin (LB-Amp_{100} Shelton Scientific) and incubated for 18 hours at 37 °C. Cultures were then diluted 1:300 into 16 L of fresh LB-Amp_{100} and incubated at 37 °C. Protein expression was induced at an OD_{600} of 0.6 by addition of isopropyl-β-D-thiogalatopyranoside (IPTG, MBI Fermentas) to a final concentration of 0.2 mM. After three hours at 26 °C, cultures were pelleted and cells resuspended in 100 mL of lysis buffer (300 mM NaCl, 50 mM NaH_2PO_4, pH 7.0). Cells were frozen until use.

3.4.3 Protein Purification. The resuspended cells were incubated for 1 hour at 4 °C in lysis buffer containing 2 mM tris (carboxyethyl) phosphine (TCEP), 1 μg/mL Leupeptin, 1 μg/mL

.

Table 3.1. Primer sequences designed for construction of CC6, CN6, CC8 and CN10 CfrA constructs

Primer Names	Primer Sequences
CfrA-5-Bam-10-His	GCGCGGATCCGCACCACCACCACCACCACCCACCACCACCACGAC GACGACGACAAGCAAAATGTAGAACTAGATAGC
CfrA-3-Xho-10H-NS	GCGCCTCGAGGTGGTGGTGGTGCTTGTCGTCGTCGTCAAAGTTAC CATTGATAG
CfrA-5-Bam-8-His	GCGCGGATCCGCACCACCACCACCACCACCACCACGACGACGAC GACAAGCAAAATGTAGAACTAGATAGC
CfrA-3-Xho-8H-NS	GCGCCTCGAGGTGGTGCTTGTCGTCGTCGTCAAAGTTACCATTGA TAG
CfrA-5-Bam-His	GCGCGGATCCGCACCACCACCACCACCACAAAATGTAGAACTAG ATAGC
CfrA-3-Xho-H-NS	GCGCCTCGAGAAAGTTACCATTGATAG
CfrA-C-Bam-5	GCGCGGATCCGCAAAATGTAGAACTAGATAGC
CfrA-N-Xho-3NS	GCGCCTCGAGTTAAAAGTTACCATTGATAG

Abbreviations used: CC6, CfrA with a C-terminal 6-histidine-tag; CN6, CfrA with a N-terminal 6-histidine-tag; CC8, CfrA with a C- terminal 6-histidine-tag; CN10, CfrA with a N- terminal 10-histidine-tag.

Enzyme cleavage sites for cloning purposes are underlined.

Aprotinin, 1 μg/mL Soybean trypsin inhibitor (STI), 1 mM Benzamidine (All from Calbiochem), 1 mM Phenylmethansulphonylfluoride (PMSF) (Sigma), 100 μg/mL Lysozyme (Sigma), 10 mM β- mercaptoethanol (Sigma) and 30 μg/mL DNase (Roche) and then lysed with 3 passes through an Emulsiflex C_3 (Avestin, Inc) at 18,000 psi. The cell extract was centrifuged at 7,000 xg for 20 minutes at 4 °C to remove the non-lysed cells and the membrane protein fraction isolated by centrifugation at 135,000 xg**.** Membrane fraction protein concentration was determined by BCA protein assay (Pierce).

Membrane proteins were solubilized by incubating 1 g of the membrane protein for 1 hour at 4 °C in lysis buffer containing 1% (w/v) n-dodecyl-β-D- maltoside (DDM, Anatrace), 2 mM TCEP, and 10 mM β-mercaptoethanol. After centrifugation at 100,000 xg, the solubilized protein in the supernatant was incubated for 1 hour at 4 °C with Superflow cobalt based resin (Clontech). The resin was transferred to a glass column and non specifically bound protein was removed with 3 buffer washes (3 column volumes each) with increasing imidazole concentration (0, 10 mM, 50 mM imidazole) (Sigma) in lysis buffer supplemented with 0.075 % (w/v) DDM. Protein was eluted from the resin in 150 mM imidazole, 300 mM NaCl, 50 mM NaH_2PO_4, and 0.075 % (w/v) DDM at pH 7.0. Protein fractions were concentrated using a Centricon 30,000 Dalton cutoff concentrator (Millipore) and then further purified on a Superdex-200 gel filtration column (GE health care) equilibrated with lysis buffer supplemented with 2 mM TCEP, 10 mM β-mercaptoethanol and 0.07 5% (w/v) DDM.

The purified CfrA was reconstituted into a lipid membrane by diluting the solubilized protein 1:20 into a solution containing 0.13 μM soybean asolectin (Sigma) and 1% (w/v) sodium cholate (Sigma) in lysis buffer. After mixing for 5 minutes, the dilute solution was placed in dialysis tubing (12, 000 - 14, 000 Dalton cutoff; Fisher) and the samples dialyzed 5 times

against 2 L of lysis buffer at 4 °C. The reconstituted vesicles were pelleted at 100,000 xg and resuspended in 5 mM Tris-HCl, 0.02 % (w/v) azide at pH 7.5 (Sigma) and stored at -80°C.

3.4.4 Sucrose Gradients. Step sucrose gradients were prepared by layering 2 ml each of 40 % (w/v), 20 % (w/v), 10 % (w/v) and 3 ml of 0 % (w/v) sucrose in a plastic centrifuge tube. 150 μg of protein was pipetted directly into the 0 % (w/v) sucrose. The sample was centrifuged for 20 hours at 100,000 xg. Fractions were assayed for both protein (BCA assay, Pierce) and lipid (Phospholipids C, Wako Chemicals) to determine lipid to protein ratios.

3.4.5 FTIR Spectroscopy. Transmission FTIR spectra were recorded on either a FTS 40 or a FTS 7000 spectrometer (Varian) both equipped with a deuterated triglycine sulphate detector. For the analysis of protein secondary structure, 200 μg of the protein was exchanged into 2 mM ^2H_2O phosphate buffer, pH 7.0, by repeated centrifugation, resuspension cycles. After 72 hours at 4 ^oC, the samples were pelleted and redissolved in 35 μl of 2 mM ^2H_2O phosphate buffer pH 7.0 and subjected to five freeze-thaw cycles. Each sample was then sandwiched between 2 CaF_2 windows separated by a 12 μm Teflon spacer and placed in a thermostatically controlled FTIR transmission cell (Harrick Scientific). Spectra were recorded at 2.0 cm^{-1} resolution signal averaging 4000 scans. For thermal denaturation, 256 scan spectra were recorded at 2°C temperature intervals between 35 °C and 95 °C. The temperature was varied with a computer-controlled circulating water bath, with 20 minute equilibrations between temperatures.

The extent of hydrogen-deuterium exchange after 72 hours in ^2H_2O was assessed by recording FTIR spectra using the attenuated total reflectance technique. The reconstituted samples were deposited from 2mM ^2H_2O pH 7.0 buffer on a germanium internal reflection

optical element, and the sample immersed in 100 mM NaCl and 5 mM NaH_2PO_4 ^2H_2O buffer (see Results). All spectra were analyzed using Grams/AI v.7.01 (Galactic) and plotted using Graphpad Prism (Graphpad Software, Inc).

3.4.6 Homology Model. The homology model was constructed using Swiss-Model (138). The plug and β-barrel domains were modelled independently using Cir and FepA, respectively, as templates (see text). Collectively the two domains represent a full length model of CfrA. The majority (95%) of the φ and ϕ angles of the model are found in favourable regions of the Ramachradran plot, with proline and glycine making up most of the remaining 5%.

3.5 Results

3.5.1 Expression, purification, and membrane reconstitution of CfrA. The *cfrA gene* was cloned from the chromosomal DNA of *C. jejuni* (NCTC 11168) and constructs containing either a C-terminal 6-His or an N-terminal 6 His-tag were placed into the pET20b vector under the control of the T7 promoter. The IPTG-induced expression of both proteins was monitored in *E. coli* strains C41 and C43, which are less sensitive to the expression of toxic proteins and recommended for the expression of membrane proteins (137). In 3 hour expression trials, the C41 strain produced higher levels of both the C-terminal and N-terminal 6-His-tagged proteins than the C43 strain (data not shown). All further expression studies were performed using the C41 strain.

The effect of inducer (IPTG) concentration, over the range of 0.2 mM to 0.8 mM, on the expression of CfrA was examined. Western blots probed using an anti-His antibody show that expression levels do not increase at concentrations above 0.2 mM IPTG (Figure 3.1A). In fact, a slight reduction in protein quantity is observed with increasing IPTG concentration, possibly due to a negative effect on cell viability. Also, the over expression of CfrA is accompanied by the production of degradation products during the 4 hour induction trials. To reduce degradation, both the N and C-terminal 6-His-tagged CfrA were expressed at lower induction temperatures of 26 °C and 18 °C (Figure 3.1B) (139). Although the amount of degradation may be reduced at lower temperatures, the quantity of expressed protein diminishes substantially. To balance the need for both quality and quantity, the remaining induction experiments and purification trials were performed with an induction temperature of 26 °C. Note that the expressed CfrA is found associated with the pelleted membrane

Figure 3.1

Expression of CfrA in *E. coli* strain C41. Transformed C41 cells were grown at 37°C, and the expression of the N-terminal His_6 CfrA examined under various induction conditions. **(A)** Representative Western blot probed with an anti-His antibody showing the expression of the N-terminal His_6 CfrA at 0, 1, 2, 3, and 4 h after induction of expression in the presence of 0.2 and 0.8 mM IPTG. Expression was performed at 37°C. **(B)** Western blot probed with an anti-His antibody comparing expression of His_6 CfrA at 37, 26, and 18°C at time zero and 3 h after induction. **(C)** SDS-PAGE gel with Coomassie blue stain (upper panel) and a Western blot probed with an anti-His antibody (lower panel) showing expression at time zero and 3 h postinduction, as well as the cellular localization of CfrA. Lane 1, $T = 0$ h prior to induction; lane 2, $T = 3$ h postinduction; lane 3, SF (soluble fraction); and lane 4, MF (membrane fraction).

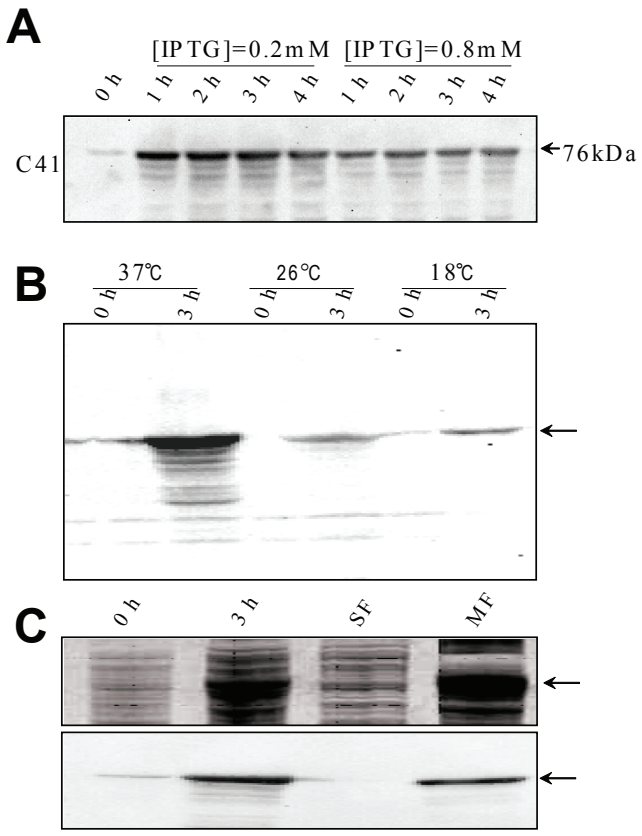
A
[IPTG]=0.2mM
[IPTG]=0.8mM
0 h
1 h
2 h
3 h
4 h
1 h
2 h
3 h
4 h
C41
76kDa
B
37℃
26℃
18℃
0 h
3 h
0 h
3 h
0 h
3 h
C
0 h
3 h
SF
MF

fraction (Figure 3.1C). To purify CfrA, we first examined various detergents for their ability to solubilize the protein from its membrane environment. Each detergent solubilization trial was performed at a concentration 1 % (w/v) above the critical micellar concentration (CMC) of the utilized detergent (140). Of the seventeen detergents tested, nine were able to solubilize appreciable amounts of CfrA from the membrane fraction. Unfortunately, a consistent maximum yield approaching only ~50 % of the total CfrA was obtained with all 9 detergents (Figure 3.2A). Increasing the detergent concentration and/or the solubilization time did not improve the quantity of solubilized protein (Figure 3.2B). One possible explanation for the incomplete solubilization is that the non-solubilized protein is found in inclusion bodies, which pellet with the membrane fraction. Consistent with this possibility, higher levels of solubilized protein were obtained using the denaturing agent guanidinium hydrocholoride as a "solubilizing" agent (data not shown). Biochemical procedures commonly used to isolate proteins from inclusion bodies also led to improved isolation of CfrA (data not shown). No further attempts were thus made to increase the yield of solubilized protein.

The C-terminal and N-terminal 6-His constructs were purified using a cobalt affinity column followed by size exclusion chromatography on a Superdex 200 column. Both the N- and C-terminal 6-His-tagged proteins showed poor binding to the affinity column, possibly due to inaccessibility of the histidine tags. A C-terminal 8-His-tagged construct was produced, but the improvement in binding to the affinity column was marginal. We finally constructed an N-terminal 10-His-tagged version of CfrA with an enterokinase cleavage site. The extended tag greatly improved CfrA affinity for the cobalt column. The expression and solubilization of the N-terminal 10-His-tagged version of CfrA were consistent with the results obtained with the 6-His-tagged version of the protein discussed above. SDS-PAGE confirms that the

Figure 3.2

Solubilization of the N-terminal 6His CfrA. Membrane fractions, containing the expressed N-terminal 6His CfrA, were incubated with the noted detergent for 1 h at 4°C and then centrifuged at 100,000 × *g*. The supernatants, which contain the solubilized protein, were then analyzed by SDS-PAGE. **(A)** Western blot with anti-His antibody of soluble fractions from detergents successful in solubilizing CfrA from the membrane. Lane 1, sodium dodecanoyl sarcosinate; lane 2, anzergent 3-14; lane 3, fos mea-10; lane 4, fos-choline; lane 5, cymal 5; lane 6, dodecyl maltoside; lane 7, decyl maltoside; lane 8, nonyl glucoside; lane 9, octyl glucoside; lane 10, control showing sample prior to solubilization. **(B)** Western blot with anti-His antibody comparing the amount of CfrA solubilized with 1- and 2-h solubilization times at both 1 and 3% DDM.

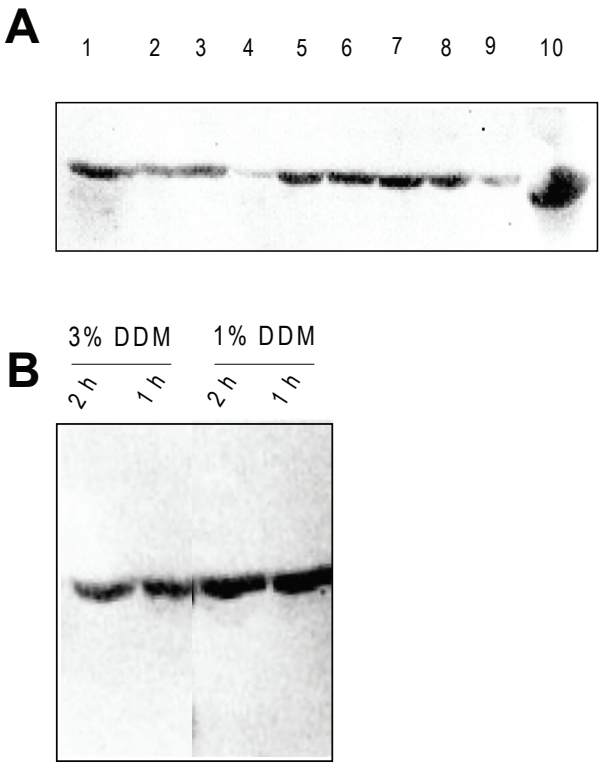
A
1 2 3 4 5 6 7 8 9 10
B
3% DDM
1% DDM
2 h
1 h
2 h
1 h

affinity column followed by size exclusion chromatography is sufficient to purify a 10-His-tagged protein with a molecular weight of 84 kDa, which is close to that expected for CfrA (76 kDa). Mass spectrometry confirmed the identity of the purified CfrA (472 residues were sequenced from a total of 696 amino acids; Proteomics Resource Centre of the Ottawa Institute of Systems Biology).

Note that a second band is observed in lane 6 and 7 on the SDS-PAGE gel running at a molecular weight of 73 kDa (Figure 3.3). β-Barrel membrane proteins tend to be highly stable structures that are resistant to SDS denaturation (141,142). A second band running at a lower molecular weight on SDS-PAGE gels has been observed with other β-barrel membrane proteins and has been attributed to protein that is not completely denatured by SDS (142). Mass spectrometry confirms that the lower molecular weight protein has the expected sequence for CfrA (131 residues were sequenced from a total of 696 amino acids; Proteomics Resource Centre of the Ottawa Institute of Systems Biology). More importantly, boiling the sample prior to SDS-PAGE eliminates the lower molecular weight component (Figure 3.3 lane 8) confirming that it is due to partially folded CfrA (141).

CfrA was reconstituted into lipid membranes by first diluting the DDM-solubilized protein above the CMC for DDM with a buffered solution containing cholate-solubilized soybean asolectin lipids, and then dialyzing away both detergents with several buffer changes. The dialysis protocol was sufficient to both decrease the two detergents to undetectable levels (data not shown; (143)) and form lipid vesicles with incorporated CfrA. The reconstituted CfrA routinely contains two distinct populations of vesicles that vary in terms of the amount of incorporated protein (Figure 3.3B). The lipid to protein ratios of the two vesicles populations were estimated by an enzymatic assay (see Experimental Procedures) to be

Figure 3.3

Expression, purification, and reconstitution of N-terminal His_{10}-tagged CfrA. **(A)** SDS-PAGE with Coomassie blue staining showing protein purity at each step of the purification of CfrA. Lane 1, protein standards; lane 2, whole-cell lysis prior to induction; lane 3, whole-cell lysis 3 h postinduction at 26°C; lane 4, membrane fraction; lane 5, detergent-solubilized protein; lane 6, affinity-purified CfrA; lane 7, affinity-purified CfrA after size-exclusion chromatography; lane 8, CfrA reconstituted into asolectin membranes. Note that only the sample in lane 8 was boiled prior to loading. **(B)** Sucrose density gradients were used to assess the reconstitution success of CfrA into asolectin lipids. A total of 150 μg of reconstituted CfrA was subjected to sucrose density gradients. Fractions of 400 μl were collected by pipetting, beginning with the least dense (fraction 1, 0% sucrose) to the most dense (fraction 28, 40% sucrose). Individual fractions were assayed for protein (red) and lipid (blue) concentration as described in Materials and Methods.

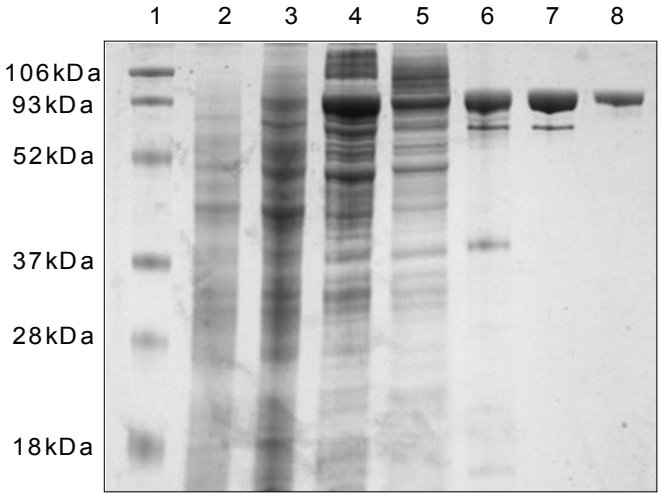
1
2
3
4
5
6
7
8
106kDa
93kDa
52kDa
37kDa
28kDa
18kDa

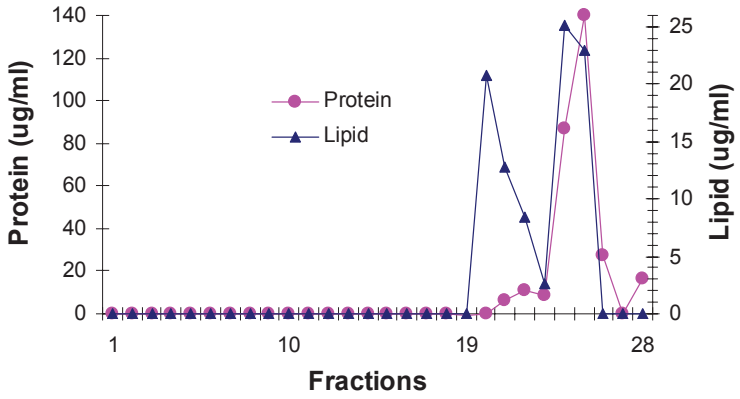
Protein (ug/ml)
Lipid (ug/ml)
Protein
Lipid
Fractions
0
20
40
60
80
100
120
140
0
5
10
15
20
25
1
10
19
28

220:1 (mol:mol) and 20:1 (mol:mol), although the assay is specific for phosphatidylcholine and thus underestimates the total lipid content. Phosphatidylcholine represents only 14-24 % of the total asolectin lipid (http://www.sigmaaddrich.com). The actual lipid to protein ratios of the two vesicle population were thus 900-1600:1 and 80-150:1 mol:mol, respectively. The less dense higher lipid to protein ratio vesicles are lost (remain in the supernatant) upon centrifugation and resuspension in $^{2}H_2O$ (see below).

3.5.2 Structural and Biophysical Characterization of CfrA. Siderophore mediated iron transporters adopt a characteristic β-barrel structure with an N-terminal plug domain located within the lumen of the β-barrel. Unlike α-helical transmembrane domain proteins, siderophore mediated iron transporters exhibit high thermal stability, yet are relatively accessible to aqueous solvent. We used Fourier transform infrared (FTIR) spectroscopy to ascertain whether affinity purified and reconstituted CfrA exhibits the structural and biophysical properties characteristic of other siderophore mediated iron transporters. For comparison purposes, we examined similar properties of an α-helical transmembrane domain protein, the nicotinic acetylcholine receptor (nAChR).

FTIR spectra of the membrane-reconstituted CfrA recorded dried from $^{1}H_2O$ buffer and in $^{2}H_2O$ buffer are presented in Figure 3.4A. The spectra exhibit intense lipid vibrations centered near 1740 cm^{-1} and 1450 cm^{-1}, as well as intense protein vibrations between 1700 cm^{-1} and 1600 cm^{-1} and centered near 1545 cm^{-1} ($^{1}H_2O$) or 1450 cm^{-1} ($^{2}H_2O$). The relative intensities of the lipid vibrations are much higher in spectra recorded in $^{1}H_2O$ than in $^{2}H_2O$, as the centrifugation/resuspension cycles used to exchange the membranes into the denser $^{2}H_2O$ buffer isolates the lower lipid:protein ratio and thus higher density vesicles. We estimated the lipid to protein molar ratio of the vesicles isolated in $^{2}H_2O$ using FTIR to be

Figure 3.4

FTIR spectra of CfrA recorded in $^{1}H_2O$ (solid line) and $^{2}H_2O$ (dashed line) buffer. The $^{1}H_2O$ spectrum was recorded after evaporating the bulk solvent under nitrogen. The spectrum of CfrA in $^{2}H_2O$ was recorded after prior exposure of CfrA to $^{2}H_2O$ buffer for 72 h at 4°C. The absorbance of $^{2}H_2O$ has been subtracted. Lipid vibrations are labeled at 1,740 cm^{-1} and 1,450 cm^{-1}. Protein amide I vibrations due to peptides in β-sheet secondary structures are labeled at 1,695 cm^{-1} and 1,629 cm^{-1}. The protein amide II vibration near 1,540 cm^{-1} undergoes a downshift in frequency upon peptide $^{1}H/^{2}H$ exchange to overlap with the lipid vibrations near 1,450 cm^{-1}. Spectra are each an average of 4,000 scans. Spectra were baseline corrected between 1,775 cm^{-1} and 1,350 cm^{-1} and normalized for presentation according to the intensities of the amide I band. The inset shows three representative amide I band contours, each recorded from separate expressions or purifications of CfrA.

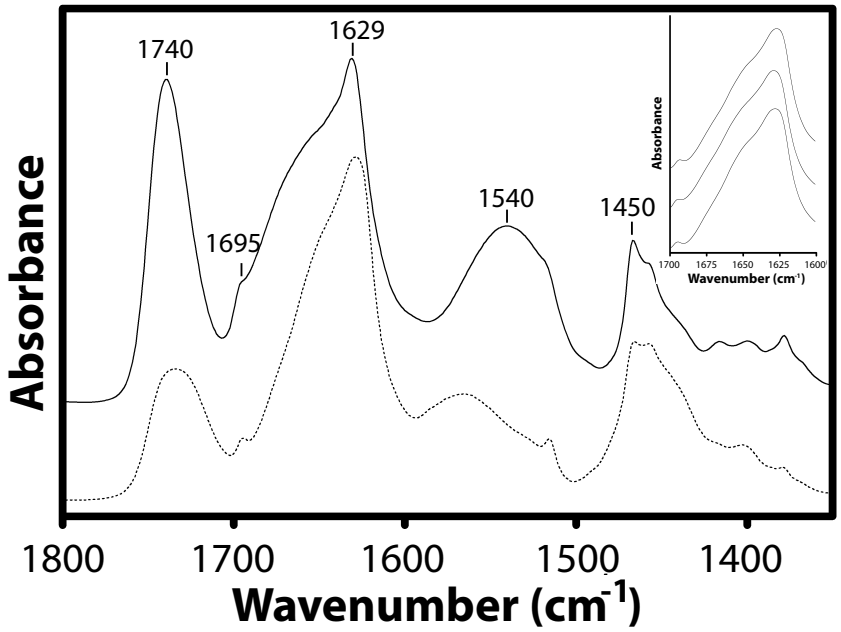
1740
1629
1695
1540
1450
Absorbance
1800
1700
1600
1500
1400
Wavenumber (cm-1)
Absorbance
1700
1675
1650
1625
Wavenumber (cm-1)

roughly 200:1 (143). This value is close to the lipid to protein ratio of the higher density CfrA vesicles isolated using the sucrose gradients (80-150:1), as judged by our enzymatic phospholipid c assay.

The secondary structure of CfrA was estimated by analyzing the protein amide I band (1600-1700cm^{-1}), which is due to the C=O stretching vibrations of the polypeptide backbone coupled to both N-H in-plane bending and C-N stretching (144). The band undergoes little change in shape upon exchange of peptide hydrogens for deuterium suggesting that a relatively small proportion of the peptides in CfrA form random/loop structures (144). In $^{2}H_2O$, the band is broad and asymmetric with a maximum near 1629 cm^{-1} and a weaker shoulder near 1695 cm^{-1}, both features are highly characteristic of predominantly β-sheet proteins, in general, and siderophore-mediated iron transporters, in particular (87,144). The reproducibility of the amide I band shape is displayed in Figure 3.4B for 3 independent reconstitutions. In contrast, α-helical proteins give rise to symmetric amide I band shapes with a maximum located near 1650 cm^{-1} (144).

Resolution enhancement reveals the component bands that contribute to the broad amide I contour. Peaks identified from the deconvolved spectrum were used as input to curve fit the amide I contour and thus estimate the secondary structure of CfrA, as shown in Figure 3.5 (145). The validity of the curve fit was assessed by comparing the resolution enhanced curve fit spectrum with the experimental resolution-enhanced data (Figure 3.5B). Both the predicted β-sheet and α-helical contents of CfrA, ~ 44 % and ~ 8 %, respectively (Table 3.2), are remarkably close to the known β-sheet and α-helical contents of similar siderophore-mediated iron transporters FhuA, FecA, and FepA (~ 48 % and ~ 6 %, respectively) (78,146). The remaining amide I component bands have been attributed to unordered

Figure 3.5

Resolution-enhanced and curve fit of the amide I band in the FTIR spectra of CfrA. **(A)** FTIR spectrum of CfrA in $^{2}H_{2}O$ (upper solid line) superimposed with the curve fit analysis (circles). Peaks identified from the resolution-enhanced spectrum (lower solid trace) were used as component bands for curve fitting and thus estimation of the secondary structure content. Spectra were baseline corrected between 1,775 cm^{-1} and 1,325 cm^{-1}. Resolution-enhanced spectral deconvolution parameters of γ of 8 and smoothing of 75% were used. **(B)** FTIR spectra of the amide I band of the resolution-enhanced experimental spectrum (solid line) and the resolution-enhanced curve fit spectrum (dashed line).

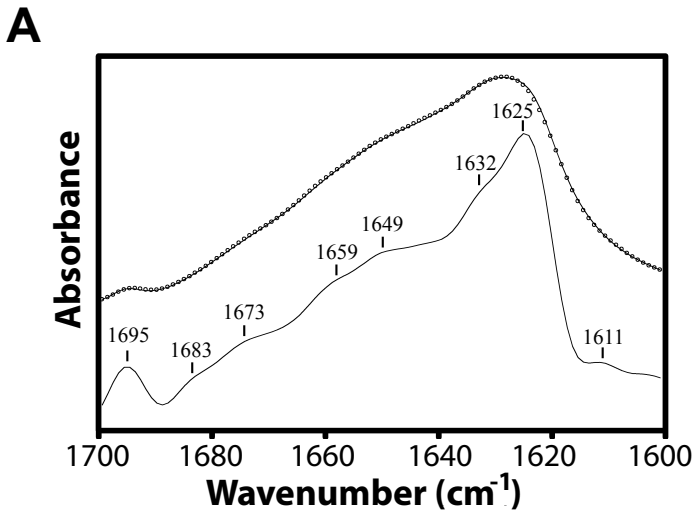
A
Absorbance
1625
1632
1649
1659
1673
1695
1683
1611
1700
1680
1660
1640
1620
1600
Wavenumber (cm-1)

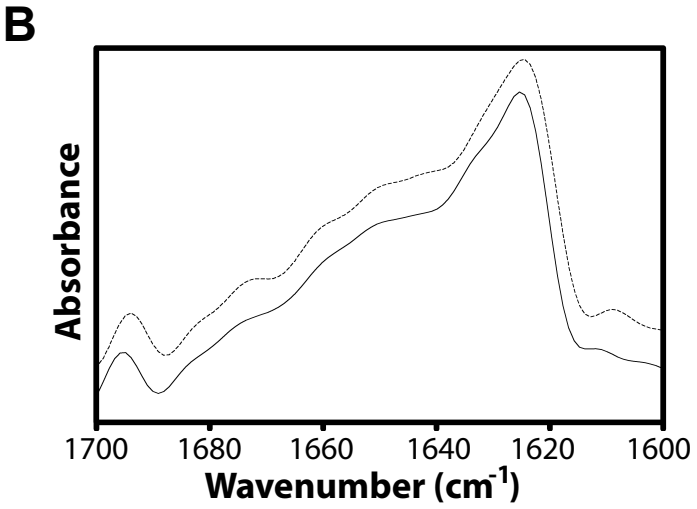
B
Absorbance
1700
1680
1660
1640
1620
1600
Wavenumber (cm-1)

Table 3.2 Secondary Structure of CfrA

Band frequency (cm^{-1}) [a]	Band assignment [b]	% Secondary Structure [c]
1695	β-Sheet	1
1683	β-Turn	6
1673	β-Sheet	6
1659	3_{10}-Helix	24
1649	α-Helix	9
1641	Unordered	17
1632	β-Sheet	12
1624	β-Sheet	25

[a] Band frequencies obtained from the resolution-enhanced amide I band (Fig 3.5)

[b] Band assignments are according to Goormaghtigh *et al* (147) and Jackson and Mantsch (146)

[c] Obtained by curve fitting the amide I band. The accuracy of the curve fit was assessed by using the procedure of Methot *et al* (145).

structures and 3_{10} helices, according to the band assignments of Jackson and Mantsch (146) and Goormaghtigh *et al* (147) , although the assignment of weak amide I component bands to specific types of secondary structures is often problematic (148).

Integral membrane proteins tend to be resistant to peptide hydrogen deuterium exchange. In many cases, the number of unexchanged peptide hydrogens remaining after prolonged exposure to ^2H_2O correlates with the proportion of residues that resides within the hydrophobic environment of the lipid bilayer (149). The amide II band, which is due to in-plane N-^{1}H bending coupled to C-N stretching, undergoes a substantial downshift in frequency from 1545 cm^{-1} to 1450 cm^{-1} upon exchange of peptide N-^{1}H for N-^{2}H. The relative intensity at 1545 cm^{-1} thus provides a measure of the extent of peptide hydrogen to deuterium exchange.

The aqueous solvent accessibility of CfrA was assessed by comparing the extent of peptide $^1H/^2H$ exchange in CfrA after precisely 72 hours of exposure to ^2H_2O to that of the α-helical transmembrane domain protein, the nicotinic acetylcholine receptor (nAChR).

The extent of peptide $^1H/^2H$ exchange in CfrA after 72 hours exposure to ^2H_2O at 4°C was measured by comparing the residual amide II band area to the amide II band areas in spectra recorded dried from ^1H_2O (100% N–^{1}H) and in ^2H_2O after boiling in ^2H_2O for 10 minutes (i.e. 100% N-^{2}H). Spectra were initially compared at both pH 7.0 (data not shown) and, from the same samples, at pH 2.0, by exchanging buffer in the FTIR sample accessory. The pH 2.0 spectra are presented in Figure 3.6 because the overlapping vibrations of carboxylic acid side chains (Asp and Glu) shift from near 1580 cm^{-1} (deprotonated, at pH 7.0) to near 1720 cm^{-1} (protonated, pH 2.0) thus providing an unobstructed view of the residual amide II band (145). This allows a more accurate assessment of the residual amide II band intensity. The

Figure 3.6

Comparison of the extent of peptide hydrogen-deuterium exchange for CfrA **(A)** and nAChR **(B)**, both after exposure to $^{2}H_2O$ buffer (pH 7.0) for 72 h at 4°C. In each case, the extent of exchange was estimated by comparing the residual amide II intensity (shaded area, peptide N-^{1}H vibrations) in spectra recorded after 72 h of exposure to $^{2}H_2O$ (blue line) to the intensities in spectra recorded from samples in $^{1}H_2O$ (black line, 100% N-^{1}H) and in $^{2}H_2O$ after exposure to conditions that lead to complete $^{1}H/^{2}H$ exchange (red line). Conditions for complete $^{1}H/^{2}H$ were different for the respective proteins: the CfrA sample was boiled for 10 min, whereas the nAChR was heated to 70°C for 10 min. The appropriate buffer spectrum has been subtracted from each spectrum. A spectrum of each sample was initially recorded at pH 7.0 (data not shown). The buffer was then switched to an identical buffer at pH 2.0 to shift the vibrations of carboxyl side chains (Asp and Glu) and thus provide an unobstructed view of the amide II band intensity. For comparison purposes, ribbon diagrams of FepA **(A)** and nAChR **(B)** show the relative proportions of each protein that are thought to reside within the lipid bilayer.

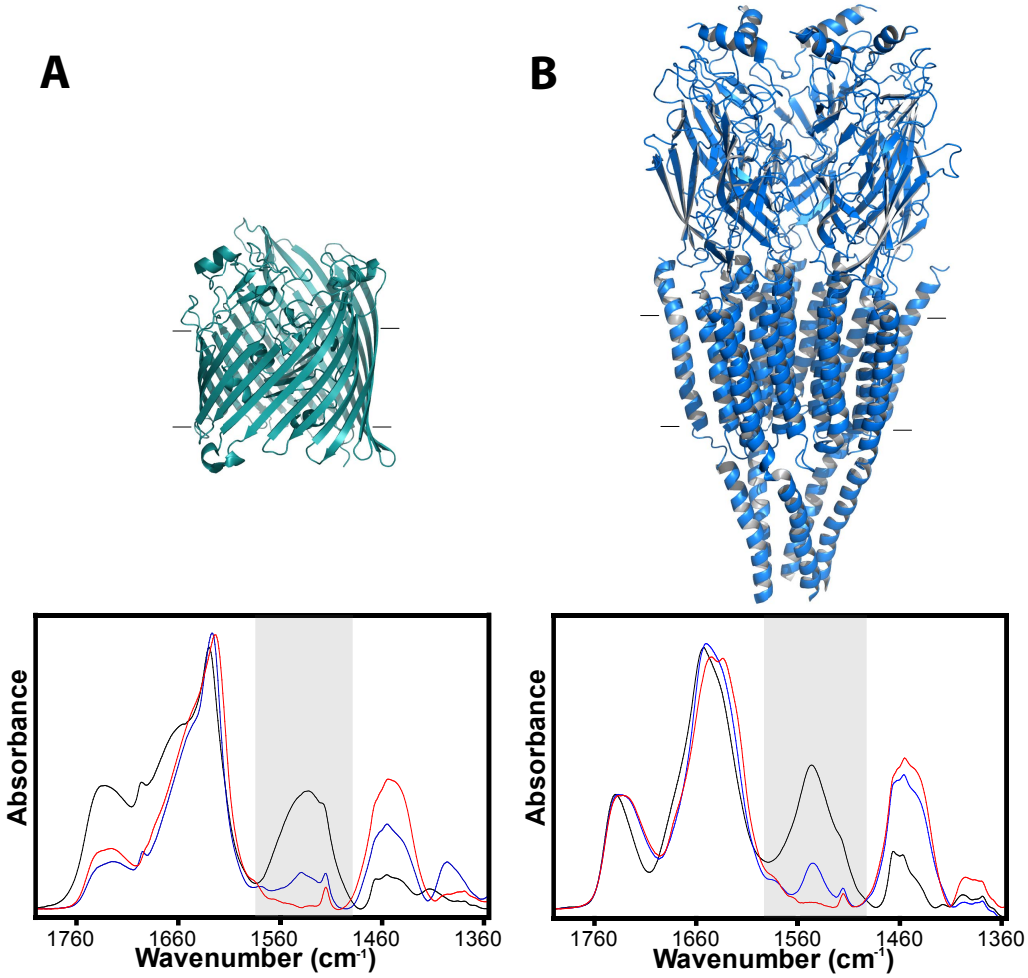
A
B
Absorbance
1760
1660
1560
1460
1360
Wavenumber (cm-1)
Absorbance
1760
1660
1560
1460
1360
Wavenumber (cm-1)

spectral analysis suggests that 75 ± 0.8 % (4 independent experiments using three different membrane preps) of the peptide N-^{1}H have exchanged for N-^{2}H in CfrA after 3 days. Note that the precision of our measurement from spectrum to spectrum is high; but the accuracy of the number is sensitive to the accuracy of the 100% N - ^{1}H value, which was calculated from a dried $^{1}H_2O$.

For comparison, we also recorded spectra under *identical* exchange conditions from another integral membrane protein, the nicotinic acetylcholine receptor (nAChR) (structure shown in Figure 3.6B). A similar percentage (75 – 80 %) of peptide hydrogens in the nAChR, which has an exclusively α–helical transmembrane domain, undergo peptide hydrogen-deuterium exchange after 72 hours exposure to $^{2}H_2O$ (150). The number of peptide hydrogens that are resistant to the $^{1}H/^{2}H$ exchange in the nAChR, however, correlates with the number of peptide hydrogens that are found in the transmembrane domain.

In contrast to the nAChR, the percentage of peptide hydrogens in CfrA that exchange for deuterium after 72 hours exposure to $^{2}H_2O$ does not correlate with the proposed number of peptide hydrogens in known siderophore-mediated iron transporter structures that are located within the transmembrane domain is much smaller than the percentage of transmembrane peptide hydrogens that are found in other siderophore-mediated iron transporters (70 % of the residues are typically found in the β-strands of the barrel, with the plug domain and N-terminal extension comprising 18 % and 12 % of the amino acids, respectively (78)). This comparison between CfrA and the nAChR highlights the fact that CfrA is relatively exposed to aqueous solution. A high solvent exposure has been noted for other β-barrel transmembrane structures, including siderophore-mediated iron transporters (80). The hydrogen-deuterium exchange data are thus also consistent with CfrA adopting a transmembrane β-barrel structure.

Finally, we examined the thermal denaturation of CfrA by recording FTIR spectra as a function of temperature in Figure 3.7. Denaturation of CfrA upon boiling in ^2H_2O for one hour leads to a substantially altered amide I band shape with new peak maxima near 1614 cm^{-1} and 1685 cm^{-1} (Figure 3.7A, bottom trace) (87). In contrast, FTIR spectra recorded from CfrA at temperatures ranging from 35°C to 95°C show no detectable changes in amide I band shape indicating that CfrA remains in its native conformation over the entire temperature range of the experiment (Figure 3.7B). The high thermal stability of CfrA is emphasized when one compares its thermal denaturation profile to that of the nAChR, which denatures at roughly 55°C (Figure 3.7C) (151). The high thermal stability CfrA is consistent with the high thermal stabilities reported for other β-barrel proteins (152). The secondary structure, hydrogen exchange characteristics, and thermal stability of CfrA are all consistent with both a β-barrel structure and the proposed role of CfrA as a predominantly β-barrel outer membrane siderophore-mediated iron transporter.

3.5.3 A Structural Model of CfrA. The FTIR data provide a structural rationale for performing sequence alignments with other siderophore-mediated iron transporters and for constructing a homology model (138). The model was first attempted using Cir, as a template, as this TonB dependent transporter has the highest sequence identity with CfrA (29% overall sequence identity, E value of $4e^{-65}$). Cir is expressed in many strains of *E. coli* where it binds and transports ferric ion complexed to linear catecholates, such as dihydroxybenzoyl serine. The crystal structure of Cir, however, exhibits poor electron density in some of the extracellular loops connecting the transmembrane β-strands (17). This coupled with the fact that the sequence of CfrA is longer than that of Cir (CfrA has 696 residues versus 663 for Cir) made it difficult to model the β-barrel. Alternatively, a structure

Figure 3.7

Thermal denaturation of CfrA. **(A)** Comparison of a spectrum of CfrA recorded at 95°C (upper trace) to a spectrum recorded after CfrA was boiled for 1 h and thus denatured (lower line). **(B)** Three-dimensional stack plot showing FTIR spectra of CfrA recorded in $^{2}H_{2}O$ at pH 7.0 with increasing temperatures from 35°C (front spectra) to 95°C (back spectra). **(C)** Changes in intensity at 1,681 cm^{-1} plotted as a function of temperature for CfrA (▵) compared to the intensity changes observed in similar spectra recorded from the nAChR (○).

A

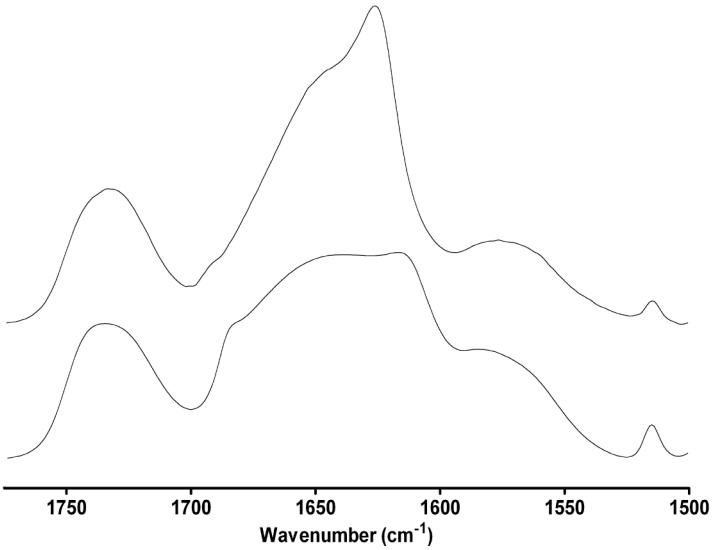
1750
1700
1650
1600
1550
1500
Wavenumber (cm-1)

B

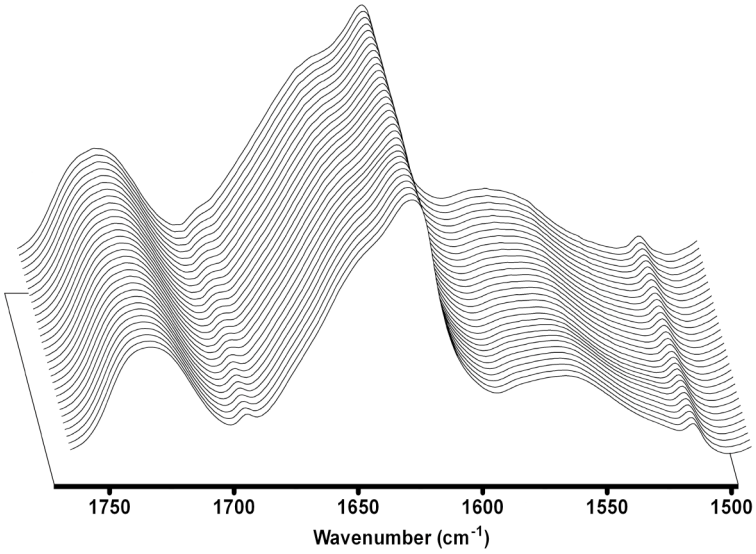
1750
1700
1650
1600
1550
1500
Wavenumber (cm-1)

C

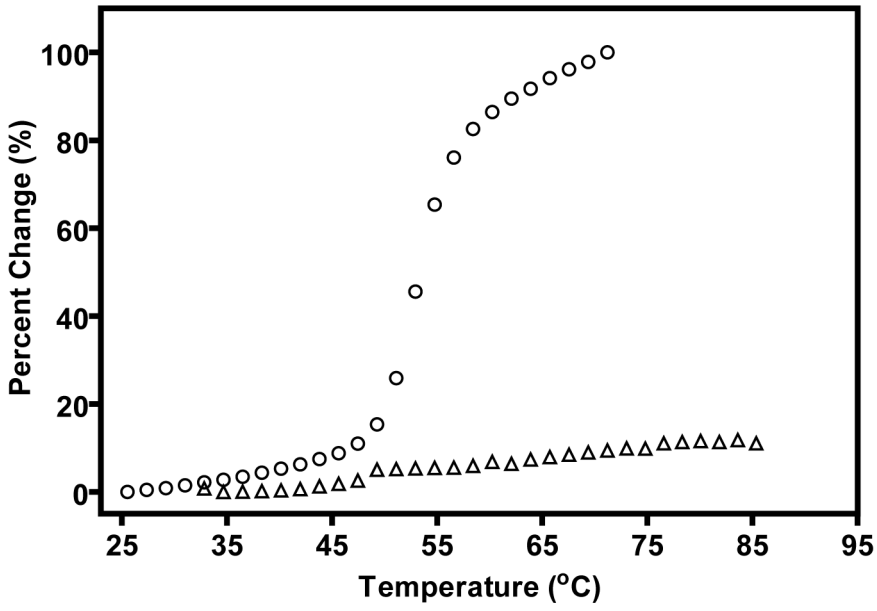
100
80
60
40
20
0
Percent Change (%)
25
35
45
55
65
75
85
95
Temperature (°C)

was generated by modeling the plug and β-barrel domains separately, using Cir as a template for the plug (45% sequence identity, E value of $1e^{-23}$) and FepA as a template for the β-barrel (24% sequence identity, E value of $6e^{-19}$). Cir and FepA were chosen as they exhibit the highest sequence identities for the independent domains modeled. FepA is also an *E. coli* TonB dependent iron transporter, but transports iron complexed to the endogenous catecholate siderophore, enterobactin (153). The three dimensional models of both the β-barrel and plug domains are shown in Figure 3.8A. A flattened schematic of the β-barrel showing conserved residues is compared to a similar structure of FepA in Figure 3.8B.

The model predicts, as expected given the chosen templates, that CfrA adopts a 22 strand antiparallel β-barrel with the N-terminal of the protein folded into the lumen of the β-barrel forming the plug domain. The strands of the β-barrel range in length from seven to 23 amino acids. The β-barrel exhibits long extracellular loops and shorter periplasmic turns connecting the β-strands. The plug, which blocks passage of large molecules from the extracellular to the periplasmic solutions, contains a β-sheet core with several loop regions (SB-1, SB-2. and SB-3) that extend towards the extracellular surface of the β-barrel. These loops likely play a role in siderophore binding and transport (see below).

The existence of several structural motifs, which are highly conserved in other siderophore-mediated transporters, provides confidence in the modeled structure of CfrA, particularly in the plug domain (80). Nine conserved structural motifs of the plug, identified by Chimento *et al*., are found in CfrA (black boxes in Figure 3.9), including the Ton box and the PGV, IRG, LIDG and RP motifs (80). The Ton box interacts with the energy transducer, TonB, and thus plays a role in the conformational switch associated with iron transport. The PGV,

Figure 3.8

Topology of iron-siderophore transporters. **(A)** Ribbon representation of the β-barrel and plug domains of the CfrA model. Barrel loops predicted to participate in ligand binding are indicated in red. Substrate-binding loops of the plug domain are also shown in red. (**B and C**) Comparison of unrolled flat representation of the barrel domain (left panel) and the plug domain (right panel) for CfrA **(B)** and FepA **(C)**. Blue boxes in the barrel domain indicate residues located in the β-strands of the barrel domain. Blue boxes in the plug domain indicate conserved motifs within the plug domain. Black circles indicate residues located in the loop region of the proteins. Residues predicted to be involved in ligand binding are indicated in black text. Residues that interact with the plug domain are also shown in yellow. The predicted position of the membrane bilayer for the barrel domain is outlined with horizontal lines.

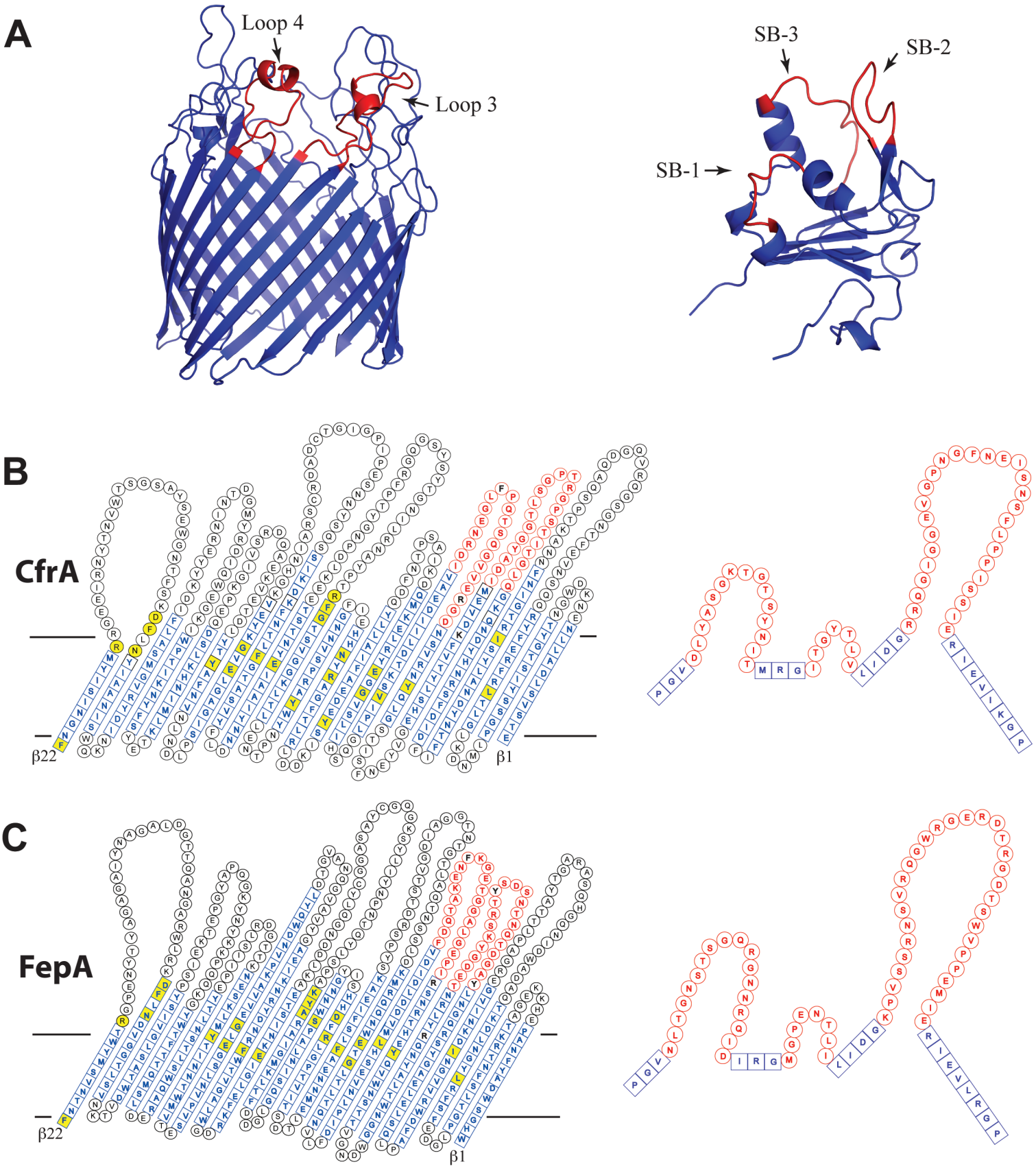
A
Loop 4
Loop 3
SB-3
SB-2
SB-1
B
CfrA
β22
β1
C
FepA
β22
β1

Figure 3.9

Alignments of CfrA model with other iron-siderophore transporters. **(A)** The aligned sequences of CfrA, Cir, and FepA were manually added to the structure-based sequence alignment of crystallized iron-siderophore transporters performed by Buchanan and coworkers. Secondary structural elements are depicted as red cylinders (helices) and blue arrows (β-strands). Conserved residues, conserved motifs, and substrate-binding loops within the plug domain are indicated in yellow, black boxes, and blue boxes, respectively. Conserved residues from the barrel that interact with the plug domain are also shown in yellow. Residues that participate in binding of ferrichrome, diferric dicitrate, and enterobactin, as discussed in the text, are indicated by red circles. **(B)** Sequence alignments of CfrA with enterobactin transporters from difference bacterial species. Bacterial species: e, *Escherichia coli*; s, *Salmonella enterica serovar Typhimurium*; p, *Pseudomonas aeruginosa*; b, *Bacillus pertussis*.

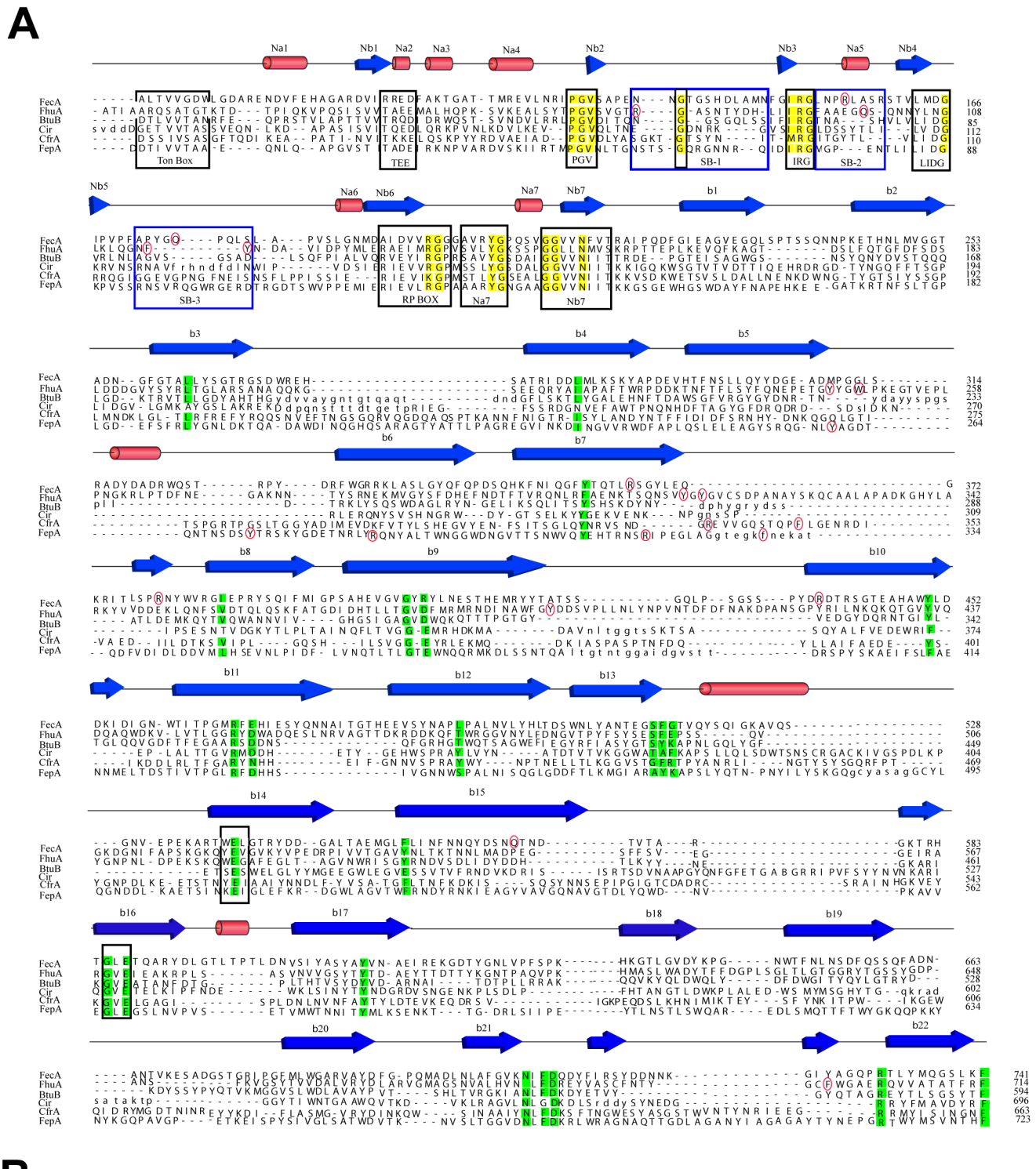
A
Na1
Nb1
Na2
Na3
Na4
Nb2
Nb3
Na5
Nb4
FecA
FhuA
BtuB
Cir
CfrA
FepA
Ton Box
TEE
PGV
SB-1
IRG
SB-2
LIDG
Nb5
Na6
Nb6
Na7
Nb7
b1
b2
SB-3
RP BOX
Na7
Nb7
b3
b4
b5
b6
b7
b8
b9
b10
b11
b12
b13
b14
b15
b16
b17
b18
b19
b20
b21
b22
B
eFepA
sFepA
pFepA
bFepA
CfrA

IRG, LIDG, and RP motifs define the location of the three loops of the plug domain (SB-1, SB-2, SB-3) that play a role in substrate binding. These binding loops are held in place by a charge cluster involving two conserved arginine residues in the IRG and RP motifs. These arginines form salt bridges with two glutamate residues located in strands 14 and 16 of the β-barrel, as discussed below (80). The location of these and other motifs allow us to define with precision the location of the different secondary structures in the plug domain sequence of CfrA, as well as the potential residues in SB-1, SB-2, and SB-3 of the plug that likely interact with the putative substrate(s) of CfrA.

Although the lower sequence conservation in the β-barrel domain makes the precise definition of some of the β-strands in the β-barrel equivocal, several conserved residues are present. In particular, two acidic residues observed at conserved locations of β-strands 14 and 16 of the barrel likely form a charge cluster with the conserved arginine residues located in the IRG and RP motifs of the plug domain (see above). These conserved glutamic acid residues, shaded blue in Figures 3.8 and 3.9, allow us to accurately place the sequence in register in these two β-strands. Other conserved residues in the β-barrel have also been shown to form interactions with the plug domain and thus provide further confidence in the sequence alignment of CfrA with the other siderophore-mediated iron transporters (grey in Figures 3.8 and 3.9) (80). Unfortunately, these conserved residues are found mostly in the C-terminal half of the β-barrel.

The identified conserved residues/structural motifs in our homology model provide confidence in our modeled structure and allow us to compare the sequence of CfrA to those of other siderophore mediated iron transporters, particularly in regions thought to play an important role in siderophore binding and/or transport. Current data indicates that CfrA acts

as a transporter of ferric enterobactin (126). FepA is the endogenous *E. coli* enterobactin transporter. We thus expected CfrA to exhibit a high sequence similarity with FepA in regions thought to play a role in enterobactin binding/transport. As shown in the sequence alignments of Figure 3.8B and the homology model of Figure 3.9, however, there are considerable sequence variations suggesting that the mechanisms used by CfrA and FepA to interact with ferric enterobactin may differ substantially (see Discussion).

3.6 Discussion

3.6.1 Expression, Purification, Reconstitution, and Structural Characterization of CfrA.

We report here the successful full length cloning and expression of an outer membrane protein implicated in siderophore-mediated iron transport in the enteric pathogen, *C. jejuni*. The protein was expressed in the *E. coli* strain, C41, with typical yields of ~ 7 mg of purified CfrA per 16 L of culture, of which 4-5 mg were typically reconstituted into lipid bilayer vesicles. While these yields are less than anticipated, they are not entirely unexpected for the expression of a *C. jejuni* membrane protein in *E. coli*. For example, Mamelli *et al.* were able to express the *C. jejuni* membrane protein, CadF in *E.coli* in large quantities, but they were only able to do so with a small truncated version of the protein (142). The truncated CadF was also targeted to inclusion bodies. We were unable to completely solubilize CfrA from the membrane fraction (which includes inclusion bodies) suggesting that some of the expressed protein may be targeted to inclusion bodies. Further, high-level expression of CfrA led to degradation of the expressed protein. *E. coli* may not be efficient at expressing *C. jejuni* membrane proteins. Despite the encountered problems with the expression of CfrA, we were still able to obtain intact protein in milligram quantities, which is sufficient for structural characterization.

We also present an efficient protocol for the reconstitution of the expressed and purified CfrA into lipid membranes. We utilized the relatively mild detergent, DDM, to solubilize and purify CfrA from the bacterial cell membranes, as it is an excellent detergent for maintaining membrane protein structure/function in the solubilized state. Unfortunately, DDM has a very low critical micellar concentration and is thus difficult to remove by

dialysis to form reconstituted protein-lipid vesicles. Consequently, protein incorporated vesicles are often formed in the presence of exogenous lipids using hydrophobic BioBeads to remove the DDM. In our hands, however, we find this approach leads to loss of protein and incomplete detergent removal (data not shown). We therefore diluted our DDM solubilized CfrA with sufficient cholate-solubilized exogenous lipid to bring the concentration of DDM below its critical micellar concentration. We then dialyzed away both detergents and efficiently formed protein-lipid complexes. We found this simple dilution/dialysis procedure removed both DDM and cholate from the solution to undetectable levels. Sucrose gradients confirm that the CfrA is associated with lipids – although two populations of vesicles with differing lipid-protein ratios were typically formed.

The ability to efficiently reconstitute CfrA into lipid bilayers opens the door for more detailed biochemical and biophysical studies of CfrA structure and function. Reconstituting CfrA in the presence of other components of the TonB system may allow us to probe in detail the mechanisms of siderophore mediated iron transport.

FTIR spectra of the purified and reconstituted CfrA are highly characteristic of a predominantly β-sheet protein. We estimated the secondary structure content of CfrA to be ~ 44 % β-sheet and ~ 10 % α-helix, both are surprisingly close to the secondary structure of the iron transporter FecA estimated from the crystal structure (78). More importantly, the FTIR spectra of CfrA are similar to those recorded from another siderophore-mediated iron transporter, FhuA demonstrating the similarity in structure (87). CfrA also exhibits a high thermal stability and is resistant to SDS denaturation, yet is relatively accessible to solvent and thus undergoes relatively extensive peptide hydrogen-deuterium exchange. These findings are all consistent with CfrA adopting a transmembrane β -barrel, as similar biophysical properties have been observed for other transmembrane β -barrel proteins

(32,141) . The data accumulated in this study provide the first structural evidence that CfrA adopts a topology consistent with a siderophore-mediated iron transporter.

3.6.2 Homology Model of CfrA. Our homology model of CfrA created using Cir and FepA as templates for the plug and β-barrels, respectively, provides additional structural evidence that CfrA is a siderophore-mediated iron transporter. The model exhibits many of the conserved sequences/structural motifs found in other siderophore mediated iron transporters, including the Ton box, PGV, IRG, RP, and LIDG motifs of the plug domain. Numerous conserved residues in the β-barrel domain that, in other siderophore-mediated iron transporters, interact with conserved residues in the plug domain are also found at equivalent sites in CfrA. Of particular interest are two glutamic acid residues (E484 and E547) of β-strands 14 and 16, which form a charge cluster with arginines in the IRG and RP boxes of the plug domain.

3.6.3 Selectivity of Siderophore Binding. C. jejuni grows in culture using exogenously supplied ferric-enterobactin as an iron source (126). CfrA deletion mutants of *C. jejuni*, however, are not capable of transporting ferric-enterobactin, suggesting that CfrA is an enterobactin transporter (126). Based on these data, we expected our homology model and sequence comparisons to reveal binding site motifs consistent with those found in the *E. coli* enterobactin transporter, FepA.

We first compared our homology model and the sequence of CfrA with the structures and sequences of FhuA and FecA, as structures of both of these siderophore-mediated iron transporter have been solved in the presence of bound siderophores. The structures provide direct insight into the nature of siderophore-transporter interactions (78,154). FhuA

transports the cyclic hexapeptide, ferrichrome, which coordinates iron using hydroxamate functional groups. Ferrichrome interacts with FhuA predominantly via aromatic residues located in the third binding loop of the plug domain, SB-3 (F115 and Y116), and loops three (Y244 and W246), four (Y313 and Y315), five (Y391), and eleven (F702) of the β-barrel. R81 and Q100 of the plug SB-1 and SB-2 binding loops, respectively, interact directly with the hydroxamate functional groups that chelate the bound ferric iron (154). Significantly, both the structural model of CfrA and the sequence comparisons reveal an absence of aromatic residues at comparable sites to FhuA, even taking into account possible errors in the registers of the individual β-strands. The arginine and glutamine residues of SB-1 and SB-2 in FhuA are also missing, although a lysine residue is located close by in SB-1 of CfrA. The homology model predicts that iron-bound ferrichrome is not a high affinity substrate for CfrA in agreement with the inability of *C. jejuni* NCTC 11168 to acquire iron from ferrichrome (Dr. Stintzi; personal communication).

Structures of FecA have been solved with both diferric dicitrate and dicitrate bound to the plug and β-barrel domains (78). In contrast to FhuA, the binding site of FecA exhibits a large number of positively charged arginines that interact with the highly negative citrate molecule. These include R155 of SB-1, R365 of β-strand 7, R380 of loop 4, and R438 of β-strand 10. Two other residues involved in binding, Q176 and Q570, are found in SB-3 and β-strand 15, respectively (78). Even allowing for substantial flexibility in the registers of the β-strands, there are few positively charged residues in CfrA that could play a comparable role in substrate binding. As expected, the sequence alignment and modeled structure thus predict that ferric citrate is also not a substrate for CfrA.

Finally, we compared the modeled structure and sequence of CfrA with that of FepA. Although bound ferric-enterobactin was not resolved in the published structure of FepA, thus precluding direct structural analysis of FepA-enterobactin interactions, there is considerable biochemical data available concerning FepA-enterobactin interactions (81,153,155). The catecholate siderophore, enterobactin, has a net negative charge, suggesting that aromatic and basic residues play a role in siderophore binding (156). These postulates are supported by mutagenesis studies with FepA, which show that the Y260A and F329A play a role in enterobactin binding affinity and transport efficiency, although Y260 appears to be essential to both processes (81,155). Combinatorial mutations of two aromatic residues, Y272A and F329A, or two arginine residues, R286A and R316A, suggest the involvement of all four residues in binding/transport. As shown in Figure 3.8B, Klebba and colleagues have demonstrated the across species conservation of both aromatic and positively charged residues in a region of FepA that contains most of the residues known to play an important role in ferric enterobactin binding/transport (155).

Surprisingly, the sequence of CfrA does not match up as well with that of FepA in the regions of the protein that are predicted to play a role in substrate binding as might be expected for an enterobactin transporter. CfrA does not exhibit a tyrosine residue at a position comparable to Y260 of FepA, even allowing for considerable errors in the aligned register of the two sequences. This variation is significant because Y260 is the only residue in FepA identified so far that upon mutation alone (i.e. not in combination with another residue) leads to a substantial reduction in binding affinity/transport (157). CfrA also lacks a tyrosine or other comparable aromatic residue at a position consistent with Y272 in FepA. CfrA does exhibit a positively charged lysine at a position that matches R286 in FepA. A

shift in the sequence will bring F338 of CfrA in register with the F329 in FepA (Figure 3.8B) and thus R336 of CfrA to within two residues of R316 of FepA, but this shift in register would then shift Y328 of CfrA out of register with its conserved counterpart in FepA.

The striking lack of sequence conservation between CfrA and FepA in a region known to be central to enterobactin binding in FepA is illustrated clearly in Figure 3.8B. Also, the three binding loops of the plug domain, shown to interact directly with bound siderophores in FhuA and FecA, exhibit little sequence similarity between CfrA and FepA in terms of either aromatic or charged residues (blue boxes in Figure 3.8A). The structural/sequence comparisons show that the putative enterobactin binding site of CfrA exhibits substantial sequence variations relative to comparable regions of the enterobactin binding site of FepA.

An intriguing possibility is that CfrA lacks key residues involved in ferric-enterobactin binding, and thus has a lower binding affinity for the siderophore. Lower affinity enterobactin binding might correlate with a broader siderophore binding selectivity. Unlike *E. coli*, the genome of *C. jejuni* appears to code for only one TonB-dependent siderophore transporter as *Cj*0178 was recently shown to mediate iron acquisition from ferric-lactoferrin (158). Given that CfrA is potentially the lone siderophore transporter in *C. jejuni*, it may have evolved to bind and transport a broader range of siderophores with lower affinity, in order to ensure survival of *C. jejuni* in hostile environments.

Given that *C. jejuni* is a common food borne pathogen that leads to considerable health problems, this microorganism is of considerable interest as a therapeutic target. Deletion of the *cfrA* gene greatly diminishes the virulence of *C. jejuni* in chick colonization assays (126). Inhibitors of CfrA function should thus be effective at treating *C.jejuni* infection. The

sequence and structural comparisons strongly suggest that CfrA from *C. jejuni* and FepA from *E. coli* bind enterobactin using different mechanisms/binding interactions. Given that the two proteins exhibit structural differences in their enterobactin binding sites, it may be possible to exploit the structural differences between CfrA and FepA to develop CfrA-specific therapeutics. Such an approach might allow one to target CfrA containing *C. jejuni* in the intestine, while leaving the endogenous micro flora unharmed.

In summary, we have cloned, expressed, purified, membrane reconstituted, and structurally characterized a 76 kDa protein that has been identified as the potential siderophore-mediated iron transporter in *C. jejuni*, CfrA. We show that CfrA is membrane associated and can be expressed in *E. coli* and purified/reconstituted into a membrane environment in milligram quantities sufficient for structural characterization. The protein exhibits a predominantly β-sheet secondary structure, is highly thermally stable, and has peptide hydrogens that are relatively accessible to aqueous solvent, consistent with other siderophore-mediated iron transporter. Structure-based sequence alignments and a homology model show that CfrA exhibits all of the conserved structural motifs found in other siderophore-mediated iron transporters, particularly in the proposed plug domain. Our analysis provides the first structural evidence that CfrA is the siderophore mediated iron transporter in *C. jejuni.* There are substantial sequence variations in the putative siderophore binding site of CfrA relative to other siderophore-mediated iron transporters including the enterobactin transporter FepA. The data suggest that CfrA and FepA use different mechanism to interact with the siderophore enterobactin.

4 CfrA CRYSTALLIZATION

4.1 Introduction

Both the homology model of CfrA and sequence alignments described in Chapter 3 reveal the absence of critical residues in CfrA that have been implicated in enterobactin binding/transport in other TBDT. The absence of the conserved residues suggests a unique mode of binding of enterobactin to CfrA, which could be exploited for therapeutic purposes. We proposed that CfrA possesses a decreased binding affinity for enterobactin that may lead to a broader substrate specificity (159). A broad substrate specificity would be beneficial as *C. jejuni* is unable to produce siderophores endogenously and thus must scavenge siderophores produced by the host endogenous micro flora (126). The proposal that CfrA has a broad substrate specificity was recently shown experimentally by Naikare *et al* (160). CfrA was able to transport a number of different enterobactin analogs demonstrating promiscuous binding (160).

To investigate the molecular determinates of binding to CfrA, I set out to crystallize CfrA in the presence and absence of enterobactin. I initially used the expression and purification protocol developed in Chapter 4 to produce in n-dodecyl-β-D-maltoside (DDM) solubilized CfrA as a starting point for crystallization. A clear path from DDM-solubilized CfrA to protein crystals, however, was unavailable, as diverse conditions had been used previously to crystallize other TBDT. For example, FepA was concentrated to 15mg/ml in 0.025 M MOPS (pH 7.0), 0.05 % LDAO, 0.1 M NaCl, 20 % glycerol and 2 mM NaN_3 and then mixed with 14 % polyethylene glycol (PEG1000), 0.05 M Tricine (pH 8.0), 0.0125 M MOPS (pH 7.0), 0.055 % LDAO, 0.35 M NaCl, 1.75 % heptane 1,2,3-triol, 15 % glycerol and 2 mM NaN_3 to generate crystals that diffracted to 2.4 Å (19). By comparison, FhuA was concentrated to 10-20 mg/ml in 0.01 M ammonium acetate and 0.0 8% C_{10}DAO and mixed

with 13-16 % PEG6000, 0.1 M sodium cacodylate (pH 6.4) to generate crystals that diffracted to 3.0 Å (161). As the conditions varied dramatically, I started with broad screens and commenced with hundreds of crystallization trials in the hope of a positive hit leading to crystal refinement. In concert, I attempted crystallization under conditions that had proven successful with other TBDT

This chapter describes the progress made towards solving a high-resolution crystal structure. This research identified conditions that reproducibly led to protein crystals and culminated in a 5 Å resolution structure of the CfrA β-barrel.

4.2 Experimental Procedures

4.2.1 Materials. n-dodecyl-β-D-maltoside (DDM) anagrade and n-dodecyl-N-N-dimethylamine-N-oxide (LDAO) anagrade were from Affymetrix (Santa Clara, CA). Crystallization plates and cover slides were from Hampton research (Aliso Viejo, CA). FTS40 spectrometer, originally from Digilab now Agilent Technologies (Santa Clara, CA). Goldengate™ attenuated total internal reflection accessory was from SpecAc (Orington, Kent, U.K). The Superdex200 and MonoQ columns were from GE healthcare (Baie d'Urfe, Quebec). The Superflow Talon resin was purchased from Clontech (Mountain View, CA).

4.2.2 Constructs, Expression and Purification of CfrA. CfrA was expressed, solubilized and purified in either DDM or n-dodecyl-N-N-dimethylamine-N-oxide (LDAO) as described in Chapter 3 (159). Briefly, membrane proteins were solubilized by incubating 1 g of the membrane protein for 1 hour at 4 °C in lysis buffer (300 mM NaCl and 50 mM NaH_2PO_4 (pH 7.0)) containing either 0.65 % (w/v) LDAO or 1 % DDM, 2 mM TCEP, and 10 mM β-mercaptoethanol. After centrifugation at 100,000 xg, the solubilized protein in the supernatant was incubated for 1 hour at 4 °C with Superflow cobalt based resin. The resin was transferred to a glass column and non specifically bound protein was removed with 3 buffer washes (3 column volumes each) with increasing imidazole concentration (0, 10 mM, 50 mM imidazole) in lysis buffer supplemented with 0.1 % (w/v) LDAO. Protein was eluted from the resin in 150 mM imidazole, 300 mM NaCl, 50 mM NaH_2PO_4, and 0.075 % (w/v) DDM at pH 7.0. Protein fractions were concentrated using a Centricon 30,000 Dalton cutoff concentrator and then further purified on a Superdex-200 gel filtration column equilibrated with gel filtration buffer (300 mM NaCl and 25 mM Tris-HCl (pH7.0)) supplemented with 2

mM TCEP, 10 mM β-mercaptoethanol and 0.1% (w/v) LDAO. The eluted CfrA was then concentrated to 10mg/ml in 150mM NaCl and 25mM Tris-HCl (pH 7.0).

4.2.3 Fourier Transform Infrared Spectroscopy (FTIR). Hydrogen/deuterium infrared spectra were recorded on a Digilab FTS40 spectrometer using a Golden-Gate™ attenuated total internal reflection accessory. 3 μl of the CfrA (~1 mg/ml) in gel filtration buffer was dried down onto the accessory under a gentle stream of N_2 gas. After collecting a 128 scan spectrum at 4 cm^{-1} resolution, 4 μl of ^2H_2O was added and another 128 scan spectrum collected.

4.2.4 Crystallization. Crystallization was preformed by hanging drop vapor diffusion at 20°C. All screens were conducted in 24 well VDX plates with siliconized glass cover slides. Except where noted, 1 μl of approximately 10mg/ml protein solution in 25 mM Tris-HCl (pH 7.0), 0.15 M NaCl and either 0.1 % LDAO or 0.1 % DDM was deposited on a cover slide and 1 μl of reservoir was added, mixed by pipetting, and inverted over 1ml of reservoir solution. Initial crystallization trials were prepared with DDM-solubilized CfrA concentrated to 10 mg/ml in 150 mM NaCl and 25 mM Tris-HCl (pH 7.0).

4.2.5 Ferric-Enterobactin. Ferric-enterobactin was prepared by dissolving 100 nmol of enterobactin in 100 μl of methanol followed by the addition of a solution of 100 nmol of $FeCl_3$ in 100μl of water. The solution was incubated for 2 hours at room temperature before the addition of 100 μl of 1 M $NaHPO_4$ (pH 7.4). The final volume of 1 ml was prepared after dilution with H_2O. The solution was centrifuged at 14,000 rpm for 1 minute to pellet free iron.

4.3 Results

4.3.1 Crystallization trials in DDM. The purification protocol developed in Chapter 3 used DDM for both solubilization and purification of CfrA, so DDM-solubilized CfrA was used in my initial crystallization trials (159). Initial broad screens were constructed in-house varying the pH range (pH 4.5 – 9.0), the precipitant (polyethylene glycol 600, polyethylene glycol 1000, polyethylene glycol 4000, polyethylene glycol monomethyl ether 2000, polyethylene glycol 6000, polyethylene glycol 3350, ammonium sulfate, sodium chloride, and 2-methyl, 2, 4-pentanediol) and the salt concentration (sodium chloride, potassium chloride, magnesium acetate, calcium acetate and magnesium sulfate) of the reservoir (Table 4.1). The hanging drop method for crystallization was attempted, with a 1 μl of protein solution deposited on a glass cover slide followed by the addition of 1 μl of reservoir solution. After mixing, the cover slip was inverted over 1 ml of reservoir solution. A screen of approximately 500 trials resulted in various precipitates and phase separations, but with no crystalline material (data not shown). The results of the initial trials gave no clear direction for additional trail attempts.

4.3.2 Purification in LDAO. DDM produces a micellar belt of approximately 30 kDa. The size of micellar belt can be deleterious to the formation of high resolution crystals by hindering protein-protein contacts needed for crystal formation (21,22,162). Different detergents were thus explored in an attempt to limit micellar belt size and drive crystal formation. The detergent LDAO forms small micellar belts (17kDa) and has proven successful for the crystallization of other TonB dependent transporters (19,163,164). As an

Table 4.1 Crystallization constituents tested [a]

	Name	pH range tested	Concentration tested
Buffers [b]	Sodium Acetate	4.5-5.5	25mM - 100mM
	Sodium Citrate	4.5-6.0	25mM - 100mM
	4-(2-hydroxyethyl)-1-piperazineethanesulfonic acid (HEPES)	6.0-7.0	25mM - 100mM
	N-(2-acetamido) iminodiacetic acid (ADA)	6.0-8.0	25mM - 100mM
	Tris-hydrochloride	7.0-9.0	25mM - 100mM
Precipitants [c]	Polyethylene Glycol 600		5% - 40%
	Polyethylene Glycol 1000		5% - 40%
	Polyethylene glycol monomethyl ether 2000		5% - 40%
	Polyethylene Glycol 3350		5% - 40%
	Polyethylene Glycol 4000		5% - 40%
	Polyethylene Glycol 6000		5% - 40%
	Polyethylene Glycol 20000		5% - 25%
	Ammonium Sulfate		0.8M - 2.4M
	Sodium Chloride		1.0M - 3.0M
	2-Methyl-2,4-pentanediol		10% - 65%
Salts [d]	Sodium Chloride		50mM-150mM
	Potassium Chloride		50mM-150mM
	Magnesium Acetate		50mM-150mM
	Calcium Acetate		50mM-150mM
	Magnesium Sulfate		50mM-150mM

[a] Crystallization trials were conducted systematically where one constituent was varied at a time over the concentration indicated. Various combinations were explored those showing positive results were further refined and explored.

[b] Increments of 0.2 pH units and 25mM concentrations were tested for each buffer within the ranges indicated

[c] Concentration increments of 5% were tested for polyethylene glycol and 2-methyl-2,4-pentandediol precipitants within the range indicated. Concentration increments of 0.2M were tested for Ammonuim Sulfate and Sodium Chloride within the range indicated.

[d] Concentration increments of 25mM were tested for the salts tested within the range indicated

added benefit, the addition of other amphiphiles, such as alcohols, has been shown to further decrease the micellar belt size (163).

I therefore decided to attempt crystallization with LDAO-solubilized CfrA. LDAO proved successful in the solubilization and purification of CfrA from the outer membrane with structural characteristics in agreement with previously published work (Figure 4.1A-C) (159). Briefly, CfrA purified in LDAO resulted in a pure, homogenous solution as indicated by a representative SDS-PAGE gel in Figure 4.1A and the gel filtration profile from the Superdex200 column in Figure 4.1B. Note the second band running at a lower molecular weight on the SDS-PAGE gel has been confirmed as CfrA (159). β-barrel membrane protein structures are known to be resistant to denaturation by sodium dodecyl sulfate (SDS) resulting in two bands on an SDS-PAGE gel (141,142). A predominantly β-strand secondary structure was shown by FTIR analysis (Figure 4.1C). Comparable yields were obtained in the presence of LDAO and DDM (data not shown).

4.3.3 Crystallization trials in LDAO. A second attempt at the initial broad screen of 500 conditions in the presence of LDAO was undertaken. The crystallization set up was consistent with earlier trials. The majority of reservoir conditions yielded different degrees of precipitates and phase separations similar to the DDM screen. Three reservoir conditions, however, yielded discrete areas of birefringence (Figure 4.2A). Birefringence is an intrinsic property of most macromolecules. A protein crystal is birefringent because the crystals have anisotropic character generating 2 indices of refraction (165). The reservoir conditions leading to birefringence consisted of: 1) 100 mM sodium citrate (pH 5.6), 100 mM NaCl and 30 % PEG3350; 2) 100 mM sodium citrate (pH 5.6), 100 mM NaCl and 30 % PEG6000 and 3) 25 mM Tris (pH 8.4), 100 mM NaCl and 30 % PEG3350. Screening within the

Figure 4.1

Production and structural characterization of detergent solubilized CfrA. **(A)** 1 g of membrane fraction was solubilized with 0.65% LDAO for 1 hour at 4°C. Soluble fraction was batch bound to cobalt based affinity resin for 1 hour at 4°C. Peak fractions from the affinity column were pooled (lane 1), concentrated (lane 2) and subjected to a subsequent gel filtration column. Peak fractions were collected (peak fractions lane 3-5), pooled and concentrated (lane 6) and used for crystallization trials. **(B)** Representative gel filtration profile. The bracket denotes the region collected for crystallization trials. **(C)** Infrared spectra of purified detergent solubilised CN10 recorded after gentle drying from $^{1}H_2O$ buffer. Note the prominent peak at 1629 cm^{-1} indicative of β-strand secondary structure.

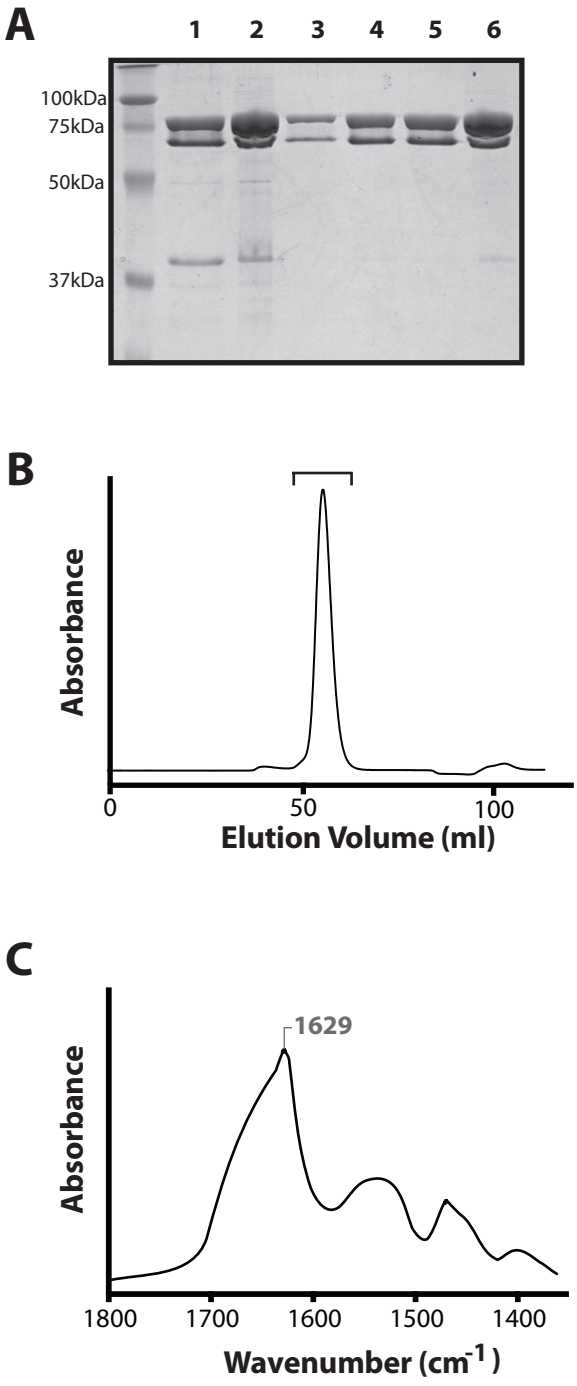
A
1
2
3
4
5
6
100kDa
75kDa
50kDa
37kDa
B
Absorbance
0
50
100
Elution Volume (ml)
C
1629
Absorbance
1800
1700
1600
1500
1400
Wavenumber (cm-1)

Figure 4.2

Schematic representation of optimization of the base crystallization condition. **(A)** Birefringent material seen with (i) citrate (~ pH 5.7) and (ii) Tris-HCl buffer (~ pH 7.0). **(B)** Crystal morphology from screen of buffers and precipitants: (i) 100 mM MES (pH 5.5), 100 mM NaCl and 20 % PEG3350, (ii) 25 mM Tris-HCl (pH 7.0), 100 mM NaCl and 3 M $(NH_4)_2SO_4$, (iii) 25 mM Tris-HCl (pH 7.0), 100 mM NaCl and 20 % PEG6000, (iv) 100 mM MES (pH 5.7), 100 mM NaCl and 24 % PEG3350. **(C)** Crystal drops of 100 mM MES (pH 5.5-6.5), 100 mM NaCl and 20 % PEG3350 at (i) 15°C and (ii) 20°C. **(D)** Crystallization drops of different total volumes maintaining a 1:1 ratio of protein solution to precipitant: (i) 2 μl, (ii) 4 μl, and (iii) 6 μl.

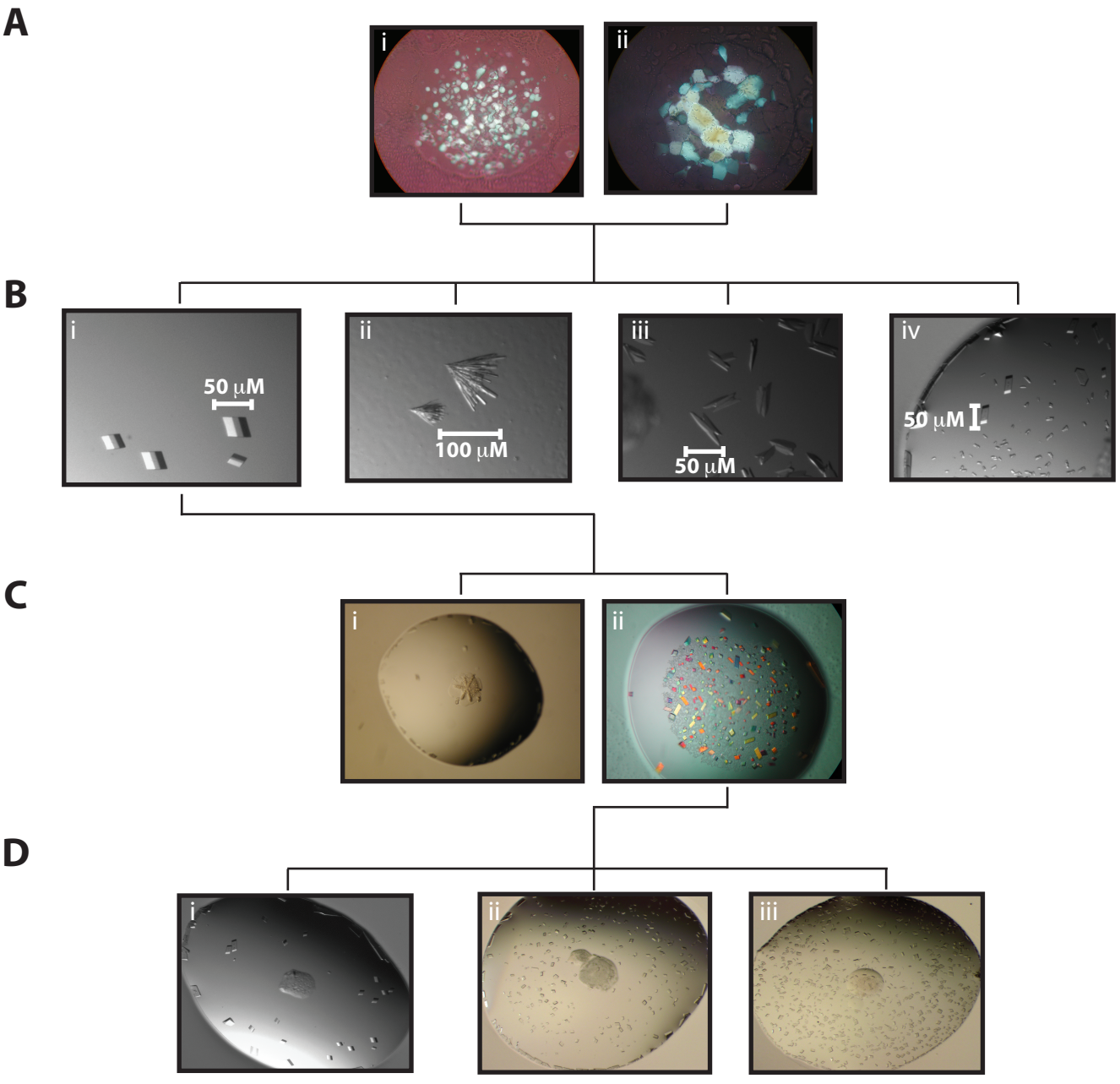
A
i
ii
B
i
50 μM
ii
100 μM
iii
50 μM
iv
50 μM
C
i
ii
D
i
ii
iii

desired pH range across precipitants PEG3350 and PEG6000 yielded small thin 3-dimensional crystals specifically in the condition of 100 mM NaCl, 100 mM MES with 20 % PEG3350 or 20 % PEG6000. Optimizing the buffer concentration, buffer pH, salt concentration, precipitant type and precipitant concentration yielded the most favorable crystals by visual inspection. The final base condition consisted of 100 mM MES (pH 5.5-6.5), 100 mM NaCl, and 20 % PEG3350 where the crystals appeared after approximately 2 weeks and continued to grow for an additional 2 - 3 weeks (Figure 4.2B).

To improve the possibility of producing high quality crystals, screening across pH was included in all screens as the appearance of visually appealing crystals at a given pH varied from screen to screen. Crystallization was conducted at 15°C and 20°C to determine the optimal temperature (Figure 4.2C). Reducing the crystallization temperature delayed the appearance of CfrA crystals and did not significantly improve the physical appearance of the crystals. Thus, the following trials were conducted at 20°C. Crystallization trials with different ratios of protein solution to precipitant solution (0.5:1 or 1:0.5) eliminated the development of CfrA crystals (data not shown). Maintaining a consistent ratio of 1:1 for the protein solution to reservoir with a larger drop volume resulted in an inverse relationship between the number/size of crystals and size of drop (Figure 4.2D). 2 μl of protein solution with 2 μl of reservoir solution resulted in an increase in the number of crystals, however the crystals were smaller than when 1 μl protein solution was added to 1 μl of reservoir solution. The 3 μl of protein solution with 3 μl of reservoir solution resulted in a further increase in the number of crystals, but these crystals were smaller still. Subsequent crystallization conditions were completed with 1 μl of protein solution to 1 μl of reservoir solution at 20°C.

4.3.4 Optimization of crystallization. Various additives have been shown to be advantageous in the formation of highly ordered protein crystals. An in house screen testing the use of alcohol additives (heptanetriol, 2 methyl 2,4 pentanediol (MPD), isopropanol) resulted in crystals; however, the appearance of crystals in the presence of heptanetriol and isopropanol were inconsistent. The mechanism by which the alcohols aid in crystallization is unknown; however, there is speculation that the alcohols further reduce the size of the micellar belt (163). Optimization revealed an ideal concentration in the reservoir solution of 1.5% MPD. In addition to in house screens, various screens purchased from Hampton Research were tested. Also, Figure 4.3 gives a visual representation of the results that were typically found during the screening process. To further improve the crystal conditions, I reduced the detergent concentration during the purification process from 0.1% to 0.05% (data not shown). Ideally, the presence of detergent micelles should be limited in order to facilitate crystallization (162). The reduction in detergent concentration resulted in crystal formation overnight; however, these crystals were extremely delicate and did not diffract to high resolution (see below). Additional screens with metal additive (iron, cobalt, manganese and nickel) were attempted, as CfrA is an iron transporter. The presence of iron at varying concentrations (0.04 mM-0.1 mM) produced 3-dimensional crystals with extremely sharp edges (Figure 4.3G).

4.3.5 Crystallization with ligand. Crystallization of proteins with the cognate substrate has been shown to improve crystallization, increase resolution and give insight into the molecular determinants of binding. Therefore, I decided to prepare crystallization trials with apo-enterobactin and ferric-enterobactin. The enterobactin was a kind gift from Dr. Alain Stintzi. The procedure for preparing ferric-enterobactin is depicted in Figure 4.4A showing

Figure 4.3

Crystal morphologies obtained using Hamption Research and a metal screens. **(A)** 100 mM cacodylate; **(B)** 20 mM n-octyl β D glucoside; (C) 100 mM sodium formate; **(D)** 100 mM succinic acid; **(E)** 15 % isopropanol; **(F)** 0.15 mM nonyl β-D thiomaltoside. **(G)** 0.01 M iron.

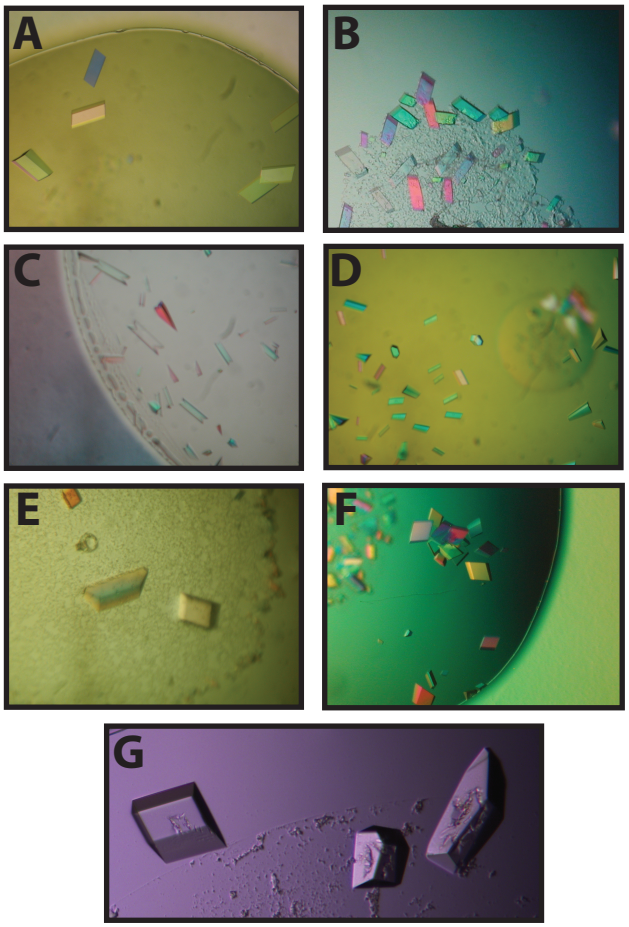
A
B
C
D
E
F
G

the characteristic red color of ferric-enterobactin. The addition of the $NaHPO_4$ caused the solution to turn red. To ensure the production of ferric- enterobactin, I recorded the absorbance spectrum of the final product as ferric-enterobactin has a characteristic peak intensity at approximately 500 nm (166). As can be seen in Figure 4.4, the production of ferric-enterobactin resulted in an intense absorption at approximately 500 nm confirming the preparation of ferric-enterobactin. A large screen was conducted varying the amount of ferric-enterobactin / enterobactin to protein (0.5:1, 1:1 and 1:0.5 [mol:mol]) to determine ideal conditions for crystallization. Small crystals formed in all conditions with no improvement seen in resolution (see below).

4.3.6 Synchrotron results. Due to time constraints and logistical complications, only a small fraction of the crystals (162) were tested at the European Synchrotron and Radiation Facility (ESRF) in Grenoble, France over an eight month time period. The majority of the crystals tested derived from 100 mM MES (pH 5.5-6.5), 100 mM NaCl, 0.15 % MPD and 20 % PEG3350. The best diffraction pattern to date was obtained from a crystal grown in 100 mM MES (pH 5.7), 100 mM NaCl, 0.15 % MPD and 20 % PEG3350 cryoprotected in 50 % PEG3350 (Figure 4.5A). The initial image diffracted to approximately 3.0 Å with subsequent images at decreasing resolution (Figure 4.5B). The resulting structure was modeled at a 5.0Å resolution and is not sufficient for amino acid side chain information. Overall, the model shows a 22 anti-parallel β-barrel protein (Figure 4.5).

4.3.7 LPS experiments. It has been well documented for TBDT that lipopolysaccharides (LPS) are a critical factor to be considered when attempting crystallography. A specific amount of LPS is critical for crystallization of certain TBDT (32). LPS is a large component of the outer leaflet of the outer membrane of gram-negative bacteria. Thus, LPS readily

Figure 4.4

Production and characterization of ferric-enterobactin. **(A)** Schematic representation with images for the production for ferric-enterobactin. The initial 100 nmol of $FeCl_3$ appeared transparent with the 100 nmol of enterobactin appeared cloudy. Mixing of the two solutions resulted in a cloudy mixture. The addition of 1 M $NaHPO_4$ resulted in an intense red solution which is characteristic of ferric-enterobactin. The final addition of H_2O to a final volume of 1ml maintained the red color. A solution of H_2O is presented alongside the final ferric-enterobactin to demonstrate the color difference. **(B)** The visible spectra of ferric-enterobactin showing the highly characteristic absorbance at approximately 500 nm. The individual constituents used to produce ferric-enterobactin lack absorbance intensity in the 500 nm region. Only upon mixture of the $FeCl_3$ with the enterobactin does an intensity at 500 nm appear.

A

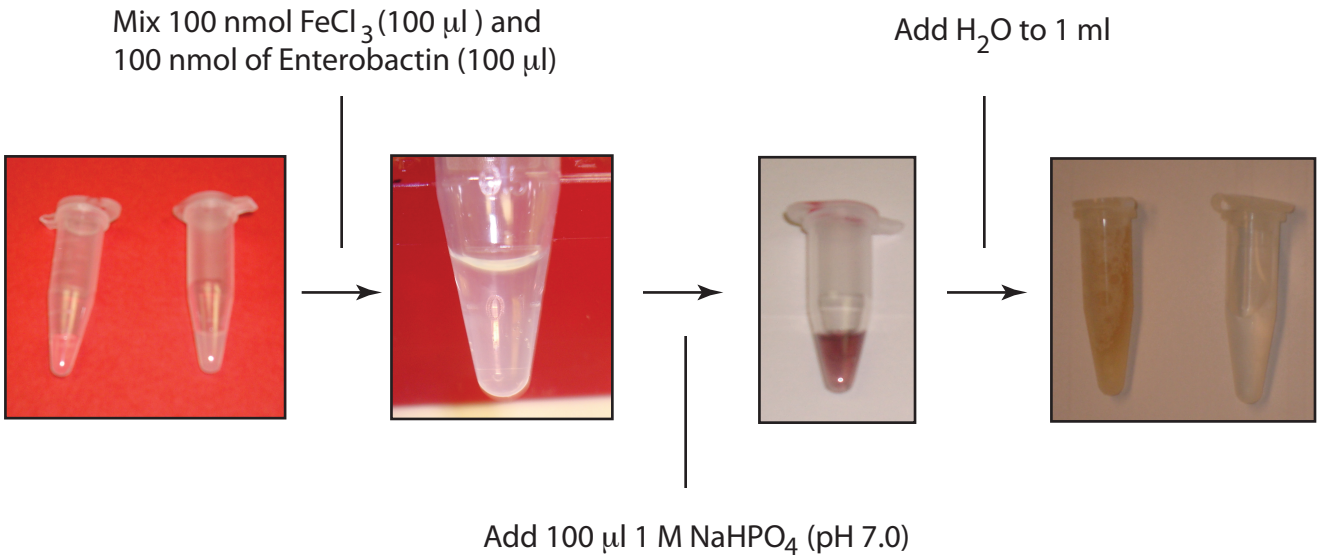
Mix 100 nmol $FeCl_3$ (100 µl) and
100 nmol of Enterobactin (100 µl)
Add H_2O to 1 ml
Add 100 µl 1 M $NaHPO_4$ (pH 7.0)

B

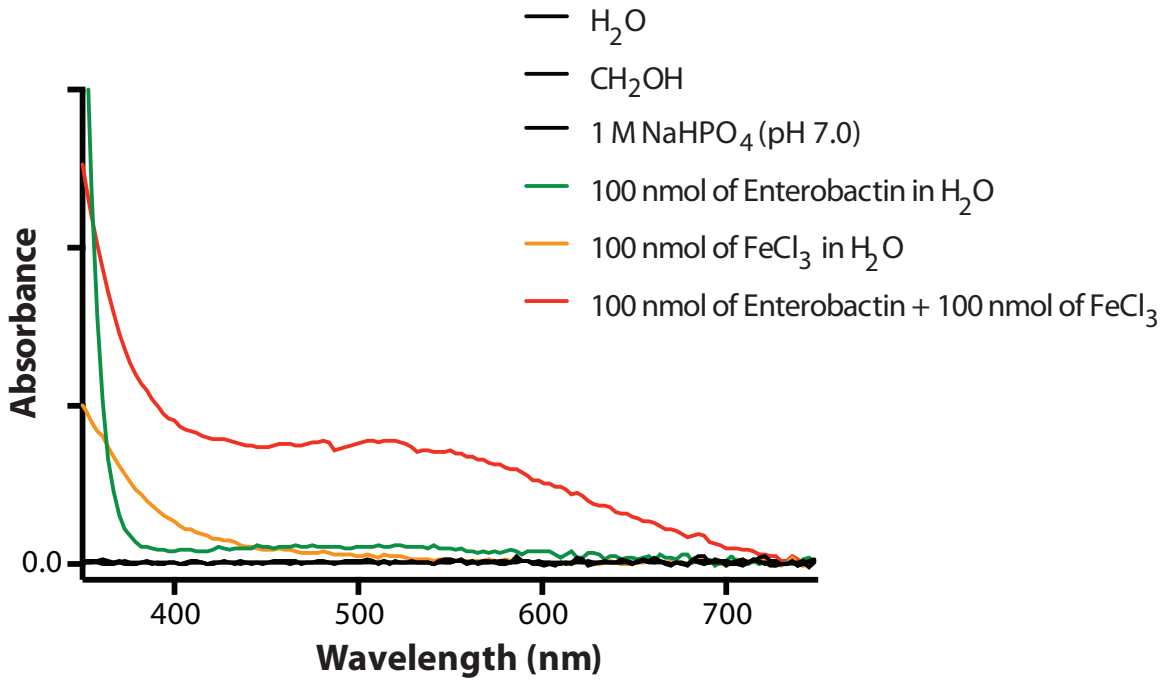
H_2O
CH_2OH
1 M $NaHPO_4$ (pH 7.0)
100 nmol of Enterobactin in H_2O
100 nmol of $FeCl_3$ in H_2O
100 nmol of Enterobactin + 100 nmol of $FeCl_3$
Absorbance
0.0
400
500
600
700
Wavelength (nm)

Figure 4.5

The structural characterization of CfrA by X-ray crystallography. **(A)** Representative crystal in cryoloop prior to acquisition of diffraction data. **(B)** The first diffraction pattern acquired for the crystal that diffracted to approximately 3.6 Å. **(C)** The final model of CfrA at approximately 5.0 Å.

A

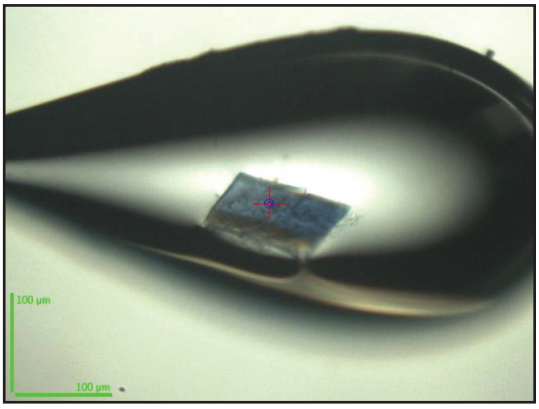

B

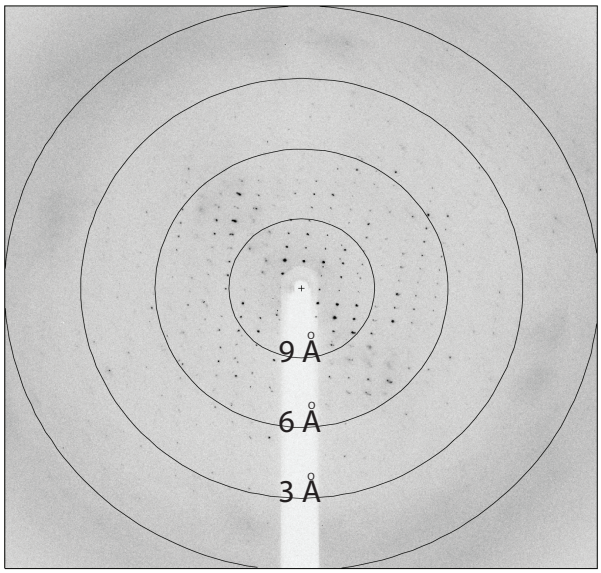

C

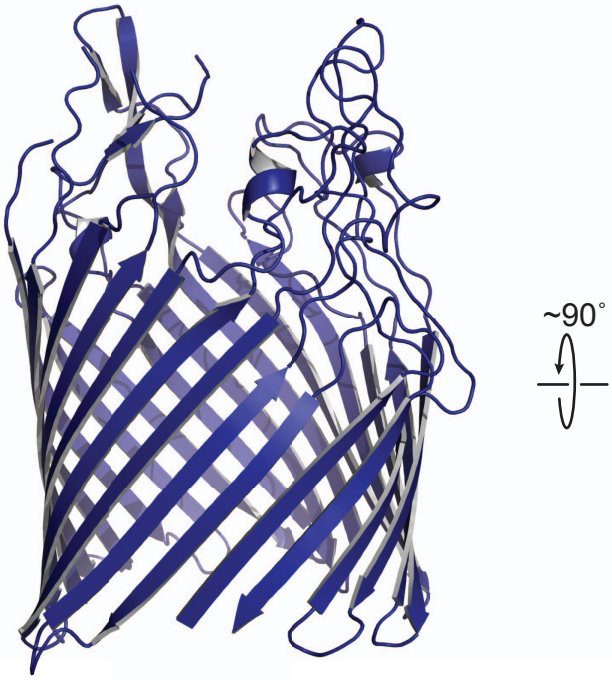



purifies with outer membrane proteins (161,167). I decided to investigate if the detergent-solubilizd pure CfrA co-purifies with LPS. I ran three separate purifications of CfrA alongside a LPS standard on an SDS-PAGE gel followed by silver staining to determine if LPS is present in the pure CfrA samples (Fig 4.6A) (168). Small amounts of LPS were found in two of the pure samples of CfrA. In an attempt to remove the LPS from the purified sample, I decided to run an anion-exchange column as the calculated isolelectric point of CfrA is approximately 5.38. Anion exchange chromatography allows the extensive washing of the bound protein prior to elution with increasing salt concentration. The initial trial using a 1 ml MonoQ column from GE healthcare showed that CfrA binding to the anion-exchange resin was inhibited due to the high sodium chloride in the gel filtration buffer (150 mM) (data not shown). Exchange of CfrA into a low salt buffer (50 mM NaCl and 25 mM Tris-HCl [pH7.0]) allowed the successful binding of the protein to the anion exchange resin. Figure 4.6B shows the absorbance spectra of CfrA loaded onto the MonoQ column followed by 10 CV of low salt buffer. The protein was then eluted using a salt gradient. The protein eluted in the shape of one prominent peak (6 ml) with a slight shoulder (7.7 ml) into 4 fractions (Figure 4.6D). The 4 fractions were then subjected to SDS-PAGE and silver staining analysis. With approximately equal protein loading, Figure 4.6C clearly shows the presence of differing amounts of LPS in the four fractions indicating a heterogeneous population of protein in relation to amount of LPS presence. Crystal trials with the established base condition were attempted with the individual fractions. All four fractions produced crystals; however, the second fraction produced crystals adopting a different morphology: very thin, very large plates (data not shown). Increasing the wash in low salt from 10 CV to 15 and 20 CV drastically reduced the appearance to the shoulder at 7.7 ml (Fig 4.6D). The SDS-PAGE gels stained with both coomassie blue and silver are

Figure 4.6

The presence of LPS in pure detergent-solubilised CfrA creates a heterogeneous population. **(A)** Comparison of three separate purifications of CN10 by SDS-PAGE and subsequent silver staining. Approximately 10 μg of pure CfrA was loaded per sample and stained using a SilverQuest™ Silver Staining Kit from Life technologies. Lanes 1 and 2 were samples from two purifications from cobalt based affinity chromatography. Lanes 3 through 5 were final purified samples from three separate purifications. 1 μg of LPS standard was loaded in lane 6. **(B)** Absorbance trace of CfrA during anion-exchange chromatography. 125 μg of purified CfrA was exchanged into 50 mM NaCl and 25 mM Tris-HCl (pH 7.0) and loaded onto a 1 ml MonoQ column from GE healthcare. The column was washed with 10 CV of low salt buffer prior to salt gradient. Absorbance (black trace) and salt concentration (dashed trace) are presented. The protein eluted in three fractions (1-3) with the shoulder isolated to fraction 3. **(C)** Comparison of fractions 1, 2, 3 from anion exchange column by SDS-PAGE and silver stain. Approximately 10 μg of protein was loaded per lane. Lane 1: initial sample prior to exchange into low salt for anion exchange chromatography. Lane 2: sample loaded onto anion exchange column in low salt. Lane 3: fraction 1 off the anion exchange column. Lane 4: fraction 2 off the anion exchange column. Lane 5: fraction 3 (shoulder) off the anion exchange column. Arrow denotes the location of LPS. **(D)** Absorbance trace of CfrA during anion-exchange chromatography. Approximately 250 μg of detergent-solubilized CfrA was exchanged in 50 mM NaCl and 25 mM Tri-HCl (pH 7.0) divided into two aliquots and loaded onto a 1ml MonoQ column: (i) 10 CV wash in low salt prior to salt gradient (same trace presented in B), (ii) 15CV wash low salt prior to salt gradient, and (iii) 20 CV wash low salt prior to salt gradient. Note the prominent peak at 6 ml changes very little between samples; however, the presence of the shoulder at 7.7 ml is substantially reduced with increased washing in low salt. **(E)** Comparison of fractions 1, 2, 3 off anion exchange column by SDS-PAGE Coomassie stain (top) and silver stain (bottom). Approximately 10 μg of protein was loaded per lane. Lane 1: protein sample from cobalt based affinity resin. Lane 2: protein sample from size exclusion column after exchange into low salt buffer. Lane 3-4: peak fractions from anion exchange column washed with 10 CV prior salt gradient. Lane 5-6: peak fractions from anion exchange column washed with 15 CV prior salt gradient. Lane 7: peak fractions from anion exchange column washed with 20 CV prior salt gradient. 1 μg of LPS standard was loaded in lane 8.

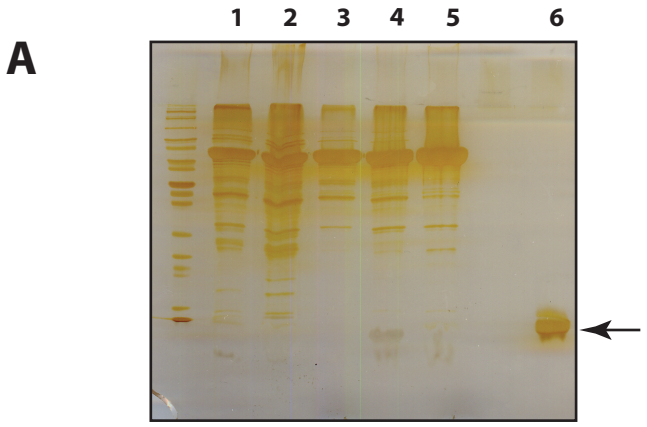
A
1 2 3 4 5 6

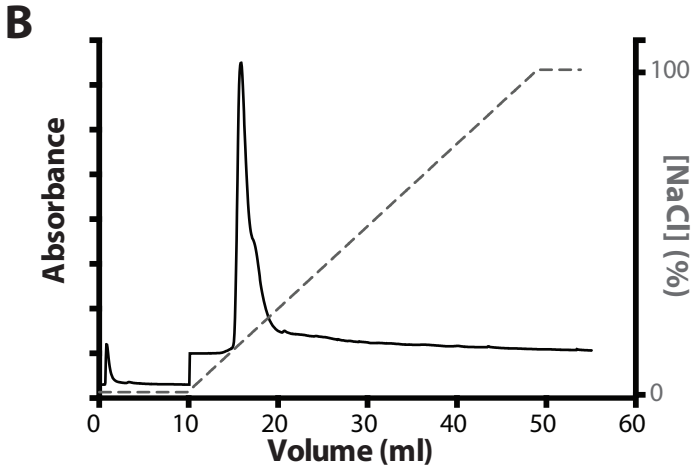
B
Absorbance
100
[NaCl] (%)
0
0 10 20 30 40 50 60
Volume (ml)

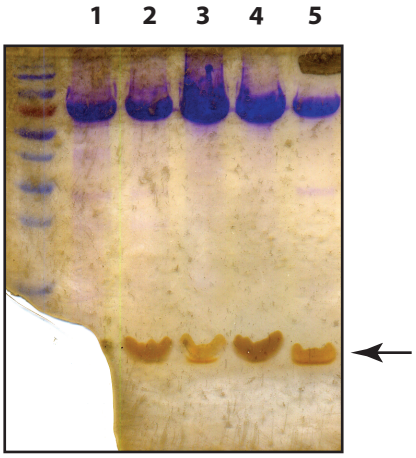
C
1 2 3 4 5

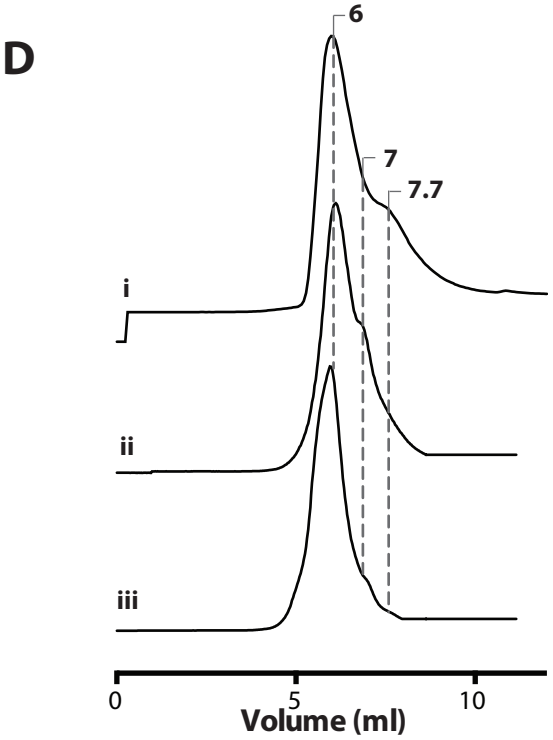
D
6
7
7.7
i
ii
iii
0 5 10
Volume (ml)

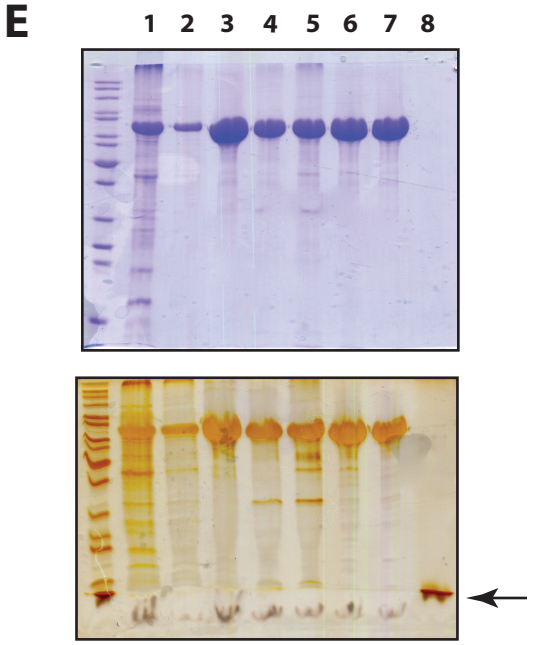
E
1 2 3 4 5 6 7 8

presented in Figure 4.6E. Although, it is difficult to discern the actual amount of LPS, the presence of a prominent shoulder by anion exchange chromatography does decrease with increasing low salt wash volumes. Crystallization trials were not attempted on the fractions from this experiment due to time constraints. It is interesting to speculate that the disappearance of the shoulder may aid in the formation of highly ordered crystals.

4.4 Discussion

Substantial progress was made towards the acquisition of high-resolution structural information of CfrA. Hundreds of crystallization trials were performed leading to the identification of conditions that reproducibly produced large, 3 dimensional and sharp edged crystals. However, the data acquisition from these crystals proved logistically difficult. At the first appearance of crystals, I travelled to McGill University to test the quality of the crystals on their home source. These crystals diffracted poorly (~22 Å). Membrane proteins are known to diffract poorly on home sources due to the relatively weak strength of the beam. The initial trip, to France and the ESRF, approximately a year later, for a period of 4 months, resulted in a 5 Å model of CfrA. This data was acquired four days before returning to Canada and were from a crystallization plate that had been set up approximately three months prior. Of note, the crystal that resulted in the 5 Å model of CfrA was grown in identical conditions as the crystals tested at McGill University. This large discrepancy in diffraction further reinforces the need for consistent access to a synchrotron for the acquisition of high-resolution structural information of CfrA.

Upon my return to Canada, I attempted crystallization trials in the presence of metals resulting in crystals of large size with sharp edges grown in the presence of iron. Crystals, grown in the presence of iron, were tested on the home source present at the University of Ottawa. The crystals diffracted to approximately 8Å, a substantial improvement from 22Å previously seen via a home source. This was extremely encouraging as crystals that diffracted to 22Å via home source resulted in a 5Å model of CfrA. A result of 8Å via a home source suggested an atomic level model was in the immediate future. Crystal grown in the presence of iron were shipped to the ESRF for a collaborator to test. The crystals were

held at French Customs for 12 hours and upon arrival at the ESRF the dewar and multiple loops were damaged. Most of the crystals were lost possibly due to rough handling.

Subsequent trips for two months yielded no improvement in resolution. It is interesting to speculate that incubation time played a role in the increased resolution seen for the one crystal. As mentioned, approximately 162 crystals were tested at the ESRF. 162 crystals is a relatively small number considering the target is a membrane protein. Perhaps with more consistent access to synchrotron facility an increase number of crystals could have been tested yielding a high-resolution structure.

The model at 5Å did provide some informative information. The average non-protein content of protein crystals is approximately 40% (169). In contrast, the non-protein content of the CfrA crystal was calculated to be 60% non-protein, demonstrating a large volume of the crystal was either solvent or the micellar belt. This would greatly reduce protein-protein crystal contacts. Reducing the detergent concentration may improve the ability to form crystal contacts. Note that reducing the detergent concentration from 0.1% to 0.05% LDAO resulted in fragile crystals. Exploring detergent concentrations between 0.1% and 0.05% may yield an intermediate between increased diffraction and relatively robust crystals. Perhaps the large loops are obstacles with respect to protein-protein contacts; if so, limited proteolysis may produce a more compact core aiding in the close association between monomers necessary for protein-protein contacts.

The CfrA construct produced and characterized in Chapter 3 and used for crystallization in Chapter 4 has a 10-histidine tag linked to the *cfrA* gene through an enterokinase cleavage site. Enterokinase proved extremely inefficient at cleaving the histidine tag under the

conditions tested. The production of a new construct with Herpes simplex (HRV) 3C protease site would be a priority. Other groups have had success with internal affinity tags (161).

Although, high-resolution structural information was not acquired for CfrA during the course of this research, I'm confident, given access to the proper equipment, the structure of CfrA can be solved at high resolution.

5 THE EXPRESSION, PURIFICATION, AND STRUCTURAL CHARACTERIZATION OF THE ISOLATED PLUG DOMAIN

5.1 Introduction

The mechanism of transport through TonB dependent transporters is controversial. Ferric-siderophores are known to bind to the extracellular side through interactions with residues from both the barrel and plug domains. The binding of a ferric-siderophore leads to a conformational change in the TonB box, which is located at the N-terminus of the plug domain, and extends into the periplasmic space. The TonB box then interacts with the TonB complex, which extends up from the cellular membrane towards the outer membrane. The physical interaction between the TonB complex and the TonB box leads to an energy dependent conformational change in the plug domain that facilitates transport of the ferric-siderophore (107). The physical interaction may lead to an energy-dependent TonB mediated increase in tension on the plug domain (TonB may pull on the plug) leading to partial unfolding and thus the creation of a path for transport of ferric-siderophore across the membrane (170). Alternatively, the energy provided by the TonB complex may facilitate amino acid side chain rearrangement within the barrel forming a channel to allow the ferric-siderophore into the periplasm. Given the size of ferric-siderophore and position of the plug domain, some form of conformation change in the plug domain is required for transport (32,171,172). The plug thus exhibits a dynamic structure, an understanding of which is essential for understanding transport.

The plug domain is approximately 17 kDa, soluble and thus amendable to NMR. However, structural characterization by NMR requires an isotopically labeled pure protein sample. The objective of this project was to gain insight into the conformational dynamics of the plug domain and its involvement in mechanism of transport by NMR techniques. This chapter

describes the cloning, expression, purification and preliminary NMR analysis for the isolated plug domain.

5.2 Experimental Procedures

5.2.1 Constructs. The plug domain was constructed using pCN10 as a template using PCR with primers listed in Table 5.1. PCR was preformed in an Eppendorf Mastercycler Gradient (Eppdendorf) with 30 cycles of 94°C for 15 s, 55°C for 30 s, and 68°C for 1 min. PCR products were ligated into the pET20b vector (Novagen). The ligation mixture was transformed into chemically competent *E. coli* XLI-Blue without further manipulation. Resulting transformants were screened for plasmids of appropriate size and digested checked for presence of insert. Inserts were sequenced for sequence integrity. The final plasmid used in these studies was designated pPLUG.

5.2.2 Plug expression in LB. Chemically competent *E.coli* strain C41(DE3) was transformed with pPLUG and grown on Luria-Bertani (LB) Broth plates supplemented with 100 μg/ml of ampicillin (Amp_{100}). After overnight incubation, single colonies were sub cultured into 50 ml of LB broth supplemented with Amp_{100} and incubated approximately 18 hours at 37°C. Cultures were then diluted 1:100 into fresh LB broth supplemented with Amp_{100} and placed at 37°C. Protein expression was induced at an optical density at 600 nm of 0.6 by the addition of 0.2 mM IPTG (MBI fermentas) for 3 hours 37°C. The culture were pelleted, resuspended in lysis buffer (0.3 M NaCl, 0.05 M NaH_2PO_4 [pH 7.0]) and frozen until use.

5.2.3 Plug expression with ^{15}N-labelled NH_4Cl in M9 Minimal Media. Chemically competent *E.coli* strain C41(DE3) was transformed with pPLUG and grown on LB agar plates with Amp_{100}. After overnight incubation, single colonies were sub cultured into 50

Table 5.1. Primer sequences designed for construction of the isolated plug domain sequence

Primer	Sequence
CfrA-5-Bam-10-His	GCGCGGATCCGCACCACCACCACCACCACCACCACCACG ACGACGACGACAAGCAAAATGTAGAACTAGATAGC
Plug-3-Xho-stop	GCGCCTCGAGTTATTTATCACTTACTTT

[a] Enzyme cleavage sites for cloning purposes are underlined.

ml of LB broth supplemented with Amp_{100} and incubated approximately 18 hours at 37°C. Cultures were diluted 1:20 into 1 L of fresh LB broth supplemented with Amp_{100} and placed at 37°C. Once an optical density of 0.6 was reached, the culture was pelleted by slow speed centrifugation and resuspended in 1 L of fresh M9 minimal media (0.05 M Na_2HPO_4, 0.02 M KH_2PO_4, 0.02 M $MgSO_4$, 0.02 M glucose, 0.01 % (v/v) of Gibco MEM Vitamin Solution (Life technologies), and 0.0001 M $CaCl_2$) supplemented with 0.02 M ^{15}N-labelled NH_4Cl (Sigma) and Amp_{100}. After a 1 hour acclimatization the cells were induced with a final concentration of 0.2 mM IPTG for 3 hours.

5.2.4 Plug purification. The resuspended cells were lysed by sonication and the soluble fraction isolated by slow speed centrifugation. The soluble proteins were incubated for 1 hour at 4°C with 5ml of Superflow cobalt based resin (Talon). The resin was pelleted and resuspended in 10 ml of lysis buffer twice before being placed in a disposable column and washed with three column volumes (CV) of lysis buffer followed by 6 CV of lysis buffer supplemented with 0.01 M imidazole. The plug was then eluted with lysis buffer supplemented with 0.05 M imidazole. Protein fractions were concentrated using a Centricon 10 kDa cutoff concentrator and further purified using a Superdex200 gel filtration column (GE healthcare) in gel filtration buffer (0.15 M NaCl and 0.025 M Tris-HCl [pH7.0]) .

5.2.5 Fourier Transform Infrared Spectroscopy (FTIR). Hydrogen/deuterium infrared spectra were recorded on a Digilab (now Agilent Technologies; Santa Clara, CA) FTS40 spectrometer using a Golden-GateTM attenuated total internal reflection accessory (SpecAc; Oprington, Kent, U.K.). 3 μl of the plug (~1 mg/ml) in gel filtration buffer were dried down onto the accessory under a gentle stream of N_2 gas. After collecting a 128 scan spectrum at 4cm^{-1} resolution, 4 μl of ^2H_2O was added and another 128 scan spectrum collected. For the

more detailed amide I band analyses and for thermal stability measurements, approximately 200 μg of the plug was deposited on a CaF_2 window with a gentle stream of N_2 gas followed by rehydration with 8 μL of ^2H_2O. A 4000 scan spectrum was recorded at 2 cm^{-1} resolution and 22.5°C on a Digilab (now Agilent Technologies; Santa Clara, CA) FTS7000 spectrometer. 128 scan spectra were then acquired at 1˚C intervals from 35°C – 75°C. The temperature was varied with a computer controlled circulating water bath, with 20 min equilibrations between temperatures. Spectra were analyzed using GRAMS/AI software (Thermo Scientific; Waltham, MA). Residual water vapor was subtracted using the method of Reid *et al* (173). Resolution enhancement was performed between 1900cm^{-1} and 1300cm-1 using a $\gamma = 8$ and a bessel smoothing function set to 75%. Thermal denaturation was measured as the change in intensity at 1617 cm^{-1} and was evaluated using Graphpad Prism (La Jolla, CA).

5.3 Results

5.3.1 Expression of the plug domain. The plug domain was cloned from the full length pCN10 construct with a N-terminal 10His tag and was placed into a pET20b vector under the control of the T7 promoter. The expression of the plug was first optimized in LB broth. The IPTG induced expression of the construct was monitored in *E. coli* strain C41, as full length CfrA expressed at optimal levels in this cell type (159). Robust expression was seen after 3 hours induction with 0.0002 M IPTG (Figure 5.1A-top panel).

To produce isotopically labeled protein for NMR studies, the protein must be expressed in minimal media supplemented with the isotopically labeled metabolite to facilitate the incorporation of the isotopically labeled atom into the protein of interest. Initially, the overnight cultures were diluted 1:20 into 200 ml of fresh M9 minimal media supplemented with Amp_{100} and placed at 37°C. Once an optical density of 0.6 was reached, the culture was pelleted by slow speed centrifugation and resuspended in 1 L of fresh M9 minimal media. After a 1 hour acclimatization the cells were induced with a final concentration of 0.0002 M IPTG for 4 hours. Unfortunately, this protocol did not produce the required amount of protein for NMR experiments. In agreement, *E. coli* strain BL21, the parental strain of C41, has been shown to grow sub optimally in M9 minimal media (137,174). Marley *et al* showed that growth of the initial cell mass in LB broth does not effect the incorporation of the isotopically labeled atom into the expressed proteins when cells are pelleted and then transferred into M9 minimal media prior to protein expression (175). The initial cell growth in :B broth followed by induction of the plug domain in minimal media allowed production

Figure 5.1

Purification and structural characterization of the plug domain. **(A)** Expression of the plug domain in C41 *E. coli* cells in (i) LB and (ii) M9 Minimal Media. The plug expressing C41 *E.coli* cells were grown to an optical density of 0.6 and induced with the indicated concentration of IPTG for 3 hours. Note: an additional one hour of acclimatization was needed prior to induction for the plug expressed in minimal media; lane 1: prior to induction, lane 2: three hours post induction with 0.2 mM IPTG, and lane 3: 3 hours post induction with 1 mM IPTG. Arrows denotes the protein band that represents the plug domain. **(B)** Summary of the plug domain purification protocol. The soluble fraction was isolated from lysed C41 *E. coli* resuspended in lysis buffer by slow speed centrifugation (lane 1), washed three times with 10 ml of lysis buffer (lane 2-4) followed by a 30 ml wash with lysis buffer supplemented with 10 mM imidazole (lane 5). The plug domain was eluted off the cobalt resin with lysis buffer supplemented with 50 mM imidazole (lane 6), concentrated (lane 7), subjected to size exclusion chromatography (lane 8) and concentrated for subsequent analysis (lane 9). Arrows denotes the protein band that represents the plug domain.

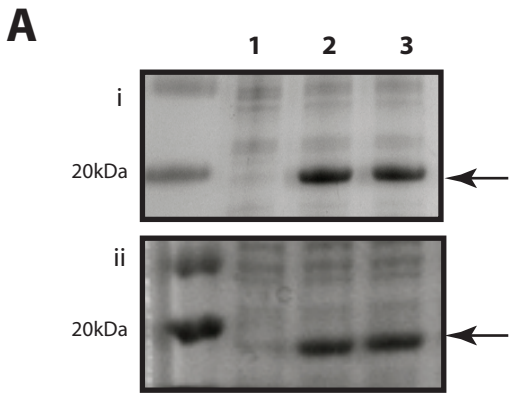
A
1
2
3
i
20kDa
ii
20kDa

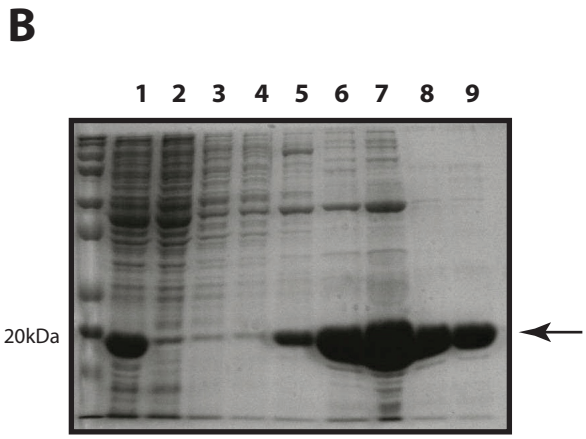
B
1
2
3
4
5
6
7
8
9
20kDa

of a sufficient amount of protein for structural studies (~1 g of purified plug / 1 L of culture) (Figure 5.1A-bottom panel). Briefly, the overnight cultures were diluted 1:20 into 200ml of LB broth supplemented with Amp_{100} and placed at 37°C. Once an optical density of 0.6 was reached, the cells were then isolated by slow speed centrifugation, resuspended in M9 minimal media with ^{15}N-labelled ammonium chloride and allowed to acclimatize for 1 hour followed by a 3 hour induction with 0.2 mM IPTG.

5.3.2 Purification of plug. The soluble protein fraction was isolated and subsequently purified by immobilized metal affinity chromatography charged with cobalt (Clontech). Batch binding followed by an extensive washing procedure allowed elution of relatively pure plug with 0.05 M imidazole (Figure 5.1B). Small scale purification revealed that the plug remained bound to the resin in the presence of 0.01 M imidazole with a large amount eluting in the presence of 0.05 mM imidazole (data not shown). Further washing with 0.15 M imidazole revealed that the majority of the protein had been displaced; thus, the plug was eluted off the column with 0.05 M imidazole. A subsequent size exclusion chromatography step resulted in the isolation of pure plug.

Of interest during the purification, the plug domain purifies as two peaks on the gel filtration column (Figure 5.2A). Isolation of one peak followed by reapplication to the size exclusion column results in the redistribution of the sample into two peaks suggesting an equilibrium between two states (Figure 5.2A). NATIVE PAGE revealed the presence of two bands; whereas, SDS-PAGE show a single band further suggesting an equilibrium. (Figure 5.2B & 5.2C).

Figure 5.2

The re-distribution of the plug demonstrated by size exclusion chromatography. **(A)** The plug domain was expressed and purified as described previously. The final trace for the purified plug domain is presented in blue. The peaks at 14.8 ml (peak 1) and 15.5 ml (peak 2) were isolated and concentrated. The sample isolated from peak 1 was reapplied to the size exclusion column to yield the red trace. The sample isolated from peak 2 was reapplied to the size exclusion column to yield the green trace. Peak 1 was isolated from both the red and green trace and reapplied to the size exclusion column and produced the purple trace. Peak 2 was also isolated from both the red and green trace and reapplied to the size exclusion column producing the black trace. Note the redistribution of the peaks. **(B)** SDS-PAGE Gel of the experiment describe in (A); lane 1: peak 1 from the blue trace, lane 2: peak 2 from the blue trace, lane 3: peak 1 from the green trace, lane 4: peak 1 from the red trace, lane 5: peak 2 from the green trace, and lane 6: peak 2 from the red trace. **(C)** NATIVE PAGE of purified plug domain. The plug domain was purified from LB (lane 1-2) or M9 Minimal Media (lane 3-4) and approximately 6 μg were subjected to NATIVE PAGE analysis. Samples were run in duplicate.

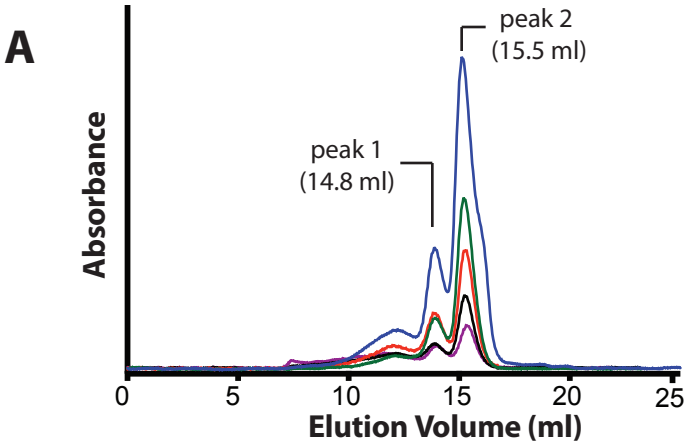
A
peak 2
(15.5 ml)
peak 1
(14.8 ml)
Absorbance
0
5
10
15
20
25
Elution Volume (ml)

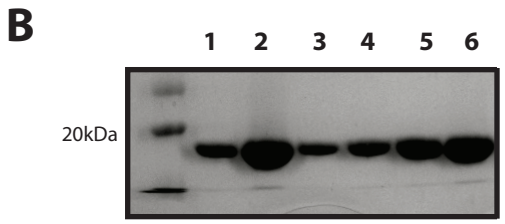
B
1 2 3 4 5 6
20kDa

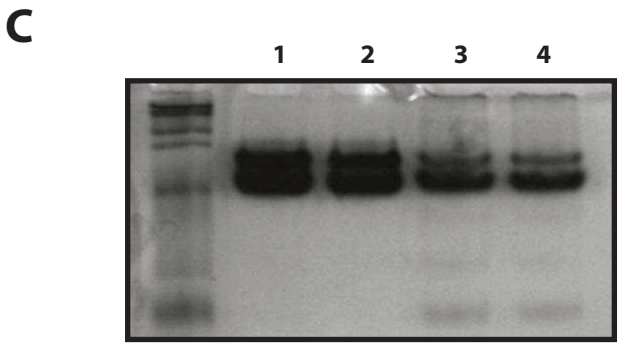
C
1 2 3 4

5.3.3 Structural and Biophysical characterization of the plug domain. The N-terminal of TBDT adopts a characteristic structure. A previous homology model of the plug domain suggests that the domain adopts a structure comparable to the N-terminal of other siderophore transporters (159). The plug domain is a mixed αβ globular structure. I used Fourier transform infrared spectroscopy (FTIR) to determine whether affinity purified plug exhibits the structural and biophysically properties predicted for the isolated plug domain. FTIR spectra of the isolated plug domain dried from $^{1}H_2O$ buffer and rehydrated in $^{2}H_2O$ are presented in Figure 5.3A. The spectra exhibit intense protein vibrations between 1700 cm^{-1} and 1600 cm^{-1} and centered near 1545 cm^{-1} ($^{1}H_2O$) or 1450 cm^{-1} ($^{2}H_2O$).

The secondary structure of the plug domain was qualitatively assessed by analyzing the protein amide I band (1600 to 1700 cm^{-1}), which is due to the C=O stretching vibration of the polypeptide backbone coupled to both N-H in-plane bending and C-N stretching (145) (Figure 5.3A). The amide I band is particularly useful as specific secondary structural elements absorb at distinct wavenumbers. α-helices absorb between 1648cm^{-1} and 1660cm^{-1} and β-sheets absorb between 1625cm^{-1} and 1640cm^{-1} (146). In $^{2}H_2O$, the amide I band is broad and asymmetric with a maximum at 1639 cm^{-1} and a prominent shoulder around 1660 cm^{-1}. Resolution enhancement reveals the component bands that contribute to the amide I contour (Figure 5.3B). The prominent peaks centered at 1634cm^{-1} and 1657cm^{-1} represent β-sheet and α-helical structures respectively consistent with the predicted secondary structure of the plug domain as a mixed αβ structure (146).

The amide II band, which is due to in-plane N-H bending coupled to C-N stretching, undergoes a downshift to in frequency from 1545cm^{-1} to 1450 cm^{-1} upon exchange of peptide N-^{1}H to N-^{2}H. Thus the relative intensity at 1545 cm^{-1} provides a measure of the

Figure 5.3

Structural characterization of the plug domain by FTIR. **(A)** Infrared spectra of purified plug domain recorded after gentle drying from $^{1}H_2O$ buffer (black trace) and rehydrated with $^{2}H_2O$ buffer (gray trace). **(B)** Resolution-enhanced and curve fit of the amide I band in the FTIR spectra of the plug domain. Peaks identified from the resolution-enhanced spectrum were used as an estimation of the secondary structure content. Spectra were baseline corrected between 1,775 cm^{-1} and 1,325 cm^{-1}. Resolution-enhanced spectral deconvolution parameters of γ of 8 and smoothing of 75 % were used. **(C)** Thermal denaturation curve of purified plug domain recorded after gentle drying from $^{1}H_2O$ buffer and rehydration with 8 μl of $^{1}H_2O$ buffer. The curve was fit with a Boltzmann sigmoid from which the T_d was calculated using Graphpad Prism software. Spectra were recorded every degree from 35°C to 75°C.

A

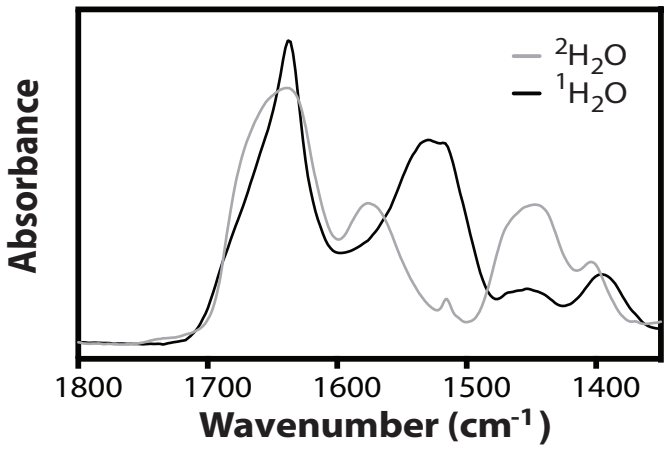
^2H_2O
^1H_2O
Absorbance
1800
1700
1600
1500
1400
Wavenumber (cm^{-1})

B

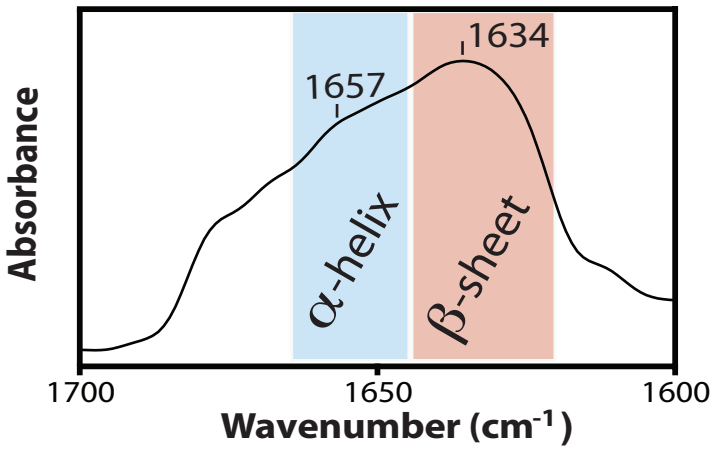
1634
1657
α-helix
β-sheet
Absorbance
1700
1650
1600
Wavenumber (cm^{-1})

C

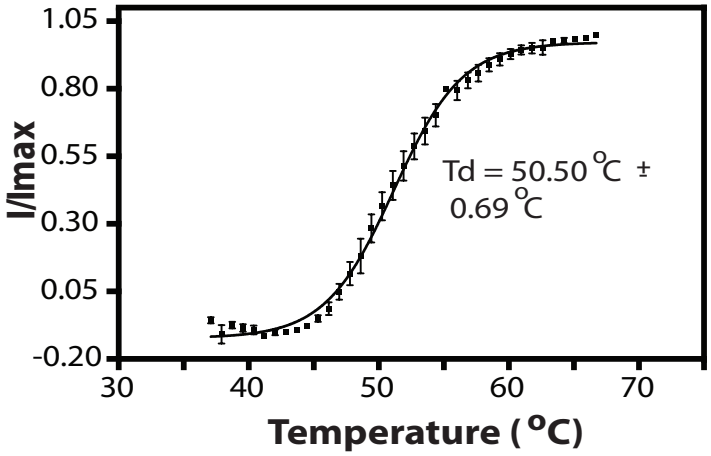
1.05
0.80
0.55
0.30
0.05
-0.20
I/Imax
Td = 50.50 °C ±
0.69 °C
30
40
50
60
70
Temperature (°C)

extent of peptide hydrogen-to-deuterium exchange (145). The large decrease in intensity at 1545 cm^{-1} immediately after exposure to deuterium indicates that the majority of the amide protons have undergone N-^{1}H to N-^{2}H exchange. This is consistent with our previous work where the full length CfrA showed a high level of solvent accessibility (159). The thermal stability of the plug domain was also accessed. The plug domain undergoes thermal denaturation with 50% denaturation occurring at approximately 50°C (Figure 5.3C).

Preliminary 2D Heteronuclear Single Quantum Coherence (HSQC) NMR Spectrum. A preliminary 2D HSQC NMR spectrum was recorded from the purified ^{15}N-labeled plug domain. The spectrum shows approximately the expected number of peaks. The plug construct is composed of 151 amino acids. In a HSQC spectrum, a peak for each amino acid should be observed with the exception of proline (7 proline residues in the plug domain). I expect to see approximately 145 peaks. The peaks are dispersed along the ^{1}H ppm scale suggesting that the plug domain is folded. Unfortunately, detailed analysis of the spectra is difficult due to the coexistence of two states as determined by SDS-PAGE, NATIVE PAGE and gel filtration analysis (Figure 5.4).

Figure 5.4

Preliminary NMR spectra (^{1}H-^{15}N HSQC) of purified plug domain at 37°C. The wide dispersion of peaks indicate a folded structure; however, the presence of two states complicates the acquisition of NMR data for structure determination. The red circles highlight regions associated with folded proteins. The blue square show the peaks associated with glycine residues. The green square show peaks associated with the side chains of glutamine and asparagine.

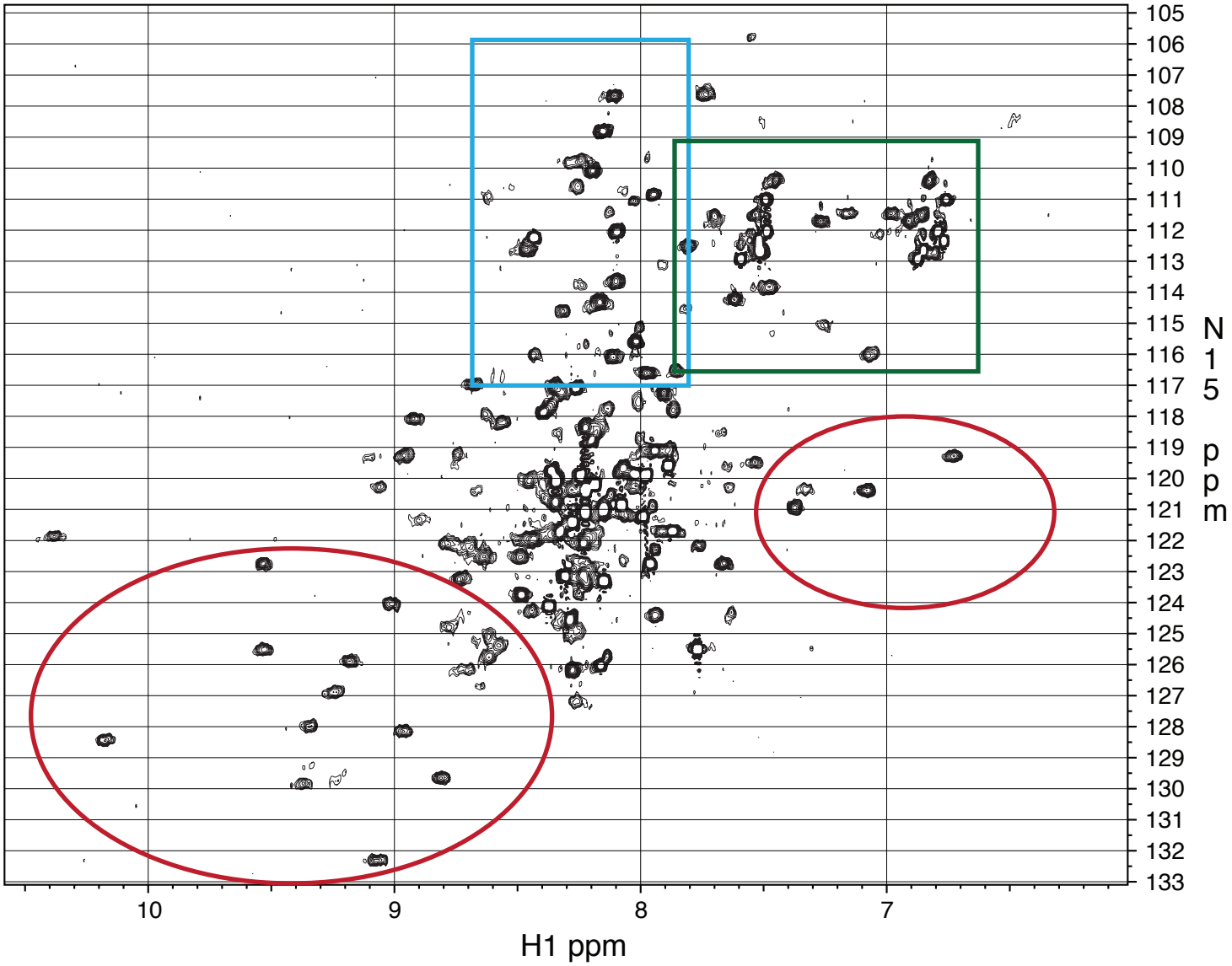
105
106
107
108
109
110
111
112
113
114
115
116
117
118
119
120
121
122
123
124
125
126
127
128
129
130
131
132
133
N
1
5
p
p
m
10
9
8
7
H1 ppm

5.4 Discussion

Substantial progress has been made towards my goals of characterizing the structure and dynamics of the isolated plug domain to gain insight into the mechanism of ferric-enterobactin transport through TBDT. The isolated plug domain maintains structural integrity and exhibits a mixed αβ structure consistent with prediction based on homology modeling and previously published characterization of the isolated plug domain from TpbA (109,159). The isolated plug domain has a thermal denaturation temperature of approximately 50°C. Boiling temperatures were required for effective denaturation of the full length CfrA. The substantially lower thermal denaturation temperature of the plug domain is consistent with what is known regarding the stability of β-barrel proteins as the majority of β-barrel stability is governed by the hydrogen bonding between the β-strands (40). In contrast, the expression and purification of the FepA plug domain resulted in the very little secondary structural elements that underwent little to no change by circular dichroism upon increasing temperatures (83). Perhaps, the plug domain of FepA aggregated during the purification process due to areas of increased hydrophobic content (see below). The rapid and complete ^{1}H-^{2}H exchange of the plug domain was unexpected. It is known that soluble proteins require denaturation followed by refolding to fully complete the ^{1}H-^{2}H exchange (145). For comparison, myoglobin, a soluble protein of comparable size, does not undergo complete solvent exchange after immediate or prolonged exposure to $^{2}H_2O$ (176). This phenomenon further supports a highly dynamic structure for the isolated plug domain.

Sufficient ^{15}N-labelled plug domain was produced for NMR experiments. The 2D HSQC spectra shows roughly the number of peaks expected for the plug domain. These are well dispersed along the ^{1}H ppm scale suggesting a folded structure. Unfortunately, the coexistence of two states after the purification protocol complicates the acquisition of 2D HSQC spectra. Due to time constraints, I was unable to continue with this project. To move forward towards the acquisition of experimental data regarding the dynamics of the plug domain, the coexistence of the two states of the plug domain must be eliminated. Another group made the observation that the FepA plug domain purified larger then expected (83). Both plug domains from FepA and the homology model of the CfrA plug domain have a high percentage of hydrophobic amino acids (~30% and 40% respectively). A number of hydrophobic residues are present on the mixed β-strand that forms the "floor" of the plug domain and clearly occludes the transport of large metabolites from the extracellular solution into the periplasm (Figure 5.5). Two monomers of either protein could easily dimerize at this interface. There is also an additional potential dimerization interface on the plug domain of CfrA due to the presence of hydrophobic residues located between substrate binding loop 1 and a substrate binding loop 2. To circumvent the oligomerization, I would start with various mutants eliminating hydrophobic residues on the mixed β-sheet and ideally this may elevate the oligomerization of the plug domain.

The ability of the plug domain to fold independently of the barrel, exist as a distinct domain, bind ligand, even though predominantly unfolded, at an affinity about 100 fold less than the full length protein, and refold after denaturation supports the hypothesis by which the plug domain partially unfolds from the interior of the barrel to allow transport of the ferric siderophore (83,108). I would even speculate partial rearrangement/unfolding is required to

Figure 5.5

Surface representation of the plug domains from **(A)** FepA (1FEP) (153) and **(B)** the homology model of CfrA indicating hydrophobic residues in blue. Both structures possess a concentration of hydrophobic amino acids on the mixed β-sheet. The homology model of the plug domain for CfrA indicates another location of a hydrophobic residue cluster between substrate binding loop 1 and 2 indicated by the red circle.

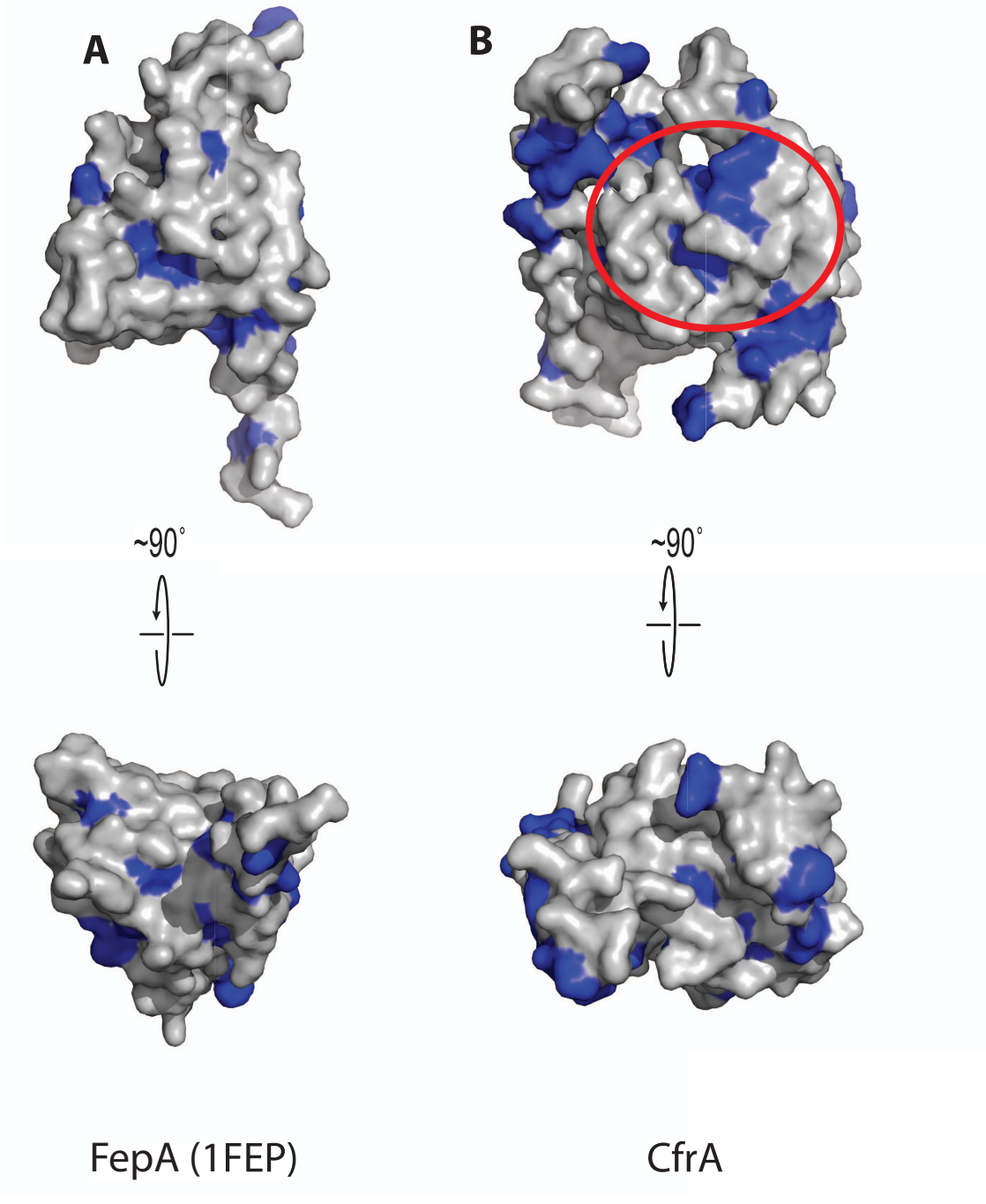
A
B
~90°
~90°
FepA (1FEP)
CfrA

lower the affinity for the ligand facilitating the transfer of the ligand to the periplasmic binding protein. This is supported by affinity measurements. FepA has a 0.1nM affinity for ferric-enterobactin (81). The isolated plug has been shown to possess an affinity of approximately 100 fold less than the full length protein thus approximately 10 nM (83). The periplasmic protein responsible for transporting ferric-enterobactin from FepA to the ATP binding cassette, FepB, has been shown to have an affinity for ferric-enterobactin of 35nM (177). Therefore, in order for the plug domain to release the ferric-siderophore, some form of conformational change must happen. The unfolding of the plug domain seems likely as reconstitution of FhuA into planar lipid bilayers results in ion conduction in the presence of 4M urea with ion conduction inhibition when the 4 M urea is subsequently removed suggesting some form of unfolding to allow an ion conduction pathway (178). Taken together, the data supports a mechanism by which the plug is partially or completely unfolded out of the barrel.

PART II

6 THE ROLE OF INTRAMEMBRANE AROMATICS IN PENTAMERIC LIGAND GATED ION CHANNEL LIPID SENSING

The human brain is the location for information consolidation and thought processes. The ability to observe, play and learn stem from the intricate cellular communication within the brain. Neuronal communication is essential for consciousness and for life as we know it. Pentameric ligand-gated ion channels (pLGIC) are membrane proteins involved in fast chemical communication between cells in the central nervous system and at neuromuscular junctions. pLGICs are associated with various neurological disorders, such as schizophrenia, epilepsy and Alzheimer's disease, and are prominent targets for numerous pharmaceuticals (3). pLGICs also play a role in addiction, sedation, anxiety and cognitive disorders (179). Even subtle changes in pLGIC activity have profound effects on human biology (180). Understanding pLGICs thus has important biological and pharmacological consequences (181).

6.1 Electrical Excitability

The brain is composed of a vast number of cells called neurons, which are the building blocks responsible for the processing and transmission of electrical information. A typical neuron is composed of five functionally distinct regions. The dendrites are responsible for receiving information from the environment and delivering the information to the soma. The soma is the central cell body where the electrical information received from the dendrites is combined and passed along to the axon hillock. The axon hillock, with sufficient stimuli, is responsible for firing of the action potential. The axon hillock leads into the axon, an elongated fibre, that transmits the action potential to the axon terminus. The axon endings are then responsible for the transmission of information to the adjacent neuron (Figure 6.1).

The transmission of information both between and within neurons is highly dependent on the action of transmembrane ion channels, which ultimately influence membrane potential. The

Figure 6.1

Schematic diagram of a typical neuron showing the location of the dendrites, soma, axon hillock, axon and axon endings.

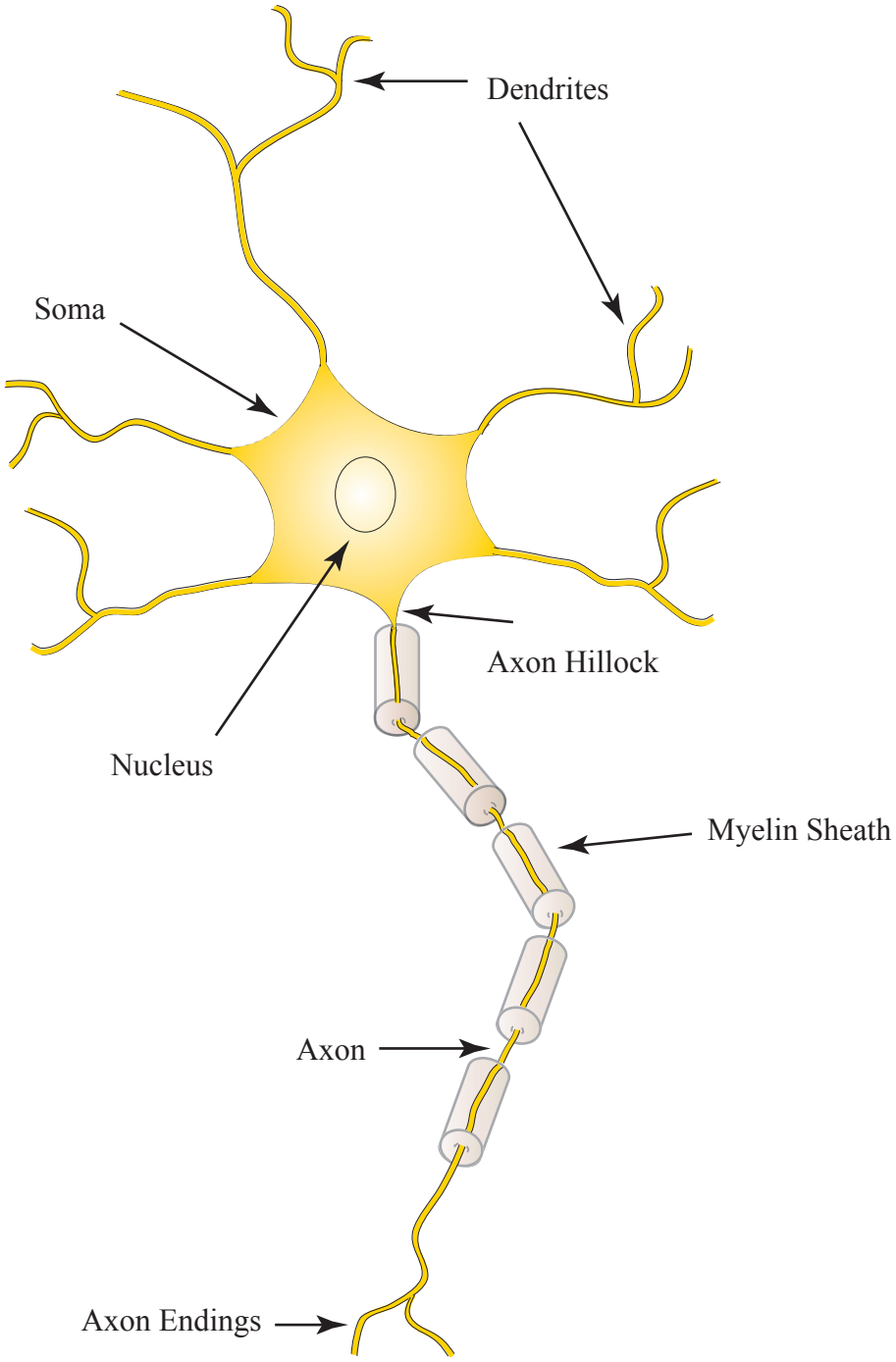
Dendrites
Soma
Axon Hillock
Nucleus
Myelin Sheath
Axon
Axon Endings

resting membrane potential results from an imbalance of electrical charge across the membrane. The imbalance of charge is maintained by the activity of three transmembrane proteins: the Na^+-K^+ pump and both the Na^+ and K^+ leak channels. The Na^+-K^+ pump uses ATP hydrolysis to actively drive 3 Na^+ ions out of the cell and 2 K^+ ions into the cell to generate a large concentration gradient of both ions across the membrane. Cell membranes are more permeable to K^+ ions than to Na^+ ions, as there are more K^+ leak channels than Na^+ leak channels. The K^+ ions diffuse down their concentration gradient through the K^+ leak channels. The net efflux of K^+ ions causes the interior of the neuron to become more negative, thus counterbalancing the driving force for K^+ efflux. Na^+ ions also diffuse down their concentration gradient via the Na^+ leak channel into the cell; however, the import of Na^+ ions is typically matched by the export of Na^+ ions by the Na^+-K^+ pump. The net balance of ions across the membrane gives a neuron a resting membrane potential of approximately -70mV.

6.2 Transmission of electrical signals

Neurons receive information through the reception of chemical or physical stimuli at the dentrites, triggering the influx of either cations or anions into the cell, as discussed in more detail below. An influx of cations increases the membrane potential generating an excitatory depolarizing current; whereas, an influx of anions decreases the membrane potential leading to an inhibitory, hyperpolarizing current. The strength of the depolarizing or hyperpolarizing current is directly proportional to the intensity and frequency of the stimulus. A single neuron may receive both excitatory and inhibitory inputs simultaneously. Currents initiated at different sites within the dendrite combine as they travel along the membrane to the axon hillock. If the summation of the excitatory and inhibitory inputs result in a membrane

potential of -55 mV, the threshold point, voltage-gated Na^+ channels open, initiating an action potential - a transient membrane depolarization. The influx of Na^+ ions, which diffuse along the axon results in successive membrane depolarizations, thus propogating the electric signal along the length of the axon. When the action potential reaches the axon terminal, the resulting depolarization leads to the activation of voltage-gated Ca^{2+} channels, resulting in an influx of Ca^{2+} ions increasing the intracellular Ca^{2+} ion concentration. This stimulates the fusion of neurotransmitter-loaded vesicles with the presynaptic membrane and the subsequent release of neurotransmitter into the synaptic cleft (the interface between the two neurons).

6.3 Synaptic communication

Neurotransmitters released from a presynaptic membrane diffuse across the synaptic cleft and bind to neurotransmitter receptors located on the postsynaptic neuron. There are two fundamental types of neurotransmitter receptors: ionotropic and metabotropic receptors.

Ionotropic receptors are transmembrane proteins that form ligand-gated ion channels. These receptors act directly on neuronal membrane potential. Binding of neurotransmitter to a ligand gated ion channel induces a conformation change within the protein resulting in the opening of the ion channel. The rapid influx of ions causes a local depolarization/hyperpolarization of the membrane, initiating the transmission of the electrical signal in the post synaptic neuron thus continuing the conduction of information (Figure 6.2) (182).

Metabotropic receptors are transmembrane receptors that act indirectly through the activation of a secondary messenger. For example, binding of agonist to a G-protein coupled receptor, a metabotropic receptor, induces a conformational change in the receptor, initiating the

Figure 6.2

A simplified view of neurotransmission. The steps involved in communicating an action potential from one neuron to another (or to a muscle cell) via a chemical intermediate are labeled and outlined in the figure and text.

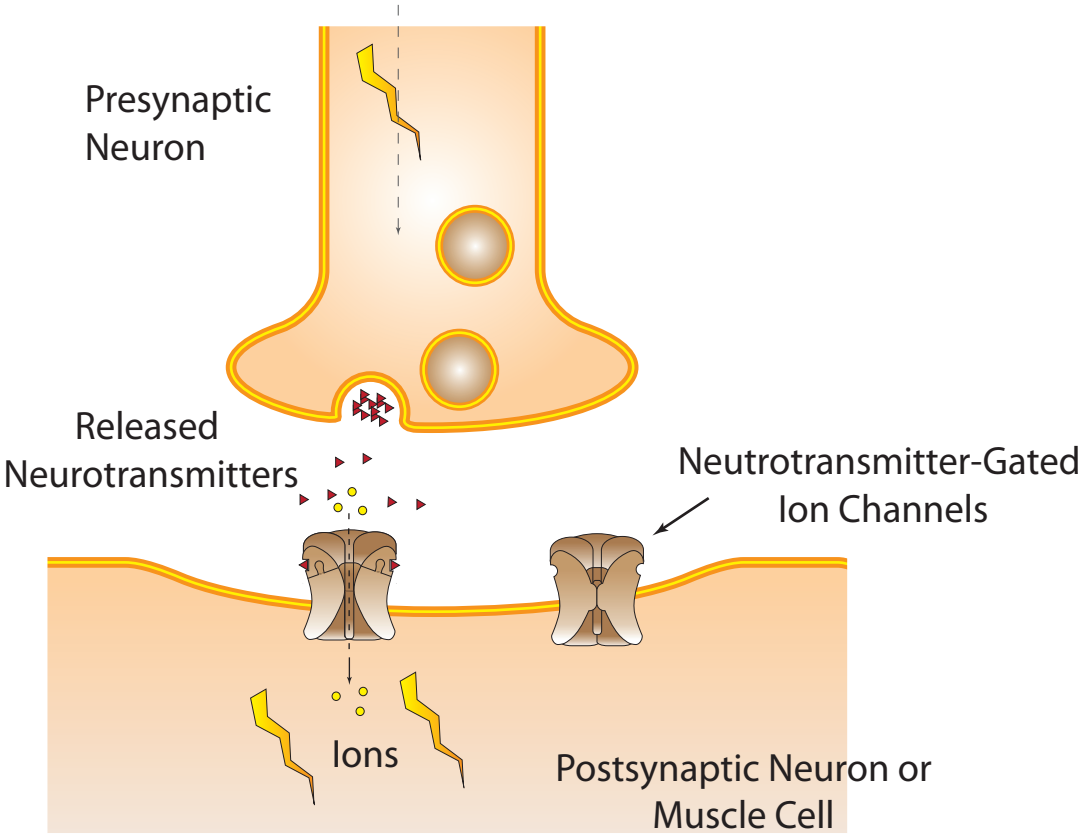
Presynaptic
Neuron
Released
Neurotransmitters
Neutrotransmitter-Gated
Ion Channels
Ions
Postsynaptic Neuron or
Muscle Cell

release of activated G proteins. The G proteins then bind to ion channels influencing their activity thus modulating neuronal membrane potential (183).

The complex relationship between excitatory/inhibitory input and ionotropic and metabotropic receptors presents various means to modulate the strength of a synaptic response. Synaptic communication, neurotransmitter, and neurotransmitter receptors are of increasing interest as evidence suggests a prominent role in neuroplasticity and neurodegenerative diseases (184-186). Synapses are known to decrease in number during neurodegenerative diseases. Increased understanding of synaptic communication may thus shed light on alternative approaches to treating neurodegenerative diseases (187).

6.4 Pentameric Ligand Gated Ion Channels

The second part of my thesis research focused on the superfamily of pentameric ligand gated ion channels (pLGICs), which, as noted, are central to fast synaptic communication. There are two main types of pLGICs based on ion selectivity. The cation selective excitatory channels include the nicotinic acetylcholine (nAChR), the serotonin ($5HT_3R$) and the zinc (ZAC) receptors, while the anionic inhibitory selective channels include the γ-aminobutyric acid ($GABA_A$ and $GABA_{A-\rho}$) and the glycine receptor (GlyR). Both excitatory and inhibitory pLGICs assemble from multiple subunits into homopentamers or heteropentamers. For example, neuronal nicotinic nAChRs form from different combinations of α-subunits (α2 – α10) and non-alpha subunits (β2-β4). The combination of several different subunits and the capacity to form heteropentamers provides a wealth of structural and functional diversity (188).

6.5 The Prototypic Member of the pLGICs

The prototypic pLGIC, the nicotinic acetylcholine receptor (nAChR) from *Torpedo,* is a 270 kDa transmembrane protein formed from four homologous subunits arranged in an $\alpha_2\beta\gamma\delta$ stoichiometry. The *Torpedo* nAChR is homologous to both human muscle type and neuronal nAChRs. Due to both its homology and high natural abundance, the *Torpedo* nAChR has been studied extensively and will be a prominent focus of this introduction on pLGICs (188). The nAChR exists in a conformational equilibrium between an agonist responsive resting state and an agonist unresponsive desensitized state. Binding of agonist to the resting state induces a conformation change in the receptor to an open state allowing the flow of cations through the ion channel. Prolonged exposure to agonist induces a conformational change to a desensitized state where the receptor binds agonist but no longer conducts ions.

In 2005, a refined model of the nAChR structure at 4 Å was solved by cryo-electron microscopy (cyro-EM) (Figure 6.3A) (189). The cyro-EM structure shows that the 5 subunits ($\alpha_2\beta\gamma\delta$) arrange pseudo-symmetrically around the central pore forming the ion channel. Each subunit includes an N-terminal extracellular domain (ECD) consisting of an N-terminal α-helix followed by a β-sandwich formed from 10 β-strands (β1-β10), 4 transmembrane α-helices (M1-M4), and a cytoplasmic domain (CD). The transmembrane (TM) α-helices from the 5 subunits arranged concentrically with M2 from each subunit lining the pore, M1 and M3 shielding M2 from the lipid environment, and M4 in direct contact with the lipid environment (Figure 6.3B) (190). The agonist binding site is situated in the ECD at the interface between α and δ and α and γ subunits, while the ion channel resides approximately 50 Å away in the transmembrane domain (TMD) (189). The permeation pathway is occluded by a constriction near the center of the bilayer formed by

Figure 6.3

The 4Å cyro-electronmicroscopy structure of the nAChR from *Torpedo Californica* (2BG9*)* (189). **(A)** The nAChR structure in the plane of the membrane. Colored to highlight the functional agonist binding (red), transmembrane gating (blue), and cytoplasmic (green) domains. **(B)** The TM helices of the nAChR shown from the extracellular solution illustrating the circular arrangement with M2 lining pore, M3 and M1 shielding M2 from the lipid environment and M4 in direct contact with the lipid environment. Side chains of residues forming part of the channel gate (αL251 and αV255, as well as analogous β-,γ-, and δ-subunit residues) are shown in yellow spheres.

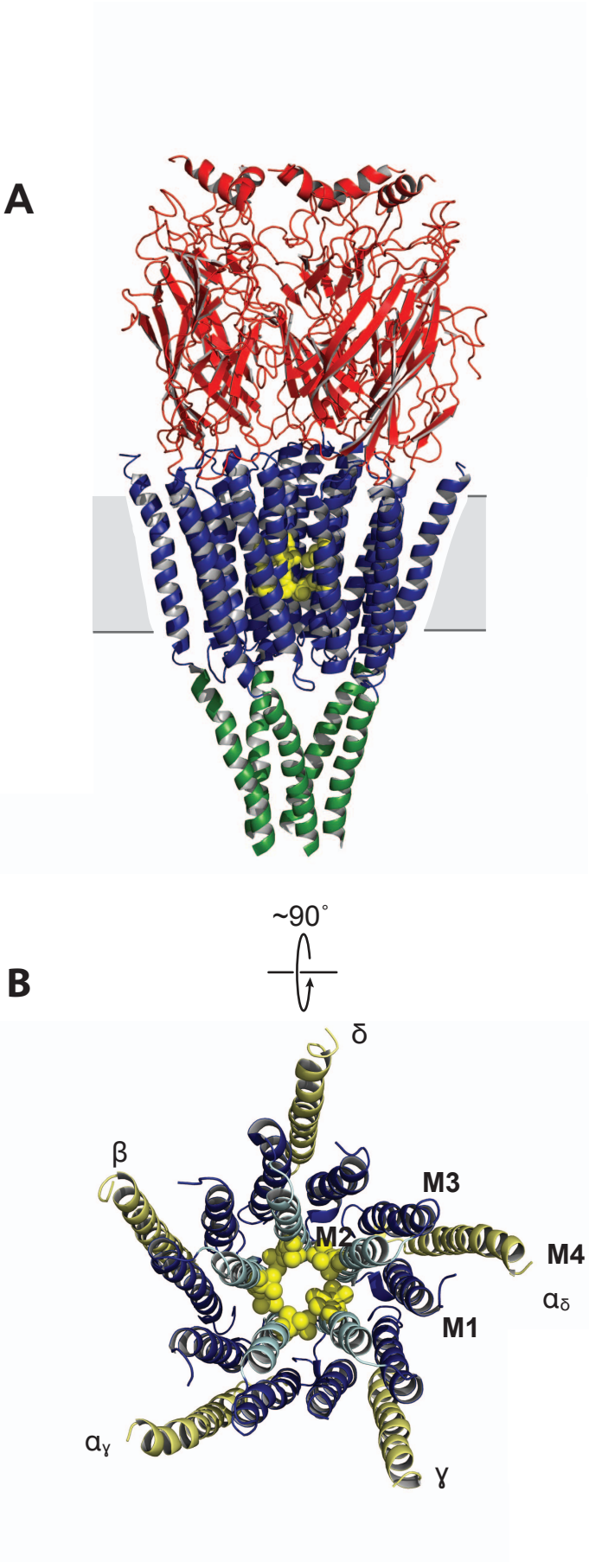
A
~90°
B
δ
β
M3
M2
M4
αδ
M1
αγ
γ

hydrophobic residues (αL251 (9'), αV255(13')), and analogous residues on the adjacent subunits. This constriction is too narrow (6 Å) to allow the flow of hydrated ions (8 Å), and too hydrophobic to compensate for the loss of the hydration shell surrounding the positive ion (191,192). How agonist binding leads to channel gating is still a matter of speculation.

6.6 pLGIC Agonist Binding

Knowledge regarding agonist binding to the nAChR was originally obtained from crystals structures of the acetylcholine binding protein (AChBP), a homolog of the nAChR agonist binding domain (193,194). The homo-pentameric AChBP is present at the synaptic cleft of mollusks, and acts to modulate the synaptic response by sequestering acetylcholine (193). The AChBP subunits exhibit the highest degree of homology with the nAChR α7 and α9 subunits (194,195). Each subunit of the AChBP includes a short N-terminal α-helix followed by a β-sandwich formed from 10 β-strands (β1-β10), similar to the ABD of the nAChR (194). Residues in the AChBP that are involved in agonist binding are conserved across the nAChR family (193). Three orthologs have been studied extensively and have been shown to bind known AChR agonists (carbamylcholine, acetylcholine, nicotine, and epibatidine) and antagonists (the conotoxin ImI, methyllycaconitine, and α-bungarotoxin) (193,196-198). The significant homology and similar pharmacological profiles of AChBP with the nAChR has lead to the use of the AChBP to determine the molecular determinants of agonist binding in the nAChR.

The binding site is located at the interface between subunits with contributing residues from both subunits, designated the principal and complementary subunits. The principal subunit contributes residues from loops A, B, and C (grey in Figure 6.4) while the complementary subunit contributes residues from loops D, E, and F (taupe in Figure 6.4B). Conserved

Figure 6.4

Agonist Binding to the AChBP. **(A)** Cartoon representation of the AChBP with (1UV6) (197) and without agonist (2BYQ) (196) showing the large movement of the C-loop upon agonist binding. The N-terminal of AChBP and the agonist are not shown for clarity. **(B)** Agonist binding site for the AChBP showing key residues from the principal subunit (grey) in purple (W143, Y89, Y192 and Y185) and key residues from the complementary subunit (taupe) in teal (W53, M114, and L112).

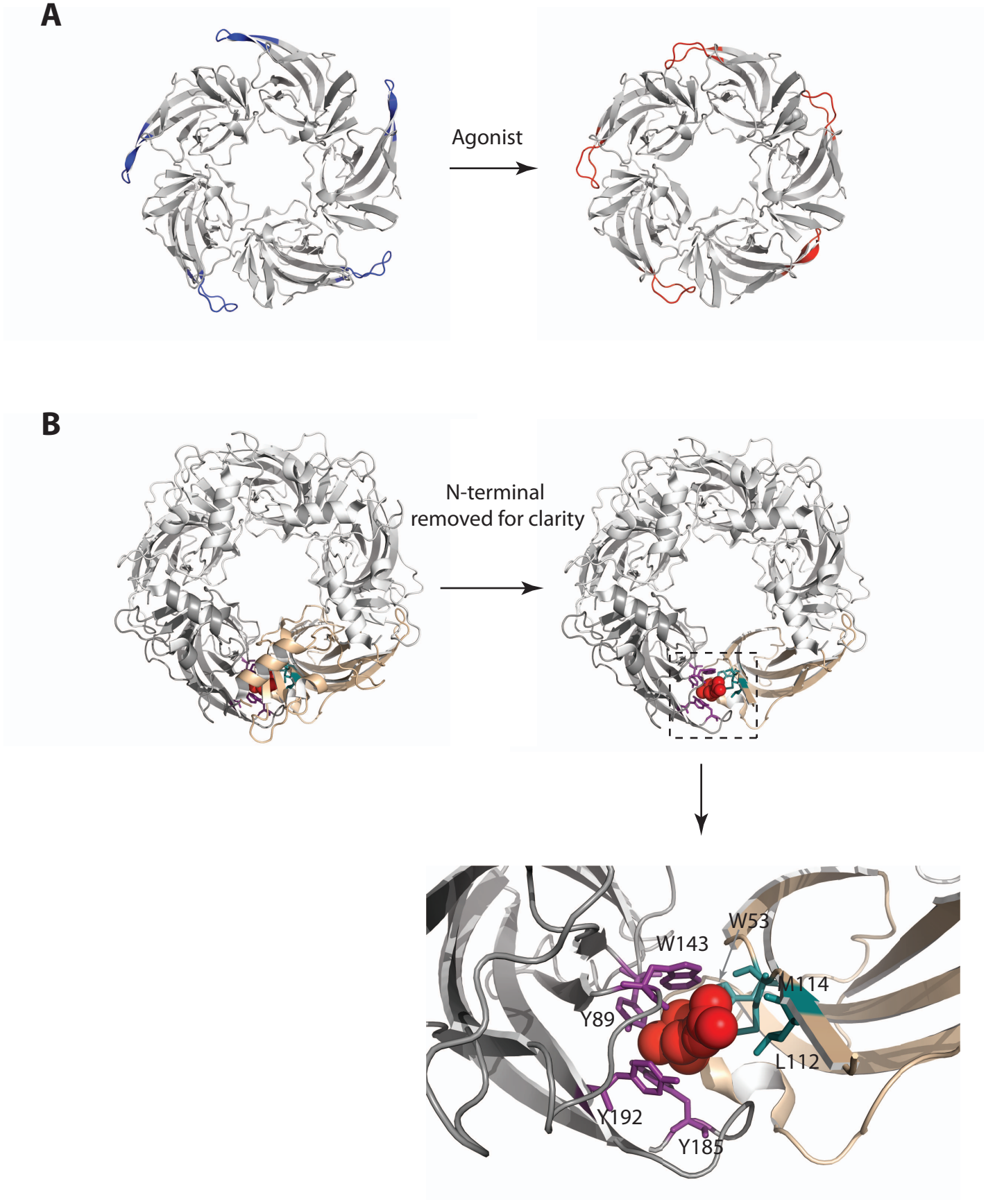
A
Agonist
B
N-terminal
removed for clarity
W53
W143
M114
Y89
L112
Y192
Y185

aromatic residues on loops A (Y89), B (W143) and C (Y185 and Y192) on the principal subunit form an "aromatic box" around the charged amine of the bound agonist contributing cation-π interactions (Figure 6.4B; residue numbering corresponds to *Lymnaea stagnalis* AChBP) (191). The complementary side contributes additional aromatic contacts through Trp53 (loop D) and hydrophobic contacts through Leu112 and Met114 (both loop E). The participating residues from the complementary subunit vary between orthologs accounting for AChBP ortholog specific binding affinities (193).

In the unbound state, loop C of the principal subunit extends away from the protein allowing agonist access to the binding site. In the agonist bound state, loop C transitions approximately 7 Å towards the channel pore effectively capping the binding site and burying the bound agonist (Figure 6.4A) (191,196,197). Interestingly, loop C is further removed from protein forming a bigger cavity in the antagonist bound state. In total, loop C has the ability to move approximately 11 Å in order to facilitate binding (191).

6.7 Coupling Binding to Gating

As noted, agonist binding leads to a conformation change in the C-loop which in turn leads to gating of the ion channel located in the TMD approximately 50 Å away (189). Transmission of signal demands the involvement of the interface between the two distinct domains: the ECD and TMD (199). Studies of pLGIC chimeras show that the complementarity at this interface is essential for efficient coupling of agonist binding to channel gating (199-201). Although a covalent interaction is present between the ECD (β10) and TMD (M1), contact between the ECD and the TMD is mediated primarily by non-covalent interaction between loops of the ECD (β1-β2, β6-β7 and β8-β9) and the M2/M3 linker of the TMD (Figure 6.5) (189). In the nAChR structure, αArg 209 located on pre-M1

Figure 6.5

The interface between the agonist binding and transmembrane domains. A single subunit of the nACHR (2BG9) viewed from the plane of the membrane, highlighting the coupling interface (dashed box) and the "vice"-like interactions of both the β1-β2 loop and β6-β7 loop with the M2-M3 linker . Post-M4 is colored orange. B6-β7 loop is colored green (residues αV132 and αF135 are represented as spheres). β1-β2 loop is colored blue (residues αE35 and αV46 are represented as spheres). M2-M3 linker is colored purple (αP272 is represented as spheres).

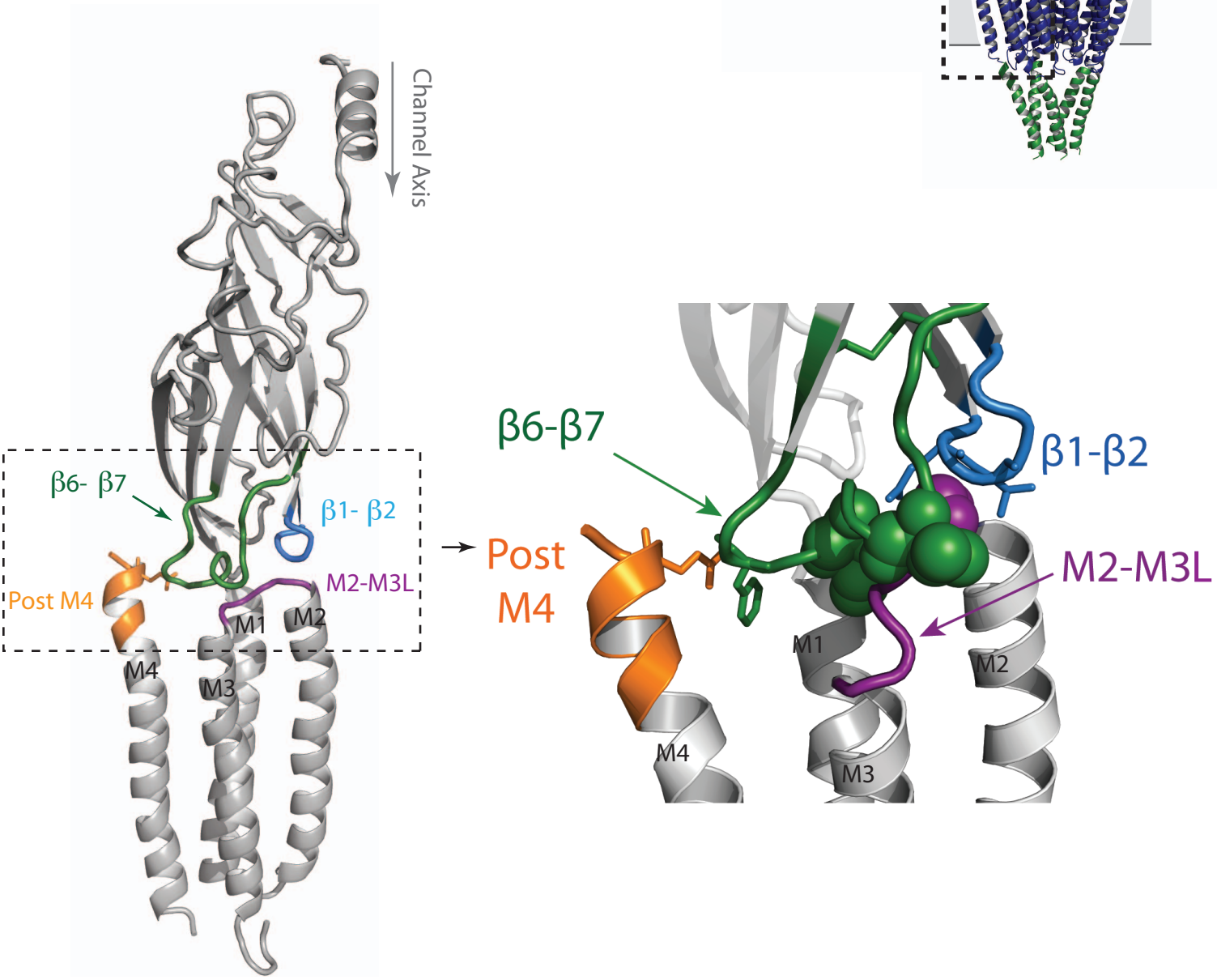
Channel Axis
β6- β7
β1- β2
Post M4
M2-M3L
M1
M2
M4
M3
β6-β7
β1-β2
Post
M4
M2-M3L
M1
M2
M4
M3

(amino acids bridging β10 and M1) extends into the hydrophobic interior of the ECD to form a salt bridge with αGlu45 on the β1-β2 loop. This electrostatic interaction allows the positioning of adjacent αVal46 with αGlu45 to form an inverted "V" surrounding αPro272 situated on the M2-M3 linker. Residues from the β6-β7 (αV132 and αF135) also form an inverted "Y" further securing the position of the M2-M3 linker (191). The formation of a clamp-like structure from residues αVal46, αGlu45, αV132, and αF135 of the ECD essentially clamping the M2-M3 linker in a specific position likely influencing the orientation of the M2 pore upon agonist binding.

Upon agonist binding, the C-loop sequesters the agonist likely causing a displacement of β10 and thus αArg209. Through the electrostatic interaction between αArg209 and αGlu45, the β1-β2 loop would be pulled in the direction of the agonist binding site (Figure 6.6). The positioning of αGlu45 and αVal46 of the β1-β2 loop as a "V" surrounding the M2-M3 linker would likely influence the positioning in the M2-M3 linker eliciting a change of orientation of the pore lining M2 α-helices leading to gating (188). Although recent cryo-EM structures of the closed and open state of the nAChR has led to the proposal that the β-subunit is responsible for communicating agonist binding to the pore, mutagenesis studies data suggest that the α-subunit is primarily responsible for the transmission of the signal (202).

6.8 The Uncoupled nAChR

nAChR function is extremely sensitive to its lipid environment (203-209). When placed in phosphatidylcholine membranes containing cholesterol and anionic lipids, the nAChR gates open in response to agonist binding. In the absence of these activating lipids, the nAChR adopts an uncoupled conformation where agonist binding does not induce channel gating (Figure 6.7) (209). Note that functionally uncoupled neuronal nAChRs have been observed

Figure 6.6

The interface between the agonist binding and transmembrane domains illustrating a mechanism by which agonist binding may lead to channel gating. Upon agonist binding, the C-loop sequesters the agonist likely displacing β10. The displacement of β10 pulls β1-β2 through the interaction between R209 (red sticks) and E45 (blue sticks). The displacement of β1-β2 likely influences the positioning of the M2-M3 linker via "vice"-like interactions thus eliciting a change in the pore lining M2 α-helices leading to gating.

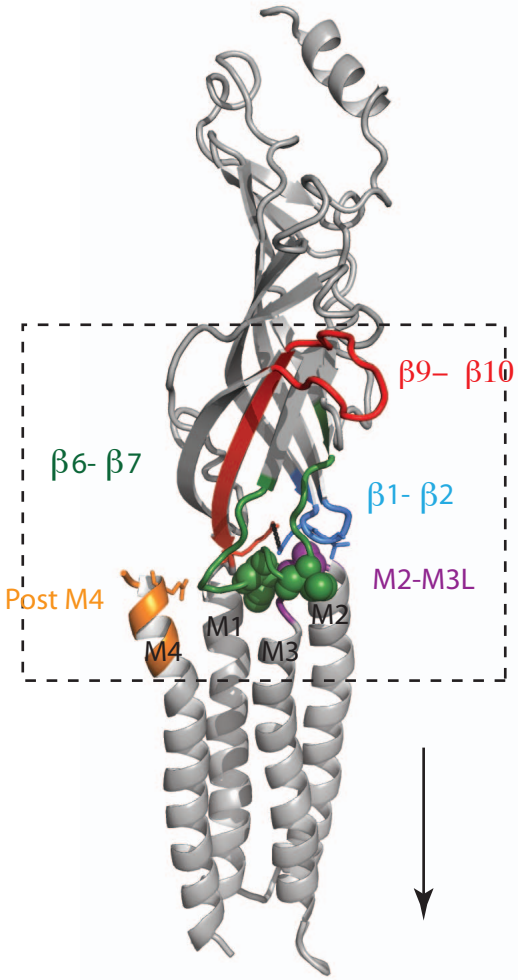
β9– β10
β6- β7
β1- β2
M2-M3L
Post M4
M1
M2
M4
M3


Agonist
Binding Site
1
C-loop closes over bound
agonist likely displacing β10
2
Displacement of β10 pulls β1-β2
through interactions between
R209 and E45
3
The displacement of β1-β2 likely
influences the positioning of the M2-M3 linker
via the "vice" like interactions thus eliciting a
change in the pore lining M2 α-helices
leading to gating
M4
M1
M2
M3

Figure 6.7

The conformational equilibrium of the nAChR. Binding of agonist to the resting state (R) induces a conformational change in the receptor to the open state (O). Prolonged exposure to agonist induces a conformational change to a desensitized state (D) where the receptor no longer responds to agonist. An uncoupled state (U) has recently been identified. In the uncoupled state, agonist binding does not lead to channel gating.

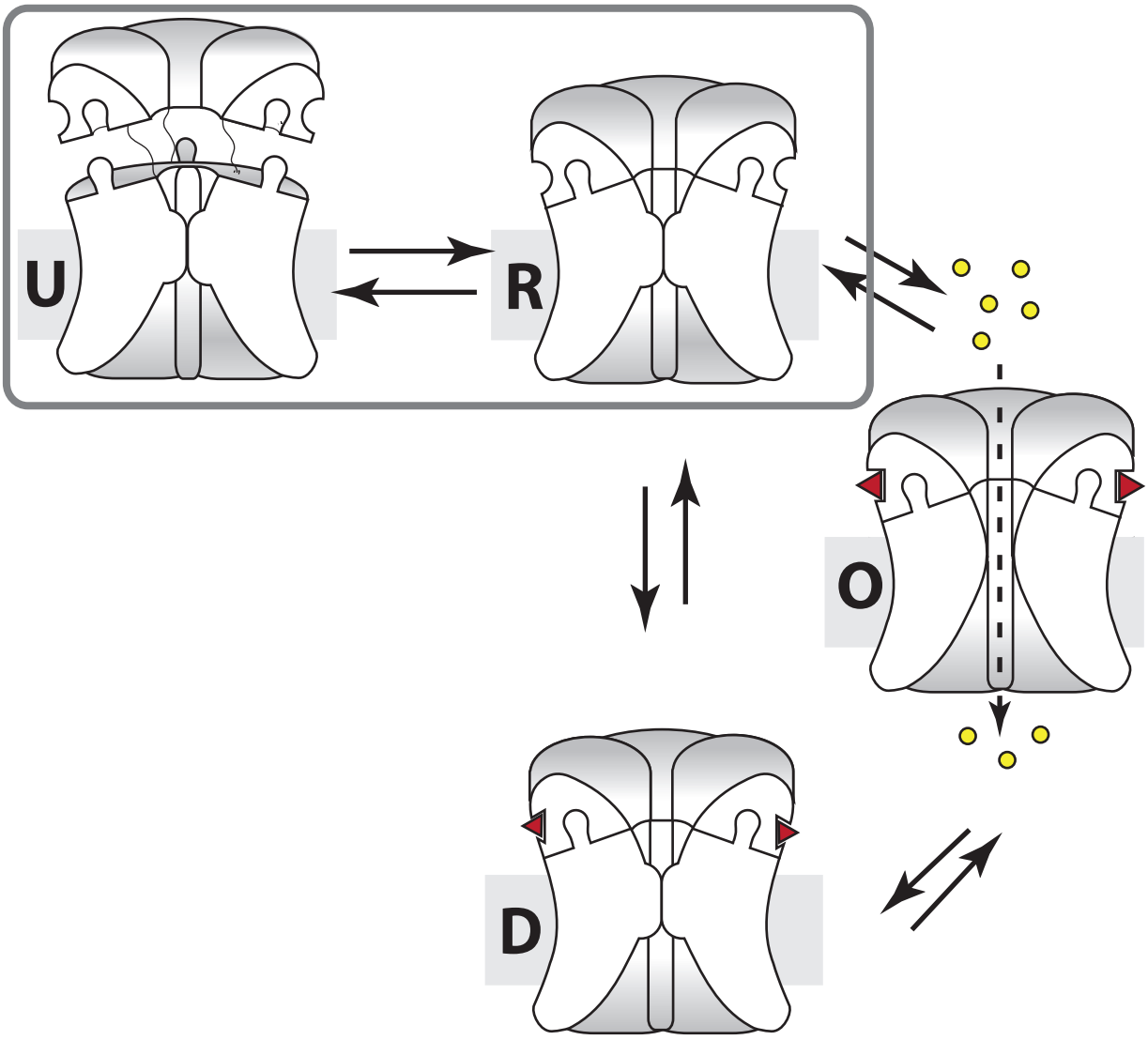
U
R
O
D

in heterologous expression systems, suggesting that uncoupling may be a characteristic feature of all pLGICs (210,211). Uncoupled nAChRs could represent a pool of non-functional receptors that can be awakened to potentiate synaptic communication. In fact, uncoupled nAChRs are able to transition to agonist-responsive "coupled" conformations in membranes with relatively thick hydrophobic cores, such as those found in lipid rafts (212). As even subtle changes in the pLGIC response can have dramatic effects on synaptic communication, transitions from uncoupled to coupled conformations could play an important role in pLGIC biology.

The uncoupled state of the nAChR is characterized by a resting state like binding affinity, but an inability to undergo agonist induced conformation change. The uncoupled nAChR also undergoes more extensive peptide N-^{1}H/N-^{2}H exchange, suggesting that regions of the protein that are buried from solvent in the resting or desensitized states, become solvent exposed in the uncoupled state (212).

The structure of the nAChR provides insight into the mechanism by which lipids influence coupling of binding and gating. The transmembrane helix M4 is the most lipid exposed transmembrane helix and is thus likely involved in translating the biophysical membrane properties to the altered protein conformation. Significantly, the C-terminal of M4 (post M4) extends beyond the bilayer to interact directly with the β6-β7 loop which, as noted, plays a key role in signal transduction. The post M4 - β6-β7 interaction may be responsible for positioning the β6-β7 loop to optimize interactions between the ECD and TMD. In the model of uncoupling, it has been proposed that the M4 disengages from the helical bundle of M1+M3 disturbing the interactions between the ECD and TMD thus causing the ECD to disengage from the TMD (Figure 6.8). On the other hand, a tight association between M4

Figure 6.8

A model of uncoupling. The model proposes that M4 disengages from the helical bundle of M1+M3 disturbing the interactions between the ECD and TMD thus causing the ECD to disengage from the TMD. A tight association between M4 and M1+M3 may promote effective interactions between post-M4 (orange) and the β6-β7 loop (green) leading to effective interactions ECD and TMD. PA – phosphatidic acid. Chol – cholesterol.

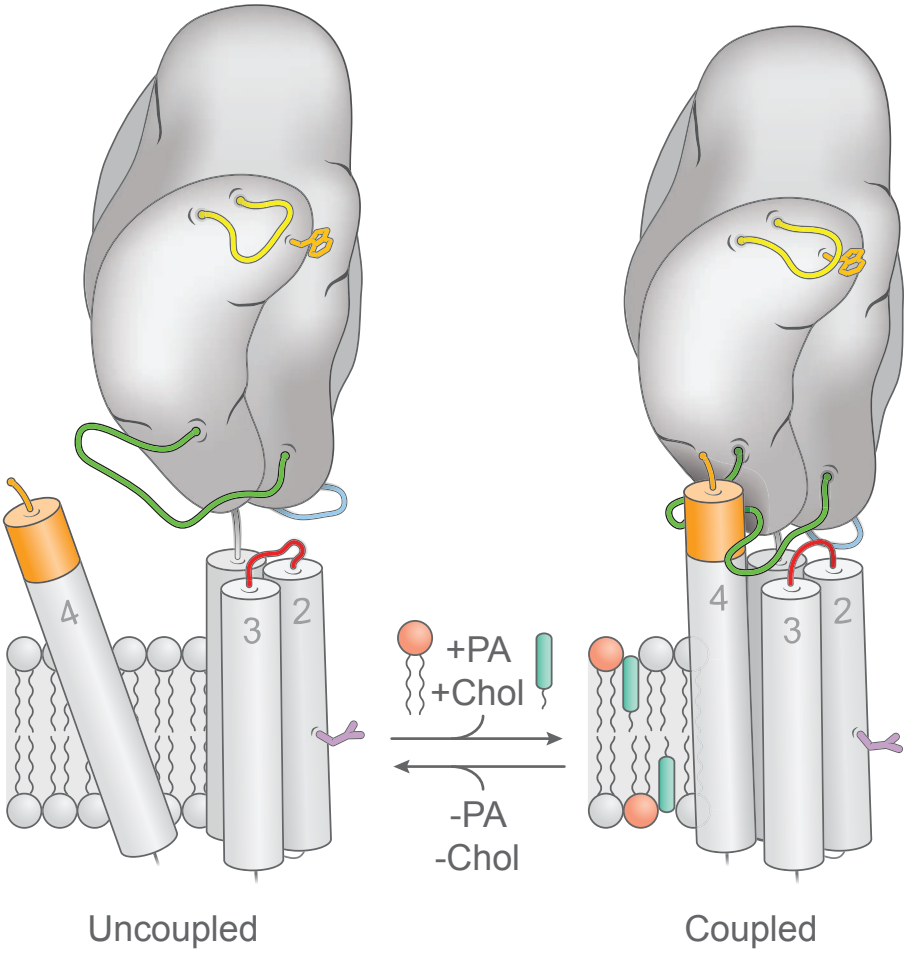
4
3
2
+PA
+Chol
-PA
-Chol
4
3
2
Uncoupled
Coupled

and M1+M3 may promote effective interactions between post-M4 and the β6-β7 loop leading to effective interactions between the ECD and TMD. Effectively, M4 may act as an allosteric modulator of nAChR function.

6.9 A potential role for intramembrane aromatics in uncoupling.

During heterologous expression in *Xenopus laevis* oocytes, the homologous glycine receptor (GlyR) is proteolytically cleaved within the cytoplasmic M3-M4 loop yielding two separate polypeptide fragments of 35 kDa (the ECD all the way to M3) and 13 kDa (M4). Despite proteolysis, the two fragments remain tightly associated in the GlyR pentamer leading to an agonist responsive pLGIC (213). Expression of the 35 kDa fragment alone led to a misfolded GlyR that accumulates as intracellular aggregates. Co-expression of both fragments, however, restores both pentamer assembly and function. Interestingly, the restoration of pentamer assembly and GlyR function was found to be highly dependent on the formation of aromatic-aromatic interactions at the interface between M4 and M1+M3. These experiments demonstrate that there is an equilibrium between M4 associated with M1+M3 and M4 solvated by lipid, consistent with the above model of uncoupling (214). This observation led to the hypothesis that intramembrane aromatic interactions at the M1/M3/M4 interface may influence M4 binding to M1+M3 in the folded state, and may thus influence the propensity of a pLGIC to adopt an uncoupled conformation.

6.10 Prokaryotic pLGICs

In 2005, several prokaryotic homologs of the nAChR were identified using sensitive sequence profile searches (215). Structures of two prokaryotic nAChR homologs, ELIC and GLIC, have subsequently been determined (Figure 6.9A) (216,217). ELIC is a pLGIC from *Erwinia chrysanthemi* that activates upon binding of primary amines, such as cysteamine

Figure 6.9

3D Structure and TMD aromatics in ELIC, GLIC, and the *Torpedo* nAChR**. (A)** 3D structures of ELIC (2VLO; left) (217), GLIC (3EHZ, center) (233) and the *Torpedo* nAChR (2BG9, right) colored to highlight the functional agonist binding (red), transmembrane gating (blue), and cytoplasmic (green) domains. **(B)** Structure of a single TMD from each pLGIC (α-subunit for the nAChR) highlighting differences in the coupling interface. Significantly, post-M4 of ELIC is absent in the crystal structure. In addition the β6-β7 and the β1-β2 loops only form weak interactions with the M2-M3 linker.

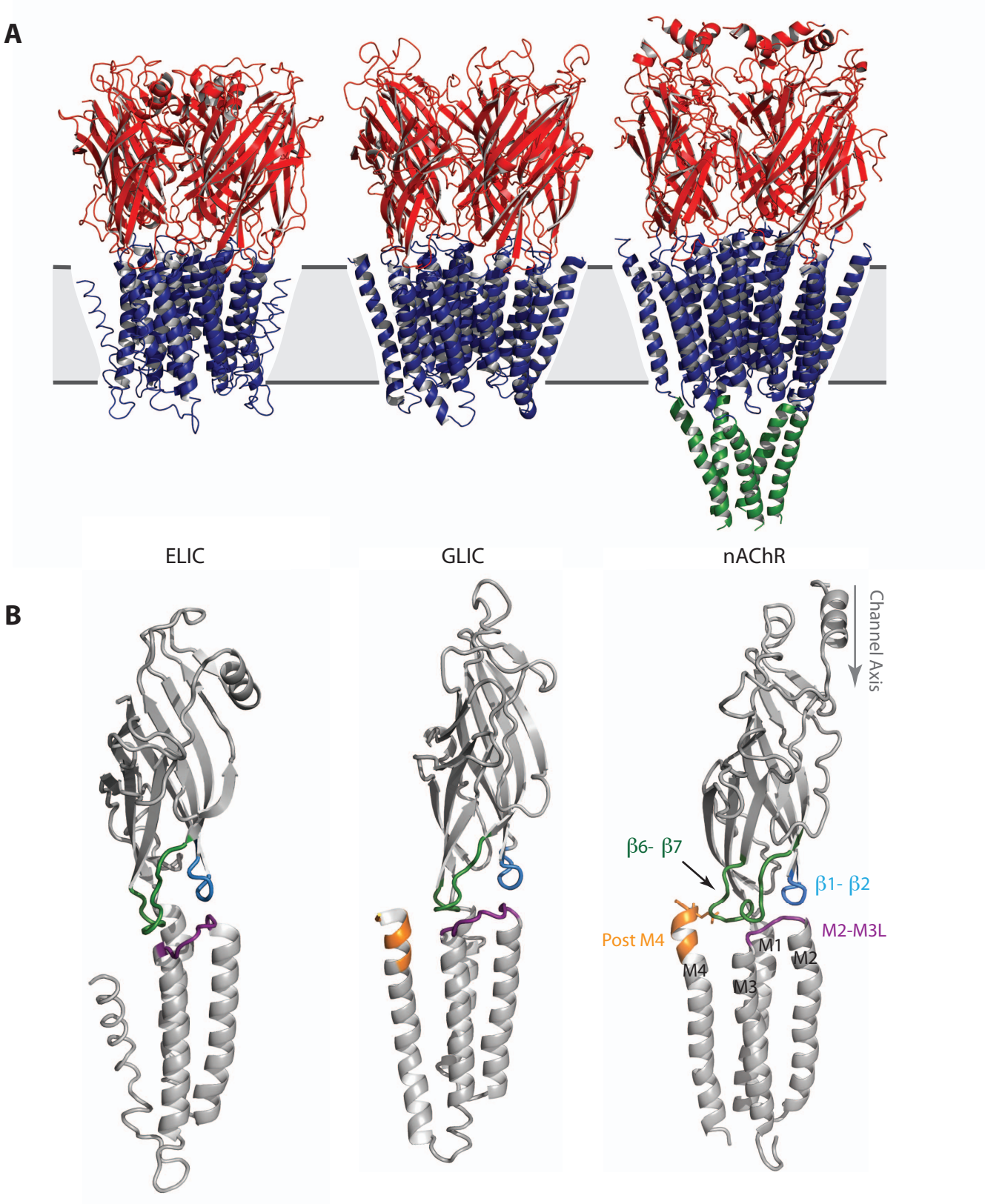
A
ELIC
GLIC
nAChR
B
Channel Axis
β6- β7
β1- β2
M2-M3L
Post M4
M1
M2
M4
M3

(218). GLIC is a pLGIC from *Gleobacter violaceus* that activates in response to the binding of protons (i.e. a decreases in extracellular pH) (219). The overall architecture of the prokaryotic pLGICs is strikingly similar to that of the nAChR (Figure 3.9A). Both ELIC and GLIC possess an N-terminal extracellular domain (ECD), consisting of a N-terminal α-helix followed by a β-sandwich formed from 10 β-strands (β1-β10), and 4 transmembrane α-helices (M1-M4) (216,217). One marked difference between the prokaryotic homologs and the nAChR is the absence of the cytoplasmic domain in ELIC and GLIC.

There are, however, some surprising differences between the prokaryotic pLGIC structures and that of the nAChR. As noted in the nAChR structure, post M4 extends beyond the bilayer interacting with the β6-β7 loop facilitating tight association of M4 with the M1+M3. The β6-β7 and β1-β2 loops also form vice like interactions with the M2-M3 linker (191). In contrast, in ELIC M4 is displaced from the remaining helical bundle M1+M3 with no interactions between post-M4 and the β6-β7 loop. In fact, the post M4 of ELIC (RGTIL) is absent in the crystal structure suggesting a highly mobile structure. In addition, the β6-β7 and β1-β2 loops form only weak interactions with the M2-M3 linker (Figure 6.9B). These structural features are strikingly similar to the structural changes proposed for the uncoupled nAChR. It has been suggested that detergent-solubilization of ELIC leads to an uncoupled conformation (191). The latter interpretation is supported by a recent crystal structure of an ELIC mutant. Even though this mutant, when expressed in *Xenopus oocytes*, gates open in response to agonist binding and exhibits no propensity to desensitize, no change in pore diameter was observed upon agonist binding to the crystallized ELIC, suggesting that the crystallized structure corresponds to an uncoupled state (220).

Comparisons between the nAChR, GLIC and ELIC reveal a gradient of aromatic residues at

the interface between M4 and M1+M3 (Figure 6.10). The nAChR possesses the fewest aromatic interactions at the M1/M3/M4 interface, with ELIC and GLIC exhibiting an increasing number of intramembrane aromatic interactions. In light of the discovery that aromatic-aromatic interactions play a key role driving interactions between M4 and M1+M3, the model of uncoupling predicts that the nAChR would exhibit a greater propensity to adopt an uncoupled conformation than either GLIC or ELIC (214). Preliminary functional studies of membrane-reconstituted GLIC supports this interpretation (221). The nAChR, with very few aromatic interactions, adopts an uncoupled receptor in phosphatidylcholine (PC) membranes lacking anionic lipids and cholesterol. As noted, the uncoupled nAChR is characterized by inability to undergo agonist induced conformational change, and increased levels of peptide ^{1}H-^{2}H exchange relative to GLIC in control asolectin membranes. In contrast, GLIC, with an abundance of aromatic interactions, retains the ability to undergo agonist induced conformational change in PC membranes and exhibits no change in peptide ^{1}H-^{2}H exchange compared to GLIC in control membranes (221). As ELIC contains an intermediary amount of aromatics at the interface, we predict that ELIC will exhibit an intermediate propensity to adopt an uncoupled conformation. Comparing/contrasting their structural and functional sensitivities to lipids thus provides an opportunity to gain insight into the mechanisms by which lipids influence pLGIC function.

The goal of the work presented in this section was to test the hypothesis that intramembrane aromatics play a role in the coupling of binding and gating and thus ultimately in the lipid sensitivities of pLGIC. We predict that the reduced number of aromatic interactions at the interface between M4 and M1+M3 in ELIC should lead to an increased propensity to adopt an uncoupled conformation when compared to GLIC, and a decreased propensity to adopt an

Figure 6.10

Structure of a single TMD from nAChR (2BG9, left) (189), ELIC (2VLO; center) (217), GLIC (3EHZ, right) (233) and the *Torpedo* nAChR (α-subunit for the nAChR) (189) highlighting aromatic residues on M1, M3, and M4 as yellow sticks.

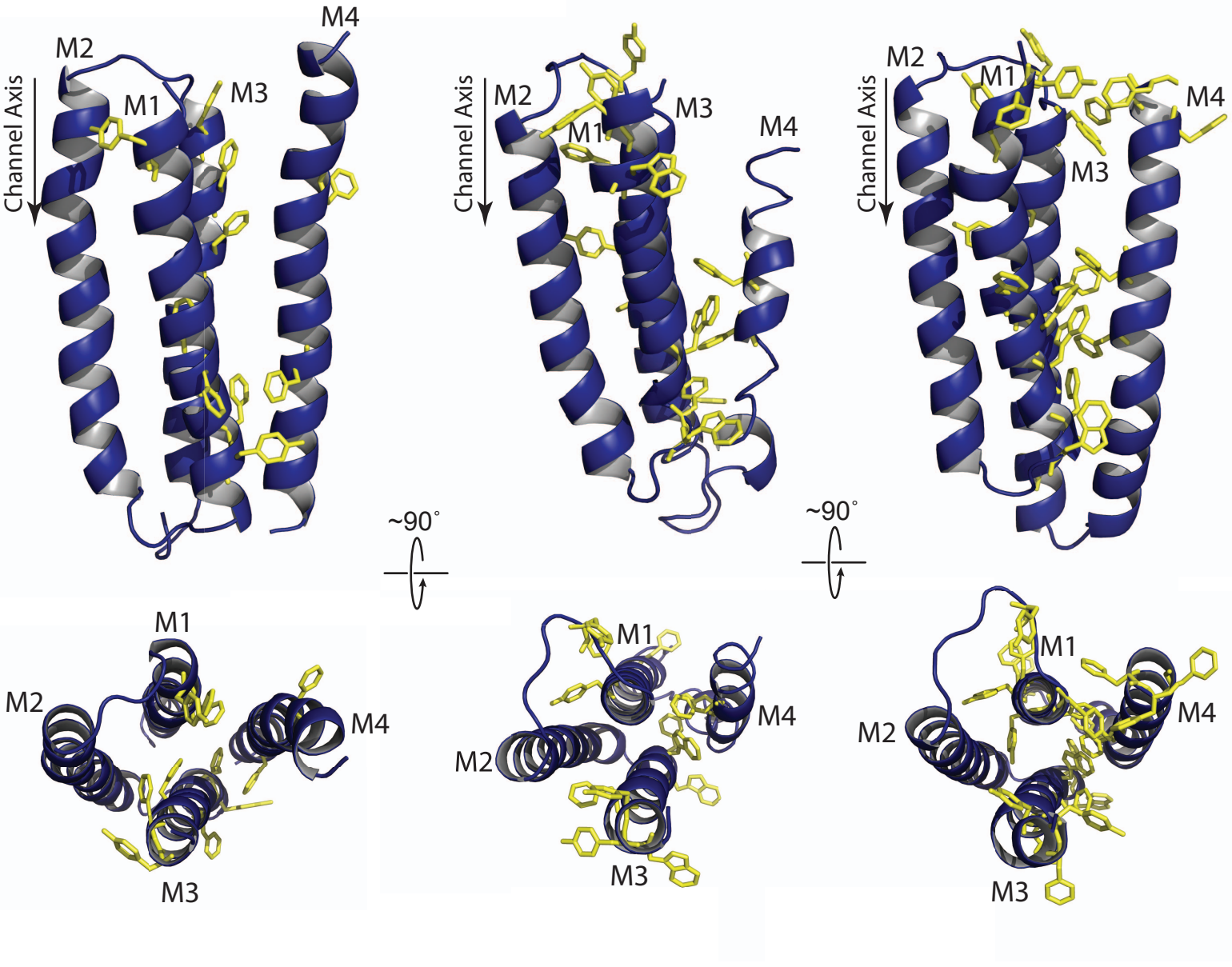
M4
M2
M1
M3
Channel Axis
~90˚
M1
M2
M4
M3
nAChR
ELIC
GLIC

uncoupled conformation when compared to the nAChR. To test this hypothesis, I developed a protocol for the expression, purification, and membrane reconstitution of ELIC. I also explored, through heterologous expression in *Xenopus laevis* oocytes, the effect of intramembrane aromatic additions to ELIC on the coupling of agonist binding to channel gating. The results of these experiments support our model of uncoupling, but also suggest that intramembrane aromatic residues may play a role dictating the efficiency of gating and thus the susceptibility of different pLGICs to potentiation.

7 MANUSCRIPT:

2. **Casey L. Carswell** and John E. Baenziger (2014) The ligand-gated ion channels ELIC and GLC exhibit distinct structural and functional sensitivities to lipids. Submitted to the Journal of Biological Chemistry.

7.1 Preface

This is the second of three manuscripts included in this thesis. This manuscript was first submitted to the Journal of Biological Chemistry (Jan, 2014). This paper focuses on the lipid sensitivities of prokaryotic homologs of the pLGIC. Using FTIR techniques, this work shows that two prokaryotic homologs of the pLGIC exhibit different functional sensitivities to their surrounding lipid environments.

I expressed, purified, reconstituted, and collected all FTIR experiments presented in this manuscript. Purified nAChR was supplied by Daniel Therien and Jiayin Sun. I wrote the manuscript in collaboration with my supervisor.

7.2 Abstract

The prokaryotic pentameric ligand gated ion channels (pLGIC) GLIC and ELIC are excellent models for probing the molecular basis of pLGIC function. We compare here the structures, thermal stabilities, and lipid sensitivities of membrane reconstituted GLIC and ELIC. While both membrane reconstituted proteins exhibit similar biophysical properties, the thermal stability of ELIC is lower and its structural integrity more sensitive to environmental factors than that of GLIC. In particular, the ability of ELIC to undergo agonist-induced channel gating is sensitive to the composition of its surrounding membrane environment, while that of GLIC is not. Structural comparisons suggest that aromatic interactions play a role in the packing of transmembrane α-helices and thus in transmembrane domain stability. Increasing transmembrane domain stability may correlate inversely with structural and functional lipid sensitivity.

7.3 Introduction

The ability of the nicotinic acetylcholine receptor (nAChR) to undergo agonist-induced channel gating is sensitive to lipids (181,206,207,222-224). Varying levels of both cholesterol and anionic lipids in phosphatidylcholine (PC) membranes stabilize varying proportions of agonist-responsive nAChRs (207,209,225-227). In PC membranes lacking both activating lipids, the nAChR adopts an uncoupled conformation that binds agonist, but usually does not undergo agonist-induced conformational transitions (208,212). The lipid exposed transmembrane α-helix M4 from each subunit likely plays a role in lipid sensing (189,228-231). One model proposes that lipids modulate the binding of M4 to the adjacent transmembrane α-helices, M1 and M3, with M4 binding promoting effective interactions between the transmembrane domain (TMD) and the agonist binding domain (ABD) to enhance channel gating (208,212).

Definitive insight into the mechanisms of lipid-sensing in pentameric ligand-gated ion channels (pLGICs) will require the ability to characterize the effects of changing lipid environments on site-directed mutants designed to test specific mechanistic hypotheses, such as the M4 lipid-sensor model described above. In contrast to the nAChR (232), the homologous prokaryotic pLGICs, GLIC and ELIC (Figure 7.1A), are both expressed in relatively large quantities in *E. coli* and are thus amenable to such biophysical studies. Preliminary experiments show that membrane-reconstituted GLIC is more stable (i.e. a higher denaturation temperature) and has a reduced structural/functional sensitivity to lipids than the nAChR. In membranes that lock the nAChR in an uncoupled conformation, GLIC retains the ability to undergo agonist-induced channel gating (221).

Figure 7.1

3D Structure and TMD aromatics in ELIC, GLIC, and the *Torpedo* nAChR**. (A)** 3D structures of ELIC (2VLO; left) (217) (, GLIC (3EHZ, center) (233) and the *Torpedo* nAChR (2BG9, right) (189) colored to highlight the functional agonist binding (red), transmembrane gating (blue), and cytoplasmic (green) domains. **(B)** structure of a single TMD from each pLGIC (α-subunit for the nAChR) highlighting aromatic residues on M1, M3, and M4 as yellow sticks.

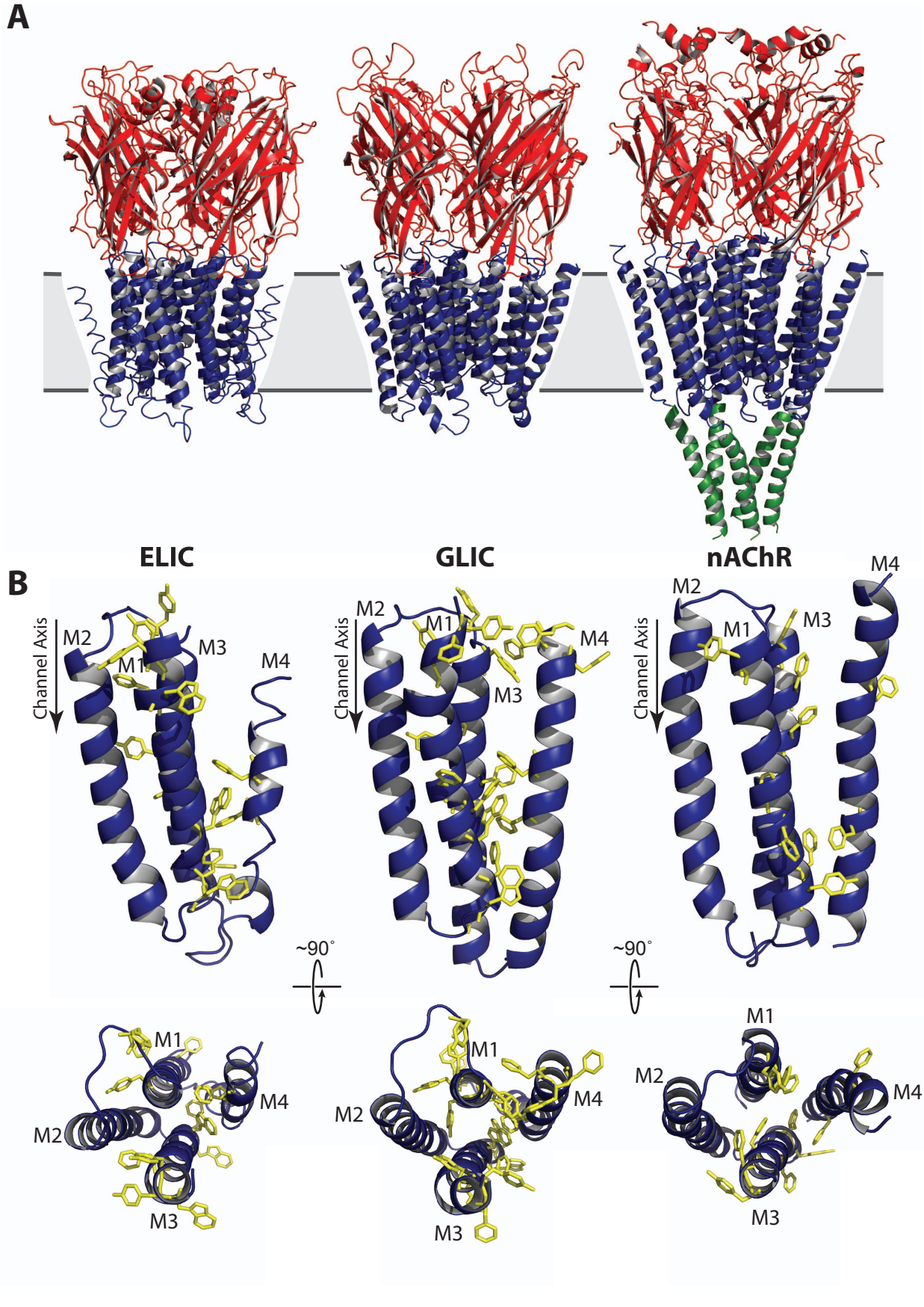
A
ELIC
GLIC
nAChR
B
Channel Axis
M1
M2
M3
M4
~90˚

Structural comparisons reveal an extensive network of aromatic residues in the TMD of GLIC, but relatively few aromatics in the *Torpedo* nAChR (Figure 7.1B). Given that aromatic interactions promote the binding of the M4 "lipid sensor" to the adjacent transmembrane α-helices, M1 and M3, during pLGIC folding (214), we hypothesized that increased aromatic interactions render the GLIC TMD structure more stabile and thus less sensitive to variations in the surrounding membrane environment. In other words, the extensive aromatic interactions promote M4 binding to M1/M3 in GLIC, even in the absence of activating lipids (221). Interestingly, ELIC exhibits fewer aromatic interactions at the interface between M4 and M1/M3 than GLIC (Figure 7.1B). If aromatic interactions play a role stabilizing M4 binding, and thus influence both TMD stability and lipid sensing, then ELIC should exhibit an increased propensity to adopt an uncoupled conformation compared to GLIC.

Here, we compare the structural and biophysical properties of membrane reconstituted ELIC and GLIC. In agreement with our hypothesis, we find that the ELIC structure is more sensitive to a variety of environmental factors, including ionic strength, temperature, and surrounding lipids. In contrast to GLIC, ELIC does not undergo agonist-induced channel gating in the minimal PC membranes that stabilize an uncoupled nAChR. The subtle differences in the lipid sensitivities of ELIC and GLIC demonstrate the utility of these two homologs as models for teasing out the molecular features underlying lipid-sensing. Our data support the proposed role for intramembrane aromatic interactions in dictating lipid sensitivity.

7.4 Experimental Procedures

7.4.1 Materials. Soybean asolectin (L-α-phosphatidylcholine, type II-S) and cysteamine were from Sigma (St. Louis, MO). 1-palmotyl-2-oleoyl-*sn*-glycero-3-phosphocholine was from Avanti (Alabaster, AL). Dodecylmaltoside (DDM) was from Affymetrix (Santa Clara, CA). A pET-26b expression vector containing the pelB signal sequence followed by a $(His)_{10}$-Tag and then the maltose binding protein fused to the N-terminus of ELIC through a *Herpes simplex* (HRV) 3C protease site was kindly provided by Dr. Raimund Dutzler. A C-terminal alanine, a cloning artifact not present in the Genbank sequence (accession number POC7B7), was removed.

7.4.2 Preparation of ELIC proteoliposomes of ELIC. ELIC was expressed, purified, and reconstituted into proteoliposomes as described previously for GLIC (221), but with several modifications. ELIC was expressed in the BL21(DE3) strain of *E. coli*. Two litre cultures of transformed BL21 cells were grown in Terrific Broth containing 50 μg/mL kanamycin at 37˚C to an OD_{600} of ~1.2 a.u, and the cultures induced overnight at 26˚C with 200μM IPTG. Cells were harvested, resuspended in Buffer A (150 mM NaCl, 50 mM NaH_2PO_4, pH 8.0) in the presence of Roche Complete™ antiprotease tablets (Branford, CT), and lysed with an Avestin Emulsiflex-C5 homogenizer (Ottawa, Canada). Membrane fractions were solubilised in 1 % DDM in Buffer A, and the ELIC fusion protein bound to an amylose affinity resin. After treatment with HRV 3C protease (Calbiochem; Gibbstown, NJ), ELIC was eluted in 0.0 2% DDM and further purified in Buffer B (150 mM NaCl, 10 mM NaH_2PO_4, pH 8.0) on a Superose 6 10/300 gel-filtration column (GE Healthcare; Little Chafont, UK).

The purified ELIC in 0.02 % DDM in Buffer B was slowly diluted to a ratio of at least 1:4 (vol:vol) with a solution of lipids solubilised in 0.625 % cholate in Buffer B to give a 2:1 (w/w) lipid-to-protein ratio (159). After gently mixing for ~30 minutes, the protein/detergent/lipid mixture was dialyzed five times at 4˚C against 2 L of Buffer B leading to turbid solutions of proteoliposomes, which were harvested by ultracentrifugation. The incorporation of ELIC into the liposomes was assessed by discontinuous sucrose-density gradient centrifugation (208).

7.4.3 Fourier transform infrared spectroscopy (FTIR). Infrared spectra were recorded on either a Digilab (now Agilent Technologies; Santa Clara, CA) FTS40 or FTS575 spectrometer. The hydrogen/deuterium infrared spectra (Figure 7.2A) were recorded using a Golden-Gate^{TM} attenuated total internal reflection accessory (SpecAc; Oprington (Kent, U.K.)). 5-10 μl aliquots were dried gently under N_2 gas. 128 scan spectra were recorded at 4 cm^{-1} resolution both before and after rehydration with ^2H_2O (221).

For more detailed amide I band analyses, samples were exchanged into ^2H_2O Buffer A for precisely 24 hours at 4˚C, and then stored at -80 ^oC until use (spectra are recorded in ^2H_2O to eliminate the strong overlap between the absorptions of ^1H_2O and the protein vibrations of interest). Approximately 200 μg of ELIC was then deposited on a CaF_2 window with a gentle stream of N_2 gas, followed by rehydration with 8 μL of ^2H_2O. 4000 scan spectra were recorded at 2 cm^{-1} resolution and then processed with GRAMS/AI software (Thermo Scientific, Waltham, MA) (208). Resolution enhancement was performed between 1900 cm^{-1} and 1300 cm^{-1} using a $\gamma = 7$ and a Bessel smoothing function set to 70%. Intensity changes in the amide I band at either 1680 or 1620 cm^{-1} were plotted as a function of temperature to monitor the thermal denaturation (T_d). The T_d was calculated by fitting the data (GraphPad

Prism; GraphPad Software, Inc., La Jolla, CA) with a Boltzmann sigmoidal, where the fraction denatured $F_d=y_{initial}+[(y_{final}-y_{initial})/(1+\exp((T_d-x)/m_b))$.

7.4.4 Electrophysiology. Electrophysiology was performed using a two electrode voltage clamp apparatus (OC-725C oocyte clamp; Holliston, MA). Oocytes were injected with either 0.2 ng of ELIC cRNA or 100-200 ng of membrane-reconstituted ELIC and allowed to incubate overnight at 16˚C in ND96+ buffer (5 mM HEPES, 96 mM NaCl, 2 mM KCl, 1 mM $MgCl_2$, 1 mM $CaCl_2$, and 2 mM Pyruvate). Injected oocytes were placed in a RC-1Z oocyte chamber (Harvard Apparatus; Hamden, CT) containing HEPES buffer (150 mM NaCl, 0.5 mM $BaCl_2$ and 10 mM HEPES, pH 7.0). Currents through the plasma membrane in response to cysteamine concentration jumps were measured with the transmembrane voltage clamped at either -40 mV or -60 mV. The oocytes chamber was perfused with HEPES buffer (10 mM HEPES, 150 mM NaCl, 0.5 mM $BaCl_2$, pH=7.0) at a rate of ~5 mL/min.

7.5 Results

7.5.1 Membrane reconstitution of ELIC. ELIC was first reconstituted into asolectin membranes (aso-ELIC) using a protocol that consistently leads to folded and functional membrane incorporated GLIC (221). Although this protocol was efficient at membrane-incorporation (Figure 7.2), it was initially difficult to detect the thermal denaturation of membrane incorporated ELIC, raising the possibility that ELIC did not adopt a native-like folded and thus functional conformation. The latter was a particular concern because although the purification and ultimately crystallization of both GLIC and ELIC has been *relatively* straightforward (216,217,233), purification and membrane reconstitution of conformationally active *Torpedo* nAChR was initially challenging, highlighting the structural sensitivity of the nAChR to environmental factors, such as lipids (234). Furthermore, it has been suggested that detergent solubilization of ELIC leads to a non-activatable conformation similar to the uncoupled nAChR (191,220).

Using an infrared micro-sampling accessory (143), we established that ELIC maintains its secondary structure and peptide hydrogen exchange characteristics throughout purification and membrane-reconstitution (Figure 7.2B). The amide I band shape in infrared spectra of ELIC, however, differs slightly from that of GLIC, making it inherently more difficult to characterize its thermal denaturation (see below). The sucrose density gradient step, which is typically used to purify proteoliposomes from unincorporated and aggregated protein (208), seemed to contribute to a lack of reproducibility in the thermal denaturation data. More importantly, brief exposure of the ELIC proteoliposomes to low ionic strength ^2H_2O buffer (a technical step in the preparation of samples for infrared spectroscopy) led to marked effects

Figure 7.2

Structure of ELIC during purification, membrane reconstitution, and sample preparation. **(A)** Sucrose density gradients show that ELIC incorporates efficiently into proteoliposomes (interface between 0 and 20% sucrose). Protein-free liposomes run at the interface between 0% and 20% sucrose, whereas low lipid-to-protein ratio unincorporated protein aggregates run at the interface between 35% and 70% sucrose**.** **(B**) Infared spectra from ELIC gently dried under N_2 gas (*black lines*) and immediately after rehydration with ^2H_2O (*gray lines*). Spectra are from ELIC *i*, after elution from the amylose resin, *ii,* after a first size-exclusion column, and *iii,* after a second size-exclusion column. Note that both the amide I band shape and the levels of peptide N-^{1}H/N-^{2}H exchange (as judged by the amide II band intensity) are maintained throughout purification. **(C)** infrared spectra showing aso-ELIC exchanged into ^2H_2O Buffer A (*i*) or ^2H_2O phosphate buffer (no added salt) (*ii*). The amide I bands both before (*gray*) and after deconvolution (*black*) are presented on the left. The non-deconvolved amide II bands are presented on the right. Spectra were deconvolved using GRAMS/AI v.7.01 software (Thermo Galactic) with γ=7 and a Bessel smoothing function set at 70%. **(D)** Thermal denaturation of aso-ELIC exchanged into ^2H_2O Buffer A **(●)** and ^2H_2O phosphate buffer **(□).**

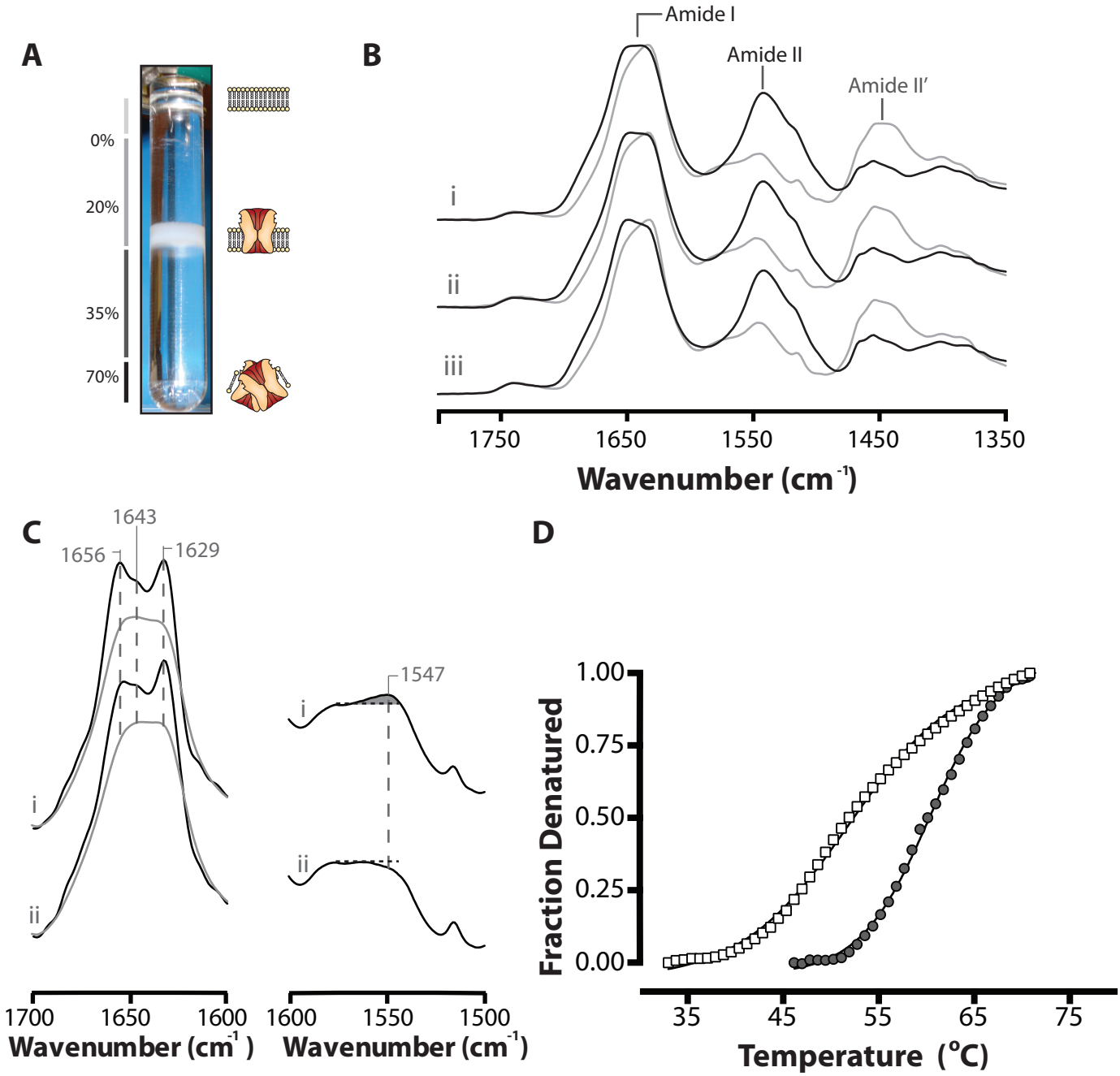
A
0%
20%
35%
70%
B
Amide I
Amide II
Amide II'
i
ii
iii
1750
1650
1550
1450
1350
Wavenumber (cm-1)
C
1643
1656
1629
i
ii
1700
1650
1600
Wavenumber (cm-1)
1547
i
ii
1600
1550
1500
Wavenumber (cm-1)
D
Fraction Denatured
1.00
0.75
0.50
0.25
0.00
35
45
55
65
75
Temperature (°C)

on ELIC structure, including a decrease in the cooperativity of unfolding, a 5-10 ^{o}C drop in the thermal denaturation temperature, and an increased level of peptide N-^{1}H/N-^{2}H exchange (Figure 7.2C and 7.2D). These are similar to the structural changes in the nAChR that occur upon formation of the uncoupled state (208,212).

Our purification and membrane reconstitution experiments suggested that the structure of ELIC is less stable than that of GLIC, consistent with its reduced thermal stability, as discussed below. We therefore adapted our purification/reconstitution/sample preparation protocols to minimize potentially detrimental effects on ELIC structure. As ELIC incorporates efficiently into proteoliposomes, the sucrose density gradient purification step was eliminated. The ELIC proteoliposomes were exchanged into $^{2}H_2O$ Buffer A, instead of low ionic strength $^{2}H_2O$ phosphate buffer (i.e. buffer lacking added salt). As a precautionary measure, the sample exchange time in $^{2}H_2O$ was also reduced to 24 hours. 24 hours in $^{2}H_2O$ Buffer A is sufficient to reach consistent and relatively stable levels of peptide N-^{1}H/N-^{2}H exchange.

As discussed below, these three minor adjustments to our protocols led to folded and functional membrane incorporated ELIC. In light of the sensitivity of ELIC structure to low ionic strength, we re-evaluated the structure and thermal stability of both membrane reconstituted GLIC and the nAChR, but observed no effects of low ionic strength with either protein (Table 7.1). Previous studies have shown that the nAChR concentrates endogenous divalent cations throughout purification and membrane reconstitution, even in the presence of divalent cation chelators (235,236). We speculate that the unique surface electrostatic potential of ELIC may play a role in the structural sensitivity of ELIC to low ionic strength (Figure 7.3).

Table 7.1 Thermal Stability of ELIC

Reconstitution	T_d[a]	n
aso-ELIC	59.7 ± 3.5 (51.6 ± 1.3)	4 (4)
PC-ELIC	65.1 ± 2.2	4
aso-GLIC	68.5 (68.8 ± 1.5[b])	1 (5)
PC-GLIC	(70.4 ± 0.9[b])	4
aso-nAChR	53.0 ± 2.1 (55.4 ± 1.0[b])	2 (2)
PC-nAChR	(52.4 ± 0.1[c])	6

[a] Thermal denaturation temperatures of membrane incorporated pLGICs after 24 h equilibration in ^2H_2O Buffer A at 4 ^oC. Values in brackets refer to the thermal denaturation temperatures after 72 h equilibration in ^2H_2O phosphate buffer at 4 ^oC. See text

[b] from Labriola et al (221)

[c] from daCosta & Baenziger (209)

T_d represents the thermal denaturation temperature and n represent the number of replicates

Figure 7.3

Surface electrostatic potential of the ABD and TMD of ELIC, GLIC and the nAChR. Vacuum electrostatic potential calculated in PyMol.

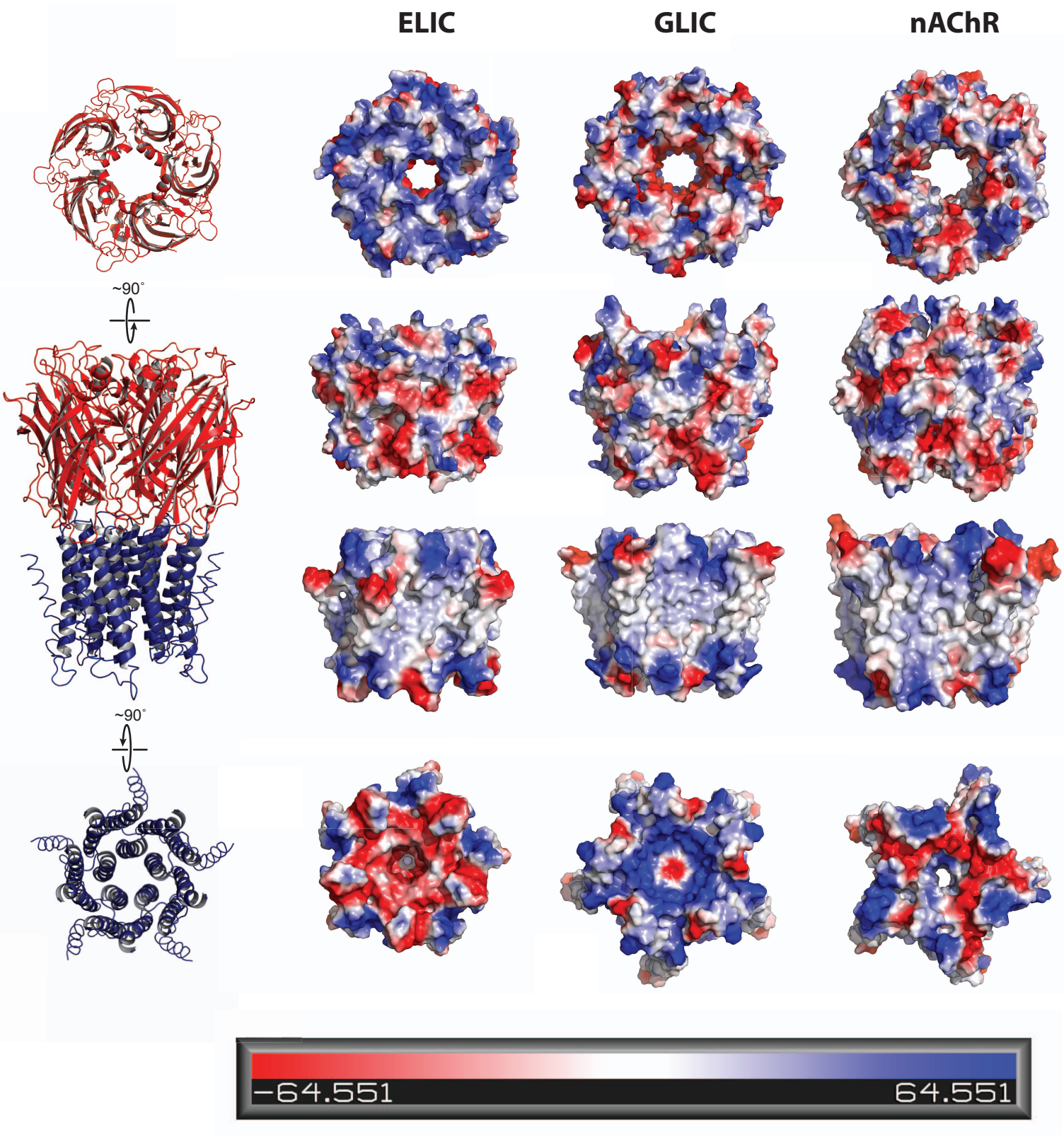
ELIC
GLIC
nAChR
~90˚
~90˚
−64.551
64.551
($K_b T / e_c$)

7.5.2 Structure of membrane-reconstituted ELIC. We characterized the structure and peptide N-^{1}H/N-^{2}H exchange characteristics of membrane incorporated ELIC using infrared spectroscopy. Infrared spectra recorded from ELIC proteoliposomes exhibit two relatively intense protein vibrations. The amide I band (primarily C=O stretching; 1700-1600 cm^{-1}), which provides insight into protein secondary structure, and the amide II band (primarily N-^{1}H bending; centered near 1547 cm^{-1}), which serves as a measure of the level of peptide N-^{1}H to N-^{2}H exchange (Figure 7.4).

The amide I contour in spectra recorded from proteoliposomes gently dried from $^{1}H_2O$ exhibits a peak maximum near 1655 cm^{-1}, due to the vibrations of α-helix and loop/random secondary structures, and a prominent broad shoulder between 1640 and 1625 cm^{-1}, due primarily to the vibrations of β-sheet. Immediately after exposure to $^{2}H_2O$ buffer, the amide I band shape becomes more symmetric, as the rapid exchange of solvent exposed α-helical/loop (likely the latter) peptide N-^{1}H to N-^{2}H shifts their frequency from 1655 cm^{-1} down to near 1645 cm^{-1} (Figure 7.4A). This rapid peptide N-^{1}H/N-^{2}H exchange also leads to an immediate loss of amide II band intensity, as this vibration shifts down in frequency to near 1450 cm^{-1} (primarily N-^{2}H bending). Similar rapid spectral changes upon exposure to $^{2}H_2O$ are also observed with GLIC and both the *Torpedo* nAChR and the human α4β2 nAChR (208,221,232) and are likely characteristic of the large solvent-exposed ABD.

A more detailed assessment of secondary structure was performed after recording higher fidelity spectra from ELIC proteoliposomes exchanged into $^{2}H_2O$ for 24 hours at 4 ^{o}C. The resulting amide I contour still exhibits intense amide I component bands at frequencies characteristic of both α-helix/loop and β -sheet, as shown clearly upon resolution enhancement (Figure 7.4B). Curve fitting suggests roughly 30% α-helix and 35% β-sheet,

Figure 7.4

Structural comparisons of membrane reconstituted ELIC, GLIC and the nAChR as probed by infrared spectroscopy**. (A)** Infrared spectra of aso-ELIC recorded after gentle drying from $^{1}H_2O$ buffer (*black*) and immediately after addition of $^{2}H_2O$ (*gray*). Note the immediate changes in amideI band shape (1700-1600 cm^{-1}), and the immediate decrease in amide II band intensity (1547cm^{-1}), both indicative of the rapid peptide N-^{1}H/N-^{2}H exchange of solvent-exposed peptide hydrogens. **(B)** The structure-sensitive amide I (*left*) and amide II (right) bands in infrared spectra recorded after 24 h of equilibration in $^{2}H_2O$ at 4°C from aso-ELIC (*i*) and PC-ELIC (*ii*), and after 72 h equilibration in $^{2}H_2O$ at 4°C for aso-GLIC (*iii*) PC-GLIC (*iv*), aso-nAChR (*v*), and PC-nAChR (*vi*) (11,19). The amide I bands are shown both before (*gray*) and after resolution enhancement (*black*). The relative intensity of the amide II vibration is best assessed relative to the intensity of the adjacent broad peak between 1560 cm^{-1} and 1600 cm^{-1} due to aspartic and glutamic acid. Spectra are the averages of at least three spectra recorded from two different purifications/reconstitutions.

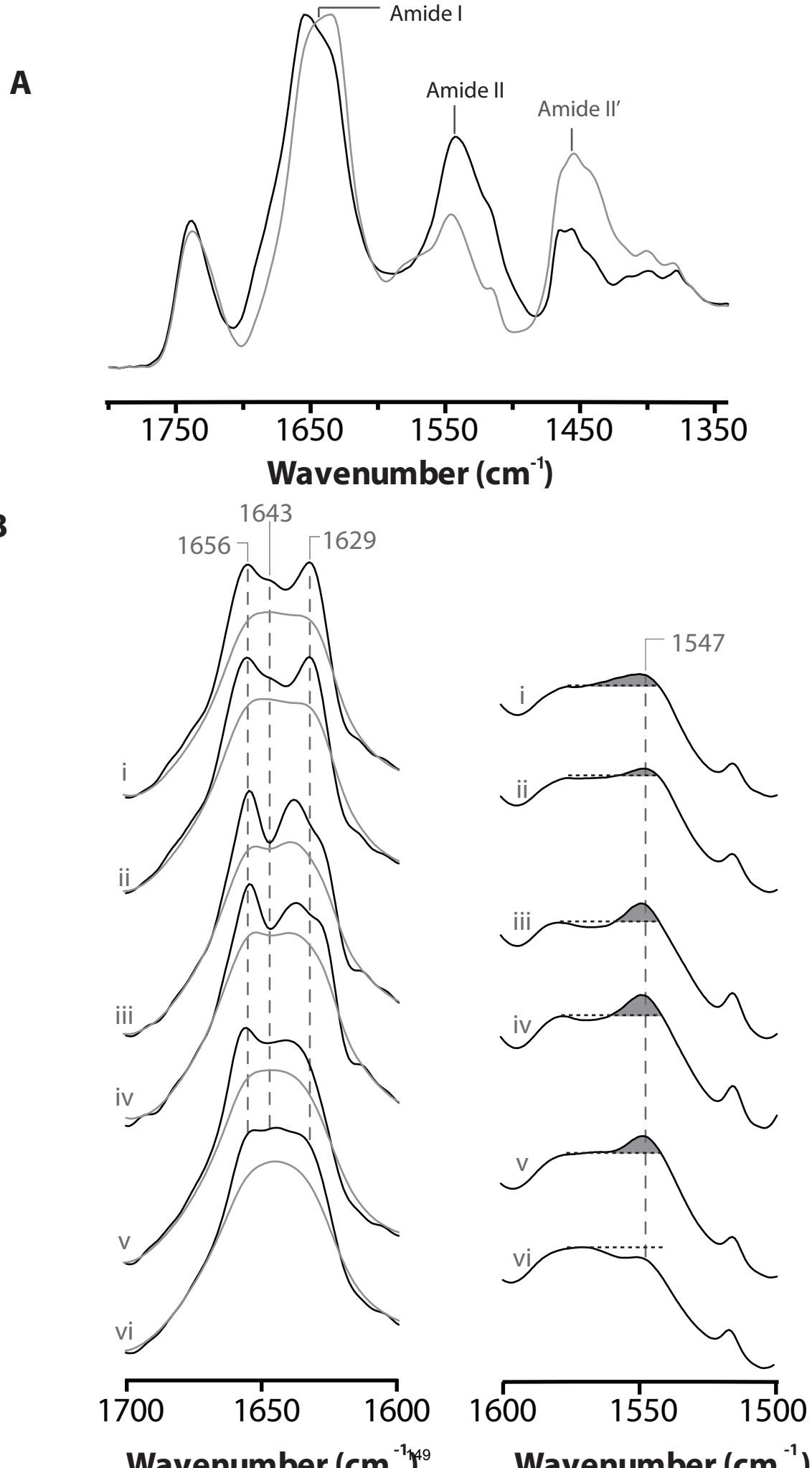
A
Amide I
Amide II
Amide II'
1750
1650
1550
1450
1350
Wavenumber (cm-1)
B
1643
1656
1629
1547
i
ii
iii
iv
v
vi
1700
1650
1600
1600
1550
1500
Wavenumber (cm-1)
Wavenumber (cm-1)

Figure 7.5

Representative curve fits of the amide I bands from **(A)** aso-ELIC and **(B)** PC-ELIC. In each case, the left set of spectra include the experimental amide I absorbance contour (black line), the superimposed curve fit (closed circles), and the individual component peaks summed to curve fit the amide I contour. The two spectra on the right correspond to the deconvolved experimental spectrum (top) and the deconvolved curve fit spectrum (bottom). Spectra were deconvolved using GRAMS/AI v.7.01 software (Thermo Galactic) with γ=7 and a Bessel smoothing function set at 70%. **(C)**, band assignments and curve fit estimates.

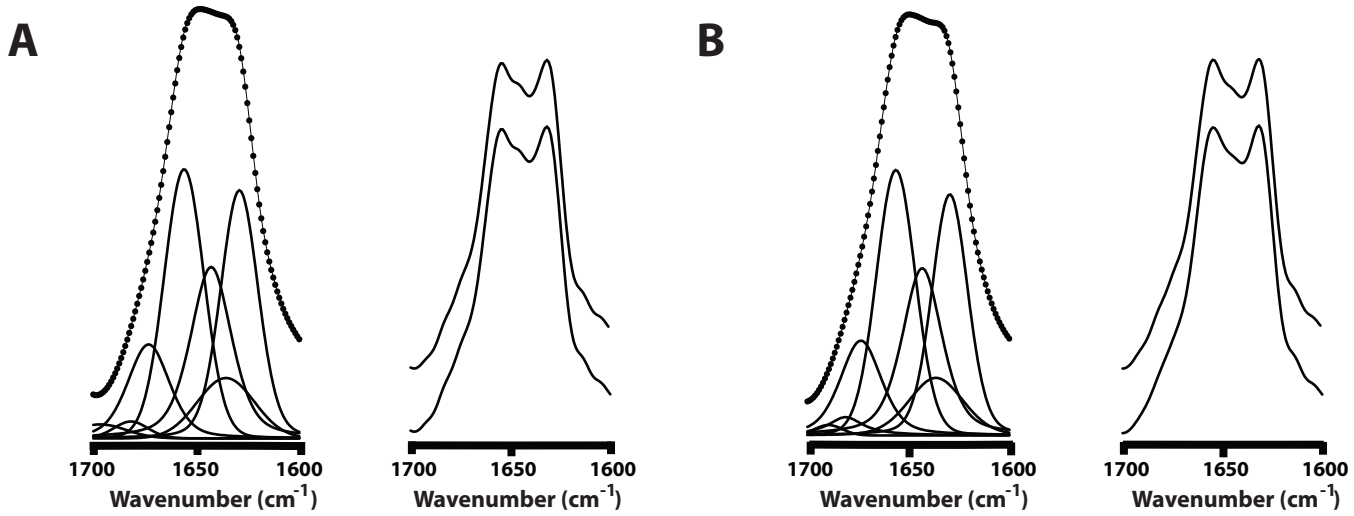

C

Table 7.2 ELIC Secondary Structure in reconstituted membranes

Band frequency (cm^{-1})	Band Assignment	ASO-ELIC	PC-ELIC
1697	T	2	1
1682	T	2	1
1674	T + β	12	12
1656	α	28	29
1643	loop/random	22	22
1636	β	9	9
1629	β	26	25

estimates that compare well with the crystal structure (roughly 35% α-helix and 30% β-sheet) (Figure 7.5). Note that the strong intensity remaining near 1655 cm^{-1} due to protiated, and thus solvent shielded, α-helical/loop structures (likely the former) suggests the existence of a large population of exchange-resistant and likely transmembrane α-helices, as has also been characterized in both GLIC and the nAChR (148,150,208,221,232).

7.5.3 Thermal stability of membrane reconstituted ELIC. Infrared spectra recorded as a function of increasing temperature reveal changes in the amide I band shape that are characteristic of protein denaturation (Figure 7.6). Unfolding also leads to the complete exchange of the previously "exchange-resistant" peptide hydrogens. Monitoring amide I changes with increased temperature led to a measured thermal denaturation temperature for aso-ELIC of 59.7 ± 3.5 ^{o}C, which is intermediate between that of aso-GLIC (~69 ^{o}C) and aso-nAChR (~54 ^{o}C) (Figure 7.7 and Table 7.1).

Note that resolution enhancement and curve fitting of the amide I bands show that the spectra of both GLIC and ELIC exhibit two components in the β-sheet region near 1635 and 1630 cm^{-1}, but in ELIC the latter vibration is more intense. As denaturation is characterized by an increase in intensity of an overlapping vibration centered near 1620 cm^{-1}, the greater intensity near 1630 cm^{-1} in spectra of ELIC makes it inherently more difficult to accurately monitor the thermal unfolding process. Thermal denaturation curves yielded consistent thermal denaturation temperatures, but greater variability in the cooperativity of unfolding (defined by the Boltzmann slope) (see Experimental Procedures). Given this variability, we do not report Boltzmann slopes for the denaturation curves.

Figure 7.6

Thermal Denaturation spectra of **(A)** aso-ELIC and **(B) P**C-ELIC. The left panel depicts a stacked plot of spectra collected for thermal stability characterization of the reconstituted ELIC. Representative traces are shown from 35°C to 76°C, front to back. Spectra were collected at 1°C increments. Spectra were deconvolved using GRAMS/AI v.7.01 software (Thermo Galactic) with γ=7 and a Bessel smoothing function set at 70%. The right panel depicts spectra collected at 36°C (black line) and 76°C (gray line) showing full exchange of the N-^{1}H to N-^{2}H upon denaturation.

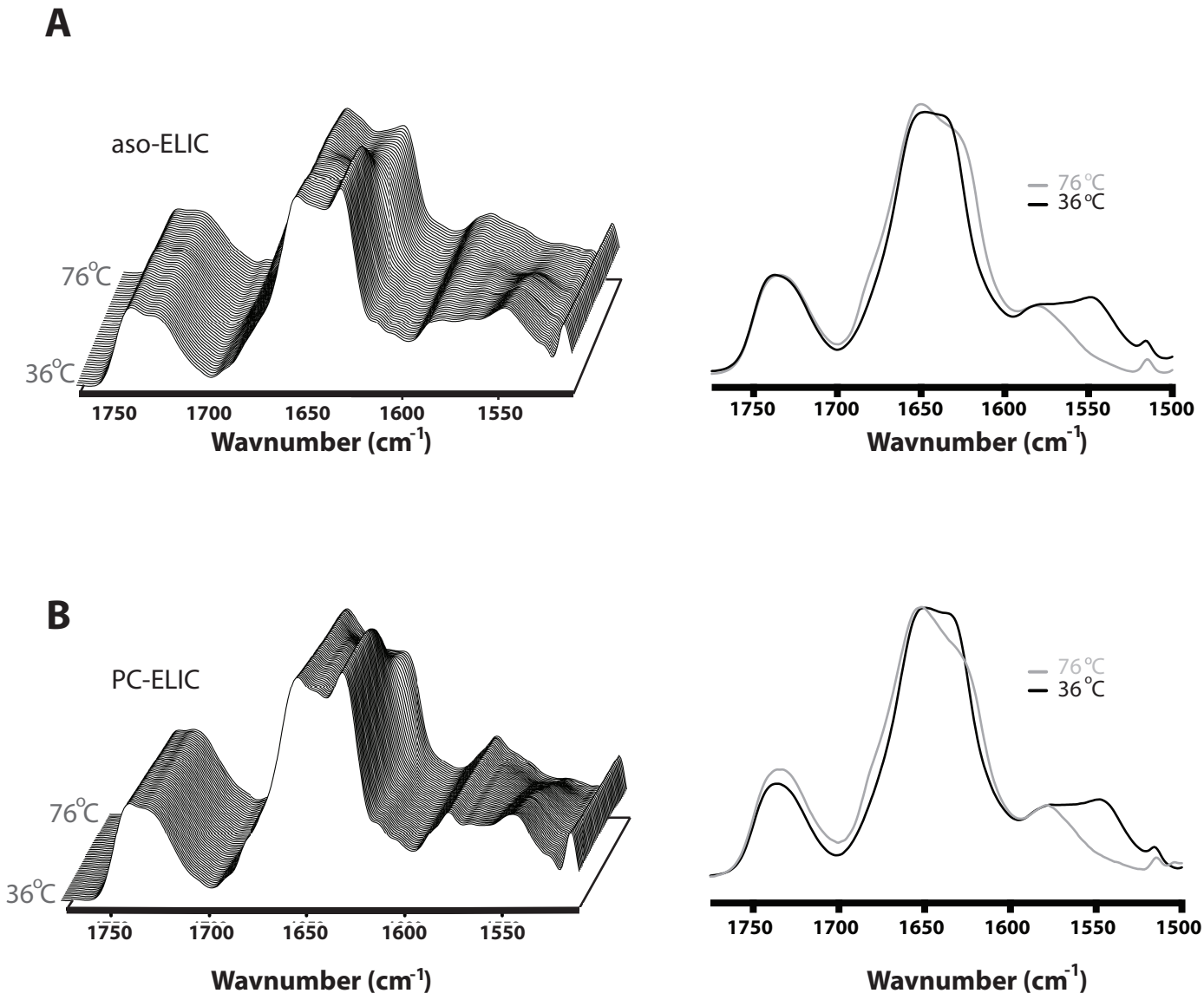
A
aso-ELIC
76°C
36°C
1750
1700
1650
1600
1550
Wavnumber (cm-1)
76°C
36°C
1750
1700
1650
1600
1550
1500
Wavnumber (cm-1)
B
PC-ELIC
76°C
36°C
1750
1700
1650
1600
1550
Wavnumber (cm-1)
76°C
36°C
1750
1700
1650
1600
1550
1500
Wavnumber (cm-1)

Figure 7.7

Representative thermal denaturation curves for ELIC (black), GLIC (dark gray) and the nAChR (light gray). aso-ELIC (●), PC-ELIC (○), aso-GLIC (▲), PC-GLIC (△), aso-nAChR (■), and PC-nAChR (□). Each curve was fit with a Boltzmann sigmoid (see Experimental Procedures).

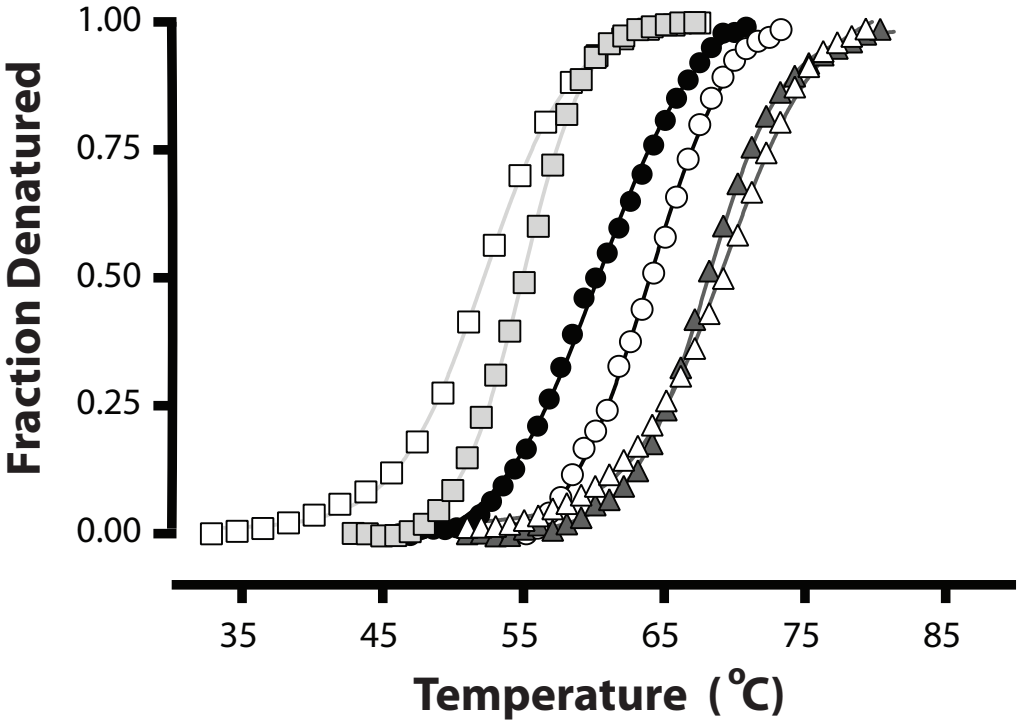
1.00
0.75
0.50
0.25
0.00
Fraction Denatured
35
45
55
65
75
85
Temperature (°C)

7.5.4 Gating of membrane-reconstituted ELIC. The relatively low lipid-to-protein ratio ELIC proteoliposomes are ideal for spectroscopy, but not useful for direct measurements of channel activity using electrophysiology approaches. We indirectly probed the activity of membrane reconstituted ELIC by first injecting the aso-ELIC into *Xenopus laevis* oocytes and then monitoring the appearance of cysteamine-activated currents across the oocyte plasma membranes (237,238). A similar indirect approach has been used previously to characterize agonist-induced gating of membrane reconstituted GLIC and the nAChR (221). Cysteamine did not elicit measurable dose responses in uninjected oocytes (Figure 7.8). In contrast, oocytes injected with aso-ELIC gave reproducible currents that respond to cysteamine in a dose-dependent manner yielding an EC_{50} of 1.12 ± 0.4 mM (n=10), a value similar to that observed for oocytes expressing ELIC on the membrane surface after cRNA injection (1.01 ± 0.2 mM, n=10, data not shown). The reconstituted aso-ELIC thus retains the ability to gate open in response to cysteamine binding. Of interest, the essentially identical EC_{50} values observed with both aso-ELIC and ELIC cRNA injected oocytes contrasts the differences observed in EC_{50} values for proton activation of oocytes injected with either aso-GLIC or GLIC cRNA (221). The EC_{50} for activation of aso-GLIC injected oocytes is shifted to higher proton concentrations, relative to oocytes injected with GLIC cRNA.

7.5.5 Effects of an uncoupling lipid environment on ELIC structure. We next compared the structural and functional properties of aso-ELIC to that of ELIC reconstituted into the minimal PC membranes (PC-ELIC) that stabilizes an uncoupled nAChR. The uncoupled PC-nAChR binds agonist, but does not usually undergo agonist-induced conformational transitions (208,212). PC-nAChR exhibits undergoes more extensive peptide N-^{1}H/N-^{2}H

Figure 7.8

Cysteamine-induced response of membrane–reconstituted ELIC. **(A)** Representative whole cell electrophyiosology recordings measured at a -60mV holding potential in response to cysteamine jumps from uninjected oocytes and oocytes injected with aso-ELIC and PC-ELIC (*left panel*). Averaged dose-response curves to cysteamine (aso-ELIC; *n=10* and PC-ELIC; *n=24*) (*right panel*). The inset represents the peak current achieved at a cysteamine concentration of 4mM. **(B)** Representative whole cell electrophyiosology recordings measured at -20mV in response to pH jumps from uninjected oocytes and oocytes injected with aso-GLIC and PC-GLIC (*left panel*). Averaged dose-response to pH (*right panel*). The inset represents the peak current achieved upon exposure of oocytes injected with the indicated reconstituted membranes at pH 3.5. The dose response curves from oocytes injected with membrane-reconstituted GLIC were normalized assuming a pH_{50} of 2.90. These proton-induced currents are sensitive to the inhibitor amantadine, whereas the endogenous acid-sensitive channels are not.

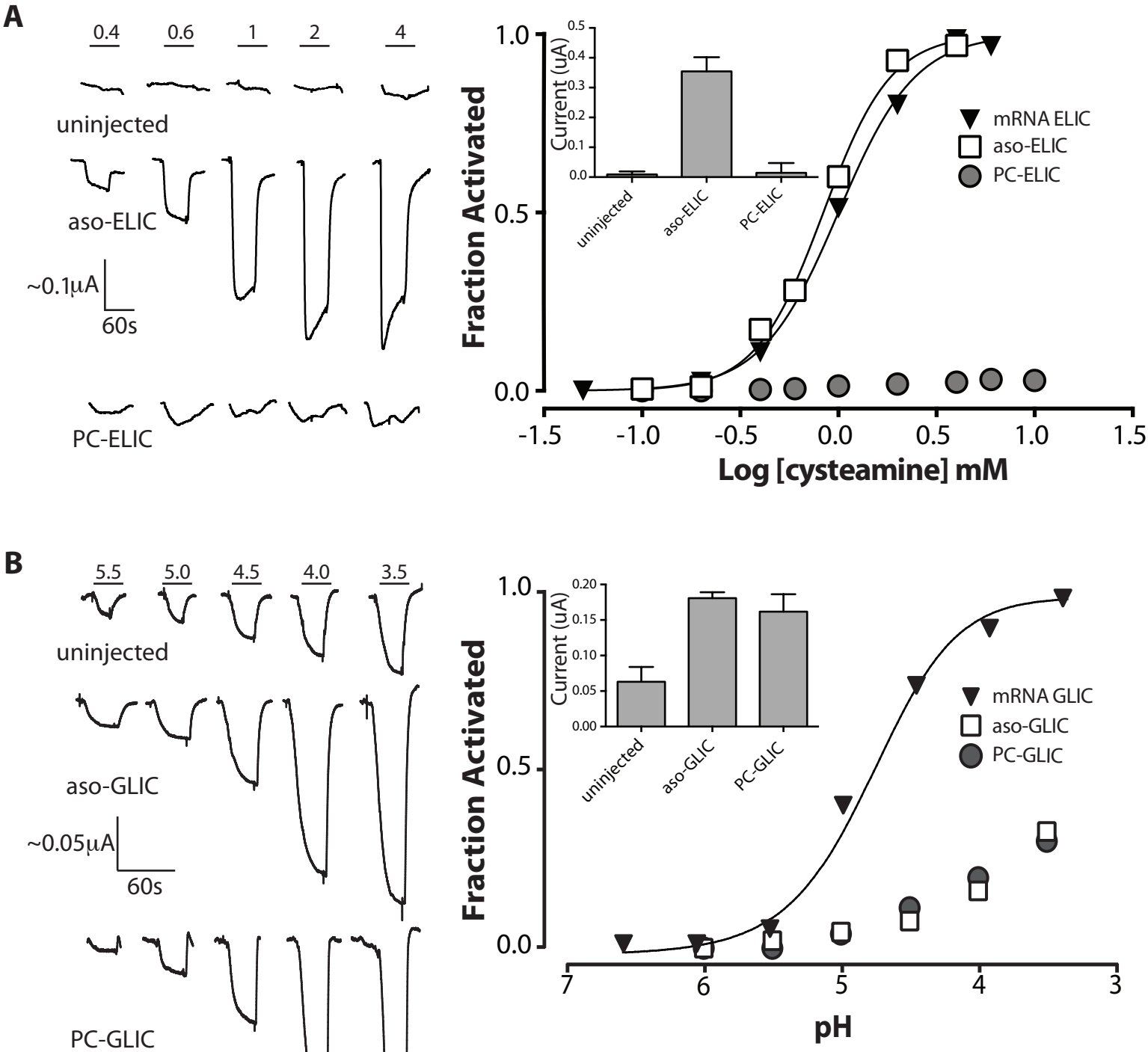
A
0.4
0.6
1
2
4
uninjected
aso-ELIC
~0.1μA
60s
PC-ELIC
Fraction Activated
1.0
0.5
0.0
-1.5
-1.0
-0.5
0.0
0.5
1.0
1.5
Log [cysteamine] mM
mRNA ELIC
aso-ELIC
PC-ELIC
Current (uA)
0.5
0.4
0.3
0.2
0.1
0.0
uninjected
aso-ELIC
PC-ELIC
B
5.5
5.0
4.5
4.0
3.5
uninjected
aso-GLIC
~0.05μA
60s
PC-GLIC
Fraction Activated
1.0
0.5
0.0
7
6
5
4
3
pH
mRNA GLIC
aso-GLIC
PC-GLIC
Current (uA)
0.20
0.15
0.10
0.05
0.00
uninjected
aso-GLIC
PC-GLIC

exchange than the resting or desensitized nAChR, leading to a reduced amide II band intensity and a slightly enhanced downshift in amide I component band intensity from 1655 cm^{-1} to near 1645 cm^{-1} (Figure 7.4B). PC-nAChR also undergoes thermal denaturation at slightly lower temperatures, and the cooperativity of denaturation is reduced (Figure 7.7 and Table 7.1)(208). Weakened interactions leading to an increased physical separation between the ABD and TMD may account for both the structural and functional differences of the nAChR in asolectin versus PC membranes (208). It was proposed that M4 binding to M1/M3 to promote effective interactions between post-M4 and the Cys-loop is essential for channel gating.

The structure and biophysical properties of the homolog GLIC are essentially indistinguishable in asolectin and PC membranes, suggesting that GLIC does not exhibit the same propensity to adopt an uncoupled conformation as the nAChR (Figure 7.4) (221). Similarly, we detect little if any structural difference between aso-ELIC and PC-ELIC (Figure 7.4). The amide I and amide II bands of aso-ELIC and PC-ELIC are virtually superimposable, with similar levels of peptide N-^{1}H/N-^{2}H exchange and essentially no variability in amide I component band intensity near 1655 cm^{-1} and 1645 cm^{-1}. The thermal denaturation temperature of PC-ELIC (65.1 ± 2.2) is actually higher than that of aso-ELIC (59.7 ± 3.5) (Figure 7.7 and Table 7.1), a trend also observed with aso- versus PC-GLIC. The data suggest that ELIC does not adopt a conformation in PC membranes similar to the uncoupled nAChR.

7.5.6 Effects of an uncoupling lipid environment on ELIC function. The injection of both aso-nAChR and PC-nAChR into frog oocytes leads to the appearance of nAChR binding sites on the plasma membrane, but only aso-nAChR giver rise to acetylcholine induced

currents (221). It has been suggested that the reconstituted membranes retain their lipid environment after fusion with the oocyte plasma membrane (238). The lack of channel activity is consistent with PC-nAChR adopting an uncoupled conformation where agonist binding is "uncoupled" from channel gating. In contrast, the injection of either aso-GLIC or PC-GLIC into oocytes led to proton activated currents across the plasma membrane suggesting that GLIC is functional in both membrane environments (Figure 7.8). This conclusion is consistent with structural and peptide N-^{1}H/N-^{2}H exchange characteristics of both aso-GLIC and PC-GLIC, which suggest a resting-like conformation in both membranes (221).

Given the infrared data suggesting a resting conformation for PC-ELIC, we expected that the injection of PC-ELIC membranes into oocytes would lead to the appearance of cysteamine-induced currents across the oocyte plasma membrane, as observed with aso-ELIC. Despite numerous attempts under varying conditions (varying amounts of PC-ELIC and varying characterization times after injection), however, we were unable to see a dose-response to cysteamine suggesting that agonist binding and gating are, at best, weakly coupled in PC membranes (Figure 7.8). Although ELIC does not adopt an uncoupled conformation identical to that of the nAChR, ELIC function is sensitive to the surrounding membrane environment. A simple PC bilayer is not sufficient to promote optimal coupling of agonist binding to channel gating.

7.6 Discussion

Cholesterol and anionic lipids are required in a reconstituted membrane to obtain optimal nAChR function (181,205-207,222-227,239), although membrane physical properties play a role (212). Membranes influence function by both conformational selection and kinetic mechanisms. In other words, they stabilize differing proportions of activatable versus non-activatable conformations (209,225), and influence the rates of transitions between these conformations, respectively (212). Lipids may exert these effects by interacting with interstitial sites between different α-helices in the transmembrane domain (240,241) or by interacting with the lipid-protein interface (208,240,242,243)

Recent studies have focused on the potential role for the most lipid exposed transmembrane α-helix, M4, in lipid sensing (229-231). The C-terminus of M4 (post-M4) extends beyond the lipid bilayer to interact directly with the Cys-loop, one of the key structures implicated in the allosteric pathway leading from the agonist-site to the channel gate (244,245). Lipids could influence nAChR gating by altering the binding of M4 to its adjacent transmembrane α-helices, M1 and M3, thus influencing post-M4/Cys-loop interactions. The hypothesis that a lipid-dependent modulation of post-M4/Cys-loop interactions alters channel gating is supported by considerable anecdotal data (see (208)), but direct testing still requires functional studies performed on site-directed nAChR mutants reconstituted into different membrane environments.

Given the difficulties expressing nAChRs in sufficient quantities for structural studies (232), we have turned to the prokaryotic pLGICs, GLIC and ELIC, to investigate the underlying mechanisms of pLGIC lipid sensing. The first step in such mechanistic studies is the non-

trivial requirement to reconstitute folded and functional ELIC and GLIC into model membranes. While the membrane reconstitution of folded and functional GLIC is relatively straightforward (221), generating folded membrane reconstituted ELIC proved to be more problematic. We found the structural integrity of ELIC to be sensitive to a variety of environmental factors (see Results). The thermal stabilities of aso-ELIC and PC-ELIC are both lower than the stabilities of aso-GLIC and PC-GLIC (Table 1). As discussed below, the reduced structural stability of ELIC relative to GLIC may correlate with a greater functional sensitivity to lipids.

With minor alterations to our purification, membrane reconstitution, and sample preparation protocols, we reproducibly generated folded and functional ELIC in asolectin membranes. Specifically, aso-ELIC exhibits the expected mixed α-helix/β-sheet secondary structure with both a substantial portion of the polypeptide backbone undergoing rapid peptide N-^{1}H/N-^{2}H exchange, and another portion resistant to peptide N-^{1}H/N-^{2}H exchange after prolonged exposure to $^{2}H_2O$. The former population is likely due to those peptide hydrogens located primarily in loop structures of the ABD that are exposed to aqueous solvent. The latter is likely due to α-helical peptide hydrogens found in the TMD. Aso-ELIC undergoes thermal denaturation at temperatures slightly above the nAChR. In addition, injection of aso-ELIC into frog oocytes led to the appearance of cysteamine-induced currents across the plasma membrane, showing that aso-ELIC undergoes channel gating in response to agonist binding. The structure and biophysical properties of membrane incorporated ELIC are similar to those of membrane incorporated GLIC and the nAChR (208,221,232).

A key goal of this work was to examine the structural and functional properties of ELIC in the minimal PC membranes that stabilize an uncoupled nAChR. The uncoupled nAChR is

distinguished from resting or desensitized nAChRs by enhanced levels of peptide N-^{1}H/N-^{2}H exchange after prolonged exposure to $^{2}H_2O$, suggesting that peptide hydrogens normally buried from aqueous solvent become solvent exposed. The uncoupled nAChR also has a slightly lower thermal denaturation temperature, and the cooperativity of unfolding is reduced. It has been suggested that reduced physical interactions leading to an increased physical separation between the ABD and TMD accounts for the structural, biophysical, and functional properties of the uncoupled PC-nAChR (208,221,232).

We noted previously that PC-GLIC does not exhibit the structural and biophysical properties characteristic of the uncoupled state (221). PC-GLIC also retains the ability to undergo agonist-induced channel gating. The GLIC TMD thus does not require "activating lipids" to maintain effective coupling of agonist binding to channel gating.

In contrast, we found that the structure and functional properties of ELIC in PC membranes are distinct from those of both the nAChR and GLIC. On the one hand, PC-ELIC does not exhibit structural features characteristic of the uncoupled conformation. Specifically, the ELIC peptide hydrogen exchange kinetics are similar in both asolectin and PC membranes. PC-ELIC also undergoes thermal denaturation at temperatures that are slightly higher than that of aso-ELIC. On the other hand, injection of PC-ELIC into frog oocytes, does not lead to the appearance of cysteamine-induced currents suggesting that the minimal PC membranes are not sufficient to promote channel gating. While PC-ELIC does not adopt an uncoupled conformation equivalent to the uncoupled PC-nAChR, the efficiency of channel gating in ELIC is greatly reduced. ELIC is thus more sensitive to its membrane environment than GLIC.

Comparison of the GLIC, ELIC, and nAChR structures reveals elements that may contribute to the variable lipid sensitivities. The reduced propensity of GLIC to adopt an uncoupled conformation may reflect the extensive aromatic network at the interface between the transmembrane α-helices. Aromatic interactions promote M4 binding during folding of the homologous glycine receptor (214). In the context of the M4 lipid-sensor model, the extensive aromatic network at the interface between M4 and M1+M3 in GLIC (Figure 7.1B) may lead to high affinity binding of M4 to M1+M3 even in PC membranes lacking "activating lipids". The intramembrane aromatic interactions may reduce the propensity of GLIC to adopt an uncoupled conformation.

ELIC has fewer aromatic interactions at the M1/M3/M4 interface than GLIC, but more than the nAChR. The aromatic interactions at this interface in ELIC are also located exclusively between the bilayer center and the cytoplasmic side of the bilayer - ELIC lacks the three interacting aromatic residues found in GLIC near the extracellular membrane surface. One possible explanation for our data is that the available aromatic interactions located at the M1/M3/M4 interface are sufficient to stabilize a conformation where M4 is bound relatively tightly to M1+M3 during purification and reconstitution of ELIC into PC bilayer, whereas the lack of comparable aromatic interactions in the nAChR leads to a conformation where M4 binding is lost. The absence of aromatic interactions in ELIC near the extracellular surface, however, may weaken interactions between post-M4 to M1+M3 so that in PC membranes ineffective interactions between post-M4 and the Cys-loop inhibit channel gating. This interpretation is consistent with the ELIC crystal structures, where the final five residues in post-M4 are unresolved and thus do not stably interact with the Cys-loop.

Significantly, it has been suggested that the crystallized ELIC does not undergo channel gating (191,220)

Finally, it is intriguing that while ELIC exhibits a greater propensity to adopt a conformation in PC membranes where the coupling of binding and gating is ineffective, the EC_{50} for cysteamine-induced channel gating is the same with oocytes that are injected with aso-ELIC (1.12 ± 0.4 mM) or ELIC cRNA (1.01 ± 0.2 mM). In contrast, the EC_{50} for proton-induced gating of GLIC is different with oocytes injected with aso-GLIC and GLIC cRNA. A shifted EC_{50} is also observed in electrophysiological studies of high lipid-protein ratio GLIC asolectin proteoliposomes (246). Proton-induced gating of GLIC is thus sensitive to its membrane environment. One speculative interpretation is that the differences in EC_{50} reflect the involvement of an intramembrane protonation site in gating (247) - such a site could be sensitive to its surrounding lipids. A role for an intramembrane proton binding site in channel gating would also account for the varying EC_{50} values observed when GLIC is expressed HEK cells versus frog oocytes (219,247).

In summary, we have developed a protocol that reproducibly leads to membrane reconstituted ELIC that adopts a folded and functional conformation. We show that ELIC exhibits different structural and functional sensitivities to lipids than both GLIC and the nAChR. Future mutagenesis studies combined with more extensive electrophysiological characterization should allow us test specific mechanistic hypotheses to explain the different lipid sensitivities of GLIC and ELIC, and thus gain detailed insight into the mechanisms underlying pLGIC lipid sensing. Our data further point to a role of an intramembrane aromatic network at the interface between M4 and M1+M3 in both pLGIC structural stability and in lipid sensing.

8 MANUSCRIPT:

3. **Casey L. Carswell,** J.P. Daniel Therien, Peter D. Juranka, Julian A. Surujballi, and John E. Baenziger (2014) Intramembrane aromatics facilitate the gating of pentameric ligand-gated ion channels and govern susceptibility to potentiation. Submitted to the Journal of Neuroscience January 2014.

8.1 Preface

This is the third of three manuscripts included in this thesis. This manuscript was first submitted to the Journal of Neuroscience (January 2014). This paper examines the role of intramembrane aromatics on pLGIC function. Heterologous expression of aromatic addition and deletions into pLGIC mutants show that intramembrane aromatics influence function.

I constructed the homology model of ELIC, choose the aromatics to be tested and made the figures. Peter Juranka and I constructed the mutants of ELIC. I performed the electrophysiology experiments on the WT-ELIC and mutants of ELIC. Daniel Therien and Peter Juranka constructed the mutants of GLIC. Daniel Therien, Peter Juranka, and Julian Surujballi performed the electrophysiology experiments on the WT-GLIC and mutants of GLIC. I wrote the manuscript in collaboration with my supervisor.

8.2 Abstract

The gating of pentameric ligand gated ion channels is exquisitely sensitive to lipids. We show that the lipid exposed transmembrane α-helix, M4, is an allosteric regulatory element. M4 enhances gating when effectively bound to the adjacent α-helices, M1 and M3, but inhibits gating in the absence of effective interactions. Regulatable binding of M4 thus modulates the allosteric pathway leading from the agonist site to the transmembrane gate. Variable intramembrane aromatic interactions in pLGICs influence the binding of M4 to both M1 and M3 leading to variable efficiencies of channel gating, and thus variable susceptibilities to potentiation by transmembrane allosteric regulators.

8.3 Introduction

Many pharmaceuticals and endogenous compounds target the transmembrane domains (TMD) of pentameric ligand-gated ion channels (pLGICs) to alter channel gating and thus ultimately synaptic communication (181). Structural and biophysical studies have identified the sites of action for many TMD regulators, but the mechanism(s) by which TMD binding leads to altered channel activity remain(s) to be elucidated.

The TMD of the prototypic pLGIC, the nicotinic acetylcholine receptor (nAChR) from *Torpedo*, is sensitive to lipids, with increasing levels of cholesterol and anionic lipids stabilizing increasing proportions of agonist-responsive nAChRs (207,209,225-227,236). The transmembrane α-helix, M4, (one in each nAChR subunit) is likely the site for lipid sensing (229-231). M4 is exposed to the lipid bilayer and thus ideally situated to sense bilayer physico-chemical properties (189,228) (Figure 8.1B). Mutations in M4 influence channel gating, showing that changes in M4 structure influence the primary allosteric path leading from the agonist site to the channel gate (180,248-252). Significantly, the C-terminus of M4 (post-M4) extends beyond the lipid bilayer to interact with the Cys-loop, a key structure linking the agonist site and channel gate (244,245). It has been suggested that effective interactions between post-M4 and the Cys-loop are required for the Cys-loop to adopt a conformation that participates effectively in channel gating (208). Activating lipids could enhance channel gating by promoting M4 binding to M1+M3 to strengthen post-M4/Cys-loop interactions (208,212).

Intramembrane aromatic interactions play a critical role driving the binding of M4 to M1+M3 during folding of the homologous glycine receptor (214). If aromatics drive M4 binding during folding, they must also influence the affinity of M4 for M1+M3 in the folded

Figure 8.1

The structural basis for pLGIC lipid sensing. **(A)** A side view of the unliganded resting state *Torpedo* nAChR, with the γ-subunit shown in blue (pdb code 2BG9). The agonist site Trp-149 of both α-subunits is highlighted as orange sticks. (**B)** A surface view of the transmembrane domain showing the transmembrane α-helices, M1 to M4, of the αδ-subunit in white. **(C)** A schematic of a single subunit showing the proposed role of M4 as an allosteric regulator of gating. The arrow denotes the allosteric pathway leading from the agonist site to the transmembrane gate. "Ineffective" interactions between M4 and M1/M3 are represented by a tilting of M4 away from M1/M3. Aromatic additions and deletions are used here to modulate the binding of M4 to M1/M3. **(D)** The transmembrane domain of a single subunit from the nAChR (α-subunit, left), GLIC (center; pdb code 4HFI) and ELIC (right; pdb code 2VL0), with aromatic residues at the M1/M3/M4 interface shown as blue sticks. Note that the view of the TMD in **(C)** is rotated 180° about the subunit long axis relative to the side views in (**D)** to highlight the agonist binding site.

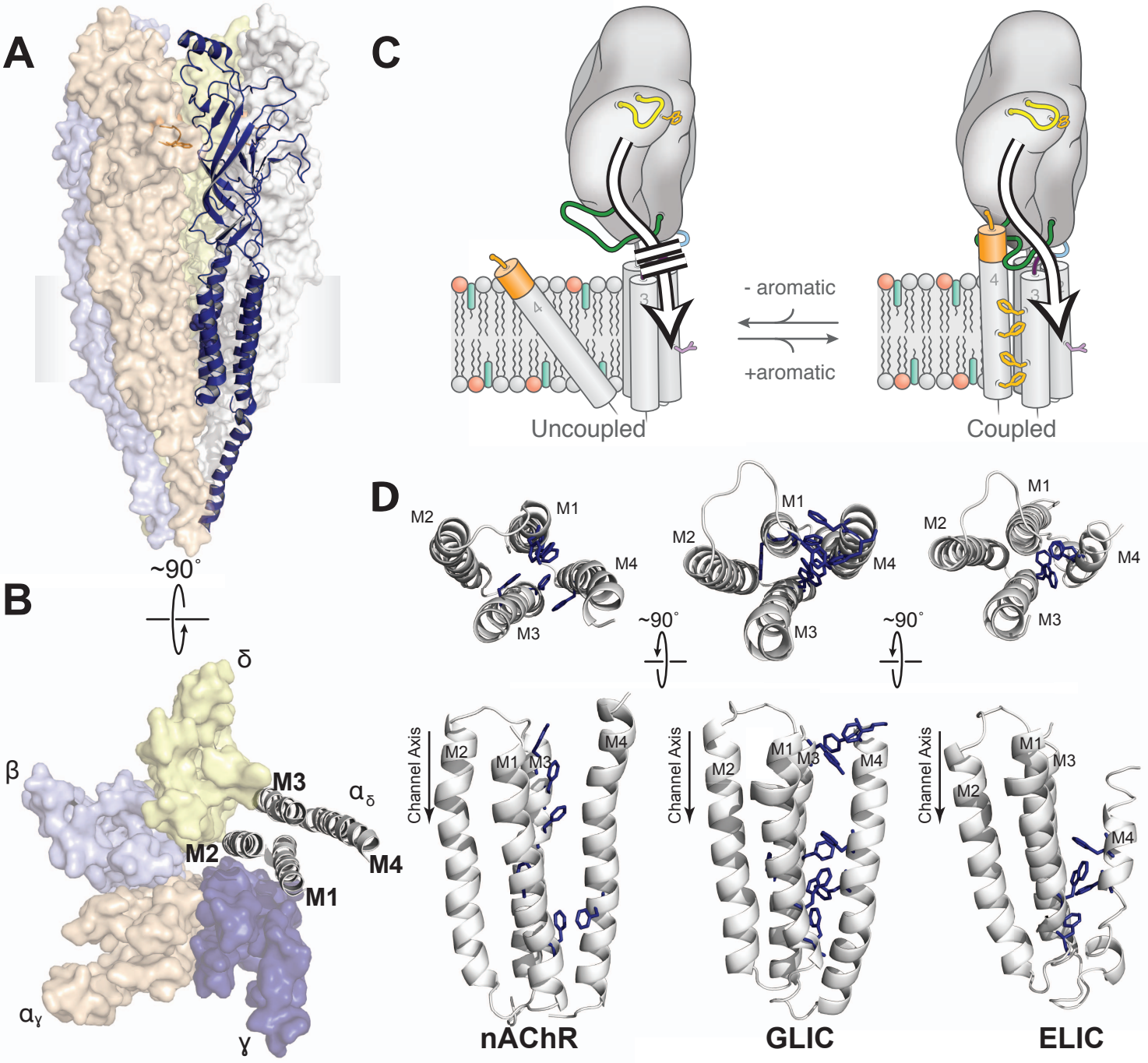
A
B
~90˚
δ
β
M3
αδ
M2
M4
M1
αγ
γ
C
- aromatic
+aromatic
Uncoupled
Coupled
D
M2
M1
M4
M3
~90˚
Channel Axis
nAChR
GLIC
ELIC

state. Surprisingly, different pLGICs exhibit different levels of aromatic residues at the M1/M3/M4 interface (Figure 8.1D) (189,217,253), raising the possibility that different pLGICs exhibit different M4 binding affinities. The M4 lipid sensor model predicts that variable M4 binding will lead to variable efficiencies of channel gating. Weaker M4 binding leading to less efficient gating should also render pLGICs more susceptible to potentiation by activating lipids or other TMD allosteric regulators.

Here we examine the role of intramembrane aromatic interactions in the gating of pLGICs. Consistent with our hypothesis, we find that eliminating intramembrane aromatic interactions at the M1/M3/M4 interface inhibit, while adding new aromatic interactions promote channel gating. Our findings show that M4 is an allosteric regulatory element and that pLGICs with few intramembrane aromatic interactions are inefficient at gating and thus have a greater potential for "potentiation".

8.4 Experimental Procedures

8.4.1 DNA constructs for oocyte expression. ELIC-pTLN was kindly provided by Dr. Raimund Dutzler (254). A C-terminal alanine, a cloning artifact not present in the Genbank sequence (accession number POC7B7), was removed. GLIC-pMT$_3$ was kindly provided by Pierre-Jean Corringer (219). The GLIC coding sequence was transferred to pSP64 without the hemagluttinin tag. Both the GLIC and ELIC plasmids have the α7 nAChR signal sequence followed by the GLIC or ELIC coding sequence. ELIC-pTLN and GLIC-pSP64 were linearized by *MluI* and *EcoRI*, respectively and used to produce capped cRNA by *in vitro* transcription using the mMESSAGE mMACHINE® SP6 kit (Ambion). All mutants were created using QuikChange™ Site Directed Mutagenesis kits (Agilent) and verified by sequencing.

8.4.2 Electrophysiology. Stage V-VI oocytes were isolated as previously described (255). Oocytes were injected with the indicated amount of cRNA and allowed to incubate one to four days at 16˚C in ND96+ buffer (5 mM HEPES, 96 mM NaCl, 2 mM KCl, 1 mM $MgCl_2$, 1 mM $CaCl_2$, and 2 mM pyruvate). Injected oocytes were placed in a RC-1Z oocyte chamber (Harvard Apparatus; Hamden, CT) containing the appropriate buffer (see below). Whole cell currents were recorded using a two electrode voltage clamp apparatus (OC-725C oocyte clamp; Holliston, MA). The whole cell currents were recorded while flowing the appropriate buffer through the oocyte chamber at a rate of 5 - 10 ml/min.

For GLIC, whole cell currents were recorded from injected oocytes (3 ng - 13 ng cRNA) immersed in MES buffer (140 mM NaCl, 2.8 mM KCl, 2 mM $MgCl_2$, and 10 mM MES).

Currents through the plasma membrane in response to pH jumps (pH 7.3 down to the indicated pH values) were measured with the transmembrane voltage clamped at voltages between -10 mV and -60 mV depending on the level of expression of each mutant GLIC. In the majority of cases, the holding potential was -20 mV. For ELIC, whole cell currents were recorded from injected oocytes (0.2 ng - 10 ng cRNA) immersed HEPES buffer (150 mM NaCl, 0.5 mM $BaCl_2$ and 10 mM HEPES, pH 7.0). Currents through the plasma membrane in response to cysteamine concentration jumps (from 0 mM up to the indicated values) were measured with the transmembrane voltage clamped at -40 mV.

8.4.3 Data Analysis. Dose responses for each mutant were acquired from at least two different batches of oocytes. Each individual dose-response experiment was fit with a sigmoidal dose-response (variable slope) and the individual EC_{50} and Hill coefficients from each experiment averaged to give the values ±standard deviation in Table 1. The I_{max} for each individual oocyte was determined independently thus normalizing expression levels. For the presented dose-response curves, the individual dose responses for each experiment were normalized, and then each data point averaged. Curve fits of the averaged data are presented in Figures 8.2 and 8.3, with the error bars referring to the standard error.

8.4.4 Homology Model. The homology model of ELIC was constructed using Swiss-Model (138) using GLIC (pdb code 3EHZ) as a template. The majority (95%) of the y and f angles of the model (the entire ELIC structure) are found in allowable regions of the Ramachandran plot (256). The homology model of ELIC was constructed to model the post M4 region in order to determine residues for aromatic substitution.

8.5 Results

The prokaryotic pLGIC, GLIC, exhibits an extensive network of intramembrane aromatic residues at the interface between M4 and M1/M3, with one cluster of three aromatic residues located near the extracellular surface of the membrane (the "post-M4 cluster") and another cluster of five aromatic residues located in the intracellular half of the membrane (the "intracellular cluster"). The close homolog, ELIC, exhibits analogous aromatic residues at the M1/M3/M4 interface, but lacks the entire post-M4 cluster and two of the aromatic residues that in GLIC are situated near the bilayer center. Through aromatic substitutions and additions to the interface between M4 and M1/M3 in both GLIC and ELIC, respectively, we modulate the binding of M4 to test the hypothesized role of intramembrane aromatics in pLGIC gating, and thus the role of M4 as an allosteric regulatory element.

8.5.1 Aromatic deletions in GLIC We first mutated each of the extra aromatic residues in GLIC to alanine, and then characterized the effects of the individual alanine substitutions on the ability of proton binding to elicit channel gating. Each individual mutation led to a right shift in the EC_{50} (i.e. the pH_{50}) for activation (Figure 8.2 and Table 8.1). Given that these mutations involve alanine substitutions of aromatic residues (i.e. neither type of side chain reversibly binds protons over the studied pH range) and that the proton binding sites are distant from the TMD (201), the changes in EC_{50} can be attributed to a reduction in the efficiency for coupling agonist binding to channel gating. We also simultaneously substituted interacting pairs of aromatic residues with alanine residues, but none of the double mutants gave observable proton activated currents. The absence of current could reflect impaired coupling of binding to gating and/or an inability of the GLIC mutants to fold and then traffic to the cell surface (214). Even the lack of trafficking to the cell surface may,

Figure 8.2

Gating is inhibited by aromatic deletions at the M1/M3/M4 interface of GLIC. **(A)** The GLIC TMD highlighting aromatic residues at the M1/M3/M4 interface (pdb code 4HFI). Aromatic residues found in both GLIC and ELIC are shown in yellow. Aromatic residues only found in GLIC are shown in red. **(B)** Representative pH dose response whole cell currents recorded from wild type (WT) GLIC and select GLIC mutants. The horizontal bars represent the time periods for the pH jumps from 7.3 to the indicated pH values. **(C)** pH dose response curves for the alanine substitutions in GLIC. See also Table 8.1.

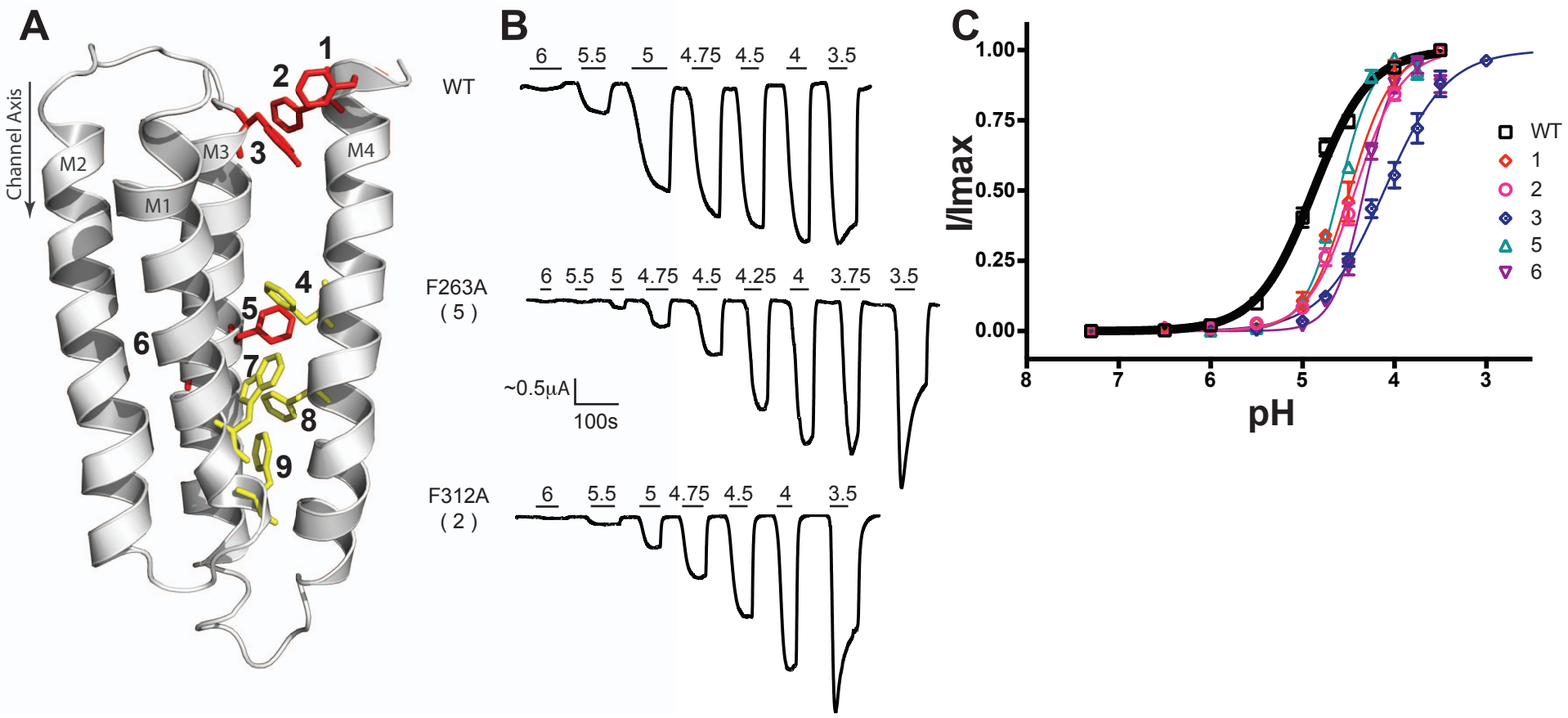
A
Channel Axis
M2
M1
M3
M4
1
2
3
4
5
6
7
8
9
B
WT
6 5.5 5 4.75 4.5 4 3.5
F263A
(5)
6 5.5 5 4.75 4.5 4.25 4 3.75 3.5
~0.5μA
100s
F312A
(2)
6 5.5 5 4.75 4.5 4 3.5
C
I/Imax
1.00
0.75
0.50
0.25
0.00
8 7 6 5 4 3
pH
WT
1
2
3
5
6

Table 8.1 Effects of Aromatic Deletions and Additions on pLGIC Gating

Aromatic Number	Mutant	Dose Response[1]			Imax Values[2]		
		EC50	Hill Slope	n	Imax (μA)	ng injected	n
GLIC							
	WT	4.89 ± 0.11	1.42 ± 0.49	22	2.95 ± 1.25	3.3	6
1	**F313A**	4.53 ± 0.01	1.71 ± 0.07	7	1.31 ± 0.28	3.3	4
2	**F312A**	4.40 ± 0.02	1.61 ± 0.11	11	2.23 ± 0.95	3.3	6
3	**Y252A**	4.60 ± 0.04	2.34 ± 0.31	12	4.87 ± 1.36[3]	24	10
5	**F263A**	4.32 ± 0.04	2.75 ± 1.19	12	2.47 ± 0.96[4]	23	11
6	**Y264A**	4.11 ± 0.20	1.38 ± 0.27	24	3.67 ± 1.21[3]	22	24
1 + 2	**F312A+F313A**				No Current[5]	21	10
1 + 3	**F312A+Y252**				No Current[5]	17	4
2 + 3	**F313A+Y252A**				No Current[5]	24	8
5 + 6	**F263A + Y264A**				No Current[5]	15	4
1 + 2 + 3	**F313A + F312A + Y252A**						
1 + 2 + 3 + 5 + 6	**F313A + F312A + Y252A + F263A + Y264A**						
ELIC							
	WT	1.01 ± 0.20	2.13 ± 0.36	11	2.77 ± 0.91	0.2	11
1	**I319F**	0.62 ± 0.18	2.48 ± 0.40	6	4.68 ± 1.45	0.2	6
2	**G318F**	0.44 ± 0.09	2.69 ± 1.05	13	3.43 ± 2.65	0.2	8
3	**V260Y**	0.47 ± 0.21	2.37 ± 0.33	4	1.35 ± 0.38	0.2	4
5	**S271F**	0.50 ± 0.21	3.44 ± 0.91	10	3.19 ± 0.38	0.4	3
6	**I272Y**	0.59 ± 0.14	2.55 ± 0.33	10	2.80 ± 0.87[6]	0.6	4
1 + 2	**I319F + G318F**	0.73 ± 0.37	3.19 ± 0.83	8	2.40 ± 0.12	0.2	2
1 + 3	**I319F + V260Y**	0.13 ± 0.05	3.01 ± 1.08	6	2.69 ± 0.76	0.4	6
2 + 3	**G318F + V260Y**	0.13 ± 0.05	2.51 ± 0.40	6	4.47 ± 3.28	0.4	6
5 + 6	**S271F + I272Y**	0.26 ± 0.09	2.24 ± 0.24	8	2.98 ± 2.77[6]	0.6	4
1 + 2 + 3	**I319F + G318F + V260Y**	0.18 ± 0.02	2.60 ± 0.16	9	2.97 ± 1.73	0.4	9
1 + 2 + 3 + 5 + 6	**I319F + G318F + V260Y+ S271F + I272Y**	0.15 ± 0.04	2.59 ± 0.35	7	1.41 ± 1.73[6]	5.0	3

[1] measurements performed 1-4 days after cRNA injection; V_{hold} ranging from -10 to -60 mV (3 - 13 ng GLIC RNA injected / 0.2 - 10 ng ELIC RNA injected))

[2] recorded (except where noted) 1 day after RNA injection with a V_{Hold} of -20 mV (GLIC) or -40mV (ELIC)

[3] measured after 4 days at a V_{hold} of -20mV

[4] measured after 4 days at a V_{hold} of -40mV

[5] no significant current observed after 4 days

[6] measured after 2 days at a V_{hold} of -40mV

however, reflect impaired binding of M4 to M1+M3, which in neuronal nAChRs is required to mask an endoplasmic retention signal located on M1 (257,258).

8.5.2 Aromatic additions to ELIC. Although the detrimental effects of the aromatic substitutions show that aromatic interactions at the interface between M4 and M1+M3 of GLIC are important, they do not prove that M4 is an allosteric regulatory element. The detrimental effects could simply reflect impaired inter-α-helix transmembrane packing, as a result of the loss of the bulky aromatic rings, leading to a TMD that is less efficient at gating. Moreover, they do not show that regulatable M4 binding to M1+M3 influences the efficiency of channel gating. ELIC, however, has fewer aromatic interactions at the M1/M3/M4 interface. If the lower number of aromatic residues leads to intrinsically weaker M4 binding to M1+M3 and less efficient gating, then the addition of aromatic interactions to promote M4 binding could improve the efficiency of channel gating - as long as the added aromatics do not lead to steric and/or chemical conflicts. ELIC thus offers the opportunity to test whether regulatable binding of M4 to M1+M3 modulates the efficiency of channel gating.

With limited structural data, it is not possible to precisely engineer optimal aromatic interactions at the M1/M3/M4 interface in ELIC. Consequently, we simply added the extra aromatic residues found at the M1/M3/M4 interface of GLIC into ELIC with the hope that some of these additions would lead to improved M4 binding. To our surprise, each of the five individual aromatic additions into ELIC shifted the EC_{50} to lower concentrations of cysteamine, whether or not interacting aromatic partners on the adjacent transmembrane α-helices are present (Figure 8.3 and Table 8.1). The left shifts in the EC_{50} observed with aromatic additions to ELIC contrast the right shifts in EC_{50} observed with aromatic deletions

Figure 8.3

Gating is potentiated by aromatic additions to the M1/M3/M4 interface of ELIC. **(A)** A homology model of the ELIC TMD (built on the GLIC structure) highlighting aromatic residues at the M1/M3/M4 interface that are conserved in both ELIC and GLIC as yellow sticks. Positions where aromatic residues are found only in GLIC are highlighted as red sticks. Each of the latter residues in ELIC was changed to the corresponding aromatic residue in the GLIC structure. **(B)** Representative cysteamine dose response whole cell currents recorded from wild type (WT) ELIC and select ELIC mutants. The horizontal bars represent the time periods for exposure to the indicated mM concentrations of cysteamine. **(C*)*** Cysteamine dose response curves for the aromatic additions into ELIC. Single and multiple substitutions are shown in the top and bottom panels, respectively. See also Table 8.1

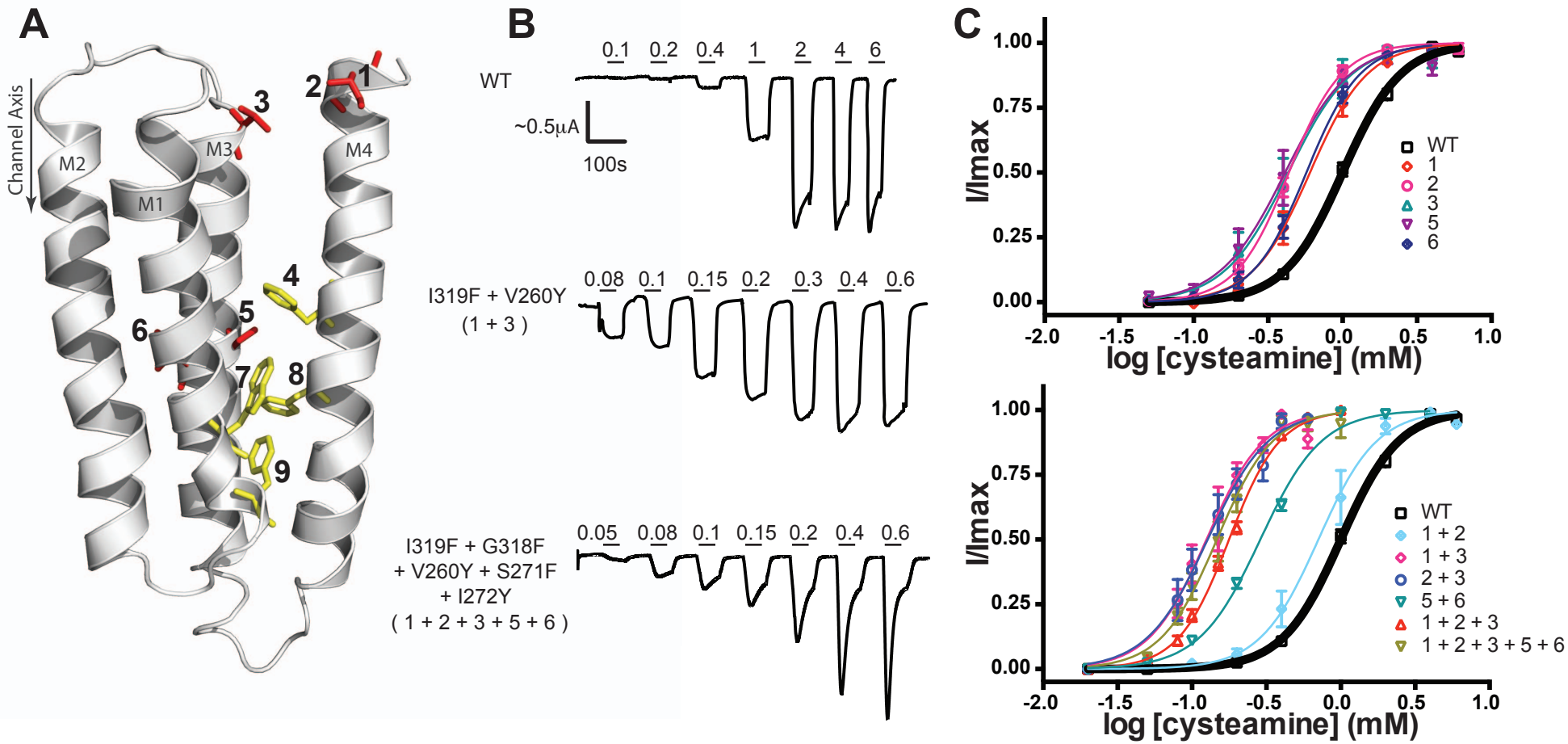
A
Channel Axis
M2
M1
M3
M4
1
2
3
4
5
6
7
8
9
B
WT
0.1 0.2 0.4 1 2 4 6
~0.5μA
100s
I319F + V260Y
(1 + 3)
0.08 0.1 0.15 0.2 0.3 0.4 0.6
I319F + G318F
+ V260Y + S271F
+ I272Y
(1 + 2 + 3 + 5 + 6)
0.05 0.08 0.1 0.15 0.2 0.4 0.6
C
I/Imax
log [cysteamine] (mM)
WT
1
2
3
5
6
1 + 2
1 + 3
2 + 3
5 + 6
1 + 2 + 3
1 + 2 + 3 + 5 + 6

from GLIC. The left shifts reflect a gain, as opposed to a loss in the efficiency of channel gating.

We next generated ELIC mutants with multiple aromatic additions, again using GLIC as a model. Again to our surprise, all but one of the multiple aromatic additions led to even lower EC_{50} values for channel gating. Engineering either the post-M4 aromatic cluster or the entire aromatic network of GLIC into ELIC shifted the EC_{50} down to ~0.1 mM cysteamine, a value roughly 10% of the EC_{50} value of wild type ELIC. Even the introduction of just two interacting aromatic partners on adjacent α-helices in the post-M4 cluster led to maximal shifts in EC_{50}. The maximal left shifts in the EC_{50} reflect a 10-fold gain in the efficiency of channel gating. Clearly, the addition of aromatic residues at the M1/M3/M4 interface enhances M4 binding to M1+M3 in a manner that potentiates channel activity.

The data show clearly that by modulating the binding of M4 to M1+M3 with aromatic deletions or additions, the coupling of agonist binding to channel gating is affected. Note that many of the aromatic deletions and additions to GLIC and ELIC, respectively, not only influence the efficiency of channel gating, but also change the desensitization kinetics, as observed by the altered rates of decay of some of the whole cell current responses (Figures 8.2 and 8.3). Although not explored further here, the data suggest that M4 binding to the adjacent transmembrane α-helices M1/M3 influences the desensitization kinetics.

8.6 Discussion

Our data show that the lipid exposed transmembrane α-helix, M4, is an allosteric regulatory element in the gating of pLGICs. Factors that inhibit M4 binding, inhibit the gating of pLGICs. Factors that promote effective M4 binding to M1+M3 enhance the gating of pLGICs. Specifically, aromatic deletions at the M1/M3/M4 interface of GLIC, which hinder M4 binding to M1+M3 (214), inhibit or eliminate channel gating, while the addition of aromatics to the M1/M3/M4 interface of ELIC, which enhance M4 binding, potentiate channel gating.

The consistency of the entire data set is quite remarkable. Every aromatic deletion at the M1/M3/M4 interface in GLIC inhibits channel activity relative to the wild type, while every aromatic addition in ELIC enhances channel activity relative to the wild type. The latter is most surprising because although aromatics enhance M4 binding to M1+M3 in the glycine receptor (214), we expected that some of the "non-optimized" aromatic additions in ELIC would lead to structural and/or chemical conflicts with residues on the adjacent TMD α-helices. The fact that every one of the aromatic additions potentiates activity highlights the ease at which effective interactions between M4 and M1+M3 can be enhanced to promote gating. The positive effects of the non-specific aromatic additions suggest that gating enhancement results from tighter binding of M4 to M1+M3, as opposed to specific inter-α-helix interactions that lead to precise orientations between the M1, M3 and M4 α-helices. The data show that intramembrane aromatics are critically important in the gating of pLGICs and that the low polarity/rigid aromatic ring, particularly of phenylalanine, is a basic structural feature that promotes transmembrane α-helix packing.

The relatively large gating enhancements observed with aromatic additions to the post-M4 region of ELIC highlight further the role for post-M4 in the modulation of channel gating. Post-M4 in both the nAChR and GLIC interacts directly with the β6-β7 loop (the so-called Cys-loop), an important link between the agonist site and the transmembrane gate (244,245). Tighter M4 binding to M1+M3 may facilitate interactions between post-M4 and the Cys-loop, leading to a Cys-loop conformation that participates optimally in channel gating (208). Consistent with this hypothesis, neurosteroids potentiate activity by interacting with post-M4 (259,260). In addition, post-M4 does not interact directly with the Cys-loop in the ELIC crystal structure (Figure 8.1). Significantly, crystallized ELIC does not undergo channel gating (220). The loss of post-M4/Cys-loop interactions, possibly as a consequence of detergent solubilization prior to crystallization, may lead to the uncoupling of binding and gating in ELIC (191).

The regulatory effects of M4 binding on channel gating support the proposed role of M4 as a lipid sensor and suggest the structural basis for lipid sensing in pLGICs. Although we alter M4 binding by aromatic substitutions/additions to the M1/M3/M4 interface, lipids could similarly influence M4 binding and thus channel gating by either direct interactions at the interfaces between M4 and either M1 or M3, as observed in the GLIC structure (216), or by altering the relative energies of M4 bound to M1+M3 versus M4 more solvated by lipid. The latter mechanism may account for the improved channel gating observed with a naturally occurring tryptophan substitution on the lipid facing surface of M4 in the muscle-type nAChR (180). Enhanced M4 binding may reduce unfavorable interactions between the bulky tryptophan and surrounding lipids.

Finally, our results show that different intramembrane aromatic networks between non-pore lining transmembrane α-helices in different pLGICs lead to variable M4 binding, different efficiencies of channel gating, and thus different potentials for TMD allosteric modulation. pLGICs with extensive aromatic networks, such as GLIC, may exhibit tighter binding of M4 to M1/M3, thus rendering the TMD less malleable and thus less sensitive to its lipid environment. Consistent with this postulate, GLIC still maintains efficient gating in lipid environments that stabilize an uncoupled nAChR (221). On the other hand, pLGICs with relatively few inter-α-helix aromatic interactions, such as ELIC and the nAChR, likely exhibit relatively weak, non-specific M4 binding, rendering the TMD relatively inefficient at coupling binding to gating and thus amenable to TMD potentiators. Consistent with this postulate, the gating of ELIC is more sensitive to membrane lipids than that of GLIC (data not shown). Intrinsically weak M4 binding may underlie the exquisite functional sensitivity of the nAChR to potentiating cholesterol and anionic lipids.

9 DISCUSSION / CONCLUSION

With over 50% of therapeutics targeting membrane proteins there is considerable interest in the acquisition of high resolution structural information to facilitate an understanding of membrane protein function and thus to help generate new therapeutics using rational drug design techniques. The structural characterization of membrane proteins is an evolving, technically challenging field. The objective of the research presented in this thesis was to structural characterize two prokaryotic membrane proteins to gain insight into their mechanisms of function.

9.1 Structural Characterization of CfrA

The majority of the work presented in this thesis was focused on CfrA, a TonB dependent transporter from *Campylobacter jejuni*. At the beginning of my Ph.D. research, the structure of CfrA was unknown. I successfully cloned, expressed, purified and reconstituted CfrA into model membranes. I then characterized the structure of membrane reconstituted CfrA by FTIR. The FTIR experiments revealed a predominantly β-strand secondary structure that is highly solvent exposed, and that exhibits a high thermal stability, biophysical properties that are all consistent with the biophysical properties of other TBDTs. More interestingly, the resulting homology model revealed the absence of conserved amino acids that have been shown to be critical for enterobactin binding/transport leading in other TBDTs. This observation led to the hypothesis that CfrA interacts with enterobactin differently than other enterobactin specific TBDT. The attractiveness of this hypothesis stems from the potential of CfrA as a *C. jejuni* specific therapeutic target. The potential specific targeting of *C.jejuni* strains could eliminate/hinder colonization liberating the substantial financial burden associated with *C. jejuni* infection.

To explore the molecular determinates of siderophore binding to CfrA, high resolution structural information was required. I therefore set out to crystallize CfrA and thus solve its crystal structure. A considerable amount of screening led to conditions resulting in the appearance of birefringence. These conditions underwent successive rounds of refinement to yield conditions that reproducibly produce large three-dimensional crystals. These refinements culminated in the production of a 5Å model of the CfrA β-barrel. Shortly afterwards, further screening revealed that improved CfrA crystals grew in the presence of iron. These crystals were the largest produced to date and diffracted to approximately 8 Å via home source. Unfortunately, logistics and time restraints did not allow a thorough screening of these new promising crystals at the ESRF. I believe that I have conditions that will produce a high resolution crystal structure of CfrA given consistent access to a synchrotron.

However, additional experiments focusing on facilitating an increase in crystal contacts could prove beneficial. The removal of the affinity tag present on the N-terminus of the protein would be my first concern. Replacing the enterokinase cleavage site with a more robust protease such as 3C HRV could aid in the formation of crystal-crystal contacts. Limited proteolysis may identify regions of the protein for removal to facilitate crystallization. In addition, decreasing the micellar belt surrounding the protein could be beneficial. Exploring detergent concentrations between 0.05 % and 0.1 % may yield a compromise between fragility and resolution.

The mechanism by which TBDT transport siderophores into the periplasm is highly debated with the consensus that a conformation change is required within the plug domain to facilitate transport. To investigate the dynamics of the plug domain, I set out to study the

isolated plug domain by NMR. I developed conditions for the expression, purification and structural characterization of the plug domain. The plug domain exhibits a mixed α/β secondary structure that undergoes complete ^{1}H-^{2}H exchange upon initial exposure to $^{2}H_2O$. The complete ^{1}H-^{2}H exchange was an interesting finding, as I would expect most globular protein to have a hydrophobic core with some peptide N-^{1}H that are resistant to ^{1}H-^{2}H exchange. For comparison, myoglobin, a soluble globular protein of equivalent size to the isolated plug domain does not undergo complete ^{1}H-^{2}H exchange after two and a half hours (176). Although anecdotal, this suggests a highly dynamic plug structure allowing high levels of solvent penetration.

Unfortunately, the apparent equilibrium of the plug domain between monomers and dimers complicates the analysis of the NMR experiment, thus conditions must be found that favor one state. The elimination of hydrophobic patches located on the mixed β-strand may abolish oligmer formation and facilitate the acquisition of NMR data. Regardless, the ability of the plug domain to fold, maintain a relatively stable dynamic structure, bind ligand, and refold after denaturation supports a hypothesis by which the plug domain partially/completely unfolds from the interior of the barrel to allow transport of the ferric-siderophore into the periplasm.

9.2 Structural and Functional Characterization of ELIC

The second goal of my thesis was to examine the role of intramembrane aromatic residues in both the lipid sensitivity and gating of pLGICs. The prokaryotic pLGIC, ELIC was first identified in 2005, and the crystal structure determined in 2008. At the start of this research project, the structural and functional characteristics of ELIC in different lipid membranes was unexplored (215,217). I successfully expressed, purified and reconstituted ELIC into

two model membrane systems and then compared its structure and propensity to adopt an uncoupled conformation to that of both the nAChR and GLIC in the same two membrane environments.

The nAChR is extremely sensitive to its lipid environment and adopts an uncoupled conformation in PC membranes characterized by increased levels of peptide ^{1}H-^{2}H exchange after prolonged exposure to $^{2}H_2O$, and by an inability to undergo agonist-induced conformational change (208). The increased levels of peptide ^{1}H-^{2}H exchange suggest the exposure of previously buried regions of the nAChR polypeptide backbone to solvent in the uncoupled state. This increased exposure may occur at the interface between the agonist binding and transmembrane gating domains. A physical separation between these two domains leading to weakened interactions at this interface could account for that inability of PC-nAChR to couple agonist binding to channel gating (208). In contrast, PC-GLIC does not adopt an uncoupled conformation. Specifically, both aso-GLIC and PC-GLIC have similar levels of peptide ^{1}H-^{2}H exchange after prolonged exposure to $^{2}H_2O$. PC-GLIC also undergoes agonist-induced conformational change, as detected subsequent to injection of the PC-GLIC membranes into *X. laevis* oocytes.

The structural characterization of membrane reconstituted ELIC presented here shows that ELIC exhibits an essentially identical mixed α/β structure in both asolectin and PC lipid membranes. No changes in the levels of peptide ^{1}H-^{2}H exchange were detected with ELIC in asolectin versus PC membranes, suggesting that ELIC in both bilayer environments adopts folded, coupled conformations. These data suggest that ELIC does not adopt a conformation in PC membranes similar to the uncoupled nAChR. However, in contrast to the injection of aso-ELIC into *X. laevis* oocytes, the injection of PC-ELIC did not lead to the appearance of

cysteamine-induced currents across the oocyte plasma membrane. It has been suggested that the reconstituted membranes retain their lipid environment after fusion with the oocyte plasma membrane (238). This suggests that the function of ELIC is abrogated in PC membranes. The minimal PC membranes do not appear sufficient to promote gating of ELIC. Note that based on the peptide hydrogen exchange data, PC-ELIC does not appear to adopt an uncoupled conformation equivalent to the uncoupled PC-nAChR. PC-ELIC must therefore adopt a structure somewhat intermediate between the uncoupled and coupled conformations observed in native membrane environments.

9.3 ELIC and the uncoupled state

ELIC has fewer aromatic interactions at the helical interface between M4 and M1+M3 compared to GLIC, but more than the nAChR. Intramembrane aromatic interactions are the driving force in the association of M4 with M1+M3 during folding of the GlyR (214). One possible explanation for my data is that the reduced number of aromatics at the helical interface between M4 and M1+M3 in ELIC leads to weaker M4 binding to M1+M3 than in GLIC. This might account for the noted increased sensitivity of ELIC to environmental factors compared to GLIC. It is plausible that fewer intramembrane aromatic interactions lead to an increased sensitivity to detergent. By comparison, the greater number of intramembrane aromatic interactions in GLIC may lead to stronger interactions between M4 and M1+M3 resulting in a protein that is less sensitive to detergent solubilization.

The argument becomes stronger when the nAChR is incorporated into the discussion. The nAChR has even fewer intramembrane aromatics than ELIC. Based on our hypothesized role for aromatics in M4 binding to M1+M3 and thus in uncoupling, the nAChR should be more sensitive to detergent solubilization and should exhibit a greater propensity to adopt an

uncoupled conformation. In agreement, it is well documented that lipids must always be present after detergent-solubilization for the nAChR to retain the ability to undergo agonist-induced conformational change (234). The absence of a high resolution crystal structure of the nAChR, despite its relative abundance, may also support the idea that fewer intramembrane aromatic interaction weaken the interactions between M4 and M1+M3. Crystallization requires a stable homogenous protein. If the interactions between M4 and M1+M3 are weak due to few aromatic interactions, the binding of M4 to M1+M3 may not be maintained after detergent-solubilization. Displacement of M4 away from M1+M3 may hinder crystallization of the nAChR.

The nAChR, ELIC and GLIC exhibit a gradient of intramembrane aromatic interactions at the helical interface between M4 and M1+M3 (nAChR<ELIC<GLIC). One notable difference between ELIC and GLIC, however, is that GLIC exhibits a cluster of aromatic residues between M4 and M1+M3 near the C-terminus of M4, while this post-M4 aromatic cluster is absent in ELIC. One explanation for our data is that the aromatic residues present in ELIC are sufficient to bind M4 to M1+M3 during purification and reconstitution so that ELIC adopts a conformation similar to that of coupled conformations. Due to the absence of the post-M4 aromatic cluster, the binding of post-M4 however may not be optimal in PC membranes to support gating. This hypothesis can be rationalized in terms of the crystal structure of ELIC. It was not possible to model the M4 as an α-helix. Most importantly, the final 5 residues in M4 (RTGIL) were not observed in the crystal structure, suggesting a relatively high degree of flexibility/mobility of post-M4 in the detergent solubilized state. As a result, there is no interaction between post-M4 and the β6-β7 loop, and the interactions between both the β1-β2 and β6-β7 loops with the M2-M3 linker are weakened, relative to

both the GLIC and nAChR structures. The ELIC crystal may represent the uncoupled conformation, which may be stabilized upon detergent solubilization. Consistent with this interpretation, no change in pore diameter was observed upon agonist binding to a crystallized ELIC mutant, which in *Xenopus* oocytes is stabilized in the open state and exhibits no propensity to desensitize (220). The lack of a detected agonist-induced conformational change supports the hypothesis that the ELIC adopts an uncoupled state in the detergent solubilized state.

9.4 Intramembrane aromatics interactions influence the propensity to form an uncoupled receptor

To test the hypothesis that increased intrahelical aromatic interactions promote M4 binding to M1+M3 thus leading to a reduced propensity to adopt an uncoupled conformation, I systematically introduced aromatic residues into ELIC at locations corresponding to the locations of aromatics in GLIC. To evaluate the effects of the aromatic substitutions on ELIC function, I heterologously expressed each mutant in *X. laevis* oocytes and characterized the gating response to cysteamine. Note that the mutations are distinct from the agonist binding side and therefore have no affect on the agonist binding affinity. All ELIC mutants tested showed a decrease in EC_{50} demonstrating an increase in coupling of agonist binding to channel gating. Consistent with the M4 lipid-sensor model, increased binding of M4 to M1+M3 does influence channel gating. In fact, the ELIC mutant with five aromatic substitutions yielded a 10 fold increase in EC_{50} compared to the wildtype. Such an increase in the efficiency of gating *in vivo* would result in dramatic affects on human biology. For example, similar changes in EC_{50} observed with a Cys to Trp mutation on the membrane exposed surface of the muscle-type nAChR lead to a severe myasthenic syndrome (180,249,261). In the context of the latter observation, our finding that altered M4 binding to

M1+M3 can influence the efficiency of gating 10-fold suggests that modulation of M4 binding to M1+M3 could play an important role in modulating synaptic communication.

I have demonstrated that increased intramembrane aromatic interaction leads to a greater propensity to adopt a coupled conformation. It is appealing to predict that the ELIC mutant with increased intramembrane aromatic interactions may be more stable upon detergent solubilization, and thus may adopt a functional conformation in the crystallized state.

9.5 Increased aromatic and lipid sensitivities *in vivo*?

It is also interesting to note that different nAChR subunits exhibit varying levels of aromatic residues at the interface between M4 and M1+M3. Figure 9.1 shows a sequence alignment of the predicted TM helices of different neuronal α-subunits, highlighting aromatic residues. Homology models of α_5, α_6 and α_7 subunits based on the α-subunit of the nAChR are also presented (Figure 9.2). The substantial differences in aromatic-aromatic interaction between subunits may translate into different affinities of M4 binding to M1+M3 leading to different efficiencies of gating.

9.6 Increased aromatic content and potentiation/inhibition *in vivo*?

Many general anesthetics influence pLGIC activity by binding to the transmembrane domain. Although some potentiate while others inhibit the activity of pLGICs, the mechanisms by which the anesthetic influence pLGIC activity remains elusive (181,262). The nAChR is extremely sensitive to its lipid environment and in the absence of activating lipids adopts an uncoupled conformation (208). M4 is ideally situated to convey the biophysical properties of the lipid bilayer to the protein, altering conformation. Lipids are proposed to allosterically modulate the nAChR by influencing the interactions between postM4 of the TMD with the β6-β7 loop of the ECD governing the propensity to adopt a

Figure 9.1

Sequence alignment of neuronal subunits of the nAChR. Predicted transmembrane α-helices are indicted below alignment with aromatic residues highlighted.

```
α7   204  KRSERFYECCK-EPYPDVTFTVTMRRRTLYYGLNLLIPCVLISALALLVFLLPADSGEKISLGITVLLSL  272
α4   217  TYNTRKYECCA-EIYPDITYAFVIRRLPLFYTINLIIPCLLISCLTVLVFYLPSECGEKITLCISVLLSL  285
α6   214  YKHDIKYNCCE-EIYTDITYSFYIRRLPMFYTINLIIPCLFISFLTVLVFYLPSDCGEKVTLCISVLLSL  282
α3   215  YKHDIKYNCCE-EIYPDITYSLYIRRLPLFYTINLIIPCLLISFLTVLVFYLPSDCGEKVTLCISVLLSL  283
α2   239  TYNSKKYDCCA-EIYPDVTYAFVIRRLPLFYTINLIIPCLLISCLTVLVFYLPSDCGEKITLCISVLLSL  307
α5   226  SKGNRTDSCC---WYPYVTYSFVIKRLPLFYTLFLIIPCIGLSFLTVLVFYLPSNEGEKICLCTSVLVSL  292
α1   229  WKHSVTYSCCPDTPYLDITYHFVMQRLPLYFIVNVIIPCLLFSFLTGLVFYLPTDSGEKMTLSISVLLSL  298
```

M1 M2

```
α7   273  TVFMLLVAEIMPATSDSVPLIAQYFASTMIIVGLSVVVTVIVLQYHHHDPDGG-KMPKWTRVILLNWCAW  341
α4   286  TVFLLLITEIIPSTSLVIPLIGEYLLFTMIFVTLSIVITVFVLNVHHRSPRTH-TMPTWVRRVFLDIVPR  354
α6   283  TVFLLVITETIPSTSLVVPLVGEYLLFTMIFVTLSIVVTVFVLNIHYRTPTTH-TMPRWVKTVFLKLLPQ  351
α3   284  TVFLLVITETIPSTSLVIPLIGEYLLFTMIFVTLSIVITVFVLNVHYRTPTTH-TMPSWVKTVFLNLLPR  352
α2   308  TVFLLLITEIIPSTSLVIPLIGEYLLFTMIFVTLSIVITVFVLNVHHRSPSTH-TMPHWVRGALLGCVPR  376
α5   293  TVFLLVIEEIIPSSSKVIPLIGEYLVFTMIFVTLSIMVTVFAINIHHRSSSTHNAMAPLVRKIFLHTLPK  362
α1   299  TVFLLVIVELIPSTSSAVPLIGKYMLFTMVFVIASIIITVIVINTHHRSPSTH-VMPNWVRKVFIDTIPN  367
```

M2 M3

```
α7   430  DPDLAKILEEVRYIANRFRCQDESEAVCSEWKFAACVVDRLCLMAFSVFTIICTIGILMSAPNFVEAVSK  499
α4   561  SPALTRAVEGVQYIADHLKAEDTDFSVKEDWKYVAMVIDRIFLWMFIIVCLLGTVGLFLPP----WLAGM  626
α6   426  SPEVEDVINSVQFIAENMKSHNETKEVEDDWKYVAMVVDRVFLWVFIIVCVFGTAGLFLQP----LLGN-  490
α3   438  SPEIKEAIQSVKYIAENMKAQNEAKEIQDDWKYVAMVIDRIFLWVFTLVCILGTAGLFLQP----LMAR-  502
α2   463  SPHMQKALEGVHYIADHLRSEDADSSVKEDWKYVAMVIDRIFLWLFIIVCFLGTIGLFLPP----FLAGM  528
α5   390  RNTLEAALDSIRYITRHIMKENDVREVVEDWKFIAQVLDRMFLWTFLFVSIVGSLGLFVPVI--YKWANI  457
α1   414  HPEVKSAIEGIKYIAETMKSDQESNNAAAEWKYVAMVMDHILLGVFMLVCIIGTLAVFAGRL--IELNQQ  481
```

M4

```
α7   500  DFA--------  502
α4   627  I----------  627
α6   491  TGKS-------  494
α3   503  EDA--------  505
α2   529  I----------  529
α5   458  LIPVHIGNANK  468
α1   482  G----------  482
```

Figure 9.2

Homology models of α_5-, α_6-, and α_7-subunit using the nAChR (2BG9) as a template illustrating intramembrane aromatics.

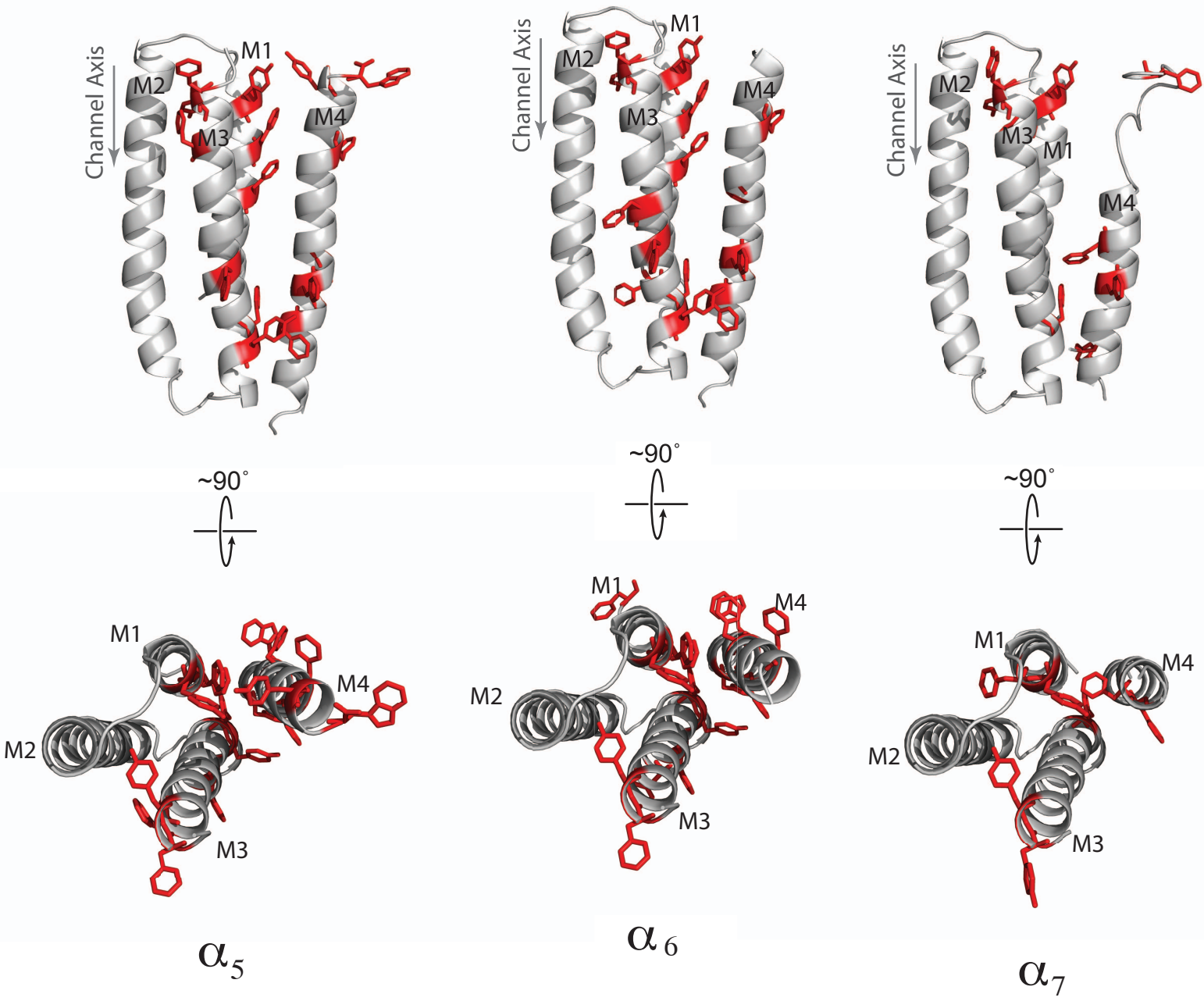
Channel Axis
M1
M2
M3
M4
~90˚
M1
M2
M3
M4
α5
Channel Axis
M1
M2
M3
M4
~90˚
M1
M2
M3
M4
α6
Channel Axis
M2
M3
M1
M4
~90˚
M1
M2
M3
M4
α7

coupled or uncouple protein conformation (208). The data presented in this thesis suggest that intramembrane aromatic interactions between M4 and M1+M3 influence the coupling of binding to gating. It is possible that general anesthetics modulate the efficiency of gating in the same manner – by influencing the interactions between M4 and M1+M3.

Recently, a structure of GLIC with propofol was published (263). Propofol is a general anesthetic that inhibits GLIC activation. The site of propofol binding is thought to be between M1 and M3 extending towards M4 (Figure 9.3). Comparing a previous structure of GLIC, presumed open, without propofol to the new structures reveals no difference in pore diameter suggesting that propofol has no direct influence on pore dimensions (263). One other possibility is that propofol binding influences interactions between M4 and M1+M3. Bound propofol extends out towards M4 and could weaken the interactions between M4 and M1+M3. If drugs, such as propofol, do influence M4 interactions with M1+M3, it is interesting to speculate that the dosage required to inhibit different neuronal nAChRs may be sensitive to the different levels of intramembrane aromatic residues at the interface between M4 and M1+M3. Aromatic mutants described in Chapter 8 could be used to probe the role of anesthetics in inhibition as described above. The aromatic mutant of ELIC with 5 aromatic additions resulted in a 10 fold increase in efficiency of gating suggesting a stronger interaction between M4 and M1+M3 compared to the wildtype ELIC. I predict that this aromatic mutant would be less sensitive to the inhibition by propofol due to the strong interactions between M4 and M1+M3. In contrast, I predict that the wildtype ELIC would be the most sensitive to inhibition by propofol, as the fewer intramembrane aromatic interactions at the M4 and M1+M3 interface likely result in weaker interactions between M4 and M1+M3.

Figure 9.3

Crystal structure of propofol bound to a pentameric ligand gated ion channel, GLIC (3P50) (263). In the crystal structure, propofol binds between M1 and M3 and extends towards M4 potentially inhibiting the interactions between M4 and the helical bundle.

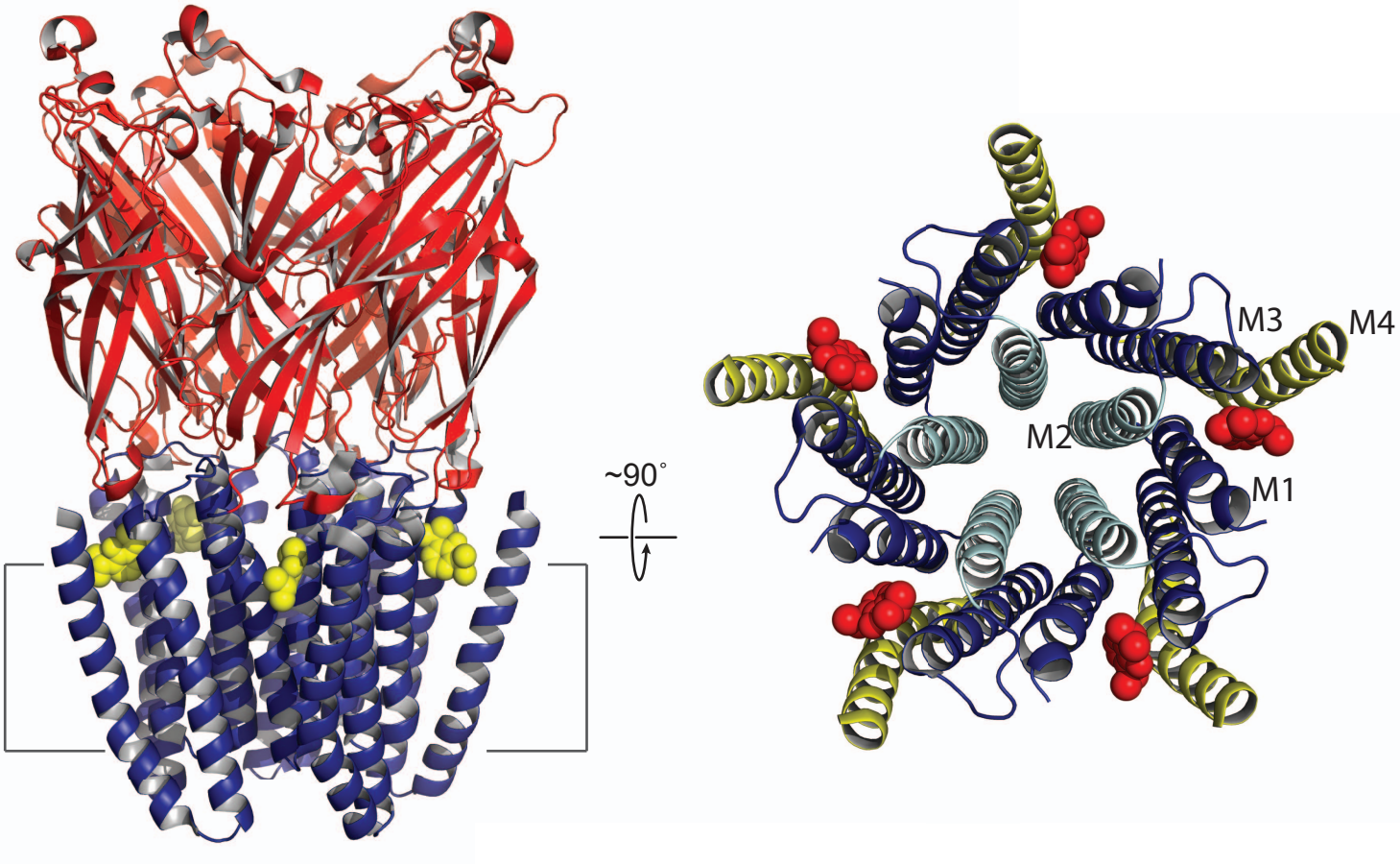
~90˚
M3
M4
M2
M1

With over 30% of the human genome predicted to be membrane proteins and over 50% of therapeutics targeted towards membrane proteins, structural characterization of membrane proteins is crucial. Further structural and functional characterization should lead to insight into both the mechanism of action of agonist and allosteric modulators that influence function. The work presented in this thesis shows substantial progress towards the structural and functional characterization of two integral membrane proteins: CfrA, a potential therapeutic target from *Campylobacter jejuni*, and ELIC, a model pentameric ligand gated ion channel, from *Erwinia chrysanthemi*.

10 REFERENCES

1. Krogh, A., Larsson, B., von Heijne, G., and Sonnhammer, E. L. (2001) Predicting transmembrane protein topology with a hidden Markov model: application to complete genomes. *J Mol Biol* **305**, 567-580
2. Arinaminpathy, Y., Khurana, E., Engelman, D. M., and Gerstein, M. B. (2009) Computational analysis of membrane proteins: the largest class of drug targets. *Drug discovery today* **14**, 1130-1135
3. Overington, J. P., Al-Lazikani, B., and Hopkins, A. L. (2006) How many drug targets are there? *Nat Rev Drug Discov* **5**, 993-996
4. Caffrey, M. (2003) Membrane protein crystallization. *J Struct Biol* **142**, 108-132
5. Tusnady, G. E., Dosztanyi, Z., and Simon, I. (2005) PDB_TM: selection and membrane localization of transmembrane proteins in the protein data bank. *Nucleic Acids Res* **33**, D275-278
6. Hedin, L. E., Illergard, K., and Elofsson, A. (2011) An Introduction to Membrane Proteins. *J Proteome Res* **10**, 3324-3331
7. Frelet-Barrand, A., Boutigny, S., Moyet, L., Deniaud, A., Seigneurin-Berny, D., Salvi, D., Bernaudat, F., Richaud, P., Pebay-Peyroula, E., Joyard, J., and Rolland, N. (2010) Lactococcus lactis, an alternative system for functional expression of peripheral and intrinsic Arabidopsis membrane proteins. *PLoS One* **5**, e8746
8. Lamping, E., and Cannon, R. D. (2010) Use of a yeast-based membrane protein expression technology to overexpress drug resistance efflux pumps. *Methods in molecular biology* **666**, 219-250
9. Jidenko, M., Lenoir, G., Fuentes, J. M., le Maire, M., and Jaxel, C. (2006) Expression in yeast and purification of a membrane protein, SERCA1a, using a biotinylated acceptor domain. *Protein expression and purification* **48**, 32-42
10. Chelikani, P., Reeves, P. J., Rajbhandary, U. L., and Khorana, H. G. (2006) The synthesis and high-level expression of a beta2-adrenergic receptor gene in a tetracycline-inducible stable mammalian cell line. *Protein Sci* **15**, 1433-1440
11. Werten, P. J. L., Remigy, H. W., de Groot, B. L., Fotiadis, D., Philippsen, A., Stahlberg, H., Grubmuller, H., and Engel, A. (2002) Progress in the analysis of membrane protein structure and function. *FEBS letters* **529**, 65-72
12. Kapust, R. B., and Waugh, D. S. (1999) Escherichia coli maltose-binding protein is uncommonly effective at promoting the solubility of polypeptides to which it is fused. *Protein Science* **8**, 1668-1674
13. Terpe, K. (2003) Overview of tag protein fusions: from molecular and biochemical fundamentals to commercial systems. *Applied microbiology and biotechnology* **60**, 523-533
14. Kefala, G., Kwiatkowski, W., Esquivies, L., Maslennikov, I., and Choe, S. (2007) Application of Mistic to improving the expression and membrane integration of histidine kinase receptors from Escherichia coli. *Journal of structural and functional genomics* **8**, 167-172
15. Albrecht, R., Zeth, K., Soding, J., Lupas, A., and Linke, D. (2006) Expression, crystallization and preliminary X-ray crystallographic studies of the outer membrane protein OmpW from Escherichia coli. *Acta Crystallogr Sect F Struct Biol Cryst Commun* **62**, 415-418
16. McPherson, A. (2004) Introduction to protein crystallization. *Methods* **34**, 254-265

17. Buchanan, S. K., Lukacik, P., Grizot, S., Ghirlando, R., Ali, M. M., Barnard, T. J., Jakes, K. S., Kienker, P. K., and Esser, L. (2007) Structure of colicin I receptor bound to the R-domain of colicin Ia: implications for protein import. *Embo J* **26**, 2594-2604
18. Cobessi, D., Celia, H., and Pattus, F. (2004) Crystallization and X-ray diffraction analyses of the outer membrane pyochelin receptor FptA from Pseudomonas aeruginosa. *Acta Crystallogr D Biol Crystallogr* **60**, 1919-1921
19. Smith, B. S., Kobe, B., Kurumbail, R., Buchanan, S. K., Venkatramani, L., Van Der Helm, D., and Deisenhofer, J. (1998) Crystallization and preliminary X-ray analysis of ferric enterobactin receptor FepA, an integral membrane protein from Escherichia coli. *Acta Crystallogr D Biol Crystallogr* **54**, 697-699
20. Pervushin, K., Riek, R., Wider, G., and Wuthrich, K. (1997) Attenuated T2 relaxation by mutual cancellation of dipole-dipole coupling and chemical shift anisotropy indicates an avenue to NMR structures of very large biological macromolecules in solution. *Proc Natl Acad Sci U S A* **94**, 12366-12371
21. Vanaken, T., Foxallvanaken, S., Castleman, S., and Fergusonmiller, S. (1986) Alkyl Glycoside Detergents - Synthesis and Applications to the Study of Membrane-Proteins. *Method Enzymol* **125**, 27-35
22. Thiyagarajan, P., and Tiede, D. M. (1994) Detergent Micelle Structure and Micelle-Micelle Interactions Determined by Small-Angle Neutron-Scattering under Solution Conditions Used for Membrane-Protein Crystallization. *J Phys Chem-Us* **98**, 10343-10351
23. Lipfert, J., Columbus, L., Chu, V. B., Lesley, S. A., and Doniach, S. (2007) Size and shape of detergent micelles determined by small-angle X-ray scattering. *The journal of physical chemistry. B* **111**, 12427-12438
24. Krueger-Koplin, R. D., Sorgen, P. L., Krueger-Koplin, S. T., Rivera-Torres, I. O., Cahill, S. M., Hicks, D. B., Grinius, L., Krulwich, T. A., and Girvin, M. E. (2004) An evaluation of detergents for NMR structural studies of membrane proteins. *J Biomol NMR* **28**, 43-57
25. Wuthrich, K. (1998) The second decade--into the third millenium. *Nat Struct Biol* **5 Suppl**, 492-495
26. Hwang, P. M., Choy, W. Y., Lo, E. I., Chen, L., Forman-Kay, J. D., Raetz, C. R., Prive, G. G., Bishop, R. E., and Kay, L. E. (2002) Solution structure and dynamics of the outer membrane enzyme PagP by NMR. *Proc Natl Acad Sci U S A* **99**, 13560-13565
27. Montaville, P., and Jamin, N. (2010) Determination of membrane protein structures using solution and solid-state NMR. *Methods in molecular biology* **654**, 261-282
28. Fernandez, C., Adeishvili, K., and Wuthrich, K. (2001) Transverse relaxation-optimized NMR spectroscopy with the outer membrane protein OmpX in dihexanoyl phosphatidylcholine micelles. *Proc Natl Acad Sci U S A* **98**, 2358-2363
29. Tamm, L. K., Abildgaard, F., Arora, A., Blad, H., and Bushweller, J. H. (2003) Structure, dynamics and function of the outer membrane protein A (OmpA) and influenza hemagglutinin fusion domain in detergent micelles by solution NMR. *FEBS letters* **555**, 139-143
30. Nielsen, N., Malmendal, A., and Vosegaard, T. (2004) Techniques and applications of NMR to membrane proteins. *Mol Membr Biol* **21**, 129-141

31. Nury, H., Dahout-Gonzalez, C., Trezeguet, V., Lauquin, G. J., Brandolin, G., and Pebay-Peyroula, E. (2006) Relations between structure and function of the mitochondrial ADP/ATP carrier. *Annual review of biochemistry* **75**, 713-741
32. Ferguson, A. D., Hofmann, E., Coulton, J. W., Diederichs, K., and Welte, W. (1998) Siderophore-mediated iron transport: crystal structure of FhuA with bound lipopolysaccharide. *Science* **282**, 2215-2220
33. Palsdottir, H., and Hunte, C. (2004) Lipids in membrane protein structures. *Biochim Biophys Acta* **1666**, 2-18
34. White, S. H., and Wimley, W. C. (1999) Membrane protein folding and stability: physical principles. *Annual review of biophysics and biomolecular structure* **28**, 319-365
35. Almen, M. S., Nordstrom, K. J., Fredriksson, R., and Schioth, H. B. (2009) Mapping the human membrane proteome: a majority of the human membrane proteins can be classified according to function and evolutionary origin. *BMC biology* **7**, 50
36. Lucas, K. A., Pitari, G. M., Kazerounian, S., Ruiz-Stewart, I., Park, J., Schulz, S., Chepenik, K. P., and Waldman, S. A. (2000) Guanylyl cyclases and signaling by cyclic GMP. *Pharmacological reviews* **52**, 375-414
37. Unwin, N. (2005) Refined structure of the nicotinic acetylcholine receptor at 4A resolution. *J Mol Biol* **346**, 967-989
38. Doyle, D. A., Morais Cabral, J., Pfuetzner, R. A., Kuo, A., Gulbis, J. M., Cohen, S. L., Chait, B. T., and MacKinnon, R. (1998) The structure of the potassium channel: molecular basis of K+ conduction and selectivity. *Science* **280**, 69-77
39. Oldham, M. L., Khare, D., Quiocho, F. A., Davidson, A. L., and Chen, J. (2007) Crystal structure of a catalytic intermediate of the maltose transporter. *Nature* **450**, 515-521
40. Wimley, W. C. (2003) The versatile beta-barrel membrane protein. *Curr Opin Struct Biol* **13**, 404-411
41. Newcomer, M. E., Jones, T. A., Aqvist, J., Sundelin, J., Eriksson, U., Rask, L., and Peterson, P. A. (1984) The three-dimensional structure of retinol-binding protein. *EMBO J* **3**, 1451-1454
42. Buchanan, S. K. (1999) Beta-barrel proteins from bacterial outer membranes: structure, function and refolding. *Curr Opin Struct Biol* **9**, 455-461
43. Andrews, S. C., Robinson, A. K., and Rodriguez-Quinones, F. (2003) Bacterial iron homeostasis. *FEMS Microbiol Rev* **27**, 215-237
44. Miethke, M., and Marahiel, M. A. (2007) Siderophore-based iron acquisition and pathogen control. *Microbiol Mol Biol Rev* **71**, 413-451
45. Grass, G. (2006) Iron transport in Escherichia coli: all has not been said and done. *Biometals* **19**, 159-172
46. Wandersman, C., and Delepelaire, P. (2004) Bacterial iron sources: from siderophores to hemophores. *Annu Rev Microbiol* **58**, 611-647
47. Schaible, U. E., and Kaufmann, S. H. (2004) Iron and microbial infection. *Nature reviews. Microbiology* **2**, 946-953
48. Weinberg, E. D. (2009) Iron availability and infection. *Biochim Biophys Acta* **1790**, 600-605
49. Cassat, J. E., and Skaar, E. P. (2013) Iron in infection and immunity. *Cell host & microbe* **13**, 509-519

50. Lieu, P. T., Heiskala, M., Peterson, P. A., and Yang, Y. (2001) The roles of iron in health and disease. *Molecular aspects of medicine* **22**, 1-87
51. Lawen, A., and Lane, D. J. R. (2013) Mammalian Iron Homeostasis in Health and Disease: Uptake, Storage, Transport, and Molecular Mechanisms of Action. *Antioxid Redox Sign* **18**, 2473-2507
52. Nairz, M., Schroll, A., Sonnweber, T., and Weiss, G. (2010) The struggle for iron - a metal at the host-pathogen interface. *Cellular microbiology* **12**, 1691-1702
53. Bullen, J. J., Leigh, L. C., and Rogers, H. J. (1968) The effect of iron compounds on the virulence of Escherichia coli for guinea-pigs. *Immunology* **15**, 581-588
54. Barnes, C. M., Theil, E. C., and Raymond, K. N. (2002) Iron uptake in ferritin is blocked by binding of [Cr(TREN)(H(2)O)(OH)](2+), a slow dissociating model for [Fe(H(2)O)(6)](2+). *Proc Natl Acad Sci U S A* **99**, 5195-5200
55. Crichton, R. R., and Declercq, J. P. (2010) X-ray structures of ferritins and related proteins. *Biochim Biophys Acta* **1800**, 706-718
56. Ward, P. P., Uribe-Luna, S., and Conneely, O. M. (2002) Lactoferrin and host defense. *Biochemistry and cell biology = Biochimie et biologie cellulaire* **80**, 95-102
57. MacKenzie, E. L., Iwasaki, K., and Tsuji, Y. (2008) Intracellular iron transport and storage: from molecular mechanisms to health implications. *Antioxid Redox Signal* **10**, 997-1030
58. Skaar, E. P. (2010) The battle for iron between bacterial pathogens and their vertebrate hosts. *PLoS pathogens* **6**, e1000949
59. Peyssonnaux, C., Zinkernagel, A. S., Datta, V., Lauth, X., Johnson, R. S., and Nizet, V. (2006) TLR4-dependent hepcidin expression by myeloid cells in response to bacterial pathogens. *Blood* **107**, 3727-3732
60. Lou, D. Q., Lesbordes, J. C., Nicolas, G., Viatte, L., Bennoun, M., Van Rooijen, N., Kahn, A., Renia, L., and Vaulont, S. (2005) Iron- and inflammation-induced hepcidin gene expression in mice is not mediated by Kupffer cells in vivo. *Hepatology* **41**, 1056-1064
61. Nemeth, E., Tuttle, M. S., Powelson, J., Vaughn, M. B., Donovan, A., Ward, D. M., Ganz, T., and Kaplan, J. (2004) Hepcidin regulates cellular iron efflux by binding to ferroportin and inducing its internalization. *Science* **306**, 2090-2093
62. De Domenico, I., McVey Ward, D., Nemeth, E., Ganz, T., Corradini, E., Ferrara, F., Musci, G., Pietrangelo, A., and Kaplan, J. (2006) Molecular and clinical correlates in iron overload associated with mutations in ferroportin. *Haematologica* **91**, 1092-1095
63. Papanikolaou, G., Tzilianos, M., Christakis, J. I., Bogdanos, D., Tsimirika, K., MacFarlane, J., Goldberg, Y. P., Sakellaropoulos, N., Ganz, T., and Nemeth, E. (2005) Hepcidin in iron overload disorders. *Blood* **105**, 4103-4105
64. Friel, J. K., Aziz, K., Andrews, W. L., Harding, S. V., Courage, M. L., and Adams, R. J. (2003) A double-masked, randomized control trial of iron supplementation in early infancy in healthy term breast-fed infants. *The Journal of pediatrics* **143**, 582-586
65. Grantham-McGregor, S., and Ani, C. (2001) A review of studies on the effect of iron deficiency on cognitive development in children. *The Journal of nutrition* **131**, 649S-666S; discussion 666S-668S
66. Lozoff, B., De Andraca, I., Castillo, M., Smith, J. B., Walter, T., and Pino, P. (2003) Behavioral and developmental effects of preventing iron-deficiency anemia in healthy full-term infants. *Pediatrics* **112**, 846-854

67. Ronnenberg, A. G., Wood, R. J., Wang, X., Xing, H., Chen, C., Chen, D., Guang, W., Huang, A., Wang, L., and Xu, X. (2004) Preconception hemoglobin and ferritin concentrations are associated with pregnancy outcome in a prospective cohort of Chinese women. *The Journal of nutrition* **134**, 2586-2591
68. Radlowski, E. C., and Johnson, R. W. (2013) Perinatal iron deficiency and neurocognitive development. *Frontiers in human neuroscience* **7**, 585
69. Flo, T. H., Smith, K. D., Sato, S., Rodriguez, D. J., Holmes, M. A., Strong, R. K., Akira, S., and Aderem, A. (2004) Lipocalin 2 mediates an innate immune response to bacterial infection by sequestrating iron. *Nature* **432**, 917-921
70. Dale, S. E., Doherty-Kirby, A., Lajoie, G., and Heinrichs, D. E. (2004) Role of siderophore biosynthesis in virulence of Staphylococcus aureus: identification and characterization of genes involved in production of a siderophore. *Infect Immun* **72**, 29-37
71. Cornelissen, C. N., and Sparling, P. F. (1994) Iron piracy: acquisition of transferrin-bound iron by bacterial pathogens. *Mol Microbiol* **14**, 843-850
72. Clarke, T. E., Tari, L. W., and Vogel, H. J. (2001) Structural biology of bacterial iron uptake systems. *Curr Top Med Chem* **1**, 7-30
73. Cornelissen, C. N., and Sparling, P. F. (1994) Identification of receptor-mediated transferrin-iron uptake mechanism in Neisseria gonorrhoeae. *Methods Enzymol* **235**, 356-363
74. Ratledge, C., and Dover, L. G. (2000) Iron metabolism in pathogenic bacteria. *Annual review of microbiology* **54**, 881-941
75. Cescau, S., Cwerman, H., Letoffe, S., Delepelaire, P., Wandersman, C., and Biville, F. (2007) Heme acquisition by hemophores. *Biometals* **20**, 603-613
76. Wooldridge, K. G., and Williams, P. H. (1993) Iron uptake mechanisms of pathogenic bacteria. *FEMS Microbiol Rev* **12**, 325-348
77. Crouch, M. L., Castor, M., Karlinsey, J. E., Kalhorn, T., and Fang, F. C. (2008) Biosynthesis and IroC-dependent export of the siderophore salmochelin are essential for virulence of Salmonella enterica serovar Typhimurium. *Mol Microbiol* **67**, 971-983
78. Yue, W. W., Grizot, S., and Buchanan, S. K. (2003) Structural evidence for iron-free citrate and ferric citrate binding to the TonB-dependent outer membrane transporter FecA. *J Mol Biol* **332**, 353-368
79. Postle, K., and Larsen, R. A. (2007) TonB-dependent energy transduction between outer and cytoplasmic membranes. *Biometals* **20**, 453-465
80. Chimento, D. P., Kadner, R. J., and Wiener, M. C. (2005) Comparative structural analysis of TonB-dependent outer membrane transporters: implications for the transport cycle. *Proteins* **59**, 240-251
81. Cao, Z., Qi, Z., Sprencel, C., Newton, S. M., and Klebba, P. E. (2000) Aromatic components of two ferric enterobactin binding sites in Escherichia coli FepA. *Mol Microbiol* **37**, 1306-1317
82. Scott, D. C., Cao, Z., Qi, Z., Bauler, M., Igo, J. D., Newton, S. M., and Klebba, P. E. (2001) Exchangeability of N termini in the ligand-gated porins of Escherichia coli. *J Biol Chem* **276**, 13025-13033
83. Usher, K. C., Ozkan, E., Gardner, K. H., and Deisenhofer, J. (2001) The plug domain of FepA, a TonB-dependent transport protein from Escherichia coli, binds its

siderophore in the absence of the transmembrane barrel domain. *Proc Natl Acad Sci U S A* **98**, 10676-10681
84. Cadieux, N., and Kadner, R. J. (1999) Site-directed disulfide bonding reveals an interaction site between energy-coupling protein TonB and BtuB, the outer membrane cobalamin transporter. *Proc Natl Acad Sci U S A* **96**, 10673-10678
85. Moeck, G. S., and Coulton, J. W. (1998) TonB-dependent iron acquisition: mechanisms of siderophore-mediated active transport. *Mol Microbiol* **28**, 675-681
86. Moeck, G. S., Ratcliffe, M. J., and Coulton, J. W. (1995) Topological analysis of the Escherichia coli ferrichrome-iron receptor by using monoclonal antibodies. *J Bacteriol* **177**, 6118-6125
87. Moeck, G. S., Tawa, P., Xiang, H., Ismail, A. A., Turnbull, J. L., and Coulton, J. W. (1996) Ligand-induced conformational change in the ferrichrome-iron receptor of Escherichia coli K-12. *Mol Microbiol* **22**, 459-471
88. Braun, V., Gaisser, S., Herrmann, C., Kampfenkel, K., Killmann, H., and Traub, I. (1996) Energy-coupled transport across the outer membrane of Escherichia coli: ExbB binds ExbD and TonB in vitro, and leucine 132 in the periplasmic region and aspartate 25 in the transmembrane region are important for ExbD activity. *J Bacteriol* **178**, 2836-2845
89. Higgs, P. I., Larsen, R. A., and Postle, K. (2002) Quantification of known components of the Escherichia coli TonB energy transduction system: TonB, ExbB, ExbD and FepA. *Mol Microbiol* **44**, 271-281
90. Postle, K. (1993) TonB protein and energy transduction between membranes. *J Bioenerg Biomembr* **25**, 591-601
91. Cadieux, N., Bradbeer, C., and Kadner, R. J. (2000) Sequence changes in the ton box region of BtuB affect its transport activities and interaction with TonB protein. *J Bacteriol* **182**, 5954-5961
92. Moeck, G. S., Coulton, J. W., and Postle, K. (1997) Cell envelope signaling in Escherichia coli. Ligand binding to the ferrichrome-iron receptor fhua promotes interaction with the energy-transducing protein TonB. *J Biol Chem* **272**, 28391-28397
93. Pawelek, P. D., Croteau, N., Ng-Thow-Hing, C., Khursigara, C. M., Moiseeva, N., Allaire, M., and Coulton, J. W. (2006) Structure of TonB in complex with FhuA, E. coli outer membrane receptor. *Science* **312**, 1399-1402
94. Shultis, D. D., Purdy, M. D., Banchs, C. N., and Wiener, M. C. (2006) Outer membrane active transport: structure of the BtuB:TonB complex. *Science* **312**, 1396-1399
95. Skare, J. T., Ahmer, B. M., Seachord, C. L., Darveau, R. P., and Postle, K. (1993) Energy transduction between membranes. TonB, a cytoplasmic membrane protein, can be chemically cross-linked in vivo to the outer membrane receptor FepA. *J Biol Chem* **268**, 16302-16308
96. Bradbeer, C. (1993) The proton motive force drives the outer membrane transport of cobalamin in Escherichia coli. *J Bacteriol* **175**, 3146-3150
97. Bradbeer, C., and Woodrow, M. L. (1976) Transport of vitamin B12 in Escherichia coli: energy dependence. *J Bacteriol* **128**, 99-104
98. Reynolds, P. R., Mottur, G. P., and Bradbeer, C. (1980) Transport of vitamin B12 in Escherichia coli. Some observations on the roles of the gene products of BtuC and TonB. *J Biol Chem* **255**, 4313-4319

99. Braun, V., and Endriss, F. (2007) Energy-coupled outer membrane transport proteins and regulatory proteins. *Biometals* **20**, 219-231
100. Chakraborty, R., Storey, E., and van der Helm, D. (2006) Molecular mechanism of ferricsiderophore passage through the outer membrane receptor proteins of Escherichia coli. *Biometals*
101. Chakraborty, R., Lemke, E. A., Cao, Z., Klebba, P. E., and van der Helm, D. (2003) Identification and mutational studies of conserved amino acids in the outer membrane receptor protein, FepA, which affect transport but not binding of ferric-enterobactin in Escherichia coli. *Biometals* **16**, 507-518
102. Ma, L., Kaserer, W., Annamalai, R., Scott, D. C., Jin, B., Jiang, X., Xiao, Q., Maymani, H., Massis, L. M., Ferreira, L. C., Newton, S. M., and Klebba, P. E. (2007) Evidence of ball-and-chain transport of ferric enterobactin through FepA. *J Biol Chem* **282**, 397-406
103. Faraldo-Gomez, J. D., Smith, G. R., and Sansom, M. S. (2003) Molecular dynamics simulations of the bacterial outer membrane protein FhuA: a comparative study of the ferrichrome-free and bound states. *Biophys J* **85**, 1406-1420
104. Eisenhauer, H. A., Shames, S., Pawelek, P. D., and Coulton, J. W. (2005) Siderophore transport through Escherichia coli outer membrane receptor FhuA with disulfide-tethered cork and barrel domains. *J Biol Chem* **280**, 30574-30580
105. Devanathan, S., and Postle, K. (2007) Studies on colicin B translocation: FepA is gated by TonB. *Mol Microbiol* **65**, 441-453
106. Smallwood, C. R., Marco, A. G., Xiao, Q., Trinh, V., Newton, S. M., and Klebba, P. E. (2009) Fluoresceination of FepA during colicin B killing: effects of temperature, toxin and TonB. *Mol Microbiol* **72**, 1171-1180
107. Noinaj, N., Guillier, M., Barnard, T. J., and Buchanan, S. K. (2010) TonB-dependent transporters: regulation, structure, and function. *Annual review of microbiology* **64**, 43-60
108. Flores Jimenez, R. H., and Cafiso, D. S. (2012) The N-terminal domain of a TonB-dependent transporter undergoes a reversible stepwise denaturation. *Biochemistry* **51**, 3642-3650
109. Oke, M., Sarra, R., Ghirlando, R., Farnaud, S., Gorringe, A. R., Evans, R. W., and Buchanan, S. K. (2004) The plug domain of a neisserial TonB-dependent transporter retains structural integrity in the absence of its transmembrane beta-barrel. *FEBS letters* **564**, 294-300
110. Jordan, L. D., Zhou, Y., Smallwood, C. R., Lill, Y., Ritchie, K., Yip, W. T., Newton, S. M., and Klebba, P. E. (2013) Energy-dependent motion of TonB in the Gram-negative bacterial inner membrane. *Proc Natl Acad Sci U S A* **110**, 11553-11558
111. Dumoulin, D., Nesbitt, A., Marshall, B., Sittler, N., and Pollari, F. (2012) Informing source attribution of enteric disease: An analysis of public health inspectors‚Äô opinions on the ‚Äúmost likely source of infection‚Äù. *Environmental Health Review* **55**, 27-36
112. Sargeant, J. M., Majowicz, S. E., and Snelgrove, J. (2008) The burden of acute gastrointestinal illness in Ontario, Canada, 2005-2006. *Epidemiol Infect* **136**, 451-460
113. Majowicz, S. E., McNab, W. B., Sockett, P., Henson, T. S., Dore, K., Edge, V. L., Buffett, M. C., Fazil, A., Read, S., McEwen, S., Stacey, D., and Wilson, J. B. (2006)

Burden and cost of gastroenteritis in a Canadian community. *J Food Prot* **69**, 651-659
114. Iovine, N. M. (2013) Resistance mechanisms in Campylobacter jejuni. *Virulence* **4**, 230-240
115. Gillespie, I. A., O'Brien, S. J., Frost, J. A., Adak, G. K., Horby, P., Swan, A. V., Painter, M. J., and Neal, K. R. (2002) A case-case comparison of Campylobacter coli and Campylobacter jejuni infection: a tool for generating hypotheses. *Emerg Infect Dis* **8**, 937-942
116. Robinson, D. A. (1981) Infective dose of Campylobacter jejuni in milk. *Br Med J (Clin Res Ed)* **282**, 1584
117. Lee, M. D., and Newell, D. G. (2006) Campylobacter in poultry: filling an ecological niche. *Avian Dis* **50**, 1-9
118. Blaser, M. J., Berkowitz, I. D., LaForce, F. M., Cravens, J., Reller, L. B., and Wang, W. L. (1979) Campylobacter enteritis: clinical and epidemiologic features. *Ann Intern Med* **91**, 179-185
119. Poropatich, K. O., Walker, C. L., and Black, R. E. (2010) Quantifying the association between Campylobacter infection and Guillain-Barre syndrome: a systematic review. *J Health Popul Nutr* **28**, 545-552
120. Walling, A. D., and Dickson, G. (2013) Guillain-Barre syndrome. *American family physician* **87**, 191-197
121. Alter, M. (1990) The epidemiology of Guillain-Barre syndrome. *Ann Neurol* **27 Suppl**, S7-12
122. Magira, E. E., Papaioakim, M., Nachamkin, I., Asbury, A. K., Li, C. Y., Ho, T. W., Griffin, J. W., McKhann, G. M., and Monos, D. S. (2003) Differential distribution of HLA-DQ beta/DR beta epitopes in the two forms of Guillain-Barre syndrome, acute motor axonal neuropathy and acute inflammatory demyelinating polyneuropathy (AIDP): identification of DQ beta epitopes associated with susceptibility to and protection from AIDP. *J Immunol* **170**, 3074-3080
123. Field, L. H., Headley, V. L., Payne, S. M., and Berry, L. J. (1986) Influence of iron on growth, morphology, outer membrane protein composition, and synthesis of siderophores in Campylobacter jejuni. *Infect Immun* **54**, 126-132
124. Pickett, C. L., Auffenberg, T., Pesci, E. C., Sheen, V. L., and Jusuf, S. S. (1992) Iron acquisition and hemolysin production by Campylobacter jejuni. *Infect Immun* **60**, 3872-3877
125. Guerry, P., Perez-Casal, J., Yao, R., McVeigh, A., and Trust, T. J. (1997) A genetic locus involved in iron utilization unique to some Campylobacter strains. *J Bacteriol* **179**, 3997-4002
126. Palyada, K., Threadgill, D., and Stintzi, A. (2004) Iron acquisition and regulation in Campylobacter jejuni. *J Bacteriol* **186**, 4714-4729
127. Holmes, K., Mulholland, F., Pearson, B. M., Pin, C., McNicholl-Kennedy, J., Ketley, J. M., and Wells, J. M. (2005) Campylobacter jejuni gene expression in response to iron limitation and the role of Fur. *Microbiology* **151**, 243-257
128. Ridley, K. A., Rock, J. D., Li, Y., and Ketley, J. M. (2006) Heme utilization in Campylobacter jejuni. *J Bacteriol* **188**, 7862-7875
129. van Vliet, A. H., Wooldridge, K. G., and Ketley, J. M. (1998) Iron-responsive gene regulation in a campylobacter jejuni fur mutant. *J Bacteriol* **180**, 5291-5298

130. Park, S. F. (2002) The physiology of Campylobacter species and its relevance to their role as foodborne pathogens. *Int J Food Microbiol* **74**, 177-188
131. van Vliet, A. H., and Ketley, J. M. (2001) Pathogenesis of enteric Campylobacter infection. *Symp Ser Soc Appl Microbiol*, 45S-56S
132. Snelling, W. J., Matsuda, M., Moore, J. E., and Dooley, J. S. (2005) Campylobacter jejuni. *Lett Appl Microbiol* **41**, 297-302
133. Nachamkin, I., Allos, B. M., and Ho, T. (1998) Campylobacter species and Guillain-Barre syndrome. *Clin Microbiol Rev* **11**, 555-567
134. Butzler, J. P. (2004) Campylobacter, from obscurity to celebrity. *Clin Microbiol Infect* **10**, 868-876
135. Ferguson, A. D., and Deisenhofer, J. (2002) TonB-dependent receptors-structural perspectives. *Biochim Biophys Acta* **1565**, 318-332
136. Schalk, I. J., Yue, W. W., and Buchanan, S. K. (2004) Recognition of iron-free siderophores by TonB-dependent iron transporters. *Mol Microbiol* **54**, 14-22
137. Miroux, B., and Walker, J. E. (1996) Over-production of proteins in Escherichia coli: mutant hosts that allow synthesis of some membrane proteins and globular proteins at high levels. *J Mol Biol* **260**, 289-298
138. Schwede, T., Kopp, J., Guex, N., and Peitsch, M. C. (2003) SWISS-MODEL: An automated protein homology-modeling server. *Nucleic Acids Res* **31**, 3381-3385
139. Auer, M., Kim, M. J., Lemieux, M. J., Villa, A., Song, J., Li, X. D., and Wang, D. N. (2001) High-yield expression and functional analysis of Escherichia coli glycerol-3-phosphate transporter. *Biochemistry* **40**, 6628-6635
140. Loll, P. J. (2003) Membrane protein structural biology: the high throughput challenge. *J Struct Biol* **142**, 144-153
141. Bonhivers, M., Desmadril, M., Moeck, G. S., Boulanger, P., Colomer-Pallas, A., and Letellier, L. (2001) Stability studies of FhuA, a two-domain outer membrane protein from Escherichia coli. *Biochemistry* **40**, 2606-2613
142. Mamelli, L., Pages, J. M., Konkel, M. E., and Bolla, J. M. (2006) Expression and purification of native and truncated forms of CadF, an outer membrane protein of Campylobacter. *Int J Biol Macromol* **39**, 135-140
143. daCosta, C. J., and Baenziger, J. E. (2003) A rapid method for assessing lipid:protein and detergent:protein ratios in membrane-protein crystallization. *Acta Crystallogr D Biol Crystallogr* **59**, 77-83
144. Tamm, L. K., and Tatulian, S. A. (1997) Infrared spectroscopy of proteins and peptides in lipid bilayers. *Q Rev Biophys* **30**, 365-429
145. Methot, N., McCarthy, M. P., and Baenziger, J. E. (1994) Secondary structure of the nicotinic acetylcholine receptor: implications for structural models of a ligand-gated ion channel. *Biochemistry* **33**, 7709-7717
146. Jackson, M., and Mantsch, H. H. (1995) The use and misuse of FTIR spectroscopy in the determination of protein structure. *Crit Rev Biochem Mol Biol* **30**, 95-120
147. Goormaghtigh, E., Ruysschaert, J. M., and Raussens, V. (2006) Evaluation of the information content in infrared spectra for protein secondary structure determination. *Biophys J* **90**, 2946-2957
148. Methot, N., Ritchie, B. D., Blanton, M. P., and Baenziger, J. E. (2001) Structure of the pore-forming transmembrane domain of a ligand-gated ion channel. *J Biol Chem* **276**, 23726-23732

149. Methot, N., and Baenziger, J. E. (1998) Secondary structure of the exchange-resistant core from the nicotinic acetylcholine receptor probed directly by infrared spectroscopy and hydrogen/deuterium exchange. *Biochemistry* **37**, 14815-14822
150. Baenziger, J. E., and Methot, N. (1995) Fourier transform infrared and hydrogen/deuterium exchange reveal an exchange-resistant core of alpha-helical peptide hydrogens in the nicotinic acetylcholine receptor. *J Biol Chem* **270**, 29129-29137
151. daCosta, C. J., Kaiser, D. E., and Baenziger, J. E. (2005) Role of glycosylation and membrane environment in nicotinic acetylcholine receptor stability. *Biophys J* **88**, 1755-1764
152. Sukumaran, S., Zscherp, C., and Mantele, W. (2004) Investigation of the thermal stability of porin from Paracoccus denitrificans by site-directed mutagenesis and Fourier transform infrared spectroscopy. *Biopolymers* **74**, 82-86
153. Buchanan, S. K., Smith, B. S., Venkatramani, L., Xia, D., Esser, L., Palnitkar, M., Chakraborty, R., van der Helm, D., and Deisenhofer, J. (1999) Crystal structure of the outer membrane active transporter FepA from Escherichia coli. *Nat Struct Biol* **6**, 56-63
154. Locher, K. P., Rees, B., Koebnik, R., Mitschler, A., Moulinier, L., Rosenbusch, J. P., and Moras, D. (1998) Transmembrane signaling across the ligand-gated FhuA receptor: crystal structures of free and ferrichrome-bound states reveal allosteric changes. *Cell* **95**, 771-778
155. Newton, S. M., Allen, J. S., Cao, Z., Qi, Z., Jiang, X., Sprencel, C., Igo, J. D., Foster, S. B., Payne, M. A., and Klebba, P. E. (1997) Double mutagenesis of a positive charge cluster in the ligand-binding site of the ferric enterobactin receptor, FepA. *Proc Natl Acad Sci U S A* **94**, 4560-4565
156. Raymond, K. N., Dertz, E. A., and Kim, S. S. (2003) Enterobactin: an archetype for microbial iron transport. *Proc Natl Acad Sci U S A* **100**, 3584-3588
157. Annamalai, R., Jin, B., Cao, Z., Newton, S. M., and Klebba, P. E. (2004) Recognition of ferric catecholates by FepA. *J Bacteriol* **186**, 3578-3589
158. Miller, C. E., Rock, J. D., Ridley, K. A., Williams, P. H., and Ketley, J. M. (2008) Utilization of lactoferrin-bound and transferrin-bound iron by Campylobacter jejuni. *J Bacteriol*
159. Carswell, C. L., Rigden, M. D., and Baenziger, J. E. (2008) Expression, purification, and structural characterization of CfrA, a putative iron transporter from Campylobacter jejuni. *J Bacteriol* **190**, 5650-5662
160. Naikare, H., Butcher, J., Flint, A., Xu, J., Raymond, K. N., and Stintzi, A. (2013) Campylobacter jejuni ferric-enterobactin receptor CfrA is TonB3 dependent and mediates iron acquisition from structurally different catechol siderophores. *Metallomics* **5**, 988-996
161. Ferguson, A. D., Breed, J., Diederichs, K., Welte, W., and Coulton, J. W. (1998) An internal affinity-tag for purification and crystallization of the siderophore receptor FhuA, integral outer membrane protein from Escherichia coli K-12. *Protein Sci* **7**, 1636-1638
162. Marone, P. A., Thiyagarajan, P., Wagner, A. M., and Tiede, D. M. (1999) Effect of detergent alkyl chain length on crystallization of a detergent-solubilized membrane protein: correlation of protein-detergent particle size and particle-particle interaction

with crystallization of the photosynthetic reaction center from Rhodobacter sphaeroides. *J Cryst Growth* **207**, 214-225
163. Herrmann, K. W. (1962) Non-Ionic-Cationic Micellar Properties of Dimethyldodecylamine Oxide. *J Phys Chem-Us* **66**, 295-&
164. Ferguson, A. D., Chakraborty, R., Smith, B. S., Esser, L., van der Helm, D., and Deisenhofer, J. (2002) Structural basis of gating by the outer membrane transporter FecA. *Science* **295**, 1715-1719
165. Echalier, A., Glazer, R. L., Fulop, V., and Geday, M. A. (2004) Assessing crystallization droplets using birefringence. *Acta Crystallogr D Biol Crystallogr* **60**, 696-702
166. d'Hardemare Adu, M., Alnaga, N., Serratrice, G., and Pierre, J. L. (2008) Oxinobactin, a siderophore analogue to enterobactin involving 8-hydroxyquinoline subunits: synthesis and iron binding ability. *Bioorg Med Chem Lett* **18**, 6476-6478
167. Beutler, B., and Rietschel, E. T. (2003) Innate immune sensing and its roots: the story of endotoxin. *Nature reviews. Immunology* **3**, 169-176
168. Davis, M. R., Jr., and Goldberg, J. B. (2012) Purification and visualization of lipopolysaccharide from Gram-negative bacteria by hot aqueous-phenol extraction. *Journal of visualized experiments : JoVE*
169. Matthews, B. W. (1968) Solvent content of protein crystals. *J Mol Biol* **33**, 491-497
170. Noinaj, N., Easley, N. C., Oke, M., Mizuno, N., Gumbart, J., Boura, E., Steere, A. N., Zak, O., Aisen, P., Tajkhorshid, E., Evans, R. W., Gorringe, A. R., Mason, A. B., Steven, A. C., and Buchanan, S. K. (2012) Structural basis for iron piracy by pathogenic Neisseria. *Nature* **483**, 53-58
171. Wiener, M. C. (2005) TonB-dependent outer membrane transport: going for Baroque? *Curr Opin Struct Biol* **15**, 394-400
172. Cascales, E., Buchanan, S. K., Duche, D., Kleanthous, C., Lloubes, R., Postle, K., Riley, M., Slatin, S., and Cavard, D. (2007) Colicin biology. *Microbiology and molecular biology reviews : MMBR* **71**, 158-229
173. Reid, S. E., and Baenziger, J. E. (1996) Subsequent subtraction of atmospheric water vapour contributions from FTIR spectra of proteins. *Biophysical Journal* **70**, Tu437-Tu437
174. Paliy, O., and Gunasekera, T. S. (2007) Growth of E. coli BL21 in minimal media with different gluconeogenic carbon sources and salt contents. *Applied microbiology and biotechnology* **73**, 1169-1172
175. Marley, J., Lu, M., and Bracken, C. (2001) A method for efficient isotopic labeling of recombinant proteins. *J Biomol NMR* **20**, 71-75
176. Baenziger, J. E., and Chew, J. P. (1997) Desensitization of the nicotinic acetylcholine receptor mainly involves a structural change in solvent-accessible regions of the polypeptide backbone. *Biochemistry* **36**, 3617-3624
177. Sprencel, C., Cao, Z., Qi, Z., Scott, D. C., Montague, M. A., Ivanoff, N., Xu, J., Raymond, K. M., Newton, S. M., and Klebba, P. E. (2000) Binding of ferric enterobactin by the Escherichia coli periplasmic protein FepB. *J Bacteriol* **182**, 5359-5364
178. Udho, E., Jakes, K. S., and Finkelstein, A. (2012) TonB-dependent transporter FhuA in planar lipid bilayers: partial exit of its plug from the barrel. *Biochemistry* **51**, 6753-6759

179. Waszkielewicz, A. M., Gunia, A., Szkaradek, N., Sloczynska, K., Krupinska, S., and Marona, H. (2013) Ion channels as drug targets in central nervous system disorders. *Current medicinal chemistry* **20**, 1241-1285
180. Shen, X. M., Deymeer, F., Sine, S. M., and Engel, A. G. (2006) Slow-channel mutation in acetylcholine receptor alphaM4 domain and its efficient knockdown. *Ann Neurol* **60**, 128-136
181. Baenziger, J. E., and Corringer, P. J. (2011) 3D structure and allosteric modulation of the transmembrane domain of pentameric ligand-gated ion channels. *Neuropharmacology* **60**, 116-125
182. Gage, P. W. (1998) Signal transmission in ligand-gated receptors. *Immunology and cell biology* **76**, 436-440
183. Betke, K. M., Wells, C. A., and Hamm, H. E. (2012) GPCR mediated regulation of synaptic transmission. *Progress in neurobiology* **96**, 304-321
184. Pedigo, N. W., Jr. (1994) Neurotransmitter receptor plasticity in aging. *Life sciences* **55**, 1985-1991
185. Martin, S. J., Grimwood, P. D., and Morris, R. G. (2000) Synaptic plasticity and memory: an evaluation of the hypothesis. *Annu Rev Neurosci* **23**, 649-711
186. Xu, Y., Yan, J., Zhou, P., Li, J., Gao, H., Xia, Y., and Wang, Q. (2012) Neurotransmitter receptors and cognitive dysfunction in Alzheimer's disease and Parkinson's disease. *Progress in neurobiology* **97**, 1-13
187. Koffie, R. M., Hyman, B. T., and Spires-Jones, T. L. (2011) Alzheimer's disease: synapses gone cold. *Molecular neurodegeneration* **6**, 63
188. Sine, S. M., and Engel, A. G. (2006) Recent advances in Cys-loop receptor structure and function. *Nature* **440**, 448-455
189. Unwin, N. (2005) Refined structure of the nicotinic acetylcholine receptor at 4Å resolution. *J Mol Biol* **346**, 967-989
190. Cymes, G. D., and Grosman, C. (2008) Pore-opening mechanism of the nicotinic acetylcholine receptor evinced by proton transfer. *Nat Struct Mol Biol* **15**, 389-396
191. Dacosta, C. J., and Baenziger, J. E. (2013) Gating of pentameric ligand-gated ion channels: structural insights and ambiguities. *Structure* **21**, 1271-1283
192. Miyazawa, A., Fujiyoshi, Y., and Unwin, N. (2003) Structure and gating mechanism of the acetylcholine receptor pore. *Nature* **423**, 949-955
193. Brejc, K., van Dijk, W. J., Klaassen, R. V., Schuurmans, M., van Der Oost, J., Smit, A. B., and Sixma, T. K. (2001) Crystal structure of an ACh-binding protein reveals the ligand-binding domain of nicotinic receptors. *Nature* **411**, 269-276
194. Smit, A. B., Syed, N. I., Schaap, D., van Minnen, J., Klumperman, J., Kits, K. S., Lodder, H., van der Schors, R. C., van Elk, R., Sorgedrager, B., Brejc, K., Sixma, T. K., and Geraerts, W. P. (2001) A glia-derived acetylcholine-binding protein that modulates synaptic transmission. *Nature* **411**, 261-268
195. Smit, A. B., Brejc, K., Syed, N., and Sixma, T. K. (2003) Structure and function of AChBP, homologue of the ligand-binding domain of the nicotinic acetylcholine receptor. *Ann N Y Acad Sci* **998**, 81-92
196. Hansen, S. B., Sulzenbacher, G., Huxford, T., Marchot, P., Taylor, P., and Bourne, Y. (2005) Structures of Aplysia AChBP complexes with nicotinic agonists and antagonists reveal distinctive binding interfaces and conformations. *EMBO J* **24**, 3635-3646

197. Celie, P. H., van Rossum-Fikkert, S. E., van Dijk, W. J., Brejc, K., Smit, A. B., and Sixma, T. K. (2004) Nicotine and carbamylcholine binding to nicotinic acetylcholine receptors as studied in AChBP crystal structures. *Neuron* **41**, 907-914
198. Billen, B., Spurny, R., Brams, M., van Elk, R., Valera-Kummer, S., Yakel, J. L., Voets, T., Bertrand, D., Smit, A. B., and Ulens, C. (2012) Molecular actions of smoking cessation drugs at alpha4beta2 nicotinic receptors defined in crystal structures of a homologous binding protein. *Proc Natl Acad Sci U S A* **109**, 9173-9178
199. Bouzat, C., Gumilar, F., Spitzmaul, G., Wang, H. L., Rayes, D., Hansen, S. B., Taylor, P., and Sine, S. M. (2004) Coupling of agonist binding to channel gating in an ACh-binding protein linked to an ion channel. *Nature* **430**, 896-900
200. Lee, W. Y., and Sine, S. M. (2005) Principal pathway coupling agonist binding to channel gating in nicotinic receptors. *Nature* **438**, 243-247
201. Duret, G., Van Renterghem, C., Weng, Y., Prevost, M., Moraga-Cid, G., Huon, C., Sonner, J. M., and Corringer, P. J. (2011) Functional prokaryotic-eukaryotic chimera from the pentameric ligand-gated ion channel family. *Proc Natl Acad Sci U S A* **108**, 12143-12148
202. Unwin, N., and Fujiyoshi, Y. (2012) Gating movement of acetylcholine receptor caught by plunge-freezing. *J Mol Biol* **422**, 617-634
203. Asmar-Rovira, G. A., Asseo-Garcia, A. M., Quesada, O., Hanson, M. A., Cheng, A., Nogueras, C., Lasalde-Dominicci, J. A., and Stevens, R. C. (2008) Biophysical and ion channel functional characterization of the Torpedo californica nicotinic acetylcholine receptor in varying detergent-lipid environments. *The Journal of membrane biology* **223**, 13-26
204. Barrantes, F. J. (2002) Lipid matters: nicotinic acetylcholine receptor-lipid interactions (Review). *Mol Membr Biol* **19**, 277-284
205. Criado, M., Eibl, H., and Barrantes, F. J. (1984) Functional properties of the acetylcholine receptor incorporated in model lipid membranes. Differential effects of chain length and head group of phospholipids on receptor affinity states and receptor-mediated ion translocation. *J Biol Chem* **259**, 9188-9198
206. Fong, T. M., and McNamee, M. G. (1986) Correlation between acetylcholine receptor function and structural properties of membranes. *Biochemistry* **25**, 830-840
207. Rankin, S. E., Addona, G. H., Kloczewiak, M. A., Bugge, B., and Miller, K. W. (1997) The cholesterol dependence of activation and fast desensitization of the nicotinic acetylcholine receptor. *Biophys J* **73**, 2446-2455
208. daCosta, C. J., and Baenziger, J. E. (2009) A lipid-dependent uncoupled conformation of the acetylcholine receptor. *J Biol Chem* **284**, 17819-17825
209. daCosta, C. J., Medaglia, S. A., Lavigne, N., Wang, S., Carswell, C. L., and Baenziger, J. E. (2009) Anionic lipids allosterically modulate multiple nicotinic acetylcholine receptor conformational equilibria. *J Biol Chem* **284**, 33841-33849
210. Li, P., and Steinbach, J. H. (2010) The neuronal nicotinic alpha4beta2 receptor has a high maximal probability of being open. *British journal of pharmacology* **160**, 1906-1915
211. Vallejo, Y. F., Buisson, B., Bertrand, D., and Green, W. N. (2005) Chronic nicotine exposure upregulates nicotinic receptors by a novel mechanism. *The Journal of neuroscience : the official journal of the Society for Neuroscience* **25**, 5563-5572

212. daCosta, C. J., Dey, L., Therien, J. P., and Baenziger, J. E. (2013) A distinct mechanism for activating uncoupled nicotinic acetylcholine receptors. *Nature chemical biology* **9**, 701-707
213. Buttner, C., Sadtler, S., Leyendecker, A., Laube, B., Griffon, N., Betz, H., and Schmalzing, G. (2001) Ubiquitination precedes internalization and proteolytic cleavage of plasma membrane-bound glycine receptors. *J Biol Chem* **276**, 42978-42985
214. Haeger, S., Kuzmin, D., Detro-Dassen, S., Lang, N., Kilb, M., Tsetlin, V., Betz, H., Laube, B., and Schmalzing, G. (2010) An intramembrane aromatic network determines pentameric assembly of Cys-loop receptors. *Nat Struct Mol Biol* **17**, 90-98
215. Tasneem, A., Iyer, L. M., Jakobsson, E., and Aravind, L. (2005) Identification of the prokaryotic ligand-gated ion channels and their implications for the mechanisms and origins of animal Cys-loop ion channels. *Genome biology* **6**, R4
216. Bocquet, N., Nury, H., Baaden, M., Le Poupon, C., Changeux, J. P., Delarue, M., and Corringer, P. J. (2009) X-ray structure of a pentameric ligand-gated ion channel in an apparently open conformation. *Nature* **457**, 111-114
217. Hilf, R. J., and Dutzler, R. (2008) X-ray structure of a prokaryotic pentameric ligand-gated ion channel. *Nature* **452**, 375-379
218. Zimmermann, I., and Dutzler, R. (2011) Ligand activation of the prokaryotic pentameric ligand-gated ion channel ELIC. *PLoS biology* **9**, e1001101
219. Bocquet, N., Prado de Carvalho, L., Cartaud, J., Neyton, J., Le Poupon, C., Taly, A., Grutter, T., Changeux, J. P., and Corringer, P. J. (2007) A prokaryotic proton-gated ion channel from the nicotinic acetylcholine receptor family. *Nature* **445**, 116-119
220. Gonzalez-Gutierrez, G., Lukk, T., Agarwal, V., Papke, D., Nair, S. K., and Grosman, C. (2012) Mutations that stabilize the open state of the Erwinia chrisanthemi ligand-gated ion channel fail to change the conformation of the pore domain in crystals. *Proc Natl Acad Sci U S A* **109**, 6331-6336
221. Labriola, J. M., Pandhare, A., Jansen, M., Blanton, M. P., Corringer, P. J., and Baenziger, J. E. (2013) Structural sensitivity of a prokaryotic pentameric ligand-gated ion channel to its membrane environment. *J Biol Chem* **288**, 11294-11303
222. Criado, M., Eibl, H., and Barrantes, F. J. (1982) Effects of lipids on acetylcholine receptor. Essential need of cholesterol for maintenance of agonist-induced state transitions in lipid vesicles. *Biochemistry* **21**, 3622-3629
223. Sunshine, C., and McNamee, M. G. (1992) Lipid modulation of nicotinic acetylcholine receptor function: the role of neutral and negatively charged lipids. *Biochim Biophys Acta* **1108**, 240-246
224. Barrantes, F. J. (2002) Lipid matters: nicotinic acetylcholine receptor-lipid interactions. *Mol Membr Biol* **19**, 277-284
225. Baenziger, J. E., Morris, M. L., Darsaut, T. E., and Ryan, S. E. (2000) Effect of membrane lipid composition on the conformational equilibria of the nicotinic acetylcholine receptor. *J Biol Chem* **275**, 777-784
226. daCosta, C. J., Ogrel, A. A., McCardy, E. A., Blanton, M. P., and Baenziger, J. E. (2002) Lipid-protein interactions at the nicotinic acetylcholine receptor. A functional coupling between nicotinic receptors and phosphatidic acid-containing lipid bilayers. *J Biol Chem* **277**, 201-208

227. Hamouda, A. K., Sanghvi, M., Sauls, D., Machu, T. K., and Blanton, M. P. (2006) Assessing the lipid requirements of the *Torpedo californica* nicotinic acetylcholine receptor. *Biochemistry* **45**, 4327-4337
228. Blanton, M. P., and Cohen, J. B. (1992) Mapping the lipid-exposed regions in the *Torpedo californica* nicotinic acetylcholine receptor [published erratum appears in Biochemistry 1992 Jun 30;31(25):5951]. *Biochemistry* **31**, 3738-3750
229. Xu, Y., Barrantes, F. J., Luo, X., Chen, K., Shen, J., and Jiang, H. (2005) Conformational dynamics of the nicotinic acetylcholine receptor channel: a 35-ns molecular dynamics simulation study. *J Am Chem Soc* **127**, 1291-1299
230. Williamson, P. T., Zandomeneghi, G., Barrantes, F. J., Watts, A., and Meier, B. H. (2005) Structural and dynamic studies of the γ-M4 trans-membrane domain of the nicotinic acetylcholine receptor. *Mol Membr Biol* **22**, 485-496
231. Antollini, S. S., Xu, Y., Jiang, H., and Barrantes, F. J. (2005) Fluorescence and molecular dynamics studies of the acetylcholine receptor γM4 transmembrane peptide in reconstituted systems. *Mol Membr Biol* **22**, 471-483
232. daCosta, C. J., Michel Sturgeon, R., Hamouda, A. K., Blanton, M. P., and Baenziger, J. E. (2011) Structural characterization and agonist binding to human α4β2 nicotinic receptors. *Biochem Biophys Res Commun* **407**, 456-460
233. Hilf, R. J., and Dutzler, R. (2009) Structure of a potentially open state of a proton-activated pentameric ligand-gated ion channel. *Nature* **457**, 115-118
234. Heidmann, T., Sobel, A., Popot, J. L., and Changeux, J. P. (1980) Reconstitution of a functional acetylcholine receptor. Conservation of the conformational and allosteric transitions and recovery of the permeability response; role of lipids. *Eur J Biochem* **110**, 35-55
235. Sturgeon, R. M., and Baenziger, J. E. (2010) Cations mediate interactions between the nicotinic acetylcholine receptor and anionic lipids. *Biophys J* **98**, 989-998
236. daCosta, C. J., Wagg, I. D., McKay, M. E., and Baenziger, J. E. (2004) Phosphatidic acid and phosphatidylserine have distinct structural and functional interactions with the nicotinic acetylcholine receptor. *J Biol Chem* **279**, 14967-14974
237. Pandhare, A., Hamouda, A. K., Staggs, B., Aggarwal, S., Duddempudi, P. K., Lever, J. R., Lapinsky, D. J., Jansen, M., Cohen, J. B., and Blanton, M. P. (2012) Bupropion binds to two sites in the Torpedo nicotinic acetylcholine receptor transmembrane domain: a photoaffinity labeling study with the bupropion analogue [^{125}I]-SADU-3-72. *Biochemistry* **51**, 2425-2435
238. Morales, A., Aleu, J., Ivorra, I., Ferragut, J. A., Gonzalez-Ros, J. M., and Miledi, R. (1995) Incorporation of reconstituted acetylcholine receptors from Torpedo into the Xenopus oocyte membrane. *Proc Natl Acad Sci U S A* **92**, 8468-8472
239. Ryan, S. E., Demers, C. N., Chew, J. P., and Baenziger, J. E. (1996) Structural effects of neutral and anionic lipids on the nicotinic acetylcholine receptor. An infrared difference spectroscopy study. *J Biol Chem* **271**, 24590-24597
240. Jones, O. T., and McNamee, M. G. (1988) Annular and nonannular binding sites for cholesterol associated with the nicotinic acetylcholine receptor. *Biochemistry* **27**, 2364-2374
241. Brannigan, G., Henin, J., Law, R., Eckenhoff, R., and Klein, M. L. (2008) Embedded cholesterol in the nicotinic acetylcholine receptor. *Proc Natl Acad Sci U S A* **105**, 14418-14423

242. Marsh, D., Watts, A., and Barrantes, F. J. (1981) Phospholipid chain immobilization and steroid rotational immobilization in acetylcholine receptor-rich membranes from *Torpedo marmorata*. *Biochim Biophys Acta* **645**, 97-101
243. Ellena, J. F., Blazing, M. A., and McNamee, M. G. (1983) Lipid-protein interactions in reconstituted membranes containing acetylcholine receptor. *Biochemistry* **22**, 5523-5535
244. Jha, A., Cadugan, D. J., Purohit, P., and Auerbach, A. (2007) Acetylcholine receptor gating at extracellular transmembrane domain interface: the cys-loop and M2-M3 linker. *J Gen Physiol* **130**, 547-558
245. Lee, W. Y., Free, C. R., and Sine, S. M. (2009) Binding to gating transduction in nicotinic receptors: Cys-loop energetically couples to pre-M1 and M2-M3 regions. *J Neurosci* **29**, 3189-3199
246. Velisetty, P., Chalamalasetti, S. V., and Chakrapani, S. (2012) Conformational transitions underlying pore opening and desensitization in membrane-embedded GLIC. *J Biol Chem*
247. Wang, H. L., Cheng, X., and Sine, S. M. (2012) Intramembrane proton binding site linked to activation of bacterial pentameric ion channel. *J Biol Chem* **287**, 6482-6489
248. Li, L., Lee, Y. H., Pappone, P., Palma, A., and McNamee, M. G. (1992) Site-specific mutations of nicotinic acetylcholine receptor at the lipid-protein interface dramatically alter ion channel gating. *Biophys J* **62**, 61-63
249. Lee, Y. H., Li, L., Lasalde, J., Rojas, L., McNamee, M., Ortiz-Miranda, S. I., and Pappone, P. (1994) Mutations in the M4 domain of Torpedo californica acetylcholine receptor dramatically alter ion channel function. *Biophys J* **66**, 646-653
250. Lasalde, J. A., Tamamizu, S., Butler, D. H., Vibat, C. R., Hung, B., and McNamee, M. G. (1996) Tryptophan substitutions at the lipid-exposed transmembrane segment M4 of Torpedo californica acetylcholine receptor govern channel gating. *Biochemistry* **35**, 14139-14148
251. Bouzat, C., Roccamo, A. M., Garbus, I., and Barrantes, F. J. (1998) Mutations at lipid-exposed residues of the acetylcholine receptor affect its gating kinetics. *Mol Pharmacol* **54**, 146-153
252. Tamamizu, S., Guzman, G. R., Santiago, J., Rojas, L. V., McNamee, M. G., and Lasalde-Dominicci, J. A. (2000) Functional effects of periodic tryptophan substitutions in the alpha M4 transmembrane domain of the Torpedo californica nicotinic acetylcholine receptor. *Biochemistry* **39**, 4666-4673
253. Sauguet, L., Poitevin, F., Murail, S., Van Renterghem, C., Moraga-Cid, G., Malherbe, L., Thompson, A. W., Koehl, P., Corringer, P. J., Baaden, M., and Delarue, M. (2013) Structural basis for ion permeation mechanism in pentameric ligand-gated ion channels. *EMBO J*
254. Zimmermann, I., Marabelli, A., Bertozzi, C., Sivilotti, L. G., and Dutzler, R. (2012) Inhibition of the prokaryotic pentameric ligand-gated ion channel ELIC by divalent cations. *PLoS Biol* **10**, e1001429
255. Laitko, U., Juranka, P. F., and Morris, C. E. (2006) Membrane stretch slows the concerted step prior to opening in a Kv channel. *J Gen Physiol* **127**, 687-701
256. Lovell, S. C., Davis, I. W., Arendall, W. B., 3rd, de Bakker, P. I., Word, J. M., Prisant, M. G., Richardson, J. S., and Richardson, D. C. (2003) Structure validation by Calpha geometry: phi,psi and Cbeta deviation. *Proteins* **50**, 437-450

257. Wang, J. M., Zhang, L., Yao, Y., Viroonchatapan, N., Rothe, E., and Wang, Z. Z. (2002) A transmembrane motif governs the surface trafficking of nicotinic acetylcholine receptors. *Nat Neurosci* **5**, 963-970
258. Pons, S., Sallette, J., Bourgeois, J. P., Taly, A., Changeux, J. P., and Devillers-Thiery, A. (2004) Critical role of the C-terminal segment in the maturation and export to the cell surface of the homopentameric alpha 7-5HT3A receptor. *Eur J Neurosci* **20**, 2022-2030
259. Paradiso, K., Zhang, J., and Steinbach, J. H. (2001) The C terminus of the human nicotinic alpha4beta2 receptor forms a binding site required for potentiation by an estrogenic steroid. *J Neurosci* **21**, 6561-6568
260. Hosie, A. M., Wilkins, M. E., da Silva, H. M., and Smart, T. G. (2006) Endogenous neurosteroids regulate $GABA_A$ receptors through two discrete transmembrane sites. *Nature* **444**, 486-489
261. Tamamizu, S., Lee, Y., Hung, B., McNamee, M. G., and Lasalde-Dominicci, J. A. (1999) Alteration in ion channel function of mouse nicotinic acetylcholine receptor by mutations in the M4 transmembrane domain. *The Journal of membrane biology* **170**, 157-164
262. Pan, J., Chen, Q., Willenbring, D., Mowrey, D., Kong, X. P., Cohen, A., Divito, C. B., Xu, Y., and Tang, P. (2012) Structure of the pentameric ligand-gated ion channel GLIC bound with anesthetic ketamine. *Structure* **20**, 1463-1469
263. Nury, H., Van Renterghem, C., Weng, Y., Tran, A., Baaden, M., Dufresne, V., Changeux, J. P., Sonner, J. M., Delarue, M., and Corringer, P. J. (2011) X-ray structures of general anaesthetics bound to a pentameric ligand-gated ion channel. *Nature* **469**, 428-431